



# Phase-field modelling and simulations of phase separation in the two-phase nuclear glass $\text{Na}_2\text{O-SiO}_2\text{-MoO}_3$

Werner Verdier

## ► To cite this version:

Werner Verdier. Phase-field modelling and simulations of phase separation in the two-phase nuclear glass  $\text{Na}_2\text{O-SiO}_2\text{-MoO}_3$ . Fluid Dynamics [physics.flu-dyn]. Institut Polytechnique de Paris, 2022. English. NNT : 2022IPPAX126 . tel-04106919

**HAL Id: tel-04106919**

**<https://theses.hal.science/tel-04106919>**

Submitted on 25 May 2023

**HAL** is a multi-disciplinary open access archive for the deposit and dissemination of scientific research documents, whether they are published or not. The documents may come from teaching and research institutions in France or abroad, or from public or private research centers.

L'archive ouverte pluridisciplinaire **HAL**, est destinée au dépôt et à la diffusion de documents scientifiques de niveau recherche, publiés ou non, émanant des établissements d'enseignement et de recherche français ou étrangers, des laboratoires publics ou privés.

# Phase-field modelling and simulations of phase separation in the two-phase nuclear glass $\text{Na}_2\text{O}-\text{SiO}_2-\text{MoO}_3$

Thèse de doctorat de l'Institut Polytechnique de Paris  
préparée à l'École polytechnique

École doctorale n°626 École doctorale de l'Institut Polytechnique de Paris (EDIPP)  
Spécialité de doctorat : Physique

Thèse présentée et soutenue à Gif-sur-Yvette, le 12 décembre 2022, par

**Werner Verdier**

Composition du Jury :

Vincent Faucher Directeur de recherche, CEA (DES/IRESNE/DTN)	Président
Franck Pigeonneau Directeur de recherche, Mines Paris (CEMEF)	Rapporteur
Laurent Talon Chargé de recherche, Université Paris-Saclay (FAST)	Rapporteur
Yann Le Bouar Directeur de recherche, CNRS/Onera (LEM)	Examineur
Mathis Plapp Directeur de laboratoire, CNRS, École Polytechnique, IPP (PMC)	Directeur de thèse
Alain Cartalade Ingénieur-chercheur, CEA Saclay (DES/ISAS/STMF)	Co-directeur de thèse

# Abstract

A safe and convenient method for the containment of high-level and long-lived nuclear waste obtained from the reprocessing of nuclear fuel is its inclusion in nuclear glasses, which are specifically designed to provide the best combination of chemical and radioactive resistance, of inclusion capacity, and of ease of industrial implementation. The SIVIT (SIMulation of VITrification) project of the CEA studies the behaviour of the glass during the vitrification process, where the glass and the waste are mixed and brought to a high temperature and then solidified. It is desirable to control a whole set of macroscopic properties (chemical, thermodynamic, mechanical...) in the produced material, and one of them in particular is the possible occurrence of phase separation. For example, during the vitrification of waste enriched in molybdenum, phase separation may occur following the nucleation and growth regime, with the molybdenum segregating to the daughter phase. The present work, as part of the SIVIT project, aims to model and simulate this phase separation at the scale of the interface separating the two liquid phases of the melted glass. To this end, the modelling must satisfy a number of constraints: tracking a fully-resolved interface; accounting for the chemical diffusion (which drives the growth dynamics) and the flow dynamics and the effects of each on the motion of the interfaces; and the respect of the equation of state of the glass. We will first examine the case of a model ternary glass, the  $\text{Na}_2\text{O}-\text{SiO}_2-\text{MoO}_3$  compound. Its phase diagram was established at the CEA of Saclay, and experimental observations with this glass are being carried out at the CEA Marcoule. Simulations of the model must also have a high numerical efficiency to allow for comparisons in three dimensions at a satisfying scale with the previously mentioned observations. To fulfil these requirements, we formulate a model based on the phase field theory with a grand potential formulation coupled to the diffusion of the chemical components and to the incompressible Navier-Stokes equations. We discretize this model with the lattice Boltzmann method and implement it in a new high-performance simulation code, LBM\_saclay, able to exploit the multi-GPU architectures of modern supercomputers. We then demonstrate the capability of the model to quantitatively reproduce the growth dynamics after nucleation and the influence of flow and sedimentation on these dynamics. This is done with an idealized equation of state. Finally, we detail at the end the method to couple the model to the thermodynamic data of the real nuclear glass.

# Résumé en français

Les déchets nucléaires de haute activité (HA) nécessitent une stratégie de confinement bien particulière. La recherche sur ce sujet a commencée en France dans les années 1950 et a montré que le verre est le matériau le plus approprié à confiner les déchets HA : un verre spécifiquement élaboré assure le meilleur compromis entre capacité d'incorporation, de mise en œuvre et de résistances (chimiques, radioactive...). Un tel verre peut alors servir lors du processus industriel de vitrification, où le verre et les déchets sont mélangés et portés à très haute température (dans un creuset froid par exemple). Après refroidissement, le verre solidifiée piège ainsi les éléments radioactifs.

Le traitement de ces déchets fait partie intégrante du cycle du combustible nucléaire et figure parmi les problématiques de recherche du CEA. Le projet inter-centre SIVIT (SIMulation de la VITrification) du CEA, dans lequel se situe ce travail, s'intéresse en particulier au comportement du verre lors de la vitrification. Ce procédé inclut des phénomènes physiques très variés, comme par exemple l'hydrodynamique du verre fondu en creuset, avec le couplage magnéto-hydrodynamique lié au chauffage par induction et les interactions fluide-parois, ou la thermo-chimie bien particulière du verre et de ses changements de phase qui sont conséquences des larges gammes de températures qu'il traverse.

Cette thèse s'intéresse à ce second volet, et plus précisément à la cinétique de la séparation de phase dans le verre. Notamment, dans le cas de la vitrification de déchets enrichis en molybdène, le verre peut se séparer en deux phases selon un mécanisme de nucléation-croissance. En effet, les propriétés chimiques particulières du molybdène fait que cet élément va se ségréger du mélange homogène initial pour former des "goutellettes" (phase fille) enrichies de cet élément qui sont immiscibles au mélange initial (phase mère) qui au contraire s'appauvrit en molybdène. La distribution et la géométrie de ces goutellettes dépendront de la thermodynamique du verre, du mélange initial, des propriétés d'interface (la tension de surface) ou même de l'écoulement. Ainsi, même si ce phénomène physique n'est qu'une partie de la phénoménologie complète du procédé de vitrification, le modéliser et le simuler reste un défi.

Dans cette thèse, nous établissons un modèle physique pour la séparation de phase dans un verre de confinement. Celui-ci répond à plusieurs contraintes nécessaires à une modélisation cohérente : le suivi d'une interface entièrement résolue ; la prise en compte de la diffusion chimique (qui pilote la dynamique de croissance) et de la dynamique d'écoulement et leur effets sur la cinétique de l'interface ; et le respect du paysage thermodynamique du verre. Nous nous intéressons d'abord à un verre ternaire modèle élaboré avec le composé  $\text{Na}_2\text{O}-\text{SiO}_2-\text{MoO}_3$ , dont le diagramme de phase a été établi au CEA de Saclay et dont les observations sont en cours au CEA de Marcoule. Les simulations de ce modèle doivent aussi démontrer un haut degré de performance pour en permettre les comparaisons en 3D et à une échelle satisfaisante avec ces observations expérimentales.

Pour répondre à toute ces contraintes, nous formulons au premier chapitre un modèle basé sur la théorie du champ de phase et son couplage à la diffusion des composants et aux équations de Navier-Stokes incompressibles. Dans la théorie du champ de phase, l'interface est représentée par un champ diffusé sur une couche d'épaisseur finie et constante. En particulier, nous étendons une reformulation en grand potentiel de la littérature au cas ternaire pour écrire un couplage cohérent avec la diffusion des



trois oxides du verre  $\text{Na}_2\text{O}-\text{SiO}_2-\text{MoO}_3$  ainsi qu'à la thermodynamique du matériau. Nous montrons aussi que le modèle admet une limite vers un modèle à interface nette avec une condition d'interface de type Gibbs-Thomson. Cette condition spécifie que l'équilibre thermodynamique local de l'interface est perturbé par sa vitesse et sa courbure ; ce dernier point est nécessaire à la description de la cinématique de croissance après nucléation.

Dans le second chapitre, nous discrétisons ce modèle avec la méthode de Boltzmann sur réseau (*Lattice Boltzmann Method*, LBM) et la programmons dans un nouveau code de simulation à haute performance portable, LBM\_saclay. La LBM est une méthode de discrétisation relativement jeune applicable aux équations de diffusion scalaires ou vectorielles comme celles qui composent notre modèle, et le code LBM\_saclay implémente cette discrétisation. Grâce à la librairie C++ Kokkos, le code est aussi capable d'exploiter les architectures des supercalculateurs modernes multi-GPU (*Graphical Processing Unit*) aussi bien qu'une machine de bureau avec un unique processeur *multithread* plus classique. Nous montrons comment sont programmés les schémas LBM et nous expliquons comment sont gérés les problématiques liées au parallélisme.

Au troisième chapitre, nous montrons la validité du modèle et de sa discrétisation bloc-par-bloc en comparant des résultats de simulations avec des problèmes aux solutions analytiques connues. Une simulation d'écoulement de double-Poiseuille valide d'abord la partie d'écoulement à deux fluides (équations du champ de phase couplées aux équations de Navier-Stokes). Ensuite, une simulation d'un couple de diffusion ternaire valide la modélisation d'un matériau ternaire diphasique sans écoulement (équation du champ de phase couplées à la diffusion chimique) et confirme aussi la reproduction d'une condition d'interface de type Gibbs-Thomson. Ces préparatifs fait, nous témoignons ensuite de notre capacité à simuler la croissance après nucléation à une large échelle (2000 gouttelettes en 3D). Des mesures en temps du nombre et du rayon des gouttelettes montrent que le régime de croissance simulé est en accord avec la théorie du mûrissement d'Ostwald. Nous exposons aussi comment l'écoulement, à travers la flottabilité, peut influencer sur ce régime. Tout ceci est fait avec une thermodynamique idéalisée ; à la fin du chapitre, nous détaillons la stratégie de couplage du modèle avec les données thermodynamique du verre  $\text{Na}_2\text{O}-\text{SiO}_2-\text{MoO}_3$ .

Une conclusion générale termine le manuscrit. Elle synthétise le travail réalisé et les résultats obtenus et énumère les extensions possibles du travail, que ce soit sur ces aspects théorique (modélisation) que numériques (efficacité de la discrétisation) pour raffiner au mieux la description d'un vrai verre de confinement.

# Contents

<b>Introduction</b>	<b>6</b>
References . . . . .	9
<b>1 Phase field theory</b>	<b>10</b>
1.1 Thermodynamics of phase separation . . . . .	10
1.1.1 Equilibrium thermodynamics . . . . .	10
1.1.2 Chemical potential and grand potential . . . . .	12
1.1.3 Kinetics: Onsager and Fick diffusion . . . . .	14
1.1.4 Surface tension . . . . .	14
1.2 Phase field models . . . . .	16
1.2.1 Minimization of an energy functional . . . . .	16
1.2.2 Time evolution: Cahn-Hilliard and Allen-Cahn equations . . . . .	17
1.2.3 Flow coupling . . . . .	19
1.2.4 Coupling the Allen-Cahn equation to the chemical diffusion . . . . .	22
1.2.5 Asymptotic Gibbs-Thomson interface condition . . . . .	24
1.3 Two-phase three component model . . . . .	24
1.3.1 Multi-component considerations . . . . .	24
1.3.2 Ternary free energies and change of variables . . . . .	27
1.3.3 Energy dimension removal . . . . .	28
1.3.4 PDE system . . . . .	29
1.3.5 Conclusion . . . . .	31
References . . . . .	32
<b>2 Numerical implementation</b>	<b>34</b>
2.1 Lattice Boltzmann method . . . . .	34
2.1.1 Discretization of a Boltzmann equation . . . . .	35
2.1.2 Reconstructed macroscopic equations, Chapman-Enskog expansion . . . . .	36
2.1.3 Time evolution algorithm . . . . .	37
2.1.4 Initial and boundary conditions . . . . .	37
2.1.5 Finite differences stencil . . . . .	38
2.1.6 LBM discretization of the two-phase three component phase field model . . . . .	38
2.2 The simulation code LBM_saclay . . . . .	41
2.2.1 High performance computing and parallelization . . . . .	41
2.2.2 The Kokkos library . . . . .	42
2.2.3 MPI domain decomposition . . . . .	43
2.2.4 Boundary conditions with the ghost layer . . . . .	44
2.2.5 Implementation of the two-phase three-component phase field model . . . . .	46

2.3	Other numerical considerations . . . . .	47
2.4	Conclusion . . . . .	47
	References . . . . .	48
<b>3</b>	<b>Simulations</b> . . . . .	<b>52</b>
3.1	Numerical units . . . . .	52
3.2	Verifications of subsets of the two-phase three-component flow model . . . . .	52
3.2.1	Two-phase flow: Double Poiseuille . . . . .	52
3.2.2	Two-phase three-component: diffusion couple . . . . .	53
3.3	Simulation of droplet growth . . . . .	60
3.3.1	Theory of Ostwald ripening . . . . .	60
3.3.2	Initial conditions . . . . .	60
3.3.3	Geometry measurements . . . . .	62
3.3.4	Simulation results . . . . .	63
3.4	Conclusion . . . . .	65
3.4.1	Opening: comparison to experiments . . . . .	72
3.4.2	Coupling to the thermodynamic potential of the $\text{Na}_2\text{O-SiO}_2\text{-MoO}_3$ glass . . . . .	72
	References . . . . .	76
	<b>Conclusion</b> . . . . .	<b>79</b>
	<b>Acknowledgements</b> . . . . .	<b>81</b>
<b>A</b>	<b>Asymptotic analysis of the two-phase three components model</b> . . . . .	<b>82</b>
A.1	Sharp- and thin-interface limit, rescaling . . . . .	83
A.2	Inner region, curvilinear coordinates . . . . .	85
A.2.1	Scale factors and differential operators . . . . .	85
A.2.2	Stretched normal coordinate and diffusive scaling . . . . .	87
A.3	Expansions and matching conditions . . . . .	87
A.4	Expansion and analysis of the ternary model . . . . .	88
A.4.1	Phase-field $O(1)$ . . . . .	88
A.4.2	Diffusion and closure $O(1)$ . . . . .	88
A.4.3	Phase-field $O(\varepsilon)$ . . . . .	89
A.4.4	Diffusion and closure $O(\varepsilon)$ . . . . .	89
A.4.5	Phase-field $O(\varepsilon^2)$ . . . . .	91
A.4.6	Diffusion and closure $O(\varepsilon^2)$ . . . . .	93
A.4.7	Summary . . . . .	95
A.4.8	Numerical application: symmetrical diffusion couple . . . . .	96
A.5	Other differential operators in curvilinear coordinates . . . . .	96
	References . . . . .	97
<b>B</b>	<b>Two papers published during this thesis</b> . . . . .	<b>98</b>
	References . . . . .	98

# Introduction

Nuclear power plants produce energy by sustaining nuclear fission using a fissile fuel. The spent fuel is then reprocessed to extract on one hand the unused fissile elements, so that the spent fuel may be recycled; and on the other hand the unusable fission by-products. These unusable products, the nuclear waste, are generally radioactive and cover a wide range of radioactivity level and lifetimes. The French nuclear industry classifies the waste according to those two properties and establishes different treatments and containment strategies for each class. One of them is the category of high level waste (*déchets HA, de haute activité*) which are accountable for about 95% of the total radioactivity of all waste in the country despite representing less than 1% of its volume [1]. The elements found in this waste include some with half-times around 30 years and activities in the terabecquerels per gram ( $10^{12}$  nuclear decays per second per gram) and all the different elements react together to form a complex chemical solution with as many as 40 different chemical species.

Because of their non-negligible lifetimes, their high radioactivity (with the accompanying heat generation), but also their significant chemical activity, high level waste requires very elaborate containment procedures. Research on its containment started in France in the 1950s and it soon showed that glass would be the most appropriate material to isolate the waste as it can achieve the best combination of thermal, chemical and radioactive impermeability [6]. Glasses specifically elaborated for this purpose are called nuclear glasses, and the process of containing nuclear waste in nuclear glasses is known as vitrification. Vitrification is conducted by mixing the calcined fission waste and the melted glass in a furnace. The recent technology used for this process is the cold crucible induction melter: it uses magnetic induction to heat up the furnace in its centre (to as high as 1300 °C) while a protective solid layer forms on its walls.

The nuclear waste, being an integral part of the nuclear fuel cycle, is a research interest of the CEA. Research on the vitrification process is primarily conducted at the CEA Marcoule, in the south of France. One aspect of this research is to find the best glass chemical compound for specific profiles of waste and furnace technology, and one particular case study is the handling of legacy waste rich in molybdenum. This element is troublesome not necessarily for its radioactivity, but because of its corrosive action against the glass and its very low solubility inside the glass [4, 6]. In a model molybdenum-enriched glass, the  $\text{Na}_2\text{O}-\text{SiO}_2-\text{MoO}_3$  compound, one can observe the typical behaviour due to the low solubility: the molybdenum oxide  $\text{MoO}_3$  segregates from the initially homogeneous melted glass to form a daughter phase enriched in molybdenum. This behaviour can be explained purely by the thermodynamics of the compound as it explores its phase diagram during heating, and at the adequate temperature and initial composition inventory, this new phase can be liquid and looks similar to the observations presented in fig. 1 (right): an ensemble of droplets carried by the mother phase in the background. This new phase appears following the mechanism of nucleation and growth, a slow and local phase separation mechanism; as opposed to the spinodal decomposition, a rapid phase separation mechanism.

The cross-department project SIVIT (Simulation of VITrification) of CEA, with support from its industrial partners EDF and Orano, aims at the simulation of the complete vitrification process as done in a cold crucible. This process has a great variety in its involved physics: the magnetohydrodynamics

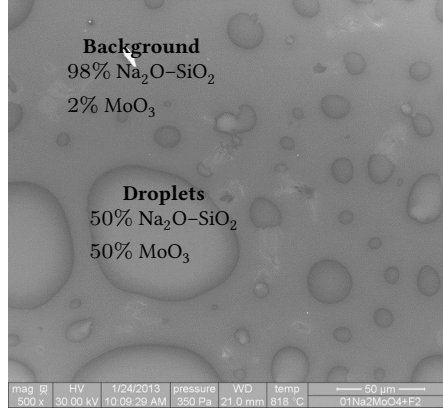


Figure 1: Experimental observations of liquid-liquid phase separation in a nuclear glass compound. The  $\text{Na}_2\text{O-SiO}_2\text{-MoO}_3$  compound separates in a similar fashion, with droplets of daughter phase separating from the mother glass matrix phase. An interface cleanly separates both phases.

of the induction heating; the purely mechanical part of the hydrodynamics, with the waste injection, the mixing with the glass frit, the stirring of both and the wall interactions; the reactive chemistry of all materials involved; the complex thermodynamics and the ensuing phenomena, such as the phase separation mentioned before; and of course, the interactions between all these phenomenologies. The present work takes place within the SIVIT project to model and simulate a restricted but precise scope of the bulk vitrification physics. Namely, we are interested in modelling the kinetics of the liquid-liquid interface of a nuclear glass as its phases separate. We will account for the influence of the fluid flow, of the diffusion of the glass' chemical components and of the thermodynamics of the glass on these kinetics.

The modelling of this phase separation process implies the construction of a coupled mathematical model for a fully resolved interface tracked in time, for a two-phase flow, and for the chemical diffusion. Two additional constraints are added: this model must have a strong thermodynamic consistency to respect the thermodynamics of the glass, and simulations of the model must have a high numerical efficiency to allow for comparisons in three dimensions at a satisfying scale with experimental observations. The ternary  $\text{Na}_2\text{O-SiO}_2\text{-MoO}_3$  compound will serve as a test case as relevant experimental data is either already available or is being collected. The physicochemistry department of the CEA of Saclay established the temperature- and composition-dependent phase diagram of this glass (see fig. 2) while experimental observations of the  $\text{Na}_2\text{O-SiO}_2\text{-MoO}_3$  phase separation in a furnace are ongoing at the CEA Marcoule.

To fulfil above-mentioned requirements, we formulate a mathematical model of coupled PDEs (partial differential equations) based on the phase field theory with a grand potential reformulation. The phase field formalism starts from a thermodynamic description of a two-phase material and produces a time-evolution PDE to track a fully resolved interface. This interface is represented as a smoothed step function over a fixed width for an indicator field (the eponymous phase field) with its bounds representing each bulk phase: this makes the phase field a diffuse interface approach to the two-phase problem, in contrast to sharp-interface approaches. The origin of the method exposes a clear and consistent way to be faithful to the thermodynamics of the material studied, including here the detail of the local diffusion of the three oxides through the interface and in the bulk phases. Since the numerical space discretization is limited by the thickness of the interface, values much larger than the real physical width (typically in the  $10^{-10}$  meter range) must be used to obtain efficient simulations. The

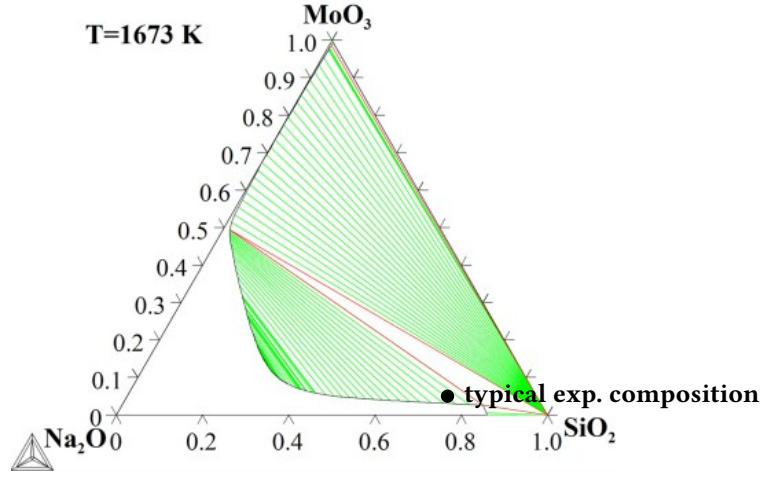


Figure 2: Phase diagram of the  $\text{Na}_2\text{O}-\text{SiO}_2-\text{MoO}_3$  glass established by the physicochemistry department of the CEA of Saclay [2]. The point of experimental interest is shown with a black dot, at about a 80%/20% mix of  $\text{SiO}_2$  and  $\text{Na}_2\text{O}$  and less than 10% of  $\text{MoO}_3$ . The composition of the individual liquid phases is read on the extremities of the green tieline on which that point sits: a daughter phase enriched at about 50% in  $\text{MoO}_3$  and a mother phase with a composition close to the initial mix. This diagram is drawn in the Gibbs triangle with the three component being the oxides  $\text{Na}_2\text{O}$ ,  $\text{SiO}_2$  and  $\text{MoO}_3$ . In the following sections of this manuscript, the three component will be noted  $A$ ,  $B$  and  $C$  instead.

effects of this upscaling can be quantified through the reconstruction of a Gibbs-Thomson interface condition, which also helps to bridge the diffuse- and sharp-interface views. The implicit representation of the interface and the controllable finite width make the phase field formalism a good candidate for a numerically efficient two-phase model. Lastly, it is easy to couple a phase field model to the incompressible Navier-Stokes equations to create a two-phase three-component flow model. These details and the derivation of the complete PDE model will be presented in chapter 1. We will explain some part of the derivation relatively quickly as they were already presented in our previously published work: the Navier-Stokes coupling introduced in ref. [5] and the mixed formulation grand potential method used in ref. [3] in the binary case.

Because the phase field model needs only a scalar field and the resolution of an additional PDE, it does not constrain our choice of numerical discretization. We thus chose the lattice Boltzmann method (LBM) as our discretization method. The LBM solves partial differential equations by acting on distribution functions as the solutions of a Boltzmann equation discretized in space and velocities. Akin to the kinetic theory of gases, the macroscopic PDE and its variables are recovered as the moments of this discrete Boltzmann equation and the distribution functions: a discrete equivalent of the Chapman-Enskog expansion. The LBM was first established as an efficient explicit scheme for the Navier-Stokes equation but it is in fact applicable to most scalar or vector PDEs with diffusive terms, like the one for the phase field and the composition. The other motivating factor is the adequacy of the LBM to high performance computations (HPC) and more precisely to modern HPC clusters powered by graphical processing units (GPUs, as opposed to the usual central processing units, CPUs). To exploit this, we have continued the development of LBM\_saclay, a high performance simulation code based on LBM schemes. The code relies on the Kokkos C++ library to run its calculations on a multithreaded CPU or a (by design) highly-parallel GPU. The MPI standard is also used to distribute the simulations on multi-CPU or multi-GPU computing nodes as found on HPC clusters. In chapter 2, we will introduce the

lattice Boltzmann method, discretize the model derived in the first chapter, and present the LBM\_saclay code and how it achieves its high parallel performance.

Once the model, its discretization and implementation are detailed, we will show in chapter 3 simulations of the two-phase three-component model ran with LBM\_saclay. We start with intermediate validations. These are done by simulating subsets of the complete model and numerically solving a few classical two-phase flows and two-phase diffusion problems, comparing the results against the known analytical solutions. Then, we simulate the growth kinetics of a population of droplets after nucleation, first without flow and then with a 3D buoyancy-driven flow. We will compare the time evolution of the droplets' mean radius to the power-law in time expected from the Ostwald ripening theory, with an exponent dependent on the property of the flow. These kinematics depend on the Gibbs-Thomson condition, which we will have proven to be indeed reconstructed both theoretically and numerically by the model. The phase field method is particularly adapted to this test case, as it can handle the disappearance and merging of interfaces with no further complications; however the initial condition requires a bit of care with an Allen-Cahn model, as will be detailed. The droplet growth simulations will be a first proof of the applicability of the complete model to describe the growth observed in the  $\text{Na}_2\text{O-SiO}_2\text{-MoO}_3$  glass. Experimental observations could not yet be made; we have instead focused our efforts on the quantification of the buoyancy effects on the ripening kinematics and on attempts to insert the real thermodynamic data of the glass compound (*ie.* the phase diagram of figure 2) into our modelling.

A general conclusion will end this manuscript. It will synthesize the work done and the results obtained and enumerate the possible extensions of the model and the description of the real nuclear glass on multiple aspects: the theoretical phase field; its discretization and the numerical efficiency of its implementation; and the parametrization of the thermodynamic, chemical, and mechanical properties of the  $\text{Na}_2\text{O-SiO}_2\text{-MoO}_3$  glass.

## References

- [1] ANDRA. *Inventaire national des matières et déchets radioactifs*. [https://inventaire.andra.fr/sites/default/files/documents/pdf/fr/in\\_-\\_edition\\_2009\\_-\\_en\\_resume.pdf](https://inventaire.andra.fr/sites/default/files/documents/pdf/fr/in_-_edition_2009_-_en_resume.pdf). Retrieved 11/10/2022. 2009.
- [2] Sébastien Bordier. “Modélisation thermodynamique des phases insolubles dans les verres nucléaires : application à la vitrification du molybdène et des produits de fission platinoides.” 2015AIXM4339. PhD thesis. 2015.
- [3] Téo Boutin, Werner Verdier, and Alain Cartalade. “Grand-potential-based phase-field model of dissolution/precipitation: Lattice Boltzmann simulations of counter term effect on porous medium.” In: *Computational Materials Science* 207 (2022), p. 111261. ISSN: 0927-0256. DOI: <https://doi.org/10.1016/j.commatsci.2022.111261>.
- [4] R. J. Short, R. J. Hand, and N. C. Hyatt. “Molybdenum in Nuclear Waste Glasses - Incorporation and Redox state.” In: *MRS Online Proceedings Library* 757 (2011). ISSN: 1946-4274. DOI: 10.1557/PROC-757-115.4.
- [5] Werner Verdier, Pierre Kestener, and Alain Cartalade. “Performance portability of lattice Boltzmann methods for two-phase flows with phase change.” In: *Computer Methods in Applied Mechanics and Engineering* 370 (2020), p. 113266. ISSN: 0045-7825. DOI: <https://doi.org/10.1016/j.cma.2020.113266>.
- [6] Étienne Vernaz and Jérôme Bruezière. “History of Nuclear Waste Glass in France.” In: *Procedia Materials Science* 7 (2014), pp. 3–9. DOI: 10.1016/j.mspro.2014.10.002.

# Chapter 1

## Phase field theory

The phase field method is the theoretical framework used for the modelling throughout this thesis work. It is a description of a two-phase material in a continuum framework, where a scalar field  $\varphi(t, \mathbf{x})$ , is used to describe the geometrical distribution of the phases as well as the interface between them. This modelling can be traced back to van der Waals [26, translation of van der Waals' original 1893 paper] in the context of liquid-gas interfaces. Van der Waals proposed that the fluid density  $\rho$  should vary continuously between the two phases across a diffuse interface and modelled the capillar energy with an integral over  $\rho$  and its gradient. The same formalism was reintroduced by Cahn and Hilliard [9] taking the example of a two-phase solution with the composition as a continuous order parameter. The Cahn-Hilliard equation, one class of phase field models, is named after them. Another class of models, where the order parameter is not conserved is based on the Allen-Cahn equation [1].

The phase field theory has a strong thermodynamic consistency. To understand this, we will first introduce the thermodynamic modelling of phase separation in sec. 1.1. Next, sec. 1.2 will present the phase field models themselves and their derivation based on the free energy of the system. We will present both the Cahn-Hilliard and Allen-Cahn equations, and explain why we prefer the latter. We will also present how the Allen-Cahn equation can be coupled to the incompressible Navier-Stokes equations or to the Onsager diffusion equation after a grand potential reformulation. With all the necessary ingredients introduced, we will finally detail in 1.3 the two-phase ternary fluid model used in our work.

### 1.1 Thermodynamics of phase separation

This section introduces the basic thermodynamic description of phase separation. It will introduce the background for the modelling made by the phase field theory, but it is not strictly necessary to understand its mathematical formulation. For a more detailed lecture, one can refer to ref. [8].

#### 1.1.1 Equilibrium thermodynamics

Take the example of a binary system with two components  $A$  and  $B$  and under the temperature  $T$ . This system may present itself as a homogeneous mixture of the two components (eg. a solvent  $A$  in a solute  $B$ ). It may alternatively separate into two stable phases, one enriched in  $A$  and another in  $B$  (eg. air bubbles in water or oil in water). The phase separation can occur in two regimes a local and stochastic nucleation, or a global and spontaneous spinodal decomposition. The thermodynamics of the system describes this situation through the change of a thermodynamic potential with respect to global parameters of the system.



In our example, we describe the system by tracking the change of a free energy  $F(N^A, N^B, T)$ , function<sup>1</sup> of the numbers of particles of  $A$ , of  $B$  and of the temperature  $T$ . Under the additional constraint that the total count of particles is constant,  $N^A$  and  $N^B$  can be reduced to a single variable of composition (here, of  $A$ ),

$$c = \frac{N^A}{N^A + N^B}. \quad (1.1.1)$$

The nature of the system's equilibrium depends on the minima of  $F(c, T)$ . When  $F$  exhibits a single minimum, the system allows only a single-phase equilibrium. The system can also allow the coexistence of multiple phases when  $F$  has multiple local minima. This situation is modelled with a double-well structure shown in figure 1.1. It can be used to map each couple  $(c, T)$  to either a single- or two-phase equilibrium as represented by the phase diagram in the same figure.

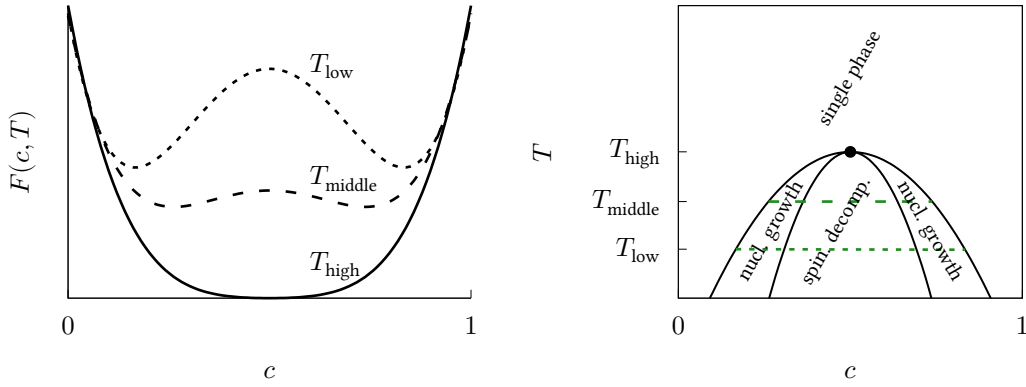


Figure 1.1: (left) Idealised double well structure of a binary system's free energy at different temperatures. The height of the energy barrier between the two wells is assumed to decrease with the temperature. At  $T_{\text{low}}$  and  $T_{\text{middle}}$  the system has a two-phase equilibrium. At  $T_{\text{high}}$ , the barrier vanished and the system now has a single-phase equilibrium. (right) The  $c$ - $T$  phase diagram produced by the previous free energy. The abscissas of the minima of  $F$  at each temperature draw the outer coexistence curve and the abscissas of its inflection points draw the inner spinodal curve. Inside the curve, the system separates into two stable phases of compositions given by the two minima of  $F$ . They can also be read at the ends of the dashed tie-lines on the phase diagram, and the fraction of each phase is given by the relative distance on the tie-line (the lever rule). These tie lines stem from the common tangent construction, detailed in the later paragraphs. Between the coexistence and spinodal curves, the energy barrier may be crossed locally due to the statistical thermal fluctuations or the presence of surfaces and impurities, in which case the system slowly and locally separates (nucleation and growth regime). In the spinodal region, it is energetically favorable for the system to separate globally and spontaneously (spinodal decomposition regime). Outside of the coexistence curve, the system is in a single phase equilibrium.

The free energy is an extensive quantity and the contribution of each phase is thus weighted by their volume fraction. We will denote the phase fraction of one phase as  $s$ ; the second phase has fraction  $1 - s$ . Given a global composition  $c$  for the system, a two-phase equilibrium is the solution of the minimization under constraint of the total free energy

$$(1 - s)F_0(c_0) + sF_1(c_1) \quad (1.1.2)$$

with  $c_0, c_1$  satisfying  $c = (1 - s)c_0 + sc_1$ ,

<sup>1</sup>The free energy is also function of the volume  $V$  occupied by the system, but we will always assume it to be constant.

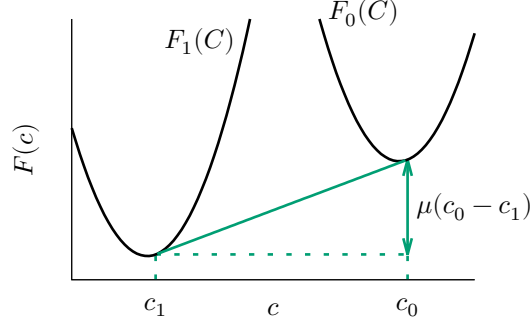


Figure 1.2: Common tangent construction for a binary system with two phases. The phases coexist at equilibrium if their individual equilibrium compositions ( $c_0$  and  $c_1$ ) and free energy contribution ( $f_0(c_0)$  and  $f_1(c_1)$ ) are such that the free energies at these abscissas share a common tangent, shown here in green. The slope of this common tangent is the quantity  $\mu$ , later defined as the chemical potential. Any point on that line is a two-phase equilibrium and corresponding phase fraction is read by the distance along that line (the “lever rule”). Note that the coexisting compositions may be close to, but are generally distinct from the abscissas of the individual minima of the two free energies.

with the subscript 0 identifying the phase at  $s = 0$ , and subscript 1 the one at  $s = 1$ . The phase free energies  $F_0$  and  $F_1$  may for example correspond to a split of the double-well structure (figure 1.1 at  $T_{\text{low}}$ ) in two parts with their own minimum. The solution can be found by introducing the Lagrange multiplier  $\mu$  and finding the unconstrained minimum of the quantity

$$(1-s)F_0(c_0) + sF_1(c_1) - \mu((1-s)c_0 + sc_1 - c) \quad (1.1.3)$$

with respect to  $s$ ,  $c_0$  and  $c_1$ . Doing so yields the following conditions for equilibrium:

$$\begin{aligned} \frac{\partial F_0}{\partial c_0} &= \frac{\partial F_1}{\partial c_1} = \mu, \\ F_0(c_0) - F_1(c_1) &= \mu(c_0 - c_1), \end{aligned} \quad (1.1.4)$$

Solving the chemical equilibrium means finding the two coexisting phase compositions  $c_0$  and  $c_1$  satisfying the two equations. The phase fraction is subsequently given by the lever rule

$$s = \frac{c_0 - c}{c_0 - c_1}. \quad (1.1.5)$$

This definition of the chemical equilibrium in terms of  $F$  can be represented graphically by the common tangent construction, shown in fig. 1.2. The next subsection discusses the physical meaning of the slope  $\mu$ .

### 1.1.2 Chemical potential and grand potential

The Lagrange multiplier  $\mu$  introduced earlier is the chemical potential. We define it here as the derivative of the system free energy with respect to its composition,

$$\mu = \partial F / \partial c, \quad (1.1.6)$$

and is thus a measure of the energy cost of a change of composition of the system.

We must keep in mind that the real thermodynamic definition of the chemical potential is as the variation of  $F$  in terms of each species' particle count and not the composition: there is strictly speaking one chemical potential for each species,  $A$  and  $B$ . However, just as we can ignore one composition variable by assuming a constant total count  $N$  of all particles, we can also ignore one chemical potential variable. In that case, one can verify that  $\mu$  as  $\partial F/\partial c$  corresponds to the true thermodynamic chemical potential of species  $A$  ( $\partial F/\partial N^A$ ) relative to the chemical potential of  $B$  ( $\partial F/\partial N^B$ ), up to a factor  $N$ .

This change of convention only serves to make calculations simpler and does not change the physical interpretation of the chemical potential. Indeed, by considering the two phases as two subsystems, the system's equilibrium naturally implies equality of their chemical potential as eq. (1.1.4) dictates: the phases coexist at equilibrium if the chemical exchanges between them cost as much energy for one phase as the other gains. The chemical potential as defined here is an intensive property conjugate to  $c$ , in analogy of the temperature being the intensive conjugate of the extensive internal energy (or of the extensive entropy).

Because  $\mu$  and  $c$  are conjugate, we are free to describe our thermodynamic system in terms of one or the other (but not both). We do so by applying a Legendre transform on  $F$  to obtain a new thermodynamic potential:

$$\Omega(\mu) = F(c(\mu)) - \mu c(\mu) \quad (1.1.7)$$

the grand potential. Note that this transformation is properly defined only if  $c$  can be expressed as a function of  $\mu$ , which in turn implies that  $\mu$  is a strictly monotonous function of  $c$ . This condition is broken if the free energy has concave parts, in which  $\partial\mu/\partial c$  becomes negative. The inverse transform is also defined, giving

$$F(c) = \Omega(\mu(c)) + c\mu(c). \quad (1.1.8)$$

Accordingly, the conjugate variables become defined by

$$\mu = \frac{\partial F}{\partial c}, \quad c = -\frac{\partial \Omega}{\partial \mu}. \quad (1.1.9)$$

in the free energy and the grand potential formulation, respectively.

We can apply the Legendre transform on the definition of the chemical equilibrium, eqs. (1.1.4). Again, we split the global grand potential  $\Omega$  into two parts for each phase and consider the phase-specific chemical potentials  $\mu_0$  and  $\mu_1$ . The calculation simply yields

$$\begin{aligned} \mu_0 &= \mu_1 (= \mu) \\ \Omega_0(\mu) &= \Omega_1(\mu) \end{aligned} \quad (1.1.10)$$

This time, the unique value  $\mu$  for the chemical potential does not come from a constrained minimization but directly from the required equality of the phase specific chemical potential. The global composition inventory is implicitly constant given the extensity of the grand potential and eq. (1.1.9).

It appears that the grand potential may be a more convenient representation of the chemical equilibrium of two thermodynamic sub-systems exchanging components (see *e.g.* [27] for a practical application). However, it would not be adequate to describe the chemical equilibrium of a closed global system<sup>2</sup> before its two phases completely separates: the spinodal decomposition regime corresponds to the composition range for which the free energy is concave in  $c$  (between its inflexion points), and as we have said the grand potential can not be defined over composition domains including such points.

We have defined the thermodynamic equilibrium of a binary chemical system in a global view. It will serve as a support to derive the local behaviour of the components inside the system, as described in the next subsection.

---

<sup>2</sup>An open system connected to a source of chemical components with fixed chemical potential would still be adequately described by the grand potential. This is in analogy of the free energy being an adequate description of the thermal equilibrium of an open system in contact with a thermostat at fixed temperature

### 1.1.3 Kinetics: Onsager and Fick diffusion

The kinetics of chemical components obeys a fundamental principle of linear irreversible thermodynamic process known as the Onsager variational principle. It establishes that the flux describing the local time-evolution of a conserved, extensive thermodynamic variable is proportional to the gradient of the conjugate intensive variable (see for instance ref. [24]). This is consistent with the global view of equilibrium thermodynamics: a system will exchange internal energy with a thermostat according to their difference in temperature, or will exchange particles ( $c$ ) with a source according to their difference in chemical potential ( $\mu$ ). We thus have the flux

$$\mathbf{j} = -M\nabla\mu \quad (1.1.11)$$

going from regions of high chemical potential to regions of low potential. The coefficient  $M$  is called the mobility coefficient and is by necessity always positive. The now time-dependent and space-dependent composition  $c(t, \mathbf{x})$  will follow the Onsager diffusion PDE

$$\partial_t c = -\nabla \cdot \mathbf{j} = \nabla \cdot M\nabla\mu. \quad (1.1.12)$$

The equation above is by definition a conservation equation which will conserve the global composition (the integral of  $c$  of the volume of the system).

The Fick diffusion equation

$$\partial_t c = D\nabla^2 c \quad (1.1.13)$$

is another kinetic description commonly seen. Historically, the Fick kinetics were introduced before Onsager's and the former does not have the fundamental thermodynamic basis the latter has. Phenomenologically however, the Fick diffusion describes the movement of components from points of high composition to regions of lower composition which is the typical behaviour observed for the kinetics of a dilute binary solution. In fact, the Fick equation can be found to be an approximation of the Onsager equation in this context. To see this, rewrite  $\nabla\mu$  as  $(\partial^2 F / \partial c^2) \nabla c$  to reveal the relation between the mobility and diffusivity coefficient

$$D = \frac{\partial^2 F}{\partial c^2} M. \quad (1.1.14)$$

For small variations of  $c$  around a reference concentration,  $F(c)$  can be expanded as a second-order polynomial in  $c$ . In this case,  $D$  and  $M$  can both be taken as constants and the Fick equation becomes a good approximation.

We shall reiterate remarks made in Cahn's 1968 lecture notes [8] on the dynamics of phase separation dynamics. The Fick diffusion equation can explain the kinetics of the system when it tends to a homogeneous mixture. However, during phase separation the components conglomerate into regions of high concentration, which would imply an "uphill" diffusion with a negative diffusion coefficient  $D$ . Mathematically, the diffusion equation with  $D < 0$  is ill-posed [16]. Thus, to describe phase separation, one must either regularize the Fick diffusion equation in some way or another, or rely on the Onsager description. In this second case, remark that the spinodal regime with a concave  $F$  free energy and the always positive mobility  $M$  indeed imply a negative diffusion coefficient, following eq. (1.1.14).

### 1.1.4 Surface tension

The modelling made throughout this section only took in account the energy contribution of volume elements of the system. This description is in fact incomplete, because there is also an energy cost associated with maintaining an interface. It costs an energy  $\sigma S$  for the system to maintain an interface of surface  $S$ . The surface tension  $\sigma$  is the energy cost of an interface per unit of surface. Intuitively, this

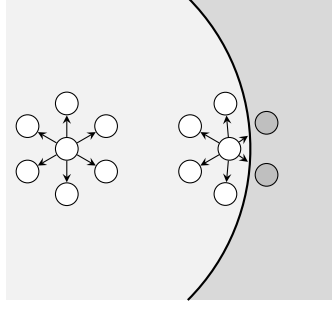


Figure 1.3: Illustration of the origin of the surface tension acting on the interface between two phases. The particles in the bulk of the phase on the left are surrounded by similar particles in all directions. They interact the same way, resulting in zero net force. In the interface region, the neighborhood of the particle also include particles from the other phase, with which they interact differently. This results in a net force pulling the interface particle inwards. At the global system's equilibrium, this surface force is balanced by the outward pressure produced by the bulk interactions.

energy cost can be thought to be due to the inhomogeneities of the interactions between the particles of the system at its interface, see fig. 1.3.

To model this energy cost, the interface can be described as the local variations of a scalar field. This field shall take constant and homogeneous values in the bulk of each phase, and go smoothly from one to another at the interfaces. Historically, in the context of liquid-gas systems, van der Waals [26] was the first to introduce this formulation in terms of the mass density, in 1893. He described the free energy  $F$  of the system as an integral over the volume  $V$  of the system and dependent on the local variation of the density  $\rho$ , which is supposed to be homogeneous in the bulk of each phase and varies continuously from one to another bulk values in interface region. After some calculations under assumptions of symmetries and boundary conditions, the free energy integral is left with a local and a first order non-local term, as

$$F[\rho] = \int_V \left( f(\rho) + \frac{1}{2} \zeta |\nabla \rho|^2 \right) dV. \quad (1.1.15)$$

The local contribution  $f(\rho)$  to the free energy density shall be identified as the double-well function seen earlier. The constant weight  $\zeta$  of the nonlocal contribution (proportional to the squared norm of the density gradient) is supposed to be constant. This non-local term represents the contribution of the density inhomogeneities to the surface tension, fitting the illustration of the surface tension given previously. The integral above will be found to be the basis of the phase field modelling.

The reader may recognize eq. (1.1.15) as a Ginzburg-Landau functional [21]. The density  $\rho$  might then be linked to the order parameter of the liquid-gas phase transition. Order parameters are a concept introduced by Landau's general theory of phase transition. It will not be necessary to detail this theory too much; here we may just present order parameters as physical quantities of the system that tells us in which phase it is. For a liquid-gas system, it is the density difference of the two phases  $\Delta\rho$ : it is non-zero ("ordered") when the phases are separated or zero ("disordered") beyond the critical point, where the liquid and gas become undistinguishable and the system is homogeneous. An order parameter is always linearly driven by an external field (here, the pressure) according to a susceptibility coefficient (the compressibility) and is always related to a conserved quantity of the system (the mass).

## 1.2 Phase field models

In this section, we will formulate the basics of the phase field theory, starting with the free energy functional and the derivation of the Cahn-Hilliard and Allen-Cahn equations. After presenting the advantages of the Allen-Cahn model, we present its coupling to the chemical diffusion kinetics and to the flow dynamics.

### 1.2.1 Minimization of an energy functional

As mentioned in the thermodynamics introduction, the phase field modelling is based on a Ginzburg-Landau functional describing the free energy of a heterogeneous system with respect to a scalar field  $\varphi(\mathbf{x})$ . The field takes a different homogeneous and constant value in each phase, and smoothly changes from one value to the other at the interfaces. The functional is

$$F[\varphi] = \int_V \left( H f_{\text{dw}}(\varphi) + \frac{\zeta}{2} |\nabla \varphi|^2 dV \right). \quad (1.2.1)$$

We shall take the convention that  $\varphi = 0$  identifies one phase and  $\varphi = 1$  the other one. In accordance, we will call these phases “phase 0” and “phase 1” and identify values proper to each phase with a subscript 0 or 1. The first term in the integral is a dimensionless form of the double well energy, as the polynomial

$$f_{\text{dw}}(\varphi) = 8\varphi^2(1 - \varphi)^2 \quad (1.2.2)$$

weighted by the bulk energy coefficient  $H$  (of dimension  $[E] \cdot L^{-3}$ ), proportional to the height of the double-well. As was established in section 1.1, the double well is a recurring structure in the modelling of phase separation. It favours regions of bulk phases with its minima at  $\varphi = 0$  and  $\varphi = 1$  (see figure 1.4). Intermediated values are penalized: the favoured interface profile is a sharp step function from 0 to 1 (a sharp interface).

The second term is the gradient energy which on the contrary penalizes sharp variations of  $\varphi$ . The coefficient  $\zeta$  (relative to  $H$ ) controls the weight of the gradient energy against the local double well energy and the minimizing profile of  $F$  will be a balance between both.

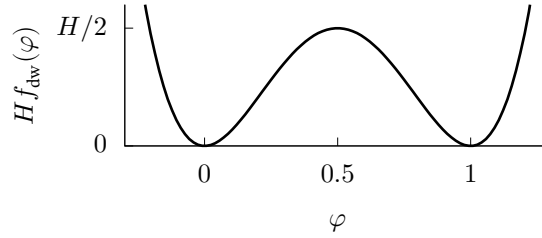


Figure 1.4: Double well function  $H f_{\text{dw}}(\varphi) = 8H\varphi^2(1 - \varphi)^2$  with its minima at  $\varphi = 0$  and  $\varphi = 1$ . The coefficient  $H$  controls the height of the energy barrier between the two minima.

This equilibrium profile can be derived analytically in the case of a planar interface. Taking it perpendicular to the  $x$ -axis, the Euler-Lagrange equation is

$$\frac{\delta F}{\delta \varphi} = \frac{\partial \left( H f_{\text{dw}}(\varphi) + \frac{\zeta}{2} \left( \frac{d\varphi}{dx} \right)^2 \right)}{\partial \varphi} - \frac{d}{dx} \frac{\partial \left( H f_{\text{dw}}(\varphi) + \frac{\zeta}{2} \left( \frac{d\varphi}{dx} \right)^2 \right)}{\partial (d\varphi/dx)} = 0, \quad (1.2.3)$$

giving the ordinary differential equation

$$H f'_{\text{dw}}(\varphi) - \zeta \frac{d^2 \varphi}{dx^2} = 0. \quad (1.2.4)$$

Its solution is the hyperbolic tangent profile (illustrated in figure 1.5)

$$\varphi^{\text{eq}}(x) = \frac{1}{2} \left( 1 + \tanh\left(\frac{2x}{W}\right) \right) \quad (1.2.5)$$

where we define the interface width  $W$  as

$$W = \sqrt{\zeta/H}. \quad (1.2.6)$$

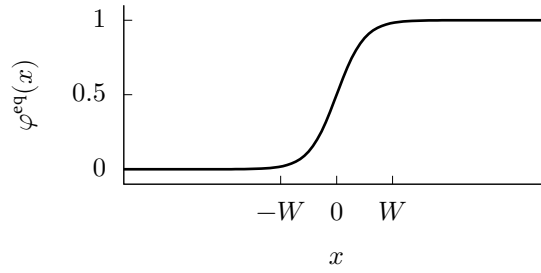


Figure 1.5: Equilibrium profile  $\varphi^{\text{eq}}$  of a plane interface along the  $x$  axis. The range  $[-W, W]$  accounts for about 98% of the transition between the bulk values.

Knowing this, one can derive the characteristic energy cost per surface of maintaining an interface, *ie.* the surface tension. This is done by inserting  $\varphi^{\text{eq}}$  into  $F[\varphi]$ ,

$$S\sigma^{\text{eq}} = F[\varphi^{\text{eq}}] = S \int_x 16H\varphi^{\text{eq}2}(1 - \varphi^{\text{eq}})^2 dx. \quad (1.2.7)$$

with  $S$  the surface of the plane interface. Using the change of variable derived from the relation  $d\varphi^{\text{eq}}/dx = 4\varphi^{\text{eq}}(1 - \varphi^{\text{eq}})/W$ , this becomes

$$\sigma^{\text{eq}} = \frac{2}{3}HW = \frac{2}{3}\sqrt{H\zeta}. \quad (1.2.8)$$

The first equality lets us interpret  $H$  as the characteristic volumic energy density within the diffuse interface.

## 1.2.2 Time evolution: Cahn-Hilliard and Allen-Cahn equations

### Cahn-Hilliard equation

Once  $F[\varphi]$  and its equilibrium are established, one can derive a PDE for the motion of the interface by asking that the time evolution of the field  $\varphi$  decreases  $F$ . One way to do so is through the diffusion flux  $\mathbf{j} = -(M_\varphi/H)\nabla(\delta F/\delta\varphi)$ , *ie.*

$$\partial_t \varphi = -\nabla \cdot \mathbf{j}_\varphi = M_\varphi \nabla^2 (f'_{\text{dw}}(\varphi) - W^2 \nabla^2 \varphi) \quad (1.2.9)$$

(in the remainder of the text, we will denote with a prime the derivative with respect to  $\varphi$ , and only those). This PDE is conservative as it derives from the divergence of a flux and one can verify that the hyperbolic tangent, eq. (1.2.5) is an equilibrium solution. For a multicomponent system, the phase field  $\varphi(t, \mathbf{x})$  is identified to the composition field  $c(t, \mathbf{x})$ , giving the canonical Cahn-Hilliard equation [9]. The quantity  $M_\varphi$  is called the mobility. In the Cahn-Hilliard equation, it coincides with the chemical mobility of the diffused species, up to a constant energy factor<sup>3</sup>.

This time evolution PDE may be recognized as a particular example of a Ginzburg-Landau model (namely “model B” in Hohenberg and Halperin’s classification [14, 12]) but Cahn and Hilliard were the first to exploit these models in the context of material sciences, hence the name of the PDE. Indeed, there is a complete analogy with the free energy integral (1.2.1) with  $\varphi(\mathbf{x}) = c(\mathbf{x})$  and van der Waals’ formalism, eq. (1.1.15). The composition field  $c(t, \mathbf{x})$  is related to the order parameter  $\Delta c$  of the chemical phase transition (see fig. 1.1 with the critical point at  $T_{\text{high}}$ ), conserves the global composition of the system (the volume integral of  $c(\mathbf{x})$ ), and responds linearly to a change of the chemical potential. Note that in the Cahn Hilliard formalism, the chemical potential is the field

$$\frac{\delta F}{\delta \varphi} = H(f'_{\text{dw}}(\varphi) - W^2 \nabla^2 \varphi) \quad (1.2.10)$$

up to an elementary volume constant factor. The first term is the contribution owing to the equilibrium thermodynamics, in analogy of eq. (1.1.6). The second generalizes the chemical potential to account for the inhomogeneities of composition. Knowing this, it is possible to interpret the Cahn-Hilliard equation either as the Onsager diffusion equation with a generalized and non-local chemical potential, or as a Fick diffusion equation regularised with a source term and an increase in the order of the space derivative. We can remark now that high order space derivative (the bi-laplacian  $\nabla^2 \nabla^2 \varphi$ ) will constrain the efficiency of numerical resolution scheme based on a stencil space discretization.

By taking the convention  $\varphi = c \in [0, 1]$  with the current shape of the double well function, we have implicitly limited our description to the case of pure alloys, where each phase is only composed of one or the other species. Taking intermediary values for  $c$  in the bulk of each phase requires a scaling of  $f_{\text{dw}}$ , which in turns changes the numerical constants in the definition of the interface width or the surface tension. In practice, this scaling can be absorbed into a change of variable of  $c$ . However, this is a sign of an important property of the Cahn-Hilliard equation: the bulk and interface properties are regulated by the same double-well function. Accordingly, the bulk and interface kinetics are regulated by the same partial differential equation and it is impossible to adjust one aspect without changing the other. This is particularly unwieldy in the case of  $W$  as it will already be constrained by the numerical resolution during simulations.

Handling this coupling is particularly complicated in some cases, typically when introducing asymmetries in the phase properties or with more than two chemical species; see ref. [25] for an example. For this reason and the numerical considerations above, we will prefer using an alternate equation as detailed in the next subsection.

### Allen-Cahn equation

Another choice is to propose a linear decrease of  $F$ , as

$$\partial_t \varphi = -\frac{M_\varphi}{\zeta} \frac{\delta F}{\delta \varphi} = M_\varphi \nabla^2 \varphi - \frac{M_\varphi}{W^2} f'_{\text{dw}}(\varphi). \quad (1.2.11)$$

<sup>3</sup>Calling  $M_\varphi$  a mobility is thus arguably a misuse of the term, but it is a common nomenclature in the phase-field literature where the energy dimension is stripped from the final equations. A mobility is by definition the coefficient linearly relating a force to the velocity it induces, making its dimensions  $[E] \cdot L^2 \cdot T^{-1}$ , the rate of diffusion of an energy. It would correspond to  $M_\varphi/H$  times an elementary volume.



This is the Allen-Cahn equation [1]. It is a diffusion equation with a non-linear source term and is not conservative. The phase field  $\varphi$  is then not identifiable as the composition and cannot be related to a physical order parameter of the system. Accordingly, the Allen-Cahn equation is can not be assimilated to a generalized chemical diffusion PDE and the coefficient  $M_\varphi$ , hereafter precized as the mobility of the phase field, only quantifies the relaxation rate of the diffuse interface to its equilibrium profile  $\varphi^{\text{eq}}$ .

However, as exposed in previous discussion on the Cahn-Hilliard equation, this restricted description is convenient. The Allen-Cahn equation is only concerned with the properties and motion of the interface. The bulk phase properties and the kinetics of components or the diffusion of any other thermodynamic quantity can be reintroduced and tuned separately through another PDE. We will detail in sec. 1.2.4 how this is done: the chemical diffusion will influence the interface motion in a much less coupled but still thermodynamically consistent manner.

The phase field literature developed a framework to study the asymptotic behaviour of the Allen-Cahn equation at very thin interface widths. It will be useful later to define a boundary condition for the coupled model at the (asymptotically sharp) interface between the phases of the chemical system; for now, we can present a first-order asymptotic result on the Allen-Cahn equation itself. One can show that the first-order analysis is equivalent to finding an equilibrium solution for  $\varphi$  describing a spherical interface moving at a constant normal velocity. Namely,

$$\varphi(t, r) = \varphi^{\text{eq}}(r - R(t)) \quad (1.2.12)$$

with  $R(t) = Vt$  the radius of the circular domain and  $V$  its normal expansion velocity. In this case,  $\partial_t \varphi = V \partial_r \varphi$  and  $\nabla^2 \varphi = (2/r) \partial_r \varphi + \partial_{rr} \varphi$ . The Allen-Cahn equation (1.2.11) then becomes

$$V(\partial_r \varphi) = M_\varphi \frac{2}{r} (\partial_r \varphi) \quad (1.2.13)$$

near the interface ( $r = R$ ), the profile  $\varphi(r)$  is solution if the solvability condition

$$V = M_\varphi \kappa \quad (1.2.14)$$

is satisfied, with  $\kappa = 2/R$  the mean curvature<sup>4</sup> of the spherical interface. From this quick calculation, we have exposed the intrinsic curvature-driven movement of the interface that is always contained in the Allen-Cahn equation.

Finally, the Allen-Cahn PDE is more convenient for a numerical scheme since it only involves second order spatial derivatives. For all these reasons (separate interface and bulk considerations, asymptotic behaviour analysis and lower-order spatial derivatives) the Allen-Cahn equation will be used in this work and preferred over the Cahn-Hilliard equation.

Before showing the coupling to the chemical diffusion in sec. 1.2.4, we will show in sec. 1.2.3 how a phase field model can be coupled to the Navier-Stokes equations to model two-phase flows.

### 1.2.3 Flow coupling

A phase field model based on either the Cahn-Hilliard or the Allen-Cahn equation can be coupled to the Navier-Stokes equations to describe a two-phase flow. The immediate way to do so is to supplement the phase field equation with an advective term  $\mathbf{u} \cdot \nabla \varphi$  with the velocity field  $\mathbf{u}$  solution of the flow PDEs. In particular, we will use the Navier-Stokes equations for a Newtonian and incompressible flow

$$\nabla \cdot \mathbf{u} = 0, \quad (1.2.15)$$

$$\rho \partial_t \mathbf{u} + \rho \nabla \cdot (\mathbf{u} \mathbf{u}^T) = -\nabla p + \rho \nabla \cdot (\nu (\nabla \mathbf{u} + \nabla \mathbf{u}^T)) + \mathbf{F}. \quad (1.2.16)$$

<sup>4</sup>The sum of its principal curvatures. For a two-dimensional circular interface,  $\kappa = 1/R$  instead.

In order, these two equations are the conservation of mass for a fluid of constant and homogeneous mass density  $\rho$  and kinematic viscosity  $\nu$ . The pressure field  $p$  is also the solution of the Navier-Stokes equations. We will not attach any particular thermodynamic significance to it; instead, it can be just considered as the Lagrange multiplier enforcing the zero-divergence constraint on  $\mathbf{u}$ . The term  $\mathbf{F}$  is a force term developed in the next paragraphs.

The two-phase character of the flow is described with the following considerations:

- the velocity field  $\mathbf{u}$  can be considered as an average of the velocities of the two fluids in the interface region (see for example sec. 2.1 of [31] or sec. II.B of [3]),
- the viscosity may differ from one phase to another. Its value in the interface is defined through the harmonic interpolation<sup>5</sup> of each phases' bulk viscosities ( $\nu_0, \nu_1$ ) by the phase field. Explicitly,

$$\nu = \nu(\varphi) = ((1 - \varphi)\nu_0^{-1} + \varphi\nu_1^{-1})^{-1}. \quad (1.2.17)$$

- We may also consider phase specific densities and interpolate them linearly,

$$\rho = \rho(\varphi) = (1 - \varphi)\rho_0 + \varphi\rho_1. \quad (1.2.18)$$

For reasons explained later, we may assume that the Boussinesq approximation holds and we will only consider this density difference in the force terms of the momentum equation. In particular, we introduce the buoyancy force

$$(\rho_0 - \rho(\varphi))\mathbf{g} = \Delta\rho\varphi\mathbf{g} \quad (1.2.19)$$

with  $\Delta\rho = \rho_0 - \rho_1$  and  $\mathbf{g}$  the acceleration vector due to gravity. We have assumed phase 0 to be the heavier phase in these expressions.

- Take into account the capillary effects on the fluid-fluid interface through a force term in the momentum equation. In 1999 Jacqmin [15] presented a simple potential form of this force in the Cahn-Hilliard formalism, as  $C\nabla(\delta F/\delta C)$ . The direct equivalent for an Allen-Cahn model would be the force  $\varphi\nabla(\delta F/\delta\varphi)$ , but it would reintroduce a high-order space derivative we wanted to avoid in the first place. Instead, we shall swap the gradient and use the form

$$\frac{\delta F}{\delta\varphi}\nabla\varphi = \frac{3\sigma}{2W}(f'_{\text{dw}}(\varphi) - W^2\nabla^2\varphi)\nabla\varphi. \quad (1.2.20)$$

It is just one of the many alternative formulations of the surface tension force in phase field models [18, 19]. We will also write it more compactly as

$$-\frac{\sigma}{W}\boldsymbol{\kappa}(\varphi) \quad (1.2.21)$$

with

$$\boldsymbol{\kappa}(\varphi) = (3/2)(W^2\nabla^2\varphi - f'_{\text{dw}}(\varphi))\nabla\varphi. \quad (1.2.22)$$

This notation is motivated by the first order asymptotic behaviour<sup>6</sup> of the right-hand side, namely  $\boldsymbol{\kappa}(\varphi) \sim f'_{\text{dw}}(\varphi)\kappa\mathbf{n}$ : a vector field that, near an interface, measures its mean curvature  $\kappa$  and is directed along its normal  $\mathbf{n}$ . It becomes the zero vector outside the diffuse interface. This is not a coincidence: by construction, the force term matches the more general continuum surface force model [6] as found in *e.g.* the volume-of-fluid and level-set methods. These are always proportional to the local curvature weighted by the local gradient ( $f'_{\text{dw}}(\varphi) \sim |\nabla\varphi|^2$ ) of the continuum variable locating the interface, as Jacqmin noted in the same reference.

<sup>5</sup>For a justification on the usage of the harmonic interpolation against a linear interpolation, see the results presented in [31].

<sup>6</sup>In this case, it can be seen by assuming  $\varphi$  at equilibrium for an interface of constant mean curvature  $\kappa$  and then expand the expression in spherical coordinates.

Knowing this, the force term  $\mathbf{F}$  in the momentum equation is

$$\mathbf{F}(\varphi) = \Delta\rho\varphi\mathbf{g} - \frac{\sigma}{W}\kappa(\varphi). \quad (1.2.23)$$

We have seen in the previous section that the Allen-Cahn equation has an intrinsic normal movement due to the interface's curvature, proportional to  $M_\varphi\kappa$ . In the modelling of two-phase flows particularly, this curvature dependence is sometimes undesirable. This is why some Allen-Cahn two-phase flow models correct the Allen-Cahn equation with a term appropriately proportional to  $-M_\varphi\kappa$  to counterbalance it. Folch et. al. [12] first expressed this counterterm as

$$M_\varphi\kappa(\varphi)|\nabla\varphi|, \quad (1.2.24)$$

with the scalar curvature field  $\kappa(\varphi)$  as

$$\kappa(\varphi) = \nabla \cdot \left( \frac{\nabla\varphi}{|\nabla\varphi|} \right). \quad (1.2.25)$$

The fraction on the right is an approximation of the interface's normal vector, making this expression coherent with the differential geometric relationship of the mean curvature and the normal vector of a surface. See also [28] for a discussion of the Allen-Cahn equation and the cancelling of curvature effects. The expression can be further manipulated by exploiting the relationships between the first order solution  $\varphi^{\text{eq}}$ , the double-well function  $f_{\text{dw}}(\varphi^{\text{eq}})$ , their derivatives and the interface's geometric quantities. Most notably, Chiu and Lin [10] used the fact that

$$\frac{M_\varphi}{W^2}f'_{\text{dw}}(\varphi) + M_\varphi\kappa(\varphi)|\nabla\varphi| \sim \frac{M_\varphi}{W}\nabla \cdot \left( \sqrt{2f_{\text{dw}}(\varphi)} \frac{\nabla\varphi}{|\nabla\varphi|} \right), \quad (1.2.26)$$

assuming  $\varphi \sim \varphi^{\text{eq}}$ . This collects the counterbalance term and the double-well source term under the divergence operator, relying on the coincidence that with the usual double-well function,

$$|\nabla\varphi| \sim \frac{4\varphi(1-\varphi)}{W} = \frac{\sqrt{2f_{\text{dw}}(\varphi)}}{W}. \quad (1.2.27)$$

Doing so ensures the resulting PDE can be written as a conservation equation (then sometimes called the ‘‘Conservative Allen-Cahn equation’’, CAC). It is of particular interest for two-phase incompressible flows when one interpolates the averaged density field like would be done with eq. (1.2.18): the conservation of  $\varphi$  guarantees the conservation of mass.

The two forms of the counterterm, eqs. (1.2.24) and (1.2.26), have the same asymptotic effect at first order (one may verify this by considering again a spherical interface with a constant velocity as done in the end of section 1.2.2). Differences are kept to the second order; instead, practical consideration will favour one form or another (ease of numerical implementation or conservation of  $\varphi$ ) or none at all. In the present case, the growth dynamics fundamentally depend on this normal velocity and the associated Gibbs-Thomson condition described later and as such we will not use a counterterm. In contrast, in a preliminary work [31] we employed the term of eq. (1.2.26) to model a liquid-gas flow with no curvature effects. In this previous work we also linearly interpolated different densities and introduced a source term in the conservation of mass, eq. (1.2.15), due to the evaporation at the interface.

We end this section by mentioning that the literature has examples of more rigorous coupling methods between the flow and the phase field. The advection field can be included in the free energy functional, and the Navier-Stokes equation with can be derived from its minimization, given the definition of an adequate stress tensor and of an entropy inequality for the diffusive processes. See for instance refs. [7, 13].

### 1.2.4 Coupling the Allen-Cahn equation to the chemical diffusion

#### Adding a diffusion field

Coupling the Allen-Cahn formalism to the diffusion of thermodynamic variable follows a simple recipe. Typically, this concerns the diffusion of a field of temperature  $T$  (“thermal” phase field model) or of a species composition  $c$ . The free energy functional shall now depend on such a field, e.g.

$$F[\varphi, c] = H \int \left( f_{\text{dw}}(\varphi) + \frac{W^2}{2} |\nabla \varphi|^2 + \frac{1}{H} f(\varphi, c) \right) dV. \quad (1.2.28)$$

The thermodynamic free energy function  $f(\varphi, c)$  must match the contribution of the each bulk phase in the extrema of  $\varphi$  and give a reasonable interpolation in the interface region, hence the dependence on  $\varphi$ . It is customary to split the two dependencies using an interpolation function  $p(\varphi)$  such that

$$f(\varphi, c) = (1 - p(\varphi))f_0(c) + p(\varphi)f_1(c) \quad (1.2.29)$$

with  $f_0, f_1$  the bulk contributions. For reasons detailed later, we choose the interpolation polynomial

$$p(\varphi) = 3\varphi^2 - 2\varphi^3 \quad (1.2.30)$$

which notably satisfies the conditions  $p(0) = 0$ ,  $p(1) = 1$  and  $p'(0) = p'(1) = 0$ .

The Allen-Cahn equation is thus supplemented with an additional source term depending on  $c$ :

$$\partial_t \varphi = M_\varphi \nabla^2 \varphi - \frac{M_\varphi}{W^2} f'_{\text{dw}}(\varphi) + \frac{M_\varphi}{W^2} \frac{1}{H} p'(\varphi) (f_0(c) - f_1(c)). \quad (1.2.31)$$

and the composition field  $c(\mathbf{x})$  is evolved using the Fick diffusion equation

$$\partial_t c = \nabla \cdot D(\varphi) \nabla c. \quad (1.2.32)$$

The diffusion coefficient  $D(\varphi)$  can be interpolated with  $\varphi$  to account for different diffusivities in each phase. Eqs. (1.2.31) and (1.2.32) would make up a model for the diffusion of chemical species in a two phase binary system, using the two fields  $\varphi(\mathbf{x})$  and  $c(\mathbf{x})$ . This two PDE system would be the analogue of the single Cahn-Hilliard equation (1.2.9) and we can now clearly see the separation between bulk and interface kinetics. The Allen-Cahn equation with its source term only handles the movement of the interface through the phase field and the Fick equation describes the diffusion in the bulk phases. The effect of the diffusion on the movement of the interface, and conversely the diffusion in the interface region, are described by interpolations; here through  $p(\varphi)$  and  $D(\varphi)$  respectively. In fact, it might be thought that interpolations are the main ingredients of the Allen-Cahn models, just as order parameters are the objects of interest in the Cahn-Hilliard models.

But this naive model present some flaws. We know that the thermodynamic equilibrium of the binary system implies in general different compositions in each phase. Yet, this model has no way to reconstruct the discontinuity of  $c$  at the interface. Even if it did, we also know that the chemical equilibrium generally does not imply the equality of the phases’ free energies; remember the common tangent construction of eq. (1.1.4). The source term of the phase field equation is thus non-zero and the hyperbolic tangent profile is no longer a stationary solution. The solution would depend on the values of  $c$  at the interface, and so would the surface tension  $\sigma^{\text{eq}}$ .

A way to resolve this issue was first found through the model of Kim, Kim and Suzuki [20]. In this formulation, the authors propose that each phase has their own composition field  $c_0(\mathbf{x})$  and  $c_1(\mathbf{x})$ , thus ensuring their discontinuity at the interface. The real composition field  $c(\mathbf{x})$  is then reconstructed by the closure relation

$$c(\mathbf{x}) = (1 - \varphi(\mathbf{x}))c_0(\mathbf{x}) + \varphi(\mathbf{x})c_1(\mathbf{x}) \quad (1.2.33)$$

thus identifying  $\varphi$  as a field of local phase fraction, in analogy of the constraint of constant global composition for a closed system as it appeared in eq. (1.1.2). One may argue that the definition phase-specific composition fields is something closer to the spirit of sharp interface model than the one of the phase field framework. We will see another strategy based on the grand potential in the next subsection, which keeps a single composition field and has a clearer link to the multi-component thermodynamics.

### Grand potential formulation

We have presented the grand potential back in sec. 1.1.2 and mentioned that it is a more convenient representation of the chemical equilibrium. Indeed, a phase field framework based on the grand potential was presented in ref. [22] to more adequately model chemical systems and we will use and extend it for our work. Details on the grand potential formalism (along with its mixed  $c$ - $\mu$  formulation, defined later) in the binary case can also be found on our published work [5] on the numerical study of a two-component porous medium. The ternary case was the subject of an internal CEA technical note [30].

The reformulation is done by replacing the free energy functional, eq. (1.2.28) with the grand potential functional

$$\Omega[\varphi, \mu] = H \int_V \left( \omega_{\text{dw}}(\varphi) + \frac{W^2}{2} |\nabla \varphi|^2 + \frac{1}{H} (1 - p(\varphi)) \omega_0(\mu) + p(\varphi) \omega_1(\mu) \right) dV \quad (1.2.34)$$

with  $\omega_{\text{dw}} = f_{\text{dw}}$ . Again, the energy contribution  $\omega_0, \omega_1$  of each phase is interpolated using the function  $p(\varphi)$ . The field of chemical potential  $\mu(\mathbf{x})$  is now the dynamical variable of the model. Since the chemical potential is by definition identical in both phases at equilibrium, it is adequate to consider its field to be continuous at the interface. The phase field PDE is very similar to the free energy one, as

$$\partial_t \varphi = M_\varphi \nabla^2 \varphi - \frac{M_\varphi}{W^2} \omega'_{\text{dw}}(\varphi) + \frac{M_\varphi}{W^2} \frac{1}{H} p'(\varphi) (\omega_0(\mu) - \omega_1(\mu)), \quad (1.2.35)$$

with the source term being by definition zero at equilibrium, thus keeping the stationary solution  $\varphi^{\text{eq}}$ .

To specify the chemical diffusion in terms of  $\mu$ , we can rely on the Onsager principle and recall eq. (1.1.12),

$$\partial_t c = \nabla \cdot M(\varphi) \nabla \mu \quad (1.2.36)$$

where  $M(\varphi)$  is the chemical mobility (not to be confused with the phase field mobility  $M_\varphi$ ). It can also be interpolated between the mobilities of each phase. A closure relation is necessary to relate the  $c$  and  $\mu$  fields and it is naturally given by the equilibrium thermodynamics as in eq. (1.1.9),

$$c(\varphi, \mu) = -\frac{\delta \Omega}{\delta \mu} = -V_e \left( (1 - p(\varphi)) \frac{\partial \omega_0}{\partial \mu} + p(\varphi) \frac{\partial \omega_1}{\partial \mu} \right) \quad (1.2.37)$$

where  $V_e = V_m / \mathcal{N}$  is the elementary volume, quotient of the molar volume  $V_m$  and the Avogadro constant  $\mathcal{N}$ . This volume is necessary to introduce since the phase contributions are specified in dimensions of energies per volume. The molar volume  $V_m$  is assumed to be constant and identical for the two components; we will reiterate and justify this hypothesis later in the detail of the full model.

The grand potential functions  $\omega_0$  and  $\omega_1$  can be inferred from the free energy densities  $f_0$  and  $f_1$  through the Legendre transform

$$\omega_0(\mu) = f_0(c) - \frac{\partial f_0}{\partial c} c, \quad (1.2.38)$$

and the same for  $\omega_1$  with  $f_1$ . The specification of  $f_0, f_1$  is left for a later section, though one may already notice that taking the free energy functions as quadratic polynomial with identical second derivatives

make the grand potential reformulation equivalent to the Kim–Kim–Suzuki model seen earlier. Compared to a Cahn–Hilliard model, we will be able to tune those separately of the double-well energy  $\omega_{\text{dw}}$ .

However, unlike the Cahn–Hilliard formulation, this model is unable to describe spinodal decomposition. As we have seen in the first section, this is due to the Legendre transform being undefined if the free energy is concave. We will not consider it an issue for our purposes: it is known that the  $\text{Na}_2\text{O}–\text{SiO}_2–\text{MoO}_3$  separates following a growth and nucleation regime during the vitrification process. We may also note that a non-involutive generalization of the Legendre transform exists [29] and is applicable to non-convex functions.

### 1.2.5 Asymptotic Gibbs–Thomson interface condition

With an Allen–Cahn coupled to the diffusion of a thermodynamic field, it is possible to extract an asymptotic Gibbs–Thomson interface condition. In our case, this condition is

$$\omega_0(\mu) - \omega_1(\mu) = -\delta\kappa - \beta V \quad \text{at the interface,} \quad (1.2.39)$$

where  $\kappa$  and  $V$  are again the mean curvature and normal velocity of the interface. The proportionality constant  $\delta$  and  $\beta$  are respectively called the capillary length (related to the surface tension) and the kinetic coefficient of the interface. This kind of condition is the result of a second order asymptotic expansion of the PDE system, and this calculation will relate  $\delta$  and  $\beta$  to the parameters of the phase field and of the grand potential functions. The detail of such an analysis can be found in appendix A.4.8 along with the calculations for the two-phase three component model. Note that the definition of the interpolation polynomial  $p(\varphi)$  as in eq. (1.2.30) was a necessary condition to obtain the Gibbs–Thomson relation. See also refs. [17, 2, 11] for important examples of this analysis in the case of a thermal models and binary chemical models.

We can thus recover the precise behaviour of the thermodynamic field at the interfaces, which was *a priori* left unspecified.

## 1.3 Two-phase three component model

The previous sections have introduced almost all the necessary ingredients to build a phase field model for a two-phase three-component liquid. We will first mention some details necessary to describe multi-component chemical diffusion, and after defining some conventions we will present the full PDE system.

### 1.3.1 Multi-component considerations

The considered system is a thermodynamic system at a fixed temperature, at a fixed volume and at fixed total counts of each component. We will label the 3 component species as  $A$ ,  $B$  and  $C$ , and only the compositions  $c^A$ ,  $c^B$  will be considered independent under the constraint  $c^A + c^B + c^C = 1$ . We shall then introduce a component-space vector notation denoted in italic bold symbols. In particular, the composition variable vector is

$$\mathbf{c} = (c^A \quad c^B)^T. \quad (1.3.1)$$

Again, two immiscible phases are present and they can exchange the three (miscible) components between themselves to reach equilibrium. In the two-phase three-component system, the two phases coexist at equilibrium if their respective compositions  $\mathbf{c}_0$  and  $\mathbf{c}_1$  satisfy

$$\begin{aligned} \mu_0(\mathbf{c}_0) &= \mu_1(\mathbf{c}_1) = \mu(\mathbf{c}), \\ \mathbf{c} &= (1-s)\mathbf{c}_0 + s\mathbf{c}_1, \\ f(\mathbf{c}) &= (1-s)f_0(\mathbf{c}_0) + sf_1(\mathbf{c}_1), \end{aligned} \quad (1.3.2)$$

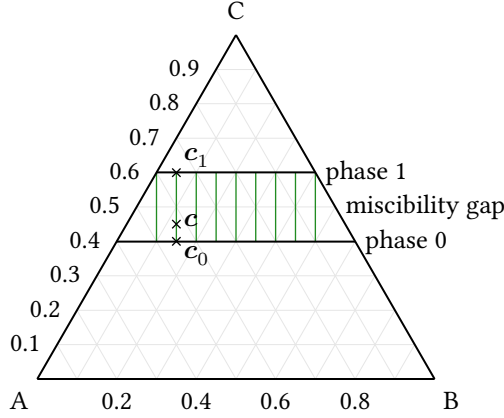


Figure 1.6: Example of an isothermal phase diagram in the Gibbs triangle for an idealized two-phase ternary system. The spectrum of solutions to the phase coexistence equilibrium (1.3.2) are graphically represented by the green tie lines (only some of them are drawn). Each tie line couple two allowed phase specific compositions  $c_0$  and  $c_1$ , which are themselves constrained to their respective phase boundaries, here the black lines such that  $c_0^A + c_0^B = 0.4$  and  $c_1^A + c_1^B = 0.6$ . They delimit the miscibility gap, in which the system is thermodynamically stable as a mix of both phases. To each tie line is associated one value of the chemical potential  $\mu$ , equal for both phases. The phase fraction  $s$  can be read by the distance on the tie line. For illustration, a particular solution with the global composition inventory  $c = (0.1925, 0.3575)^T$  and the phase fraction (of phase 1)  $s = 0.25$  is represented. The shape of the phase boundary lines and slopes of the tie-lines depend on the behaviour of the derivatives of the free energy functions  $f_0$  and  $f_1$ .

the ternary equivalent of the common tangent construction: the common tangent plane construction. The chemical potentials also become vectors in component space, namely

$$\mu = (\mu^A \quad \mu^B)^T = V_e \left( \frac{\partial f_0}{\partial c^A} \quad \frac{\partial f_0}{\partial c^B} \right)^T = V_e \left( \frac{\partial f_1}{\partial c^A} \quad \frac{\partial f_1}{\partial c^B} \right)^T. \quad (1.3.3)$$

The constant  $V_e$  will disappear later in the derivation of the model.

For consistence with the grand potential formulation, we will again assume that the equality of chemical potentials always holds and only concern ourselves with a single chemical potential variable  $\mu = \mu_0(c_0) = \mu_1(c_1)$ . In the binary case, this last assumption and the specification of the global composition inventory  $c$  and the phase fraction  $s$  were sufficient to obtain the unique solution for the phase compositions. The ternary case has now four constraints and thus one degree of freedom, which is also seen after expressing the constraints (1.3.2) in the grand potential form (one constraint for two variables)

$$\omega_0(\mu) = \omega_1(\mu). \quad (1.3.4)$$

The extra degree of freedom can be represented graphically in the isothermal phase diagram of the system, see fig. 1.6. The solutions to the chemical equilibrium form a spectrum of tie-lines, one for each couple  $c_0, c_1$  (equivalently,  $\mu$ ) satisfying the above conditions.

The diffusion or mobility coefficients now have a matrix structure in component space, namely

$$D = \begin{pmatrix} D^{AA} & D^{AB} \\ D^{BA} & D^{BB} \end{pmatrix}, \quad M = \begin{pmatrix} M^{AA} & M^{AB} \\ M^{BA} & M^{BB} \end{pmatrix} \quad (1.3.5)$$

and the chemical diffusion PDE will be then be written generally as

$$\partial_t c = \nabla \cdot (M \nabla \mu). \quad (1.3.6)$$

In practice however,  $\mathbf{M}$  will be assumed diagonal to keep the diffusion equations decoupled from each other. Note that this equation mixes the 3D-space and component-space vectors and operators. The  $\nabla$  operator acts on each component of  $\boldsymbol{\mu}$  as  $\nabla \boldsymbol{\mu} = (\nabla \mu^A \quad \nabla \mu^B)^T$ . The above equation should be read as one PDE for each component:

$$\partial_t c^\alpha = \nabla \cdot \left( \sum_{\beta} M^{\alpha\beta} \nabla \mu^\beta \right) \quad \text{for } \alpha = A, B. \quad (1.3.7)$$

We are thus ready to extend the grand potential formalism to the ternary case. We may also attempt to reformulate the chemical diffusion PDE in terms of the grand potential only as is done in [23]. It is done by expressing the global composition fields as the Legendre transform of the grand potential functional

$$\mathbf{c} = -V_e \left( \frac{\delta \Omega}{\delta \mu^A} \quad \frac{\delta \Omega}{\delta \mu^B} \right)^T \quad (1.3.8)$$

so that, by the chain rule,

$$-V_e \partial_t c^\alpha = \partial_t \left( \frac{\delta \Omega}{\delta \mu^\alpha} \right) = (\partial_t \varphi) \frac{\partial}{\partial \varphi} \frac{\delta \Omega}{\delta \mu^\alpha} + \sum_{\beta=A,B} (\partial_t \mu^\beta) \frac{\partial}{\partial \mu^\beta} \frac{\delta \Omega}{\delta \mu^\alpha}. \quad (1.3.9)$$

One can match the left-hand side terms of both eqs. (1.3.7) and (1.3.9). Before writing this out, let us define the susceptibility matrix<sup>7</sup>

$$X^{\alpha\beta}(\varphi, \boldsymbol{\mu}) = -p(1-\varphi) \frac{\partial^2 \omega_0}{\partial \mu^\alpha \partial \mu^\beta} - p(\varphi) \frac{\partial^2 \omega_1}{\partial \mu^\alpha \partial \mu^\beta}. \quad (1.3.10)$$

We may finally rewrite the diffusion PDE as

$$V_e \sum_{\beta=A,B} X^{\alpha\beta}(\varphi, \boldsymbol{\mu}) \partial_t \mu^\beta = \nabla \cdot \left( \sum_{\beta=A,B} M^{\alpha\beta} \nabla \mu^\beta \right) - V_e p'(\varphi) \frac{\partial(\omega_0 - \omega_1)}{\partial \mu^\alpha} \partial_t \varphi. \quad (1.3.11)$$

This formulation of the diffusion kinetics completely drops  $\mathbf{c}$  as a dynamical variable. The source term proportional to  $\partial_t \varphi$  is another point of similarity with the thermal phase field models [17, eq. (21)] whose heat diffusion equation includes such a term, interpreted as the release of latent heat at the interface.

However, eq. (1.3.6) is immediately seen as conserving  $\mathbf{c}$  and this property is not as clearly respected by the equation in terms of  $\boldsymbol{\mu}$  only. Furthermore, eq. (1.3.11) linearly couples the time derivative of the dynamical variables which would be inconvenient for a time explicit numerical algorithm. One may suggest diagonalizing the  $\mathbf{X}(\varphi, \boldsymbol{\mu})$  matrix, but its coefficients are in the general case functions of the fields  $\varphi$  and  $\boldsymbol{\mu}$  and the diagonalizing computation would have to be done at every point in space. For these two reasons, we will prefer using the “mixed formulation” [4] provided by eq. (1.3.6) with both the  $\mathbf{c}$  and  $\boldsymbol{\mu}$  as dynamical variables. The coherence between the two conjugate variables must be ensured through the Legendre transform, eq. (1.3.8).

In summary, the time evolution of the chemical components obeys the equations

$$\begin{aligned} \partial_t \mathbf{c} &= \nabla \cdot (\mathbf{M} \nabla \boldsymbol{\mu}), \\ \mathbf{c} &= -V_e \left( p(1-\varphi) \frac{\partial \omega_0}{\partial \boldsymbol{\mu}} + p(\varphi) \frac{\partial \omega_1}{\partial \boldsymbol{\mu}} \right). \end{aligned} \quad (1.3.12)$$

<sup>7</sup>The susceptibility matrix  $\mathbf{X}$  is named as such because it involves the second derivatives of a thermodynamic potential. One may also notice that the matrix of second derivatives of  $\omega$  with respect to  $\boldsymbol{\mu}$  is proportional to the inverse of the matrix of second derivatives of  $f$  with respect to  $\mathbf{c}$ , denoted later with the symbol  $\mathbf{K}$ .



In practice, this means evolving  $\mathbf{c}$  through the first conservation PDE and then computing  $\boldsymbol{\mu}$  as a function of  $\mathbf{c}$  with the second equation, which needs to be analytically (if applicable) or numerically inverted. We will precise this last equation by specifying  $\omega_0$  and  $\omega_1$  in the next subsection. Note that for conciseness, we have introduced the notation

$$\frac{\partial \omega}{\partial \boldsymbol{\mu}} = \left( \frac{\partial \omega}{\partial \mu^A} \quad \frac{\partial \omega}{\partial \mu^B} \right)^T. \quad (1.3.13)$$

### 1.3.2 Ternary free energies and change of variables

We will now specify the thermodynamic potential of each phase through the free energy functions  $f_0(\mathbf{c})$ ,  $f_1(\mathbf{c})$ . The grand potential functions will naturally follow.

The simplest case of convex paraboloids free energies will be assumed. This is a very convenient simplifying assumption convenient for multiple reasons. Notably, it ensures that the transform from  $\mathbf{c}$  to  $\boldsymbol{\mu}$  is always invertible and the quadratic free energies have a simple parametrization which will help us later to couple the model to thermodynamic data (sec. 3.4.2). Furthermore, as we mentioned in sec. 1.1.3, any free energy function can be reasonably approximated by a second order polynomial near a reference composition.

We can first choose to parametrize these free energies with a constant second derivative matrix  $\mathbf{K}_\pi$ , the abscissas of their minimum  $\mathbf{c}_\pi^{\min}$  and a constant energy offset  $Q_\pi$ . The index  $\pi = 0, 1$  identifies parameters belonging to phase 0 or phase 1. The free energy function then write

$$f_\pi(\mathbf{c}) = \frac{1}{2} \mathbf{K}_\pi : (\mathbf{c} - \mathbf{c}_\pi^{\min})(\mathbf{c} - \mathbf{c}_\pi^{\min})^T + Q_\pi. \quad (1.3.14)$$

The matrix of second derivatives  $\mathbf{K}_\pi$  is necessarily symmetric, and the convexity of  $f_\pi$  requires it to also be positive definite, making  $\mathbf{K}_\pi$  symmetric positive definite (SPD). The concatenation of component-space vectors implies their tensor product and  $:$  denotes the tensor double scalar product. With component indices, eq. (1.3.14) then reads

$$f_\pi(c^A, c^B) = \frac{1}{2} \sum_{\alpha, \beta=A, B} K_\pi^{\alpha\beta} (c^\alpha - c_\pi^{\min\alpha}) (c^\beta - c_\pi^{\min\beta}) + Q_\pi. \quad (1.3.15)$$

The compositions and chemical potentials are in general linearly coupled through the matrix-vector product

$$\boldsymbol{\mu} = V_e \frac{\partial f_\pi}{\partial \mathbf{c}} = V_e \mathbf{K}_\pi (\mathbf{c} - \mathbf{c}_\pi^{\min}) \quad (1.3.16)$$

(again,  $\boldsymbol{\mu}_0 = \boldsymbol{\mu}_1 = \boldsymbol{\mu}$  is implicitly assumed by chemical equilibrium).

However, this parametrization is not ideal. We can obtain a better one by applying the following transformation on  $f_\pi$ :

$$f_\pi^*(\mathbf{c}) = f_\pi(\mathbf{c}) - \frac{1}{V_e} \boldsymbol{\mu}_\pi^{\text{eq}} \cdot \mathbf{c} \quad (1.3.17)$$

with  $\boldsymbol{\mu}_\pi^{\text{eq}}$  the chemical potentials of some tie-line taken as reference. The phase compositions  $\mathbf{c}_\pi^{\text{eq}}$  of the same equilibrium are obtained by inverting eq. (1.3.16). One can verify that  $f_\pi^*$  then expands to

$$f_\pi^*(\mathbf{c}) = \frac{1}{2} \mathbf{K}_\pi : (\mathbf{c} - \mathbf{c}_\pi^{\text{eq}})(\mathbf{c} - \mathbf{c}_\pi^{\text{eq}})^T + Q^* \quad (1.3.18)$$

allowing us to drop the parametrization by  $\mathbf{c}_\pi^{\min}$  in favour of  $\mathbf{c}_\pi^{\text{eq}}$ , more directly relevant to the chemical equilibrium. The new vertical offset is  $Q^* = f_\pi(\mathbf{c}_\pi^{\text{eq}}) - \boldsymbol{\mu}_\pi^{\text{eq}} \cdot \mathbf{c}_\pi^{\text{eq}}$  which is exactly the grand potential at

equilibrium and is thus the same for both phases. The functions  $f_\pi^*$  are quadratic wells around  $\mathbf{c}^{\text{eq}}$  with a horizontal common tangent plane. The associated grand potential is

$$\omega_\pi^*(\boldsymbol{\mu}^*) = -\frac{1}{2V_e^2} \mathbf{K}_\pi^{-1} : \boldsymbol{\mu}^* \boldsymbol{\mu}^{*T} - \frac{1}{V_e} \boldsymbol{\mu}^* \cdot \mathbf{c}_\pi^{\text{eq}} + Q^* \quad (1.3.19)$$

with the change of variables  $\boldsymbol{\mu}^* = \boldsymbol{\mu} - \boldsymbol{\mu}^{\text{eq}}$ . The reference equilibrium is then at  $\boldsymbol{\mu}^* = \mathbf{0}$  which is coherent with the tangent plane being horizontally aligned. In addition, one can write the grand potential  $\omega_\pi(\boldsymbol{\mu})$  of the base ternary free energy and verify that under this change of variables

$$\omega(\boldsymbol{\mu}) = \omega^*(\boldsymbol{\mu}^*). \quad (1.3.20)$$

The thermodynamics is then entirely coherent and the change of variables only consists of modifying the reference values for the chemical potentials.

### 1.3.3 Energy dimension removal

A characteristic thermodynamic energy scale can be extracted from the  $\mathbf{K}_\pi$  matrices of the previous section. This will be useful to remove the energy dimension from the phase field equation.

Assume that phase 0 is the reference phase in some manner; in the droplet growth phenomenon, it would be the matrix phase since it is the main support of the chemical exchanges between droplets. The characteristic values of  $\mathbf{K}_0$  are its eigenvalues  $k_0^A$  and  $k_0^B$  and we will use them to define the energy-per-volume scale

$$k = (c_0^{\text{eq}A} - c_1^{\text{eq}A})^2 k_0^A + (c_0^{\text{eq}B} - c_1^{\text{eq}B})^2 k_0^B. \quad (1.3.21)$$

It corresponds to the trace of the diagonalized  $\mathbf{K}_0$  matrix under a scaling of the composition variables on the range of the tie-line

Using  $k$  and  $V_e$ , one can remove the energy dimension from the previous thermodynamic quantities. Define

$$\bar{\mathbf{K}}_\pi = \mathbf{K}_\pi / k, \quad \bar{\boldsymbol{\mu}} = \boldsymbol{\mu}^* / V_e k, \quad \bar{\omega}_\pi = \omega_\pi^* / k. \quad (1.3.22)$$

We choose to write our model with these previous conventions: the source term of the phase field equation will contain the difference of the dimensionless grand potential densities

$$\Delta \bar{\omega}(\bar{\boldsymbol{\mu}}) = -\frac{1}{2} (\bar{\mathbf{K}}_0^{-1} - \bar{\mathbf{K}}_1^{-1}) : \bar{\boldsymbol{\mu}} \bar{\boldsymbol{\mu}}^T - \bar{\boldsymbol{\mu}} \cdot (\mathbf{c}_0^{\text{eq}} - \mathbf{c}_1^{\text{eq}}). \quad (1.3.23)$$

The closure relation between the  $\mathbf{c}$  and  $\bar{\boldsymbol{\mu}}$  variables is

$$\bar{\boldsymbol{\mu}} = \bar{\mathbf{K}}(\varphi)(\mathbf{c} - \mathbf{c}^{\text{eq}}(\varphi)) \quad (1.3.24)$$

with the interpolated equilibrium composition

$$\mathbf{c}^{\text{eq}}(\varphi) = p(1 - \varphi) \mathbf{c}_0^{\text{eq}} + p(\varphi) \mathbf{c}_1^{\text{eq}} \quad (1.3.25)$$

and the interpolated matrix  $\bar{\mathbf{K}}(\varphi)$  given by

$$\begin{aligned} \bar{\mathbf{K}}(\varphi) &= \det \bar{\mathbf{K}}(\varphi) \left( \frac{p(1 - \varphi)}{\det \bar{\mathbf{K}}_0} \bar{\mathbf{K}}_0 + \frac{p(\varphi)}{\det \bar{\mathbf{K}}_1} \bar{\mathbf{K}}_1 \right) \\ \text{with } \det \bar{\mathbf{K}}(\varphi) &= (p(1 - \varphi)^2 \det \bar{\mathbf{K}}_0 + p(\varphi)^2 \det \bar{\mathbf{K}}_1 \\ &\quad + p(1 - \varphi)p(\varphi) (\bar{\mathbf{K}}_0^{AA} \bar{\mathbf{K}}_1^{BB} + \bar{\mathbf{K}}_0^{BB} \bar{\mathbf{K}}_1^{AA} - 2\bar{\mathbf{K}}_0^{AB} \bar{\mathbf{K}}_1^{AB}))^{-1}. \end{aligned} \quad (1.3.26)$$

Because the  $\mathbf{K}_\pi$  are SPD, the interpolated matrix  $\mathbf{K}(\varphi)$ , a sum with positive real coefficients, is also SPD. However, the difference of their inverse as it appears in eq. (1.3.23) may or may not be SPD. If it is,  $\Delta\bar{\omega}(\bar{\boldsymbol{\mu}})$  is also a convex quadratic and the analytical solutions to  $\Delta\bar{\omega} = 0$  can be parametrized on an ellipse.

Finally, we define the mobility matrix with the energy dimension removed

$$\bar{\mathbf{M}} = V_e k \mathbf{M} \quad (1.3.27)$$

and note that a diffusion matrix can be derived from it and the Legendre transform (1.3.24) as

$$\mathbf{D} = \bar{\mathbf{M}} \bar{\mathbf{K}}(\varphi) \quad (1.3.28)$$

which in general is also a function of  $\varphi$ .

### 1.3.4 PDE system

We now assemble the Allen-Cahn equation and the ternary Onsager diffusion equations under the grand potential mixed formulation with the incompressible Navier-Stokes equation as underlined in sec. 1.2.3. There are two remarks to be made before writing the full set of equations.

First, the definition of a characteristic thermodynamic energy scale  $k$  leads to introduce the dimensionless thermodynamic coupling parameter  $\lambda = k/H$ : the ratio of the characteristic bulk thermodynamic energy density over the characteristic interface energy density. The source term of the grand potential Allen-Cahn equation as seen in eq. (1.2.35) will be

$$\frac{\lambda M_\varphi}{W^2} p'(\varphi) \Delta\bar{\omega}(\bar{\boldsymbol{\mu}}) \quad (1.3.29)$$

with  $\Delta\bar{\omega}(\bar{\boldsymbol{\mu}}) = \omega_0(\bar{\boldsymbol{\mu}}) - \omega_1(\bar{\boldsymbol{\mu}})$ , see eq. (1.3.23).

Second, we require the Boussinesq approximation for our flow coupling for the reason presented hereafter. The chemical diffusion process can be assimilated to neighbouring components randomly exchanging places (the same way the diffusion of a solvent can be assimilated to a discrete random walk). The fluid elements tracked by the Navier-Stokes equations are composed by those same components. If the densities of the phases were to differ, it would imply that the diffusion from one to the other displaces the centre of mass of the corresponding fluid element. We would then require a backward coupling of the diffusion to the advection, and more care would be required to verify the conservation of mass. Coincidentally, this reasoning also applies if the component had different or varying molar volumes. The Boussinesq approximation and the assumption of constant and identical molar volumes are thus both essential simplifying assumptions. The buoyancy force term in the conservation of moment will have the form found in eq. (1.2.19) with a constant density difference  $\Delta\rho$ .

With that in mind, we can now compose eqs. (1.2.35), the two-phase Navier-Stokes equations from sec. 1.2.3, and the chemical diffusion equations with the closure relations of eqs. (1.3.12) to write down the full system of time evolution equations for our two-phase ternary liquid,

$$\nabla \cdot \mathbf{u} = 0, \quad (1.3.30)$$

$$\rho \partial_t \mathbf{u} + \rho \nabla \cdot (\mathbf{u} \mathbf{u}^T) = -\nabla p + \rho \nabla \cdot (\nu(\varphi)(\nabla \mathbf{u} + \nabla \mathbf{u}^T)) + \varphi \Delta \rho \mathbf{g} - \frac{\sigma}{W} \boldsymbol{\kappa}(\varphi), \quad (1.3.31)$$

$$\partial_t \varphi + \mathbf{u} \cdot \nabla \varphi = M_\varphi \nabla^2 \varphi - \frac{M_\varphi}{W^2} f'_{\text{dw}}(\varphi) + \frac{\lambda M_\varphi}{W^2} p'(\varphi) \Delta\bar{\omega}(\bar{\boldsymbol{\mu}}), \quad (1.3.32)$$

$$\partial_t \mathbf{c} + \mathbf{u} \cdot \nabla \mathbf{c} = \nabla \cdot (\bar{\mathbf{M}} \nabla \bar{\boldsymbol{\mu}}), \quad (1.3.33)$$

$$\bar{\boldsymbol{\mu}} = \bar{\mathbf{K}}(\varphi)(\mathbf{c} - \mathbf{c}^{\text{eq}}(\varphi)). \quad (1.3.34)$$

Note that 3D-space vectors with bold upright symbols (e.g.  $\mathbf{u}$ ) are to be dissociated from component-space tensors with bold italic symbols (e.g.  $\mathbf{c}$ ). There is one diffusion equation (1.3.33) and closure (1.3.34) for each component. We also remind that the expression of the surface tension's curvature measure  $\kappa(\varphi)$  is found in eq. (1.2.22); of the grand potentials difference  $\Delta\bar{\omega}(\bar{\mu})$  in eq. (1.3.23); and of the interpolations of the  $\mathbf{c}^{\text{eq}}$  vectors and the  $\bar{\mathbf{K}}$  matrices in eqs. (1.3.25) and (1.3.26) respectively.

For convenience, the parameters of the model are summarized in table 1.1.

Symbol	Description	Dimensions
$\rho$	Constant and identical density of the two-phase fluid	$[\rho]$
$\nu(\varphi)$	Harmonic interpolation of each phase's kinematic viscosity: $\nu(\varphi) = ((1 - \varphi)/\nu_0 + \varphi/\nu_1)^{-1}$	$L^2 \cdot T^{-1}$
$\Delta\rho\mathbf{g}$	Buoyancy under the Boussinesq approximation: phase density difference $\Delta\rho$ and acceleration of gravity $\mathbf{g}$	$[\rho] \cdot L \cdot T^{-2}$
$\sigma$	Surface tension of the diffuse interface	$[E] \cdot L^{-2}$
$W$	Diffuse interface width	$L$
$M_\varphi$	Diffuse interface relaxation rate	$L^2 \cdot T^{-1}$
$\lambda$	Thermodynamic coupling constant: ratio of the diffuse interface's energy density to the thermodynamic bulk energy density	$\emptyset$
$\bar{\mathbf{M}}$	Non-dimensionalized chemical mobility matrix	$L^2 \cdot T^{-1}$
$\bar{\mathbf{K}}$	Non-dimensionalized free energy second	$\emptyset$
$\mathbf{c}_\pi^{\text{eq}}$	Equilibrium compositions of phase $\pi$ on the reference tie-line	$\emptyset$

Table 1.1: Parameters of the two-phase ternary liquid phase field model. The dimensions are listed in terms of a length unit  $L$  and time unit  $T$ . The symbol  $[E]$  and  $[\rho]$  denotes arbitrary units of energy and mass density, respectively. These will be removed by making the PDE system dimensionless.

The phase field and chemical diffusion PDEs were reparametrized to remove the energy dimension. One may wish to do the same to remove the implicit energy dimension in  $\sigma$  in the NS equations, but to do so it is necessary to also make the differential operators  $\partial_t$  and  $\nabla$  dimensionless using a characteristic length scale  $L$  and velocity scale  $v$ . Doing so reveals a characteristic scale  $\rho v^2$  of the bulk kinematic energy density and allow a completely dimensionless form of the PDE system:

$$\bar{\nabla} \cdot \bar{\mathbf{u}} = 0, \quad (1.3.35)$$

$$\partial_t \bar{\mathbf{u}} + \bar{\nabla} \cdot (\bar{\mathbf{u}} \bar{\mathbf{u}}^T) = -\bar{\nabla} \bar{p} + \bar{\nabla} \cdot \left( Re^{-1}(\varphi) (\bar{\nabla} \bar{\mathbf{u}} + \bar{\nabla} \bar{\mathbf{u}}^T) \right) + \varphi Fr^{-2} \frac{\mathbf{g}}{\|\mathbf{g}\|} - We^{-1} Cn^{-1} \bar{\kappa}(\varphi) \quad (1.3.36)$$

$$\partial_t \varphi + \bar{\mathbf{u}} \cdot \bar{\nabla} \varphi = Pe_\varphi^{-1} \left( \bar{\nabla}^2 \varphi - Cn^{-2} \left( f'_{\text{dw}}(\varphi) + \lambda p'(\varphi) \Delta \bar{\omega}(\bar{\mu}) \right) \right), \quad (1.3.37)$$

$$\partial_t \mathbf{c} + \bar{\mathbf{u}} \cdot \bar{\nabla} \mathbf{c} = \bar{\nabla} \cdot (\mathbf{P} \mathbf{e}^{-1} \bar{\nabla} \bar{\mu}), \quad (1.3.38)$$

$$\bar{\mu} = \bar{\mathbf{K}}(\varphi)(\mathbf{c} - \mathbf{c}^{\text{eq}}(\varphi)), \quad (1.3.39)$$

with the dimensionless differential operators and flow fields

$$\partial_t = (L/v) \partial_t, \quad \bar{\nabla} = (1/L) \nabla, \quad \bar{\mathbf{u}} = \mathbf{u}/v, \quad \bar{p} = p/\rho v^2, \quad (1.3.40)$$

the dimensionless measure

$$\bar{\kappa}(\varphi) = \frac{3}{2} \left( Cn^2 \bar{\nabla}^2 \varphi - f'_{\text{dw}}(\varphi) \right) \bar{\nabla} \varphi \quad (1.3.41)$$

and the dimensionless numbers

$$\begin{aligned} Re(\varphi) &= \frac{vL}{\nu(\varphi)}, & Fr &= \frac{v}{\sqrt{(\Delta\rho/\rho)\|\mathbf{g}\|L}}, & We &= \frac{\rho v^2 L}{\sigma}, \\ Cn &= \frac{W}{L}, & Pe_\varphi &= \frac{Lv}{M_\varphi}, & \mathbf{Pe}^{-1} &= \frac{\bar{M}}{Lv}. \end{aligned} \quad (1.3.42)$$

In the expressions above,  $\|\mathbf{g}\|$  is the norm of the gravity acceleration vector. The dimensionless numbers are respectively the Reynolds, Froude, Weber, Cahn, phase field Péclet and chemical Péclet numbers of the flow. Remark that  $We Cn \propto \rho v^2 / H$  is the characteristic ratio of the bulk kinematic energy density against the diffuse interface energy density, the analogue of  $\lambda$  for the flow. The Schmidt numbers defined by

$$\mathbf{Sc}^{-1}(\varphi) = \frac{\bar{M}}{\nu(\varphi)} \quad (1.3.43)$$

may also be relevant.

In the simulations of growth with sedimentation presented later,  $L$  will be defined in regards to the droplets's geometry and the gravity will be the main drive of the flow. In this case, the relevant flow velocity scale is

$$v = \sqrt{\frac{\Delta\rho}{\rho}\|\mathbf{g}\|L}, \quad (1.3.44)$$

implying  $Fr = 1$  is no longer a relevant number, and that  $We$  can be replaced with the Eötvös number

$$Eo = \frac{\Delta\rho g L^2}{\sigma}. \quad (1.3.45)$$

### 1.3.5 Conclusion

In this first chapter, we have derived a theoretical model to describe a two-phase fluid with three chemical components. It follows a fully resolved interface by relying on the phase-field theory, a framework representing the interface as a diffuse interface of a scalar field. The diffusion of the chemical components is resolved in consistency with the thermodynamics of the bulk phases of the material. By using an Allen-Cahn-type model aided by a grand potential reformulation, we are able to specify the free energies for the bulks in coherence with the system's chemical equilibrium while still allowing us to tune separately these bulk properties and the interface properties: the surface tension and the interface width. The Gibbs-Thomson condition asymptotically reconstructed at the interface was established. The two-phase fluid's advection is taken into account by the Navier-Stokes equation in the case of a Newtonian and incompressible Boussinesq fluid.

There are many points of possible extension for this model. One of them is to take into account different molar volumes for the components, which would in turn allow us to relax the Boussinesq assumption. We may take a first step in that direction if we were to reinforce the consistency of the flow coupling, by inserting the advection field into the free energy functional and rederiving all the details leading to the Navier-Stokes equation. Furthermore, it may be of interest to look at other forms of the free energies, for instance to better take into account the very low composition of molybdenum in the mother phase. For the same reason, we may also want to relax the assumption of a diagonal mobility matrix.

In the following, the implicit description of the interface made by the phase field will greatly ease the discretization of the model. This will be described in the next chapter, where we will prepare the implementation of the model for simulations in a high performance code.

## References

- [1] Samuel M. Allen and John W. Cahn. “A microscopic theory for antiphase boundary motion and its application to antiphase domain coarsening.” In: *Acta Metallurgica* 27.6 (1979), pp. 1085–1095. issn: 0001-6160. doi: [https://doi.org/10.1016/0001-6160\(79\)90196-2](https://doi.org/10.1016/0001-6160(79)90196-2).
- [2] Robert F. Almgren. “Second-Order Phase Field Asymptotics for Unequal Conductivities.” In: *SIAM Journal on Applied Mathematics* 59.6 (1999), pp. 2086–2107. doi: 10.1137/S0036139997330027.
- [3] Arnaldo Badillo. “Quantitative phase-field modeling for boiling phenomena.” In: *Phys. Rev. E* 86 (4 Oct. 2012), p. 041603. doi: 10.1103/PhysRevE.86.041603.
- [4] Raphaël Bayle. “Simulation des mécanismes de changement de phase dans des mémoires PCM avec la méthode multi-champ de phase.” 2020IPPAX035. PhD thesis. 2020.
- [5] Téo Boutin, Werner Verdier, and Alain Cartalade. “Grand-potential-based phase-field model of dissolution/precipitation: Lattice Boltzmann simulations of counter term effect on porous medium.” In: *Computational Materials Science* 207 (2022), p. 111261. issn: 0927-0256. doi: <https://doi.org/10.1016/j.commatsci.2022.111261>.
- [6] J.U Brackbill, D.B Kothe, and C Zemach. “A continuum method for modeling surface tension.” In: *Journal of Computational Physics* 100.2 (1992), pp. 335–354. issn: 0021-9991. doi: [https://doi.org/10.1016/0021-9991\(92\)90240-Y](https://doi.org/10.1016/0021-9991(92)90240-Y).
- [7] Jesus Bueno and Hector Gomez. “Liquid-vapor transformations with surfactants. Phase-field model and Isogeometric Analysis.” In: *Journal of Computational Physics* 321 (2016), pp. 797–818. issn: 0021-9991. doi: <https://doi.org/10.1016/j.jcp.2016.06.008>.
- [8] John W. Cahn. “Spinodal Decomposition.” In: *Transactions of the Metallurgical Society of AIME*. Vol. 242. 1968, pp. 1191–2520.
- [9] John W. Cahn and John E. Hilliard. “Free Energy of a Nonuniform System. I. Interfacial Free Energy.” In: *The Journal of Chemical Physics* 28.2 (1958), pp. 258–267. doi: 10.1063/1.1744102.
- [10] Pao-Hsiung Chiu and Yan-Ting Lin. “A conservative phase field method for solving incompressible two-phase flows.” In: *Journal of Computational Physics* 230.1 (Jan. 2011), pp. 185–204. doi: 10.1016/j.jcp.2010.09.021.
- [11] Blas Echebarria et al. “Quantitative phase-field model of alloy solidification.” In: *Phys. Rev. E* 70 (6 Dec. 2004), p. 061604. doi: 10.1103/PhysRevE.70.061604.
- [12] R. Folch et al. “Phase-field model for Hele-Shaw flows with arbitrary viscosity contrast. II. Numerical study.” In: *Phys. Rev. E* 60 (2 Aug. 1999), pp. 1734–1740. doi: 10.1103/PhysRevE.60.1734.
- [13] Morton E. Gurtin, Eliot Fried, and Lallit Anand. “Incompressible Fluids.” In: *The Mechanics and Thermodynamics of Continua*. 2010, pp. 259–270. doi: 10.1017/CBO9780511762956.055.
- [14] P. C. Hohenberg and B. I. Halperin. “Theory of dynamic critical phenomena.” In: *Rev. Mod. Phys.* 49 (3 July 1977), pp. 435–479. doi: 10.1103/RevModPhys.49.435.
- [15] David Jacqmin. “Calculation of Two-Phase Navier–Stokes Flows Using Phase-Field Modeling.” In: *Journal of Computational Physics* 155.1 (1999), pp. 96–127. issn: 0021-9991. doi: <https://doi.org/10.1006/jcph.1999.6332>.
- [16] Barbara Kaltenbacher and William Rundell. “Regularization of a backwards parabolic equation by fractional operators.” In: *Inverse Problems and Imaging* 13.2 (2019), pp. 401–430.

- [17] Alain Karma and Wouter-Jan Rappel. “Quantitative phase-field modeling of dendritic growth in two and three dimensions.” In: *Phys. Rev. E* 57 (4 Apr. 1998), pp. 4323–4349. doi: 10.1103/PhysRevE.57.4323.
- [18] Junseok Kim. “A continuous surface tension force formulation for diffuse-interface models.” In: *Journal of Computational Physics* 204.2 (2005), pp. 784–804. issn: 0021-9991. doi: <https://doi.org/10.1016/j.jcp.2004.10.032>.
- [19] Junseok Kim. “Phase-Field Models for Multi-Component Fluid Flows.” In: *Communications in Computational Physics* 12.3 (2012), pp. 613–661. doi: 10.4208/cicp.301110.040811a.
- [20] Seong Gyoon Kim, Won Tae Kim, and Toshio Suzuki. “Phase-field model for binary alloys.” In: *Phys. Rev. E* 60 (6 Dec. 1999), pp. 7186–7197. doi: 10.1103/PhysRevE.60.7186.
- [21] L.D. Landau et al. *Statistical Physics: Theory of the Condensed State*. Course of theoretical physics. Elsevier Science, 1980. isbn: 9780750626361.
- [22] Mathis Plapp. “Remarks on some open problems in phase-field modelling of solidification.” In: *Philosophical Magazine* 91.1 (2011), pp. 25–44. doi: 10.1080/14786435.2010.486757.
- [23] Mathis Plapp. “Unified derivation of phase-field models for alloy solidification from a grand-potential functional.” In: *Phys. Rev. E* 84 (3 Sept. 2011), p. 031601. doi: 10.1103/PhysRevE.84.031601.
- [24] Tiezheng Qian. *Onsager’s variational principle and its applications*. [https://ins.sjtu.edu.cn/files/common/20160701091005\\_notes2.pdf](https://ins.sjtu.edu.cn/files/common/20160701091005_notes2.pdf). Retrieved 08/02/2021. 2016.
- [25] M.A. Rasolofomanana et al. “Diffuse-interface modelling of multicomponent diffusion and phase separation in the U-O-Zr ternary system.” In: *Computational Materials Science* 214 (2022), p. 111650. issn: 0927-0256. doi: <https://doi.org/10.1016/j.commatsci.2022.111650>.
- [26] J. S. Rowlinson. “Translation of J. D. van der Waals’ “The thermodynamic theory of capillarity under the hypothesis of a continuous variation of density”.” In: *Journal of Statistical Physics* 20 (1979), pp. 197–200. issn: 1572-9613. doi: 10.1007/BF01011514.
- [27] Hao Shiming and Zhang Xin. “Calculation of phase equilibria for the ternary system by the grand potential method.” In: *Journal of Phase Equilibria* 16 (1995), pp. 441–446. doi: 10.1007/BF02645351.
- [28] Y. Sun and C. Beckermann. “Sharp interface tracking using the phase-field equation.” In: *Journal of Computational Physics* 220.2 (Jan. 2007), pp. 626–653. doi: 10.1016/j.jcp.2006.05.025.
- [29] Hugo Touchette. *Legendre-Fenchel transforms in a nutshell*. <https://web.archive.org/web/20170407134235/http://www.physics.sun.ac.za/~htouchette/archive/notes/lft2.pdf>. Retrieved 01/03/2022. 2014.
- [30] Werner Verdier. *Modèle à champ de phase pour verres ternaires diphasiques*. Note technique DES STMF/LMSF/NT/2021-67858 (CEA internal technical report). 2021.
- [31] Werner Verdier, Pierre Kestener, and Alain Cartalade. “Performance portability of lattice Boltzmann methods for two-phase flows with phase change.” In: *Computer Methods in Applied Mechanics and Engineering* 370 (2020), p. 113266. issn: 0045-7825. doi: <https://doi.org/10.1016/j.cma.2020.113266>.

## Chapter 2

# Numerical implementation

Chapter 1 established the physical model of a two-phase three-component liquid as a system of partial differential equations. We must now explain how we bring this model to quantitative numerical simulations.

The first step is to build a discretized form of the model, meaning transforming it into an approximate form suitable for processing by a numerical computer algorithm. The most known methods to do so are the finite differences, finite volumes or finite elements schemes. Here, we will employ a relatively recent method known as the lattice Boltzmann method (LBM) [33] [20] which indirectly solves the partial differential equations by operating on distribution functions obeying a discrete Boltzmann equation and on their moments in phase space. The method and its use are presented in the first section of this chapter, which will conclude with the complete discretization of the two-phase ternary flow model.

Once the discretization and numerical resolution algorithm is established, the next step is their implementation by a computer program. The second section of this chapter will present LBM\_saclay, a simulation code for lattice Boltzmann schemes whose development was a significant part of the thesis work. We will detail the particular care taken to make this code highly performant on modern parallel architectures.

With the complete implementation, we are able to bring the model to quantitative 3D simulations of this model as will be presented in the last chapter.

### 2.1 Lattice Boltzmann method

The lattice Boltzmann method (LBM) is a discretization method for partial differential equations. It is naturally adapted to advection-diffusion equations, including vector ones such as the Navier-Stokes' momentum equation. Its algorithm is relatively simple to implement, and its memory accesses are half local and half stencil-based, making it particularly efficient numerically and easy to parallelize. This section will mostly only go over the elements of practical use for the simulations carried out in this thesis. The interested reader can refer to the book by T. Krüger et. al. [28] for more details on the method.

We may remark that since the LBM was first thought as a way to model flows, there exists whole classes of LBM-specific models for two-phase flows. For instance, the Shan-Chen pseudopotential method [42] [7] [48] and the color-gradient method [17] [12]. Over them, the phase field method has the advantage of having a rigorous thermodynamic consistency and a clear formalism for the coupling to an intensive thermodynamic diffusion field; though we may underline the similarities of the phase field theory with what is known as the early “free energy method” [43] in the LBM literature, which is also based on an energy functional and produces a diffuse interface with an hyperbolic tangent profile.



D2Q9			D3Q19		
$k$	$\mathbf{e}_k$	$w_k$	$k$	$\mathbf{e}_k$	$w_k$
0	(0, 0)	4/9	0	(0, 0, 0)	1/3
1, 2	(+1, 0), (0, +1),	1/9	1, 2, 3	(+1, 0, 0), (-1, 0, 0), (0, +1, 0),	1/18
3, 4	(-1, 0), (0, -1)		4, 5, 6	(0, -1, 0), (0, 0, +1), (0, 0, -1)	
5, 6	(+1, +1), (-1, +1),	1/36	7, 8, 9	(+1, +1, 0), (-1, -1, 0), (+1, 0, +1),	1/36
7, 8	(-1, -1), (+1, -1)		10, 11, 12	(-1, 0, -1), (0, +1, +1), (0, -1, -1),	
			13, 14, 15	(+1, -1, 0), (-1, +1, 0), (+1, 0, -1),	
			16, 17, 18	(-1, 0, +1), (0, +1, -1), (0, -1, +1)	

Table 2.1: Detail of the direction vectors  $\mathbf{e}_k$  and of the scalar weights  $w_k$  associated to each velocities of the D2Q9 and D3Q19 lattices.

The literature has many examples of the lattice Boltzmann method being used to discretize a Cahn-Hilliard or an Allen-Cahn phase field model. Some examples of the first kind of models are found from 2006 to today [51, 22, 11, 41, 31, 2]. Allen-Cahn LBM models are in comparison a bit more recent [14, 47, 38, 3]. As far as we know, our work is the first which couples a grand potential Allen-Cahn model to a lattice Boltzmann discretization with flow dynamics.

Finally, we may remark that even though the LBM is younger than other numerical methods, there are multiple instances of numerical analysis of its schemes. Some examples are [24, 4, 50].

### 2.1.1 Discretization of a Boltzmann equation

As opposed to more common discretization methods (finite differences, finite volumes...), the LBM does not directly discretize a PDE. It is first a discretization in space and velocity-space of the Boltzmann equation

$$\partial_t f(t, \mathbf{x}, \mathbf{c}) + \mathbf{c} \cdot \nabla f(t, \mathbf{x}, \mathbf{c}) = -\frac{f - f^{\text{eq}}}{\tau} + S(t, \mathbf{x}, \mathbf{c}). \quad (2.1.1)$$

The above Boltzmann equation comes from the classic kinetic theory of gases: it describes the evolution of a probability density function  $f(t, \mathbf{x}, \mathbf{c})$  of particles over the positions  $\mathbf{x}$  and velocities  $\mathbf{c}$ . The first quantity on the right-hand side is the Bhatnagar–Gross–Krook collision operator [5] which enforces the exponential relaxation of  $f$  towards the equilibrium distribution  $f^{\text{eq}}(t, \mathbf{x}, \mathbf{c})$ . An arbitrary source term  $S(t, \mathbf{x})$  is also included for later use.

In the LBM, the Boltzmann equation is discretized over space and velocity-space on a regular Cartesian grid of nodes with a spacing  $\delta x$  and a finite set of  $N_k$  velocities  $\mathbf{c}_k$ , with  $k = 0, 1, \dots, N_k - 1$  (by convention,  $\mathbf{c}_0 = \mathbf{0}$  is always the zero velocity). The directions carrying these velocities bridge the grid nodes to their neighbours and a lattice structure naturally emerges; see in particular the two examples in figure 2.1.

The Boltzmann equation is then discretized along the  $\mathbf{c}_k$  velocities (see appendix C.1 of [46] for details) to obtain the discrete Boltzmann equation

$$f_k(t + \delta t, \mathbf{x} + \mathbf{c}_k \delta t) = f_k(t, \mathbf{x}) - \frac{f_k - f_k^{\text{eq}}}{\bar{\tau}} + \delta t S_k(t, \mathbf{x}) \quad (2.1.2)$$

with  $\delta t$  a discrete time step,  $\bar{\tau} = \tau / \delta t + 1/2$ , and  $f_k, f_k^{\text{eq}}$  and  $S_k$  the discrete equivalent of the distribution function and the source term along each  $\mathbf{c}_k$ . The time step  $\delta t$  is the time taken by the distributions at velocities  $\mathbf{c}_k$  to reach the neighbouring lattice node. In consequence, we will sometime prefer writing the neighbour positions as  $\mathbf{x} + \mathbf{e}_k \delta x$ , with  $\mathbf{c}_k = (\delta x / \delta t) \mathbf{e}_k$ . Eq. (2.1.2) is the general form of the lattice Boltzmann equation (LBE) that will be used in our work.

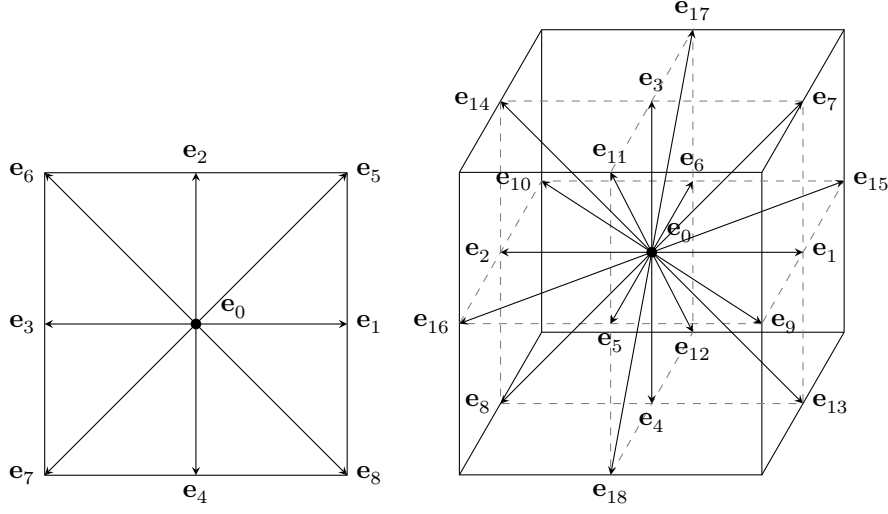


Figure 2.1: LBM lattices used in the present work, (left) D2Q9 and (right) D3Q19 (the first number refers to the dimension and the second to the total count of discrete velocities). The directions vectors  $\mathbf{e}_k$  carries each discrete velocity as  $\mathbf{c}_k = (\delta x / \delta t) \mathbf{e}_k$ . See also table 2.1.

### 2.1.2 Reconstructed macroscopic equations, Chapman-Enskog expansion

The LBM finds its use as a more general PDE discretization through the Chapman-Enskog expansion [6] [28, chap. 4]. With it, and an adequate definition for the equilibrium distribution  $f^{\text{eq}}$ , one shows that the Boltzmann equation reconstructs the desired macroscopic diffusion equation through its moments. The canonical example of this expansion is the rederivation of the Navier-Stokes equations with  $f^{\text{eq}}$  taken as the Maxwellian distribution around the macroscopic velocity  $\mathbf{u}$ . This last quantity is itself reconstructed through the moment of  $f$ , as  $\mathbf{u} \propto \int \mathbf{c} f d\mathbf{c}$ .

This property is carried over to the discrete LBE. Again, we take the example of the Navier-Stokes equations to illustrate. The equivalent of the Maxwellian distribution in the discrete phase space is the function

$$\gamma_k(\mathbf{u}) = w_k \left( 1 + \frac{\mathbf{u} \cdot \mathbf{c}_k}{c_s^2} + \frac{(\mathbf{u} \cdot \mathbf{c}_k)^2}{2c_s^4} - \frac{\mathbf{u}^2}{2c_s^2} \right) \quad (2.1.3)$$

with  $c_s^2 = \delta x^2 / 3\delta t^2$  the square of the characteristic lattice speed and  $w_k$  the lattice's scalar weights as listed in table 2.1. A discrete Chapman-Enskog expansion of eq. (2.1.2) without the source term and with  $f_k^{\text{eq}} = \rho \gamma_k$  reconstructs the compressible Navier-Stokes equations with its density, pressure and velocity fields as

$$\rho = \sum_k f_k, \quad p = \rho c_s^2, \quad \rho \mathbf{u} = \sum_k \mathbf{c}_k f_k. \quad (2.1.4)$$

The integral moments with respect to  $\mathbf{c}$  coherently discretize into sums over the finite set of velocities  $\mathbf{c}_k$ . In addition, the fluid's kinematic viscosity is identified as

$$\nu = c_s^2 \delta t \left( \bar{\tau} - \frac{1}{2} \right). \quad (2.1.5)$$

In the LBM literature, there are common ways to discretize additional source terms or to modify the equilibrium function to obtain a desired scalar or vector diffusion equation. This is exploited later to discretize our two-phase three-component flow model; it will be seen that the macroscopic reconstruction closely follows the previous example.

### 2.1.3 Time evolution algorithm

Now that the discrete Boltzmann equation and its link to the macroscopic equations are established, we explain here the numerical algorithm used to solve the LBE, eq. (2.1.2).

The algorithm is usually described in two steps:

- a local collision step, corresponding to the right-hand side of (2.1.2),

$$f_k^*(t, \mathbf{x}) = \frac{1}{\bar{\tau}} f_k^{\text{eq}}(t, \mathbf{x}) + \left(1 - \frac{1}{\bar{\tau}}\right) f_k(t, \mathbf{x}) + \delta t S_k(t, \mathbf{x}); \quad (2.1.6)$$

- and a streaming step (or advection step) which only consists of moving data along the lattice,

$$f_k(t + \delta t, \mathbf{x} + \mathbf{e}_k \delta x) = f_k^*(t, \mathbf{x}). \quad (2.1.7)$$

The split is not necessary when implementing the algorithm, but it helps underline an advantage of the method. Half of its calculations are purely local and the other half are copies with stencil pattern memory accesses. In addition, each discrete distribution  $f_k$  contributes to the update of one and only one distribution: its neighbour at  $\mathbf{x} + \mathbf{e}_k \delta t$ . Intuitively, this guarantees a level of spatial memory locality (use of memory near other recently accessed addresses [19]), necessary for efficiency.

An additional step to compute and save the moments, e.g. eq. (2.1.4), can follow the collision-streaming. Finally, the boundary conditions (see the next section) are applied and the algorithm loops back for the next time step.

### 2.1.4 Initial and boundary conditions

While the LBM algorithm can be written only in terms of distribution functions, the initial and boundary conditions are more conveniently described in terms of the macroscopic variables. To implement those, we employ basic algorithms which are detailed below.

#### Initialization at equilibrium

The simplest initialization scheme consists of setting the distribution function at equilibrium

$$f_k(0, \mathbf{x}) = f_k^{\text{eq}}(0, \mathbf{x}), \quad (2.1.8)$$

with  $f_k^{\text{eq}}(0, \mathbf{x})$  computed with the set of macroscopic fields desired at  $t = 0$ .

More elaborate initialization scheme can be found in the literature [35], but the initialization at equilibrium was considered sufficient for practical use here.

#### Periodic boundaries

Simulating a periodic domain is simply done by advecting the distribution functions from one end of the domain to the opposite. Note that since the stream stencil has diagonal directions, this can mean advecting to the opposite face, side or corner.

#### Bounceback and anti-bounceback

The bounceback algorithm reflects distributions going out of the lattice as illustrated in figure 2.2. It consists of a substitution of the stream step (2.1.7) as

$$f_{k^-}(t + \delta t, \mathbf{x}) = f_k^*(t, \mathbf{x}) \quad \text{with } k^- \text{ s. t. } \mathbf{e}_{k^-} = -\mathbf{e}_k. \quad (2.1.9)$$

This has the effect of setting the first moment of  $f$  to  $\mathbf{0}$  at the boundaries. Usually this corresponds to the advection field  $\mathbf{u}$  for flow LBEs, or to the gradient of the diffusion field for diffusion LBEs.

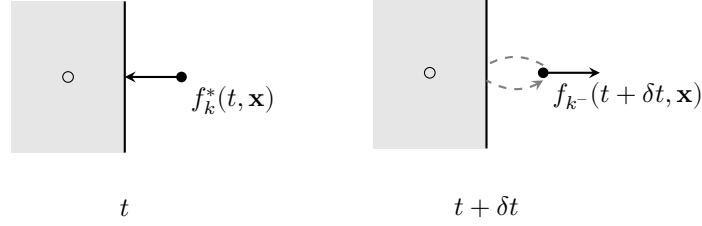


Figure 2.2: Illustration of the bounceback boundary condition. The distributions that would be advected outside the domain are instead advected back into the same node in the opposite direction, as if it was reflected by the boundary. It replaces the usual stream step. This process must still take place within  $\delta t$ : in consequence, the reflecting boundary is considered to be at a distance  $\delta x/2$  from the node, since this distance is covered twice.

The anti-bounceback follows the same scheme but with a minus sign and an added constant:

$$f_k = -f_{k^-} + 2w_k C. \quad (2.1.10)$$

It sets the zeroth moment of  $f$  to a desired value  $C$  [15] at the boundaries; typically the diffusion field in a scalar diffusion LBE, or the density and/or pressure field in a flow LBE.

### 2.1.5 Finite differences stencil

The LBEs presented later will involve a source term  $S(t, \mathbf{x})$  which itself may depend on the gradient or Laplacian of a macroscopic variable. They will be discretized with a second order finite difference stencil on the lattice directions as [30]

$$\begin{aligned} \nabla C(\mathbf{x}) &= 3 \sum_k w_k \frac{C(\mathbf{x} + \mathbf{e}_k \delta x) - C(\mathbf{x} - \mathbf{e}_k \delta x)}{2\delta x} \mathbf{e}_k, \\ \nabla^2 C(\mathbf{x}) &= 3 \sum_k w_k \frac{C(\mathbf{x} - \mathbf{e}_k \delta x) - 2C(\mathbf{x}) + C(\mathbf{x} + \mathbf{e}_k \delta x)}{\delta x^2}, \end{aligned} \quad (2.1.11)$$

where  $C$  is again a placeholder for any macroscopic field variable. On the boundaries of a non-periodic domain, this stencil is replaced by the off-centre Cartesian stencils of second order

$$\begin{aligned} \frac{\partial^2 C}{\partial x^2}(\mathbf{x}) &= \frac{2C(\mathbf{x}) - 5C(\mathbf{x} + \delta x \mathbf{e}_x) + 4C(\mathbf{x} + 2\delta x \mathbf{e}_x) - C(\mathbf{x} + 3\delta x \mathbf{e}_x)}{\delta x^2}, \\ \frac{\partial C}{\partial x}(\mathbf{x}) &= \frac{-3C(\mathbf{x}) + 4C(\mathbf{x} + \delta x \mathbf{e}_x) - C(\mathbf{x} + 2\delta x \mathbf{e}_x)}{2\delta x}, \end{aligned} \quad (2.1.12)$$

in the example of the  $x$  derivatives at the boundary perpendicular to the  $-x$  axis and with  $\mathbf{e}_x$  the corresponding unit vector.

### 2.1.6 LBM discretization of the two-phase three component phase field model

We can now write the discretized form of the two-phase three-component flow model. The strategy adopted here is to define one distribution function for each subset of the model. We denote  $v_k$  the

distributions for the two incompressible Navier–Stokes equations (1.3.30), (1.3.31);  $h_k$  the distributions for the phase field equation (1.3.32); and  $a_k, b_k$  the distributions for the diffusion of each component (1.3.33). There are examples in the literature of the opposite strategy with one distribution function for all PDEs of the continuous model: in [29], the set of lattice is extended (D2Q13) so that the second moment of a single distribution function is captured as the conservation of energy, giving the PDE of the diffusion of heat for a single-phase thermal flow. This alternative approach was not considered in our work because of its complexity relative to the one with multiple isothermal LBEs for each partial differential equation.

### Flow LBE

The distribution functions corresponding to eqs. (1.3.30) and (1.3.31) are written with  $v_k$ , and their time stepping are done with a lattice Boltzmann equation adapted from the He–Luo LBE [18] for incompressible fluids,

$$v_k(t + \delta t, \mathbf{x} + \delta x \mathbf{e}_k) = \left(1 - \frac{1}{\bar{\tau}_v}\right) v_k(t, \mathbf{x}) - \frac{1}{\bar{\tau}_v} v_k^{\text{eq}}(t, \mathbf{x}) + \delta t S_{v,k}(t, \mathbf{x}), \quad (2.1.13)$$

with

$$\bar{\tau}_v(\varphi) = \frac{\nu(\varphi)}{\delta t c_s^2} + \frac{1}{2}, \quad (2.1.14)$$

$$v_k^{\text{eq}} = w_k p + (\gamma_k - w_k) \rho c_s^2 - \frac{\delta t}{2} S_{v,k}, \quad (2.1.15)$$

$$S_{v,k} = \gamma_k (\mathbf{c}_k - \mathbf{u}) \cdot \mathbf{F}(\varphi). \quad (2.1.16)$$

See eq. (1.2.23) for the expression of the volume forces  $\mathbf{F}(\varphi)$ . The pressure and velocity fields solution of the Navier–Stokes equations are given by the moments of the  $v_k$ ,

$$p = \sum_k v_k, \quad (2.1.17)$$

$$\mathbf{u} = \frac{1}{\rho c_s^2} \left( \sum_k \mathbf{c}_k v_k + \frac{\delta t}{2} c_s^2 \mathbf{F} \right). \quad (2.1.18)$$

Note that the Boussinesq approximation simplifies the calculation of the pressure. When the density difference is taken in account in the kinetic terms of the Navier–Stokes equations, an additional term proportional to  $\nabla \rho(\varphi) c_s^2$  appears in eq. (2.1.18) (see eq. (28b) of [46]).

### Phase field LBE

Denote  $h_k$  the distribution function associated with the phase field equation (1.3.32). Its LBE is

$$h_k(t + \delta t, \mathbf{x} + \delta x \mathbf{e}_k) = \left(1 - \frac{1}{\bar{\tau}_h}\right) h_k(t, \mathbf{x}) + \frac{1}{\bar{\tau}_h} h_k^{\text{eq}}(t, \mathbf{x}) + \delta t S_{h,k}, \quad (2.1.19)$$

where

$$\bar{\tau}_h = \frac{M_\varphi}{\delta t c_s^2} + \frac{1}{2}, \quad (2.1.20)$$

$$h_k^{\text{eq}} = w_k \varphi \left( 1 + \frac{\mathbf{c}_k \cdot \mathbf{u}}{c_s^2} \right) - \frac{\delta t}{2} S_{h,k}, \quad (2.1.21)$$

$$S_{h,k} = w_k \frac{\lambda M_\varphi}{W^2} p'(\varphi) \Delta \bar{\omega}(\bar{\mu}^A, \bar{\mu}^B). \quad (2.1.22)$$

The phase field  $\varphi$  is reconstructed by

$$\varphi = \sum_k h_k + \frac{\delta t}{2} \frac{\lambda M_\varphi}{W^2} p'(\varphi) \Delta \bar{\omega}(\bar{\mu}^A, \bar{\mu}^B). \quad (2.1.23)$$

Notice that the right-hand side of this last expression also depends on  $\varphi$ : strictly speaking, computing  $\varphi(t + \delta t)$  after the stream-collision would require the same  $\varphi(t + \delta t)$  in the source term, making the calculation implicit. The same remark applies to the chemical potential fields whose reconstruction will also depend on  $\varphi$ . We sidestep this issue by using the fields from the previous time step instead. Explicitly,

$$\varphi(t + \delta t, \mathbf{x}) = \sum_k h_k(t + \delta t, \mathbf{x}) + \frac{\delta t}{2} \frac{\lambda M_\varphi}{W^2} p'(\varphi(t, \mathbf{x})) \Delta \bar{\omega}(\bar{\mu}^A(t, \mathbf{x}), \bar{\mu}^B(t, \mathbf{x})). \quad (2.1.24)$$

### Component diffusion LBE

The distribution functions  $a_k$  and  $b_k$  are used to solve the diffusion equations (1.3.33), along with the LBEs

$$\begin{aligned} a_k(t + \delta t, \mathbf{x} + \delta x \mathbf{e}_k) &= \left(1 - \frac{1}{\bar{\tau}^a}\right) a_k(t, \mathbf{x}) + \frac{1}{\bar{\tau}^a} a_k^{\text{eq}}(t, \mathbf{x}), \\ b_k(t + \delta t, \mathbf{x} + \delta x \mathbf{e}_k) &= \left(1 - \frac{1}{\bar{\tau}^b}\right) b_k(t, \mathbf{x}) + \frac{1}{\bar{\tau}^b} b_k^{\text{eq}}(t, \mathbf{x}), \end{aligned} \quad (2.1.25)$$

with

$$\begin{aligned} \bar{\tau}^a &= \frac{\bar{M}^{AA}(\varphi)}{\delta t c_s^2} + \frac{1}{2}, & a_k^{\text{eq}} &= \begin{cases} w_k \left( 3\Gamma \bar{\mu}^A + c^A \frac{\mathbf{c}_k \cdot \mathbf{u}}{c_s^2} \right), & k \neq 0, \\ c^A - 3\Gamma(1 - w_0) \bar{\mu}^A, & k = 0, \end{cases} \\ \bar{\tau}^b &= \frac{\bar{M}^{BB}(\varphi)}{\delta t c_s^2} + \frac{1}{2}, & b_k^{\text{eq}} &= \begin{cases} w_k \left( 3\Gamma \bar{\mu}^B + c^B \frac{\mathbf{c}_k \cdot \mathbf{u}}{c_s^2} \right), & k \neq 0, \\ c^B - 3\Gamma(1 - w_0) \bar{\mu}^B, & k = 0, \end{cases} \end{aligned} \quad (2.1.26)$$

where the  $\bar{\mu}^\alpha$  were computed at the previous time step by eq. (1.3.34). The factor  $\Gamma$  is a numerical tuning parameter taken here as  $\Gamma = 1/3$ . Finally, the compositions variables are given by the moments

$$c^A = \sum_k a_k, \quad c^B = \sum_k b_k. \quad (2.1.27)$$

Although  $a_k$  and  $b_k$  discretize an advection-diffusion equation like  $h_k$  did, they do not have the same form for their equilibrium distributions. This is due to the fact that the general lattice Boltzmann equation reconstructs a diffusive term in terms of the second moment of the distribution function. When the diffused variable is the same as the one under the total time derivative, the second moment and zeroth moment (times the identity matrix) coincide. The generic equilibrium function  $\gamma_k$  also has identical zeroth and second moment. When the two variables differ, the equilibrium function must be adjusted in consequence: this is why both  $c$  and  $\mu$  appear in the eqs. (2.1.26).

The same remark applies to the LBM discretization of the Cahn-Hilliard equation. In fact, the present expressions for  $a_k^{\text{eq}}$  and  $b_k^{\text{eq}}$  were derived by analogy with the LBEs for Cahn-Hilliard models, as in [22] for example.

## 2.2 The simulation code LBM\_saclay

This section details the portable and high-performance simulation code LBM\_saclay, first presented in [46]. The lattice Boltzmann scheme presented in the previous section (among others) is implemented in this code, and the simulations that will be shown in the next chapter ran with it on local workstations or GPU clusters.

Pierre Kestener built the first prototype of LBM\_saclay. The goal was to merge the efforts of multiple researchers at the CEA of Saclay who each had their own LBM code to have a single code more adapted to the modern HPC (High Performance Computing) architectures but without being constrained to them. It does so by using Kokkos [10], a C++ library for performance portability. Its further development was a significant part of the thesis work. Before the start of the thesis, the code was able to simulate a generic advection-diffusion equation and a simple two-phase flow with a conservative Allen–Cahn–Navier–Stokes model but without the capillary force. During the beginning of the thesis, this force was added and a coupling to a temperature field with a phase change term was implemented. This resulted in a model for the simulation of a liquid-gas flow with evaporation which was presented in [46] and served as a base for the later coupling to the incompressible Navier-Stokes equations of the two-phase three-component model. Other additions made to LBM\_saclay will be mentioned throughout this section.

In the following, we propose a quick summary of the HPC aspects, the use of the Kokkos and of the MPI standard for parallelism, and a detailed implementation example in LBM\_saclay with the two-phase three-component model.

### 2.2.1 High performance computing and parallelization

“High Performance Computing” (HPC) is an umbrella term covering the research and engineering of fast, distributed and efficient hardware architectures and software. It is often found in the context of numerical algorithms and simulations. For example, the TOP500 list [36] ranks supercomputers by the speed at which they can solve an enormous floating-point benchmark problem with performance in the hundred of PFlops ( $100 \times 10^{15}$  Flops, floating points operations per second). Very recently the exascale milestone ( $10^{18}$  Flops) was even reached by the Frontier system at the US Oak Ridge National Laboratory in June 2022.

Parallelization is a central component of HPC; because the performance of a single processing chip is ultimately limited by the heat generated by the dissipative processes taking place inside it, hardware architectures must find performance increases by combining multiple processors in a single unit, such as in the modern multicore and multithreaded general purpose CPUs. There are different scales of parallelization: a single multithreaded CPU will operate in parallel with its own memory (known as *shared memory parallelism*, enabled by *e.g.* the OpenMP specification or the pthreads library); multiple processing units can work in parallel and make their computation coherent by communicating together (*distributed memory parallelism*, *e.g.* with the MPI standard); and at a smaller scale, specialized floating point units will pack similar operations on multiple floating point numbers into a single processor instruction (SIMD, Same Instruction Multiple Data, also known as vectorization).

We took the example of general purpose CPUs, but modern HPC (since a bit less than 20 years [27]) increasingly relies on GPUs (Graphical Processing Units). GPUs are specialized processors originally built to accelerate 3D computer graphics, whose algorithms also involve a lot of floating point number crunching. Computer graphics rendering obeys a very strict pipeline and at first this constrained a lot the capability scope of GPU hardware and programming interfaces to be highly specialised for this pipeline. The advent of shader-based rendering allowed more generic computations and eventually led to the usage of GPUs for numerical simulations and other non-graphics usage, both in terms of hardware capabilities and software programming interfaces. Of these, we can mention OpenCL and the more

recent Vulkan (open source specifications of the Khronos group, the same behind OpenGL for graphics), OpenACC (another open source specification) and CUDA (vendor-locked to Nvidia's GPUs). These developments led GPUs to become a more powerful and energy-efficient<sup>1</sup> option for general floating point calculations.

In addition of raw processing power, memory access is a primary concern for high performance: a performance bottleneck appears if a computing unit processes data faster than it can fetch new data from main memory. In truth, the advances in memory transfer speeds did not keep up with the acceleration of computing power of successive hardware generations, and this bottleneck has become ubiquitous. In 2005 already HPC codes were increasingly becoming memory-bound rather than compute-bound [49]. This issue is handled by hardware manufacturers and cluster engineers at every level of parallelism: modern CPU cores with their own hierarchy of local caches, direct GPU-GPU memory transfer without passing through the dispatching CPU's memory, high throughput transfers (e.g. by Ethernet) between CPUs in a distributed supercomputer, etc.

As mentioned, all these points are not only hardware concerns. Parallelization introduces many new concerns for the software programmer compared to the usual sequential programming. Parallel and asynchronous computations will still depend on each other in some way in non-trivial programs, meaning they must wait for each other or communicate but without ending in a deadlock (where two parallel tasks endlessly wait for one another). Care in regard to memory accesses is necessary for a parallel program's efficiency (to cite only the basics, CPU caches prefer sequential accesses while GPUs threads prefer a pattern known as *memory coalescing* with strided accesses) and soundness (avoiding unordered asynchronous writes at the same place in memory).

Programming for a GPU requires additional tools compared to the more usual CPU programming; typically, a specialized compiler and/or a specialised application programming interface (API), which can be more or less complex and unfamiliar to usual programming languages. The different APIs vary a lot on this last point: for example, OpenCL defines a whole new C-like language in which to write GPU computations in while CUDA and OpenACC appears as more usual preprocessor directives to the usual C++ language (but only understood by their own compilers). Each API also exposes more or less low-level control to the programmer for optimizations. Finally, because of the complexity of programming GPU applications, their source code can end up being only compilable for these architectures and no other. This last point will be addressed in the next section through the Kokkos library.

We will close this subsection by re-emphasising the advantages of the physical model and its discretization for a parallel implementation. The implicit interface tracking will not introduce any new data structure or steps in the algorithm: the phase field equation is solved just like any other PDE. The LBM can work with just simple memory-contiguous arrays with high data reuse because of the stencil-like memory accesses. These are highly efficient on both CPUs and GPUs, though we may remark that even the GPU implementation of these simple stencil-based schemes are the subject of research to further improve their memory throughput [37, 26, 9, 39]. Finally, the relative ease of implementation of both saves programming efforts which can be then focused on the parallelization.

### 2.2.2 The Kokkos library

Kokkos [10] is an open-source C++ library released by the Sandia National Laboratories. It defines a single programming model for shared-model parallelism in the form of a C++ API and build system elements. The build system compiles the Kokkos API into a chosen backend. This means that a single source code using the Kokkos constructs can be compiled to run on parallel CPU (pthread, OpenMP backends) or GPU (CUDA, HIP backends) architectures with no changes to the source, only to flags given to the

<sup>1</sup>For example, for one hour of computation on the IDRIS supercomputer Jean-Zay; a single Nvidia Tesla V100 GPU consumes two to three times the power of the 20 cores of a single Intel Cascade Lake 6248 CPU [34]. However, this GPU has four to five times the flops of the theoretical peak of that CPU [1].



build system (typically CMake). The library achieves this with an heavy use of C++ templates and very few preprocessor macros: the source code will stay relatively familiar to the C++ programmer. Despite this generic aspect, Kokkos still exposes many optimizations opportunities (e.g. through memory access patterns, which the developer can also ignore and leave at its default settings); this is what Kokkos defines as the concept of *performance portability*.

The fundamental constructs of Kokkos and the ones most used in LBM\_saclay are the `Kokkos::View` type and the concept of parallel functors. A `Kokkos::View` is a generic view into a contiguous array allocated in CPU (*host*) or GPU (*device*) memory<sup>2</sup>. It supports multidimensional indexing and slicing and its memory order with respect to its dimensions can be parametrized. The concept of parallel functors (or “Kernels” as called in LBM\_saclay) defines a regular C++ class whose data and functions can be accessed and executed on a GPU; it is best illustrated by an example, see listing 1.

```
// Type of a view into a 1D array of doubles allocated in GPU memory.
using MyView = Kokkos::View<double*, Kokkos::DefaultExecutionSpace>;

struct Kernel {
    MyView view;

    DeviceFunctor(MyView v) : view(v) {}

    // The function that will be dispatched on the GPU and called
    // on a range of indices.
    KOKKOS_INLINE_FUNCTION void operator()(const int &i) const {
        // Do some work on view at index i...
        view(i) = (double) i;
    }
};

// Somewhere else, between Kokkos::initialize() and Kokkos::finalize()...
// Allocate an array of 256 doubles and execute the functor.
auto array = MyView("label", 256);
auto functor = DeviceFunctor(array);
Kokkos::parallel_for(256, functor);
```

Listing 1: C++ snippet illustrating the basic usage of Kokkos’ `View` type and functor concept.

### 2.2.3 MPI domain decomposition

Kokkos only manages the shared memory parallelism. The distributed memory parallelism in LBM\_saclay is handled separately with an implementation of MPI (Message Passing Interface), typically the Open-MPI library [13].

We define a simple Cartesian domain decomposition of the numerical domain by distributing  $m_x \times m_y \times m_z$  copies of a  $n_x \times n_y \times n_z$  subdomain (in 2D, ignore  $m_z$  and  $n_z$ ) on each MPI process. Each of these subdomains is enlarged by one lattice node in all directions: it is the layer of *ghost nodes* which serve as copies of the boundary nodes of the neighboring subdomains and which are used to implement the boundary conditions (see the next section). Each MPI process also owns a pair of buffers, one

<sup>2</sup>In the following, we will use “view” and “array” interchangeably to refer to a contiguous memory allocation managed by Kokkos. This is only adequate because in LBM\_saclay there’s only ever one view for each allocated array in use.

“send” and one “receive” buffer, for each of its subdomain’s faces (including side and corners). This is all illustrated in figure 2.3. The communications proceed with the following steps:

1. all subdomains copy the data of their two faces perpendicular to the  $\pm x$  directions into their corresponding send buffers;
2. this data is communicated through MPI into the receive buffers of the neighbouring subdomain ( $+x$  send buffer to right neighbour’s  $-x$  receive buffer,  $-x$  send buffer to left neighbour’s  $+x$  receive buffer);
3. the subdomains copy the received data in the receive buffers data into their corresponding ghost face;
4. the steps above are repeated for the  $y$ -axis faces and again for the  $z$  axis faces. Processing each axis separately ensures the corners are exchanged coherently by the *ghost cell pattern* [25]; see again figure 2.3.

By “data”, we mean the distribution functions and the intermediary macroscopic variables (including spatial derivatives). The first is necessary for the stream step, and the second is necessary for the source terms in certain LBEs when streaming from the ghost layer and for the finite differences stencils. It could have been possible to only communicate the distribution functions and then consistently rebuild the macroscopic variables in the ghost layer. Streaming from the ghost layer would however require a second ghost layer if a source term includes a finite difference calculation. This was in fact what the original version of LBM\_saclay did but this behaviour was changed during the thesis. The change was mainly motivated by an earlier investigation of a conservative Allen-Cahn reformulation of the LBM model of Safari et. al. [40] of liquid-gas phase change. The LBE for its phase field distribution included the gradient of the phase field variable (its own moment), which would have recursively required an infinite number of ghost layers. Communicating the macroscopic variables never requires more than one layer of ghost nodes. In addition, a layer with all macroscopic variables is generally represents fewer data than a layer with multiple distributions functions: for example, the two-phase ternary flow LBEs need at most 13 macroscopic variables in memory (13 double-precision floating points) for each node, while a node hosts 4 distribution functions with at minimum 9 directions (36 doubles).

Note that the 2D or 3D Cartesian aspect of the decomposition is conveniently represented by MPI’s API (the `MPI_Cart_*` family of functions). This API can define a periodic decomposition: for instance, the left neighbour of the leftmost subdomain is the rightmost subdomain. In the subdomains at the edge of the decomposition, a periodic boundary condition is thus in practice identical to a “communication” boundary condition.

#### 2.2.4 Boundary conditions with the ghost layer

Conveniently, the ghost layer can also be used to implement the boundary conditions. As mentioned before, the case of periodic boundary conditions is equivalent to the communications in a periodic subdomain decomposition: they are implementing by simply allowing streaming into and from the ghost layer. For the bounceback and anti-bounceback boundary conditions, we make use of the fact that they can both be seen as a replacement of the streaming step. They are implemented by the following strategy:

- we again allow distributions on the real (sub)domain nodes to stream into the ghost layer. Thus, at time  $t$  the distribution  $f_k^*(t, \mathbf{x})$  gets sent into the ghost layer as  $f_k(t + \delta t, \mathbf{x}_{\text{ghost}})$ .

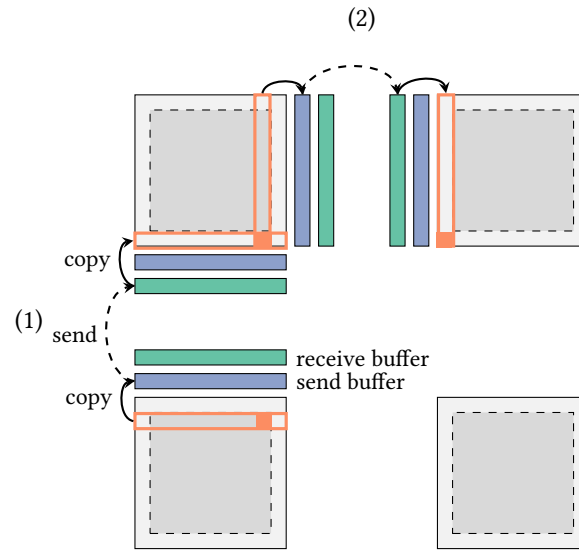


Figure 2.3: MPI domain decomposition and communications of boundary data in LBM\_saclay. An example of a 2D 2x2 decomposition is presented here ( $m_x = m_y = 2$ ). We illustrate the communication of the north boundary of the bottom-left (red outlined rectangle) subdomain into the ghost layer of its neighbor above (1). When this neighbor then communicates its eastern boundary data (2), it is seen that the corner data of the bottom-left subdomain correctly lands in the corner of the ghost layer of the top-right subdomain; this is the *ghost cell pattern*. For clarity, the other buffers and communications are not represented.

- We do not allow distributions from the ghost layer to stream into the real domain. Instead, after the stream-collision from  $t$  to  $t + \delta t$ , a kernel copies back the ghost distributions into the neighbouring real boundary nodes with the inverse directions:  $f_k(t + \delta t, \mathbf{x}_{\text{ghost}}) = f^*(t, \mathbf{x})$  is now correctly found as  $f_{k^-}(t + \delta t, \mathbf{x})$ .

A lot of the additions made to LBM\_saclay during the thesis concerned the handling of boundaries. The above specification of the boundary conditions is part of it. Before that, what LBM\_saclay effectively did was a full-way bounceback where the boundary condition only became effective after  $2\delta t$  and the anti-bounceback scheme was absent. Furthermore, an issue was found with corner nodes sometimes becoming unstable when the domain had periodic boundaries along one axis and (anti-)bounceback on another. It turned out that it was necessary to always order the application of the non-periodic boundary conditions before the periodic ones, and the fix was implemented. Lastly, we implemented the off-centre finite differences stencil mentioned in sec. 2.1.5, needed near non-periodic boundaries. We have written some utility functions which branch to the necessary stencil at a given node position and boundary conditions: the user only needs to call one function to calculate the gradient (or Laplacian) and does not need to keep track of the different cases.

### 2.2.5 Implementation of the two-phase three-component phase field model

We present here a detailed example of an LBM model implemented in LBM\_saclay by taking the case of the two phase-three component flow model. Remind that the physical model was derived in chapter 1 and its LBM discretization is found in section 2.1.6.

The main structure of the two-phase phase ternary flow model is a Kokkos kernel, namely `two_phases_ternary_flow::TimeStepKernel`<sup>3</sup>. It reads and writes data from multiple Kokkos views: one 4D array (or 3D; two or three space dimensions plus one dimension for the velocity set) for each distribution functions  $v_k$ ,  $h_k$ ,  $a_k$  and  $b_k$  (including the ghost layer), plus one `f_tmp` view to hold the distributions at  $t + \delta t$  during the stream-collision operation to avoid overwriting previous data out of order due to the parallelism. It also manipulates a view into a 3D table containing the set of macroscopic variables of interest for outputs ( $\varphi$ ,  $\bar{\mu}$ ,  $c$ ,  $p$ ,  $\mathbf{u}$ ) and/or necessary for intermediary calculations (notably the gradient and Laplacian of  $\varphi$ ). Finally, it can also read from a small structure holding the values of the physical parameters (the ones in table 1.1) which are parsed from a text file supplied by the user.

The `TimeStepKernel` has multiple variants<sup>4</sup> of the dispatched `operator()` functions:

- variant `Init` will initialize each distribution function at their equilibrium as explained in sec. 2.1.4,
- variants `VUpdate`, `HUpdate`, `AUpdate` and `BUpdate` perform the stream-collision operation for each distribution function, implementing all the schemes written in the paragraphs of sec. 2.1.6. The new distribution functions computed for  $t + \delta t$  are saved in `f_tmp`, which is then swapped for the original view once they've all been calculated. The boundary conditions are applied by a separate functor after calling each `*Update` variant.
- Variants `MacroUpdate1` and `MacroUpdate2` compute and save the macroscopic variables. There are two steps and the second must run after the first has finished working on all nodes. This is because `MacroUpdate2` computes the space derivatives of  $\varphi$  (and the values depending on them) which is itself updated by `MacroUpdate1`. In the case of periodic or MPI communication boundaries, a separate functor does a periodic copy of the macroscopic variables after the two variants.

<sup>3</sup>Found in `src/models/two_phase_ternary_flow.hpp` in the source tree

<sup>4</sup>Kokkos can understand and dispatch multiple variants of `operator()` if they're distinguished using the C++ function overloading feature with unit structs.

In addition to this functor (and other model-specific functors), a class `LBMRun`<sup>5</sup> defines the central functionalities of the simulation code. It is where the parameter text file is parsed into memory, the Views are allocated, result files are output, the model and boundary conditions kernels are dispatched and the communication strategy (sec. 2.2.3) is implemented. In particular, one time iteration of the two-phase ternary flow model is done by the function `LBMRun::update_two_phases_ternary_flow` which glues together the dispatch of the different functors.

Note that in truth, the kernels and `LBMRun` are actually C++ class templates (e.g. `LBMRun<int D, int Q>`) to specialise them for each lattice. Doing so avoid duplicating by hand the code of the LBM algorithm for each lattice (although 2D and 3D implementations still need to be written separately) with no cost at runtime. In particular, keeping the number of velocities  $Q$  a compile-time constant encourages the compiler to unroll the inner loops on all lattice directions.

## 2.3 Other numerical considerations

The numerical tooling developed during the thesis is not limited to the core calculations of `LBM_saclay`. For example, the simulation code originally could only output simulation results in the `vtk` format, an XML-based format specifically designed for Kitware’s VTK (Visualization ToolKit) library on which depends the Paraview visualization software. We have written a first version of an alternate output in the HDF5 format. It is a self-describing hierarchical format adequate for heavy scientific data. It supports compression for individual data fields, is supported by multiple visualization software, and is can be easily manipulated with the command-line interface tools distributed with the library. Pierre Kestener improved the HDF5 output of `LBM_saclay`, notably by enabling parallel I/O so that multiple MPI process may coherently write to a single output file.

We also tried to ensure the performance of the post-processing of the simulation results. We have written C++ programs also employing the Kokkos library and used them to extract data from simulations (e.g. the interface position in the later chapter’s diffusion couples, or geometrical measurements in the droplet growth simulations). We did not implement distributed memory parallelism in the post-processing tools, but we used the GNU parallel software [45] to parallelise the processing at the level of the filesystem since each time step has its own separate output file. Finally, we have used either the Paraview or the visit software [8] to visualize simulations.

## 2.4 Conclusion

Throughout this chapter we have seen how we discretize the two-phase three-component flow model and implement it in a new, high-performance and portable simulation code based on the lattice Boltzmann method. We are now one step closer to bringing the model to quantitative simulations of droplet growth by having access to highly parallel simulations. These can be quickly deployed on either a desktop workstation or a supercomputer, and we will show examples of both in the next chapter.

Before that, we shall mention the possible improvements to the numerical implementation of the model, the first candidate being the collision operator in the LBM. It is known that the simple BGK collision operator is not the best when it comes to the stability or accuracy of the simulations, and better alternatives such as the multiple-relaxation-time (MRT) [21] and two-relaxation-time (TRT) [16] are common in the literature. In practice, we have estimated that our simulations stay stable within one or two orders of magnitudes of difference between the different diffusion rates of the model (viscosities, chemical mobilities and phase field mobility). We have also considered implementing more elaborate boundary conditions, but these fell outside the scope of the immediate thesis objectives: bounceback

---

<sup>5</sup>Defined in `src/LBMRun.h`.

with moving walls (*ie.* a forced tangential velocity) would allow the simulation of a pulsed column, a liquid-liquid extraction device used at CEA Marcoule for the treatment of nuclear waste; and out-flow boundary conditions [32] could have been convenient in the early film boiling simulation or in the present glass droplet growth simulations to allow the dispersed phase to exit the numerical domain without accumulating on a bounceback wall. We participated in the supervision of the internship which investigated the addition of solid bounceback nodes within the simulation domain; this is an approach often used to model a porous media with the LBM [23, 44]. Lastly, while the performance of the code always proved very satisfying in practice (even the heaviest 3D simulations completed in under 24 hours), it would have been interesting to perform more measurements of the performance difference of the various changes made to the code during the thesis – for example, the tradeoff between the communication of macroscopic variables versus the additional ghost layer of distribution variables. There was at one point a rapid performance comparison made between the present fork of the code against the one maintained by another PhD student working on LBM\_saclay, to coarsely compare the performance relative to the architectural changes made to the code structure.

## References

- [1] Comparing the specifications listed at <https://www.nvidia.com/en-gb/data-center/tesla-v100/> and <https://www.microway.com/knowledge-center-articles/detailed-specifications-of-the-cascade-lake-sp-intel-xeon-processor-scalable-family-cpus/> accessed 26/08/2022.
- [2] Reza Haghani Hassan Abadi, Abbas Fakhari, and Mohammad Hassan Rahimian. “Numerical simulation of three-component multiphase flows at high density and viscosity ratios using lattice Boltzmann methods.” In: *Physical Review E* 97.3 (Mar. 2018). doi: 10.1103/physreve.97.033312.
- [3] Shintaro Aihara, Tomohiro Takaki, and Naoki Takada. “Multi-phase-field modeling using a conservative Allen–Cahn equation for multiphase flow.” In: *Computers & Fluids* 178 (Jan. 2019), pp. 141–151. doi: 10.1016/j.compfluid.2018.08.023.
- [4] M. K. Banda, W. A. Yong, and A. Klar. “A Stability Notion for Lattice Boltzmann Equations.” In: *SIAM Journal on Scientific Computing* 27.6 (2006), pp. 2098–2111. doi: 10.1137/040606211.
- [5] P. L. Bhatnagar, E. P. Gross, and M. Krook. “A Model for Collision Processes in Gases. I. Small Amplitude Processes in Charged and Neutral One-Component Systems.” In: *Phys. Rev.* 94 (3 May 1954), pp. 511–525. doi: 10.1103/PhysRev.94.511.
- [6] S. Chapman and T. G. Cowling. *The Mathematical Theory of Non-uniform Gases. An account of the kinetic theory of viscosity, thermal conduction, and diffusion in gases*. Vol. 38. 323. Cambridge University Press, 1954, pp. 63–64. doi: 10.2307/3609795.
- [7] Li Chen et al. “A critical review of the pseudopotential multiphase lattice Boltzmann model: Methods and applications.” In: *International Journal of Heat and Mass Transfer* 76 (2014), pp. 210–236. issn: 0017-9310. doi: <https://doi.org/10.1016/j.ijheatmasstransfer.2014.04.032>.
- [8] Hank Childs et al. “VisIt: An End-User Tool For Visualizing and Analyzing Very Large Data.” In: *High Performance Visualization—Enabling Extreme-Scale Scientific Insight*. Oct. 2012, pp. 357–372. doi: 10.1201/b12985.
- [9] Raúl de la Cruz and Mauricio Araya-Polo. “Modeling Stencil Computations on Modern HPC Architectures.” In: *High Performance Computing Systems. Performance Modeling, Benchmarking, and Simulation*. Cham, 2015, pp. 149–171. isbn: 978-3-319-17248-4.

- [10] H. Carter Edwards, Christian R. Trott, and Daniel Sunderland. “Kokkos: Enabling manycore performance portability through polymorphic memory access patterns.” In: *Journal of Parallel and Distributed Computing* 74.12 (2014). Domain-Specific Languages and High-Level Frameworks for High-Performance Computing, pp. 3202–3216. ISSN: 0743-7315. doi: <https://doi.org/10.1016/j.jpdc.2014.07.003>.
- [11] Abbas Fakhari and Mohammad H. Rahimian. “Phase-field modeling by the method of lattice Boltzmann equations.” In: *Phys. Rev. E* 81 (3 Mar. 2010), p. 036707. doi: 10.1103/PhysRevE.81.036707.
- [12] Yuhang Fu et al. “Numerical study of double emulsion formation in microchannels by a ternary Lattice Boltzmann method.” In: *Chemical Engineering Science* 146 (June 2016), pp. 126–134. doi: 10.1016/j.ces.2016.02.036.
- [13] Edgar Gabriel et al. “Open MPI: Goals, Concept, and Design of a Next Generation MPI Implementation.” In: *Proceedings, 11th European PVM/MPI Users’ Group Meeting*. Budapest, Hungary, Sept. 2004, pp. 97–104.
- [14] Martin Geier, Abbas Fakhari, and Taehun Lee. “Conservative phase-field lattice Boltzmann model for interface tracking equation.” In: *Phys. Rev. E* 91 (6 June 2015), p. 063309. doi: 10.1103/PhysRevE.91.063309.
- [15] Irina Ginzburg. “Generic boundary conditions for lattice Boltzmann models and their application to advection and anisotropic dispersion equations.” In: *Advances in Water Resources* 28.11 (2005), pp. 1196–1216. ISSN: 0309-1708. doi: <https://doi.org/10.1016/j.advwatres.2005.03.009>.
- [16] Irina Ginzburg, Frederik Verhaeghe, and Dominique d’Humières. “Two-relaxation-time Lattice Boltzmann scheme: About parametrization, velocity, pressure and mixed boundary conditions.” In: *Communications in Computational Physics* 3 (2008), pp. 427–478.
- [17] Andrew K. Gunstensen et al. “Lattice Boltzmann model of immiscible fluids.” In: *Phys. Rev. A* 43 (8 Apr. 1991), pp. 4320–4327. doi: 10.1103/PhysRevA.43.4320.
- [18] Xiaoyi He and Li-Shi Luo. “Lattice Boltzmann Model for the Incompressible Navier–Stokes Equation.” In: *Journal of Statistical Physics* 88 (3 Apr. 1997), pp. 927–944. ISSN: 1572-9613. doi: 10.1023/B:JOSS.0000015179.12689.e4.
- [19] J.L. Hennessy and D.A. Patterson. *Computer Architecture: A Quantitative Approach*. The Morgan Kaufmann Series in Computer Architecture and Design. Elsevier Science, 2002. ISBN: 9780080502526.
- [20] F. J Higuera and J Jiménez. “Boltzmann Approach to Lattice Gas Simulations.” In: *Europhysics Letters (EPL)* 9.7 (Aug. 1989), pp. 663–668. doi: 10.1209/0295-5075/9/7/009.
- [21] F. J Higuera, S Succi, and R Benzi. “Lattice Gas Dynamics with Enhanced Collisions.” In: *Europhysics Letters (EPL)* 9.4 (June 1989), pp. 345–349. doi: 10.1209/0295-5075/9/4/008.
- [22] J. J. Huang, C. Shu, and Y. T. Chew. “Mobility-dependent bifurcations in capillarity-driven two-phase fluid systems by using a lattice Boltzmann phase-field model.” In: *International Journal for Numerical Methods in Fluids* 60.2 (2009), pp. 203–225. doi: <https://doi.org/10.1002/flid.1885>.
- [23] Takaji Inamuro, Masato Yoshino, and Fumimaru Ogino. “Lattice Boltzmann simulation of flows in a three-dimensional porous structure.” In: *International Journal for Numerical Methods in Fluids* 29.7 (1999), pp. 737–748. doi: 10.1002/1097-0363(19990415)29:7<737::AID-FLD813>3.0.CO;2-H.

- [24] Michael Junk. “A finite difference interpretation of the lattice Boltzmann method.” In: *Numerical Methods for Partial Differential Equations* 17.4 (2001), pp. 383–402. doi: <https://doi.org/10.1002/num.1018>.
- [25] Fredrik Berg Kjolstad and Marc Snir. “Ghost Cell Pattern.” In: *Proceedings of the 2010 Workshop on Parallel Programming Patterns*. ParaPLoP ’10. Carefree, Arizona, USA, 2010. ISBN: 9781450301275. doi: 10.1145/1953611.1953615.
- [26] Marcin Krotkiewski and Marcin Dabrowski. “Efficient 3D stencil computations using CUDA.” In: *Parallel Computing* 39.10 (2013), pp. 533–548. ISSN: 0167-8191. doi: <https://doi.org/10.1016/j.parco.2013.08.002>.
- [27] Jens Krüger and Rüdiger Westermann. “Linear Algebra Operators for GPU Implementation of Numerical Algorithms.” In: *ACM Trans. Graph.* 22.3 (July 2003), pp. 908–916. ISSN: 0730-0301. doi: 10.1145/882262.882363.
- [28] Timm Krüger et al. *The Lattice Boltzmann Method: Principles and Practice*. Cham: Springer International Publishing, 2017. ISBN: 978-3-319-44649-3. doi: 10.1007/978-3-319-44649-3.
- [29] Pierre Lallemand and François Dubois. “Comparison of Simulations of Convective Flows.” In: *Communications in Computational Physics* 17.5 (2015), pp. 1169–1184. doi: 10.4208/cicp.2014.m400.
- [30] Taehun Lee and Paul F. Fischer. “Eliminating parasitic currents in the lattice Boltzmann equation method for nonideal gases.” In: *Phys. Rev. E* 74 (4 Oct. 2006), p. 046709. doi: 10.1103/PhysRevE.74.046709.
- [31] H. Liang, B. C. Shi, and Z. H. Chai. “Lattice Boltzmann modeling of three-phase incompressible flows.” In: *Phys. Rev. E* 93 (1 Jan. 2016), p. 013308. doi: 10.1103/PhysRevE.93.013308.
- [32] Qin Lou, Zhaoli Guo, and Baochang Shi. “Evaluation of outflow boundary conditions for two-phase lattice Boltzmann equation.” In: *Phys. Rev. E* 87 (6 June 2013), p. 063301. doi: 10.1103/PhysRevE.87.063301.
- [33] Guy R. McNamara and Gianluigi Zanetti. “Use of the Boltzmann Equation to Simulate Lattice-Gas Automata.” In: *Phys. Rev. Lett.* 61 (20 Nov. 1988), pp. 2332–2335. doi: 10.1103/PhysRevLett.61.2332.
- [34] Rafael Medeiros. *Consommation des heures de calcul*. <http://www.idris.fr/media/jean-zay/jean-zay-conso-heure-calcul.pdf> accessed 26/08/2022.
- [35] Renwei Mei et al. “Consistent initial conditions for lattice Boltzmann simulations.” In: *Computers & Fluids* 35.8 (2006). Proceedings of the First International Conference for Mesoscopic Methods in Engineering and Science, pp. 855–862. ISSN: 0045-7930. doi: <https://doi.org/10.1016/j.compfluid.2005.08.008>.
- [36] Hans Meuer et al. *TOP500.org*. <https://www.top500.org> accessed 25/08/2022.
- [37] Paulius Micikevicius. “3D Finite Difference Computation on GPUs Using CUDA.” In: *Proceedings of 2nd Workshop on General Purpose Processing on Graphics Processing Units*. GPGPU-2. Washington, D.C., USA, 2009, pp. 79–84. ISBN: 9781605585178. doi: 10.1145/1513895.1513905.
- [38] T. Mitchell, C. Leonardi, and A. Fakhari. “Development of a three-dimensional phase-field lattice Boltzmann method for the study of immiscible fluids at high density ratios.” In: *International Journal of Multiphase Flow* 107 (2018), pp. 1–15. ISSN: 0301-9322. doi: <https://doi.org/10.1016/j.ijmultiphaseflow.2018.05.004>.
- [39] Ilya S. Pershin, Vadim D. Levchenko, and Anastasia Y. Perepelkina. “Performance Limits Study of Stencil Codes on Modern GPGPUs.” In: *Supercomputing Frontiers and Innovations* 6.2 (June 2019), pp. 86–101. doi: 10.14529/jsfi190207.



- [40] Hesameddin Safari, Mohammad Hassan Rahimian, and Manfred Krafczyk. “Extended lattice Boltzmann method for numerical simulation of thermal phase change in two-phase fluid flow.” In: *Phys. Rev. E* 88 (1 July 2013), p. 013304. doi: 10 . 1103/PhysRevE . 88 . 013304.
- [41] Ciro Semperebon, Timm Krüger, and Halim Kusumaatmaja. “Ternary free-energy lattice Boltzmann model with tunable surface tensions and contact angles.” In: *Phys. Rev. E* 93 (3 Mar. 2016), p. 033305. doi: 10 . 1103/PhysRevE . 93 . 033305.
- [42] Xiaowen Shan and Hudong Chen. “Lattice Boltzmann model for simulating flows with multiple phases and components.” In: *Phys. Rev. E* 47 (3 Mar. 1993), pp. 1815–1819. doi: 10 . 1103 / PhysRevE . 47 . 1815.
- [43] Michael R. Swift et al. “Lattice Boltzmann simulations of liquid-gas and binary fluid systems.” In: *Phys. Rev. E* 54 (5 Nov. 1996), pp. 5041–5052. doi: 10 . 1103/PhysRevE . 54 . 5041.
- [44] L. Talon et al. “Assessment of the two relaxation time Lattice-Boltzmann scheme to simulate Stokes flow in porous media.” In: *Water Resources Research* 48.4 (2012). doi: <https://doi.org/10.1029/2011WR011385>.
- [45] Ole Tange. *GNU Parallel 2018*. Ole Tange, Apr. 2018. doi: 10 . 5281/zenodo . 1146014.
- [46] Werner Verdier, Pierre Kestener, and Alain Cartalade. “Performance portability of lattice Boltzmann methods for two-phase flows with phase change.” In: *Computer Methods in Applied Mechanics and Engineering* 370 (2020), p. 113266. issn: 0045-7825. doi: <https://doi.org/10.1016/j.cma.2020.113266>.
- [47] H. L. Wang et al. “Comparative study of the lattice Boltzmann models for Allen-Cahn and Cahn-Hilliard equations.” In: *Phys. Rev. E* 94 (3 Sept. 2016), p. 033304. doi: 10 . 1103/PhysRevE . 94 . 033304.
- [48] Bei Wei et al. “Study on the meniscus-induced motion of droplets and bubbles by a three-phase Lattice Boltzmann model.” In: *Chemical Engineering Science* 176 (Feb. 2018), pp. 35–49. doi: 10 . 1016/j.ces.2017.10.025.
- [49] J. Weinberg et al. “Quantifying Locality In The Memory Access Patterns of HPC Applications.” In: *SC '05: Proceedings of the 2005 ACM/IEEE Conference on Supercomputing*. 2005, pp. 50–50. doi: 10 . 1109/SC . 2005 . 59.
- [50] Wen-An Yong and Weifeng Zhao. “Numerical Analysis of the Lattice Boltzmann Method for the Boussinesq Equations.” In: *J. Sci. Comput.* 84.2 (Aug. 2020). issn: 0885-7474. doi: 10 . 1007 / s10915-020-01291-0.
- [51] H. W. Zheng, C. Shu, and Y. T. Chew. “A Lattice Boltzmann Model for Multiphase Flows with Large Density Ratio.” In: *J. Comput. Phys.* 218.1 (Oct. 2006), pp. 353–371. issn: 0021-9991. doi: 10 . 1016/j.jcp.2006.02.015.

# Chapter 3

## Simulations

In this chapter, we present the simulation performed of the two-phase ternary phase field model with flow described at the end of chapter 1. These simulations were conducted with the lattice Boltzmann formalism and the simulation code LBM\_saclay, presented in the previous chapter.

Section 3.1 will first explain the convention taken for the system of units. The following sections will then present the step-by-step validations of the model (sec. 3.2) until it is deemed ready to represent the phase separation dynamics in the  $\text{Na}_2\text{O-SiO}_2\text{-MoO}_3$  system (sec. 3.3). The chapter is closed by section 3.4.1 with ways to further reinforce the description of the model ternary glass so that we may eventually compare simulations to experimental observations.

### 3.1 Numerical units

The simulation parameters and their results are presented with their own unit system. This system is defined in terms of a characteristic length  $L$  and a characteristic time  $T$ . When a flow is present, we must also define a characteristic unit involving mass and as such we always define the fluid's density  $\rho$  as the unit density.

For each simulation,  $L$ ,  $T$  must be described. Setting this convention is convenient because the physical parameters can then be consistently presented with the same numerical value as the ones used explicitly to parametrize the simulation code.

### 3.2 Verifications of subsets of the two-phase three-component flow model

#### 3.2.1 Two-phase flow: Double Poiseuille

We first verified the two-phase flow subset of the model. The simulations are carried out with the diphasic flow model of LBM\_saclay. It corresponds to a subset of the LBE system of section 2.2.5 with the chemical diffusion equations removed and the addition of a constant force term in the momentum equation.

##### Double Poiseuille

The double Poiseuille flow is an extension of the usual single-phase Poiseuille flow test case [34]. It considers a channel of width  $2h$  with two immiscible fluids of different viscosities layered on top of

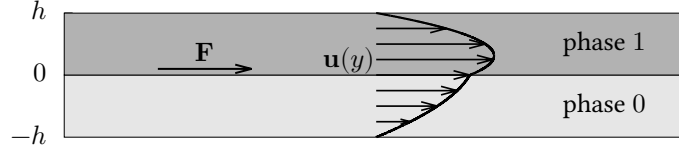


Figure 3.1: Configuration of the double Poiseuille test case. In a channel of width  $2h$ , the fluid phase 0 is layered on top of the fluid phase 1 with a plane interface between both. A constant force  $\mathbf{F}$  drives the flow. The viscosity ratio between both phases gives half-parabola profiles of varying amplitudes for the velocity along the channel axis. It is however continuous at the interface. No-slip conditions force the velocity to 0 at the walls.

each other. The flow is driven by a constant force parallel to the interface of magnitude

$$F = \frac{\rho u_c (\nu_0 + \nu_1)}{h^2} \quad (3.2.1)$$

with  $u_c$  the desired velocity along the interface. The configuration is illustrated in figure 3.1. The solution is expected to converge to the steady flow

$$u_x(y) = \begin{cases} \frac{(\nu_0 + \nu_1)u_c}{2\nu_1} \left( -\frac{y^2}{h^2} + \frac{y}{h} \frac{\nu_0 - \nu_1}{\nu_0 + \nu_1} + \frac{2\nu_1}{\nu_0 + \nu_1} \right), & 0 < y < h, \\ \frac{(\nu_0 + \nu_1)u_c}{2\nu_0} \left( -\frac{y^2}{h^2} + \frac{y}{h} \frac{\nu_0 - \nu_1}{\nu_0 + \nu_1} + \frac{2\nu_0}{\nu_0 + \nu_1} \right), & -h < y < 0, \end{cases} \quad (3.2.2)$$

assuming an infinite 2D channel along the  $x$ -axis. The channel has no-slip boundary conditions on its walls. Because the interface remains planar, the surface tension never comes into play. The gravity is also ignored.

The simulation is initialized at rest with a homogeneous pressure. The phase field initially has its equilibrium profile for a single plane interface along the  $x$ -axis at  $y = 0$ . The no-slip boundary conditions are enforced by the half bounce-back method on  $y = \pm h$  and the domain is periodic along the  $x$ -axis with a period  $2h$ . The lattice has  $256 \times 128$  nodes and the other simulation parameters are listed in table 3.1. Three viscosity ratios are simulated:  $\nu_1/\nu_0 = 1/3, 1/5$  and  $1/10$ . Figure 3.2 compares the obtained steady state velocity field against eq. (3.2.2) for each ratio. The flow simulations produce satisfying results, with only a slight departure from the analytical profile at  $\nu_0/\nu_1 = 1/10$ .

See also fig. 6b of our earlier work [28] which presents the same test case with varying density ratios. Fig. 6c of the same reference also compares the linear and harmonic phase-field interpolation of the kinematic viscosity. The much better results shown for the latter is the reason we only consider the harmonic interpolation here. In this same publication, we had also verified the double Poiseuille solution in the case of different densities, and we verified the Laplace law for a single bubble also in the case of different densities.

### 3.2.2 Two-phase three-component: diffusion couple

The diffusion couple is a test case to validate the two-phase three-component chemical diffusion, without flow. Two materials of varying composition are welded next to each other and the interface is displaced only by the diffusion across it. This setup is illustrated in figure 3.3. The problem is an extension of the free-surface Stefan problem [8] with multiple diffused variables and a discontinuity at the interface. Diffusion couples also serve as real experiments to measure diffusion coefficients of materials, as done in e.g. [21].

LBM			
lattice	D2Q9		
domain	$[-2L, 2L] \times [-L, L]$ , 256 $\times$ 128 nodes		
$\delta x$	1 $L$		
$\delta t$	$2.44 \times 10^{-5} T$		
Two-phase flow			
$\rho$	1 $\rho$		
$\nu_0$	1 $L^2 \cdot T^{-1}$		
	1/3 ratio	1/5 ratio	1/10 ratio
$\nu_1$	0.333 $L^2 \cdot T^{-1}$	0.2 $L^2 \cdot T^{-1}$	0.1 $L^2 \cdot T^{-1}$
$W$	6 $\delta x = 0.09375 L$		
$M_\varphi$	1.2 $L^2 \cdot T^{-1}$		
$\sigma$	0 $\rho \cdot v^2 \cdot L$		
$\mathbf{g}$	<b>0</b> $L \cdot T^{-2}$		
Double poiseuille			
$h$	1 $L$		
$u_c$	0.01 $L \cdot T^{-1}$		

Table 3.1: Parameters of the double poiseuille simulations with varying viscosity ratios. The length unit  $L$  is the half-width of the channel ( $h = 1 L$ ) and the time unit  $T$  is the characteristic viscous time of phase 0, namely  $L^2/\nu_0$ . The domain is discretized by the D3Q9 lattice with  $256 \times 128$  nodes.

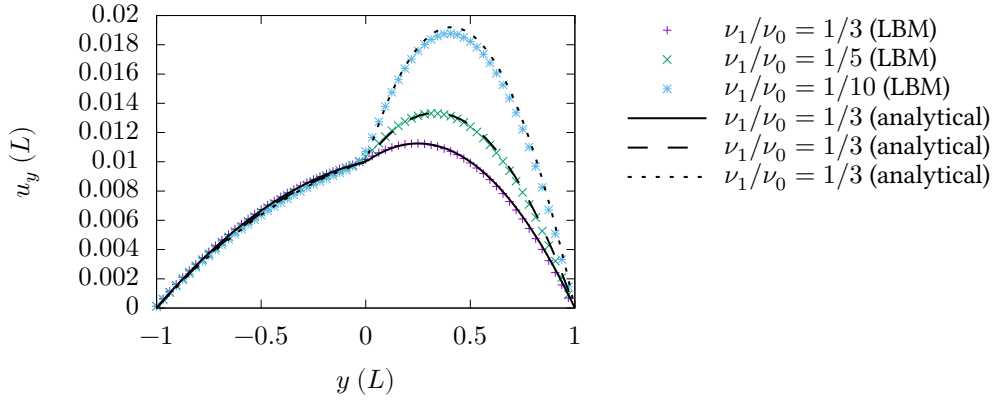


Figure 3.2: Velocity profiles for the double poiseuille test-case for different ratios of kinematic viscosities. The analytical profile of eq. (3.2.2) is plotted with black lines and is compared to the simulation results with colored symbols.

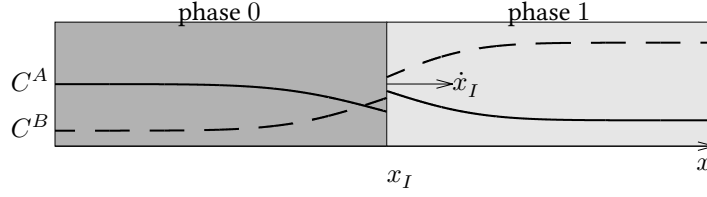


Figure 3.3: Setup of the ternary diffusion couple test case. A single planar interface split the infinite physical domain in halves, one filled with phase 0 and the other with phase 1. The composition are held constant by boundary conditions at  $\pm\infty$ . At the interface, the compositions are constrained by the thermodynamic equilibrium and the jump in the compositions and in their gradients are linked through by interface's displacement. The solution are compositions profiles in error functions branches with a discontinuity at the interface, and a interface velocity proportional to  $\sqrt{t}$ . The problem can be formulated equivalently in term of the chemical potentials  $\bar{\mu}$ , which is continuous at the interface.

The formulation and the solutions of the problem can be found in [18] and will be reiterated here. Using our phase field model, we will approximate the sharp interface problem

$$\partial_t \mathbf{c} = \begin{cases} \mathbf{D}_0 \nabla^2 \mathbf{c}, & -\infty < x < x_I(t), \\ \mathbf{D}_1 \nabla^2 \mathbf{c}, & x_I(t) < x < +\infty, \end{cases} \quad (3.2.3)$$

with  $\mathbf{D}_0$  and  $\mathbf{D}_1$  constant diffusion matrices and  $x_I(t)$  the position of the moving interface. The problem is completed with the interface conditions

$$\begin{aligned} \mathbf{c}|_{x_I^-} &= \mathbf{c}_-, \\ \mathbf{c}|_{x_I^+} &= \mathbf{c}_+, \\ \frac{dx_I}{dt} (\mathbf{c}|_{x_I^-} - \mathbf{c}|_{x_I^+}) &= -(\mathbf{D}_0 \partial_x \mathbf{c}|_{x_I^-} - \mathbf{D}_1 \partial_x \mathbf{c}|_{x_I^+}), \end{aligned} \quad (3.2.4)$$

with  $\mathbf{c}_\pm$  compositions that satisfy chemical equilibrium, which we will derive from the same free energy quadratic wells as before (sec. 1.3.2). This equilibrium does not necessarily coincide with the one taken as reference in the grand potential formulation ( $\mathbf{c}_0^{\text{eq}}$  and  $\mathbf{c}_1^{\text{eq}}$ ). The third interface condition, the balance of the diffusion fluxes, ensures that the compositions are conserved. The initial conditions

$$\begin{aligned} x_I(t=0) &= 0, \\ \mathbf{c}(t=0, x) &= \begin{cases} \mathbf{c}_{-\infty}, & -\infty < x < 0, \\ \mathbf{c}_{+\infty}, & 0 < x < +\infty, \end{cases} \end{aligned} \quad (3.2.5)$$

must also be specified.

It will be convenient to formulate the problem in the mixed  $\mathbf{c}$ - $\mu$  formulation. This is easy because of linear relationship between both variables with quadratic free energies, and the fact that the global

conservation of  $\mathbf{c}$  is not in effect in an infinite medium. The problem now writes

$$\begin{aligned} \partial_t \mathbf{c} &= \begin{cases} \bar{M}_0 \nabla^2 \bar{\mu}, & -\infty < x < x_I(t), \\ \bar{M}_1 \nabla^2 \bar{\mu}, & x_I(t) < x < +\infty, \end{cases} \\ \bar{\mu}|_{x_I^-} &= \bar{\mu}|_{x_I^+} = \bar{\mu}_\pm \quad \text{with} \quad \Delta\omega(\bar{\mu}_\pm) = 0, \\ \frac{dx_I}{dt} \left( \mathbf{c}|_{x_I^-} - \mathbf{c}|_{x_I^+} \right) &= - \left( \bar{M}_0 \partial_x \bar{\mu}|_{x_I^-} - \bar{M}_1 \partial_x \bar{\mu}|_{x_I^+} \right), \\ x_I(t=0) &= 0, \\ \bar{\mu}(t=0, x) &= \begin{cases} \bar{\mu}_{-\infty}, & -\infty < x < 0, \\ \bar{\mu}_{+\infty}, & 0 < x < +\infty. \end{cases} \end{aligned} \quad (3.2.6)$$

with  $\bar{\mu}_\pm$  the chemical potential at the interface which may again not coincide with the reference equilibrium  $\bar{\mu} = 0$ . With a sharp interface, the closure relation between  $\mathbf{c}$  and  $\bar{\mu}$  is

$$\bar{\mu} = \begin{cases} \bar{K}_0(\mathbf{c} - \mathbf{c}_0^{\text{eq}}), & -\infty < x < x_I(t), \\ \bar{K}_1(\mathbf{c} - \mathbf{c}_1^{\text{eq}}), & x_I(t) < x < +\infty. \end{cases} \quad (3.2.7)$$

As a simplifying assumption we study only the case where  $\bar{K}_0 = \bar{K}_1 = 1$ , the identity matrix, and where the mobility matrices  $\bar{M}_0, \bar{M}_1$  are diagonal. The diffusion and closure equations are thus decoupled and the solutions to the diffusion couple are known to be [18, 11, 27, 15]

$$\bar{\mu}^\alpha(t, x) = \begin{cases} \bar{\mu}_{-\infty}^\alpha + (\bar{\mu}_\pm^\alpha - \bar{\mu}_{-\infty}^\alpha) \frac{\text{erfc}\left(-x/2\sqrt{\bar{M}_0^{\alpha\alpha}t}\right)}{\text{erfc}\left(-\xi/2\sqrt{\bar{M}_0^{\alpha\alpha}t}\right)}, & -\infty < x < x_I(t), \\ \bar{\mu}_{+\infty}^\alpha + (\bar{\mu}_\pm^\alpha - \bar{\mu}_{+\infty}^\alpha) \frac{\text{erfc}\left(x/2\sqrt{\bar{M}_1^{\alpha\alpha}t}\right)}{\text{erfc}\left(\xi/2\sqrt{\bar{M}_1^{\alpha\alpha}t}\right)}, & x_I(t) < x < +\infty, \end{cases} \quad (3.2.8)$$

$$\text{for } \alpha = A, B, \quad (3.2.9)$$

$$x_I(t) = \xi\sqrt{t}. \quad (3.2.10)$$

Note that this solution is self-similar with a unique dependency on the scaled variable  $x/\sqrt{t}$ . The parameters  $\xi$  and  $\bar{\mu}_\pm$  are identified by the tie-line the system chooses at the interface. In a finite thermodynamic system this choice is determined by its global component inventory. For the infinite diffusion couple, it is instead determined by the coupling of the chemical equilibrium at the interface and the dynamical conditions (flux balance and boundary conditions at  $\pm\infty$ ). This coupling translates to  $\xi$  being a solution of the transcendental equation

$$\begin{aligned} &\frac{1}{2}\xi((\Delta c^{\text{eq},A})^2(u_0^B(-\xi) + u_1^B(\xi)) + (\Delta c^{\text{eq},B})^2(u_0^A(-\xi) + u_1^A(\xi))) \\ &= \Delta c^{\text{eq},A}(u_0^B(-\xi) + u_1^B(\xi))(\mu_{-\infty}^A u_0^A(-\xi) + \mu_{+\infty}^A u_1^A(\xi)) \\ &\quad + \Delta c^{\text{eq},B}(u_0^A(-\xi) + u_1^A(\xi))(\mu_{-\infty}^B u_0^B(-\xi) + \mu_{+\infty}^B u_1^B(\xi)) \end{aligned} \quad (3.2.11)$$

with  $u_\pi^\alpha(\pm\xi) = \sqrt{\frac{M_\pi^{\alpha\alpha}}{\pi}} \frac{\exp(-\xi^2/4M_\pi^{\alpha\alpha})}{\text{erfc}(\pm\xi/2\sqrt{M_\pi^{\alpha\alpha}})}$ ,

and  $\bar{\mu}_\pm$  are  $\xi$  are related by

$$-\frac{1}{2}\xi\Delta c^{\text{eq},\alpha} = (\mu_\pm^\alpha - \mu_{-\infty}^\alpha)u_0^\alpha(-\xi) + (\mu_\pm^\alpha - \mu_{+\infty}^\alpha)u_1^\alpha(\xi). \quad (3.2.12)$$

These equations are obtained after some manipulations by inserting the solutions (3.2.8) and (3.2.10) into the second and third equations of the system (3.2.6). Because of its transcendental nature, eq. (3.2.11) is solved numerically with the Broyden's method root-finding algorithm implemented in [19]. It is known that the equation can have either zero, one, or three solutions, each corresponding to a different tie-line. Our simulations are always in the case where  $\xi$  has only one possible value.

This sharp interface problem is approached with the two-phase ternary phase field model. This will verify the consistency of its thermodynamic subset (without flow) and in particular confirm that the proper interface conditions are asymptotically reconstructed. The reconstructed Gibbs-Thomson condition was mentioned in sec. 1.2.5; in the case of a plane interface ( $\kappa = 0$ ) and a properly tuned  $\lambda$  parameter (such that  $\beta = 0$ ), it should be equivalent to the classical condition of chemical equilibrium at the interface. The flux balance at the interface should also always be reconstructed.

We conduct two simulations of a diffusion couple, one with identical phase mobilities ("phase-symmetric"<sup>1</sup>,  $\bar{M}_0 = \bar{M}_1$ ) and the other with different phase mobilities ("phase-asymmetric"). The infinite  $x$ -axis is simulated with a 2D numerical domain of half-length  $L$  very large in comparison to the distance reached by the diffusion front. For this reason the bounce-back and anti-bounceback (enforcing  $\bar{\mu}_{\pm\infty}$  at  $\pm L$ ) can both be used with no noticeable difference. The second dimension is taken small and periodic for the simulation to be equivalent to a 1D problem. The numerical domain is then  $[-L, L] \times [0.012L, -0.012L]$  with  $3000 \times 36$  nodes of a D2Q9 lattice. The time unit  $T$  is taken as the earliest time at which a diffusion reaches  $L$ , ie.  $L^2 / \max(\bar{M}_0, \bar{M}_1)$ . The parameters are specified in table 3.2.

Figure 3.4 shows the interface displacement produced by the simulations. In both cases they respect the evolution proportional to the square root of time with an adequate coefficient. The phase-asymmetric case seems to undershoot the analytical solution a bit however; we attribute this to the fact that with phase-asymmetric mobilities, the errors made by the phase field model on the interface condition are impossible to cancel [1]. In addition, both setups have more noticeable errors in the very early times (these times are not plotted on the figures). This is expected: at  $t = 0$ , the analytical interface velocity  $dx_I/dt$  is infinite and this cannot be properly reproduced by the phase field model or the numerical discretization.

Figure 3.5 shows the composition profiles near the interface in the phase-asymmetric configuration. The natural discontinuity of the composition is respected until the diffuse interface smoothens it out. This smoothed discontinuity is seen to correspond to the phase field model locally crossing the miscibility gap over the diffuse interface, linearly interpolating from  $c_-$  to  $c_+$ . This is consistent with the fact that the phase field model interpolates the bulk thermodynamics with  $\varphi$ .

At the time these simulations were made, the values of  $\lambda$  were chosen "by hand" to obtain the best fit. However, in the phase-symmetric case, an asymptotic analysis later showed that  $\lambda = 110$  fell within the same order of magnitude as the value  $\lambda = 155.95$  that exactly cancel the dependence on the interface velocity in the Gibbs-Thomson condition as assumed in the problem formulation (see sec. A.4.8 of appendix A for more details).

These results prove that our phase field model correctly describes the thermodynamics and kinetics of a two-phase three-component interface. The reconstructed Gibbs-Thomson condition was also verified and the model is able to approach a sharp-interface problem and its solution.

<sup>1</sup>In the literature on phase change problems, problems are commonly distinguished as "symmetric" or "asymmetric" depending on the equality or not of the diffusive coefficients of each phase. This must not be confused with the property of symmetry of matrices. In particular the multi-component diffusion matrices must always be symmetric matrices, but may or may not take different values in each phase.

LBM		
lattice	D2Q9	
domain	$[-L, L] \times [0.012L, -0.012L]$ , $3000 \times 36$ nodes	
$\delta x$	$1/1500 L$	
$\delta t$	$1.481481 \times 10^{-9} T$	
Phase field		
$W$	$1.2 \times 10^{-3} L$	
$M_\varphi$	$1.2 L^2 \cdot T^{-1}$	
	phase-symmetric	phase-asymmetric
$\lambda$	110	6000
Free energy		
$\bar{K}_0$	1	
$\bar{K}_1$	1	
$c_0^{\text{eq}}$	$(0.3 \quad 0.3)^T$	
$c_1^{\text{eq}}$	$(0.4 \quad 0.4)^T$	
Mobilities		
	phase-symmetric	phase-asymmetric
$\bar{M}_0$	$\text{diag}(1.0 \quad 0.8)^T L^2 \cdot T^{-1}$	$\text{diag}(1.0 \quad 0.9)^T L^2 \cdot T^{-1}$
$\bar{M}_1$	$\text{diag}(1.0 \quad 0.8)^T L^2 \cdot T^{-1}$	$\text{diag}(0.85 \quad 0.7)^T L^2 \cdot T^{-1}$
Diffusion couple		
	phase-symmetric	phase-asymmetric
$\bar{\mu}_{-\infty}$	$(0.1 \quad -0.125)^T$	$(0.1 \quad -0.125)^T$
$\bar{\mu}_{+\infty}$	$(-0.1 \quad 0.2)^T$	$(-0.175 \quad 0.2)^T$

Table 3.2: Parameters for the two simulations of a ternary diffusion couple, one phase-symmetric and the other phase-asymmetric. In the phase-symmetric case, the solution to the transcendental equation (3.2.11) is  $\xi = -0.269824 L \cdot T^{-1/2}$ ; in the phase-asymmetric case,  $\xi = 0.039175 L \cdot T^{-1/2}$ . The length unit  $L$  is the half-length of the numerical domain and the time unit  $T$  is the earliest time at which a diffusion front reaches the domain's bounds.



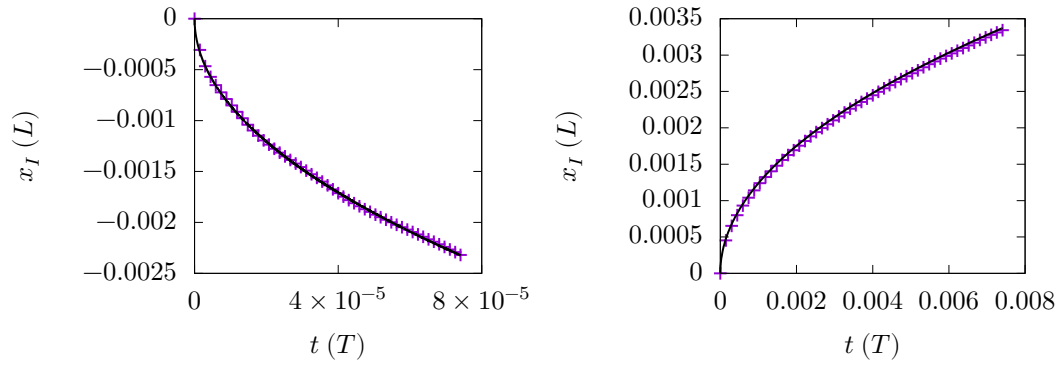


Figure 3.4: Displacement of the interface during the simulation of a (left) phase-symmetric and (right) phase-asymmetric ternary diffusion couple. The numerical solution in purple crosses is compared to the analytical solution as the black solid line.

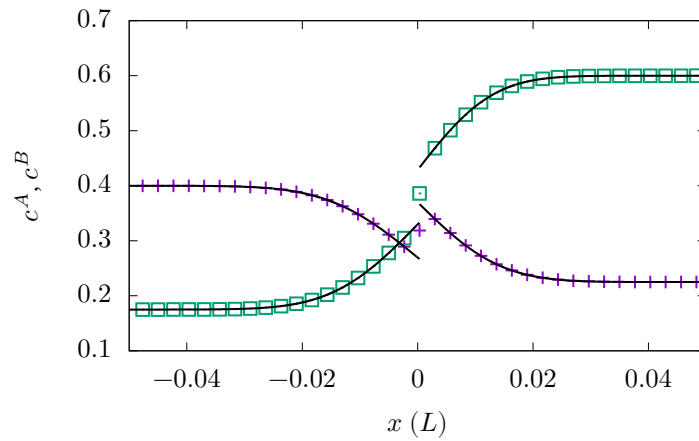


Figure 3.5: Composition profiles near the interface in the simulation of a phase-asymmetric diffusion couple. The simulated profiles appear in purple crosses ( $c^A$ ) and green squares ( $c^B$ ). The analytical profiles, derived from eqs. (3.2.7), (3.2.8) and (3.2.10), are indicated in solid black lines.

### 3.3 Simulation of droplet growth

As was mentioned in the introduction, it is known that nucleation and growth occurs in the  $\text{Na}_2\text{O}-\text{SiO}_2-\text{MoO}_3$  glass. To prepare our model to describe the interface dynamics in this system, we performed simulations of the ripening of an ensemble of randomly distributed droplets.

As section 3.3.1 will explain, the growth of nucleated droplets is usually quantified by their average radius. At late times, it is expected to follow a power-law in time and its exponent can depend on the properties of the flow, if present. Section 3.3.2 will detail the pre-nucleated initial conditions of these simulations. Section 3.3.3 then explains how this average radius is measured, and section 3.3.4 finally presents the result of the ripening simulations.

#### 3.3.1 Theory of Ostwald ripening

The Ostwald ripening is the name given to the observed redistribution of mass during grain growth after nucleation. It is driven by the surface tension, which creates a difference of chemical potentials between droplets of difference sizes. We have seen this through the Gibbs-Thomson condition (sec. 1.2.5); it tells us that the smaller a droplet is, the more it departs from the planar interface equilibrium, in terms of  $\Delta\bar{\omega}(\bar{\mu})$ . After linearizing in the chemical potential, this means that there is a diffusion of components from small droplets (“high”  $\bar{\mu}$ ) to larger ones (“low”  $\bar{\mu}$ ). To accommodate the added components without supersaturating, the larger droplets necessarily grow; conversely, the smaller droplets shrink and end up evaporating.

The classical quantitative treatment of this phenomenon is the Lifshitz-Slyozov theory [17]. It shows that the average droplet radius follows an inverse power law of time,

$$\langle R \rangle \propto t^{1/3}. \quad (3.3.1)$$

This is in a derivation when diffusion is the only transport mechanism. When a liquid flow is taken in account, and once the minority phase is sufficiently coalesced, a crossover in the exponent

$$\langle R \rangle \propto t \quad (3.3.2)$$

is expected. This was proposed by E. D. Siggia [24] by describing the hydrodynamic interaction between coalescing droplets via the lubrication theory.

We note that more advanced treatments of the diffusion-controlled kinetics of nucleation and growth can be seen in V. I. Kalikmanov’s book [12].

The literature has many examples of the application of the phase field theory to the modelling of ripening. Among recent examples without flows, Yamada et al. [33] investigate solid ripening under a temperature gradient which induces global grain migration and a greater prefactor to the  $t^{1/3}$  law; Wang et al. [31] and Ravash et al. [23] model sintering of solid grains in a liquid matrix, thus requiring careful geometrical control (by handling multiple interface and surface tensions, or the privileged crystallization directions, respectively). With flows, Henry and Tegze [10, 9] have shown the switch to a  $t$  regime in liquid-liquid systems using a Cahn-Hilliard model, and the possible departure from this regime and changes in topology if there is asymmetries in the phase fraction or the viscosities.

We intend to also show the departure from the  $t^{1/3}$  law using our alternate Allen-Cahn model. In addition, we illustrate the possible sedimentation under a gravity field (*ie.* bigger droplets will migrate faster), which according to Siggia also induces a second crossover in the power law.

#### 3.3.2 Initial conditions

In the literature, phase field approaches to ripening are often based on Cahn-Hilliard-type models. These models can evolve a random mixture of components and produce local agglomerates of daughter phase.

With our model however, droplet growth can only be simulated starting from an already nucleated state. This is due to the lack of a concave part in the bulk free energies in the grand potential formalism.

Ideally, our initial conditions should be specified for a fixed oxide inventory (in coherence with experimental conditions) and a fixed phase fraction. The phase field  $\varphi$  is then initialized with randomly positioned spherical interfaces with random volumes. The components should then be distributed inside and outside those interfaces in respect of the reference tie-line.

However, specifying the phase fraction, the global composition and the tie-line (and its endpoints) overspecifies the problem since these values are not independent. Remember that given a phase fraction  $s$  of phase 1 and a global composition  $c_{\text{inv}}$ , we have

$$c_{\text{inv}} = (1 - s)c_0^{\text{eq}} + sc_1^{\text{eq}}. \quad (3.3.3)$$

To respect this condition, we add to the background phase (phase 0) the component quantity

$$- \delta(c_0^{\text{eq}} - c_1^{\text{eq}}), \quad (3.3.4)$$

an offset along the tie-line. A positive  $\delta$  corresponds to a supersaturation, bringing the matrix composition inside the miscibility gap; a negative  $\delta$  brings the system away from the gap.

The initial dynamics of the simulation is a spherical variant of the diffusion couple where the droplets reach local equilibrium with their surrounding matrix. By supersaturating the matrix phase along the tie line, we ensure that the droplet grow by redistribution of the oversaturation to them. This is convenient because if the droplet were to shrink instead, they could all disappear before the growth dynamics can start. The dynamics indeed changes regime once the diffusion layers reach neighbouring droplets; this is reached at its earliest at a time given by the characteristic distance between droplets over the square root of the greatest mobility coefficient. Specifying a supersaturation  $\delta$  can be verified to be equivalent to specifying a phase fraction  $s$  below the one at equilibrium, given by  $|c_0^{\text{eq}} - c_{\text{inv}}|/|c_0^{\text{eq}} - c_1^{\text{eq}}|$ . However, this “lost” phase fraction would then be regained back as the local equilibria settle. We will have to keep in mind however that the specified phase fraction  $s$  will not be exactly the phase fraction at the start of the growth regime.

We detail below the initialization algorithm. It is specified for an initial phase fraction  $s$  and a global component inventory  $c_{\text{inv}}$ .

1. Define a uniform random distribution of droplet volumes around an average value  $V_{\text{avg}}$  with half-width  $\Delta V$ . Define also a uniform random distribution of random positions on the numerical domain for the droplets’ centre.
2. Sample the above distributions to define a droplet to be added to the domain. If this droplet is too close to another droplet, or too close to the numerical domain limits (with respect to a specified minimal distance criterion), discard it and sample again. Else, commit this droplet for initialization by saving its volume and position. Keep also track of the volume fraction of phase 1 thus added.
3. Repeat the above step until the phase fraction  $s$  is reached. If it is overshoot, reduce the volume of the last droplet to the necessary amount.
4. Initialization of  $\varphi$ : on all lattice nodes, search for the closest droplet and initialize the hyperbolic tangent profile using the distance to the droplet’s centre  $\mathbf{x}_0$  and its radius  $R$ , as

$$\varphi(\mathbf{x}) = \frac{1}{2} \left( 1 + \tanh \left( -2 \frac{|\mathbf{x} - \mathbf{x}_0| - R}{W} \right) \right). \quad (3.3.5)$$

5. Initialization of  $c$  and  $\bar{\mu}$ : compute the necessary (normalized) supersaturation  $\delta$  for  $s$  and  $c_{\text{inv}}$  to be consistent, as

$$\delta = \frac{1}{1 - s} \left( \frac{|c_0^{\text{eq}} - c_{\text{inv}}|}{|c_0^{\text{eq}} - c_1^{\text{eq}}|} - s \right). \quad (3.3.6)$$

Then, for all lattice nodes, set  $\mathbf{c}(\mathbf{x})$  as

$$\mathbf{c}(\mathbf{x}) = \begin{cases} (1 - \delta)\mathbf{c}_0^{\text{eq}} + \delta\mathbf{c}_1^{\text{eq}} & \text{if } \varphi(\mathbf{x}) < 1/2, \\ \mathbf{c}_1^{\text{eq}} & \text{if } \varphi(\mathbf{x}) \geq 1/2, \end{cases} \quad (3.3.7)$$

and set the chemical potential at equilibrium,  $\bar{\mu}(\mathbf{x}) = \mathbf{0}$ .

6. Flow initialization: at rest with  $\mathbf{u}(\mathbf{x}) = \mathbf{0}$ . The pressure field is left homogeneous;  $p(\mathbf{x}) = 0$ .

The homogeneous chemical potential  $\bar{\mu} = \mathbf{0}$  at initialization is not exactly consistent with the supersaturation inside the matrix but we won't consider it an issue. In the simulations, the field  $\bar{\mu}$  relaxes by itself for consistency with the composition fields. The same applies to the homogeneous initial pressure<sup>2</sup> which quickly relaxes for consistency with the buoyancy and surface tension forces.

The random distributions of droplets volumes and positions are parametrized with a seed for reproducibility. With multi-CPU or multi-GPU simulations, one must ensure that the same seed is used by all MPI processes.

### 3.3.3 Geometry measurements

#### Estimating the initial inter-droplet spacing

We wish to estimate the inter-droplet spacing  $\ell$  and the associated time  $T_D$  for the growth regime to begin. To do so, we will suppose that the initial droplet geometry is an arrangement on a regular grid of droplets of volume  $V_{\text{avg}}$ . These droplets occupy a volume fraction  $s$  in total and each droplet has a box of free volume  $V_{\text{avg}}/s$  around itself. We shall then estimate

$$\ell = (V_{\text{avg}}/s)^{1/d} \quad (3.3.8)$$

in  $d$  dimensions. The time  $T_D$  is

$$T_D = \ell^2 / \max_{\pi, \alpha} (M_{\pi}^{\alpha\alpha}) = T \quad (3.3.9)$$

and will be the time scale shown in the results.

#### Measuring the number of droplets and the mean radius

We use integrals of the phase field as estimates of the droplets' mean radius. For example, to obtain the average radius  $\langle R \rangle$  of droplets in a 2D simulation, we compute

$$\begin{aligned} \int \frac{4}{W} \varphi(1 - \varphi) d^2\mathbf{x} &\approx \sum_{\text{droplets}} 2\pi \int_0^{+\infty} \frac{4}{W} \varphi^{\text{eq}}(1 - \varphi^{\text{eq}}) r dr \\ &= 2\pi \sum_{\text{droplets}} R(1 + O(\exp(-2R/W)^2)) \\ &\approx 2\pi N \langle R \rangle. \end{aligned} \quad (3.3.10)$$

The radius estimate in 3D is

$$\int \frac{16}{W^2} \varphi(1 - \varphi) \left( \frac{1}{2} - \varphi \right) d^3\mathbf{x} \approx 4\pi N \langle R \rangle. \quad (3.3.11)$$

These estimates rely on the assumptions that

<sup>2</sup>Coincidentally, both  $\bar{\mu}(\mathbf{x})$  and  $p(\mathbf{x})$  are Lagrange multipliers. The first is related to the constraint on  $\mathbf{c}(\mathbf{x})$  to conserve the global composition inventory, and the second to the constraint on  $\mathbf{u}(\mathbf{x})$  to conserve mass.

- the equilibrium profile  $\varphi^{\text{eq}}(r) = (1 + \tanh(2(R - r)/W))/2$  is established on each droplet, with  $R$  their individual radius;
- the droplets are sufficiently spaced to separate the integral over each droplet;
- the interface width is always sufficiently small compared to the droplets' radii so that the term  $O(\exp(-2R/W)^2)$  can be neglected.

The second line in (3.3.10) is a first order Taylor expansion around  $e^{-2R/W} = 0$  applied on the result of the single droplet integral. Neglecting the term  $O(\exp(-2R/W)^2)$  is reasonable for large droplets, but it could over count the small disappearing droplets at the start of the growth regime. The assumption of spherical droplets can also be source of errors when the coalescence is too slow or frequent, or when the fluid's advection distorts the droplets too much. Nonetheless, these integrals can be evaluated quickly and in parallel by summing over all lattice nodes.

To count the droplets, we employ an algorithm for the computation of the Euler characteristic, to be understood here as the number of connected regions of  $\varphi = 1$ . An estimate akin to the one above for the droplet count can be established (at least in 2D), but the Euler characteristic algorithm also requires only a single pass over all the lattice points and avoids any of the geometry errors mentioned above. The computed count is also guaranteed to be an integer. The algorithm implemented is adapted from [32].

### 3.3.4 Simulation results

#### 2D without flow

A first simulation of an ensemble of 2738 2D droplets without convection was conducted. The parameters are listed in table 3.3 and the numerical domain is periodic. Using the integral estimates, the time evolution of the particle count  $N$  and droplet radius  $\langle R \rangle$  is tracked and presented in figure 3.6. It is seen that the mean radius does follow a power-law in time in this case with an exponent approaching the value of  $1/3$  expected from the classical theory. It takes a bit more than  $10 T$  (ten times the estimated duration of the transient droplet-matrix dynamics) for this power-law to establish clearly.

A timeline of the phase field and chemical potential fields are presented in figure 3.7. It shows the growth of the largest droplets and the disappearance of smaller ones as well as the redistribution of components and the homogenization of the chemical potentials. Refer to the figure's caption for more details.

This simulation ran on 4 Nvidia V100 GPUs on Jean-Zay, one of the cluster of the IDRIS institute<sup>3</sup>. The simulation ran for 24 million time steps, and took about 40 hours of wallclock time.

#### 2D with flow

We then proceed to simulations with hydrodynamic flow. The boundaries are again periodic and the parameters are the same as in 3.3 with the addition of the following flow parameters: a unique unit mass density  $\rho$  (the numerical unit and the characteristic density scale) and a surface tension of  $10^{-4} \rho \cdot L^3 \cdot T^{-2}$ . To study the influence of the Schmidt number on the droplet growth, we take two values for the kinematic viscosity in all phases:  $\nu_0 = \nu_1 = 1 L^2 \cdot T^{-1}$  first, and  $\nu_0 = \nu_1 = 10 L^2 \cdot T^{-1}$  second, corresponding to the Schmidt number values of  $(Sc^{AA}, Sc^{BB}) = (1, 1.25)$  and  $(Sc^{AA}, Sc^{BB}) = (10, 12.5)$  respectively. The buoyancy is not active ( $g$  and  $\Delta\rho$  are both zero).

The results are shown in fig. 3.8 and it is concluded that a higher Schmidt number increases the exponent of the power law, which departs from the value of  $1/3$  valid for purely diffusive growth. This

<sup>3</sup>The details and specifications of the Jean-Zay cluster are available at <http://www.idris.fr/eng/jean-zay/index.html>. This work was performed using HPC resources from GENCI-IDRIS (Grant 2022-R0091010339).

LBM	
lattice	D2Q9
domain	$[-28L, 28L] \times [-28L, 28L]$ , $4096 \times 4096$ nodes
$\delta x$	$2 \times 28/4096 L \approx 1.367 \times 10^{-2} L$
$\delta t$	$1.96 \times 10^{-5} T$
Phase field	
$W$	$3\delta x \approx 4.102 \times 10^{-2} L$
$M_\varphi$	$1.2 L^2 \cdot T^{-1}$
$\lambda$	155.95
Free energy	
$\bar{K}_0$	1
$\bar{K}_1$	1
$\mathbf{c}_0^{\text{eq}}$	$(0.3 \quad 0.3)^T$
$\mathbf{c}_1^{\text{eq}}$	$(0.4 \quad 0.4)^T$
Mobilities	
$\bar{M}_0^{AA}$	$1.0 L^2 \cdot T^{-1}$
$\bar{M}_0^{BB}$	$0.8 L^2 \cdot T^{-1}$
$\bar{M}_1^{AA}$	$1.0 L^2 \cdot T^{-1}$
$\bar{M}_1^{BB}$	$0.8 L^2 \cdot T^{-1}$
Droplets	
$\mathbf{c}_{\text{inv}}$	$(0.31 \quad 0.31)^T$
$s$	0.08
$V_{\text{avg}} \pm \Delta V$	$(8.0 \pm 7.5) \times 10^{-2} L^2$

Table 3.3: Parameters for the 2D simulation of droplet growth without flow. The length unit  $L$  is the half-length of the square numerical domain and the time unit  $T$  is the expected time until the start of the growth dynamics, see eq. (3.3.9). With this droplet ensemble, the average inter-droplet distance is  $\ell \approx 0.038 L$ .

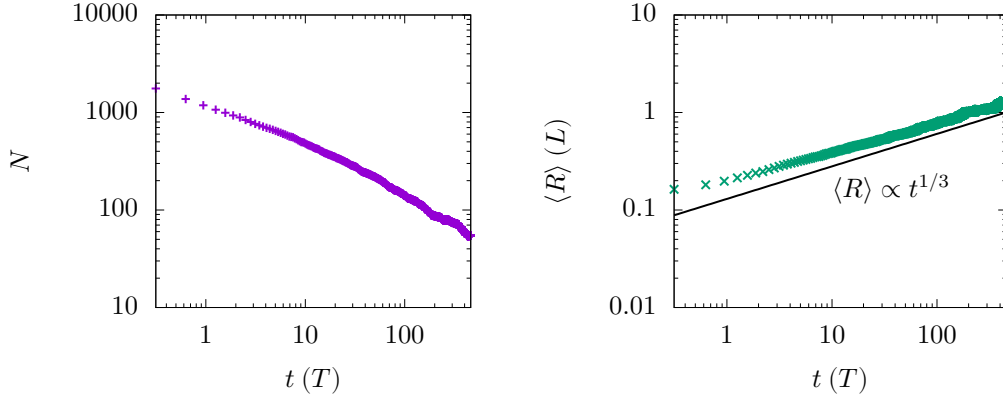


Figure 3.6: Time evolution of the droplets number and size. Both plots are in log-log scale. (Left) droplet count  $N$ . (Right) average droplet radius  $\langle R \rangle$ . The simulations' data points are in green crosses. A reference line for  $\langle R \rangle \propto t^{1/3}$  is shown with a solid black line.

is part of the expected result; a more thorough investigation of the different flow parameters is needed to attain the exponent of 1 mentioned in [24].

### 3D with buoyancy-driven flow

We present here a simulation of ripening in three dimensions. Compared to the previous 2D simulation, this simulation also models a buoyancy driving the flow and the bounceback algorithm is used on the boundaries.

In the  $\text{Na}_2\text{O-SiO}_2\text{-MoO}_3$  glass, the nucleated droplets are enriched in molybdenum, a relatively heavy element. Hence, we propose to simulate a buoyant droplet phase to model sedimentation, which might be observed in experiments with sufficient amount of  $\text{MoO}_3$ . In addition, the buoyancy acceleration is expected to cause another crossover in the power law for the growth of the droplet radius [24].

The amplitude of the buoyancy is quantified with the Eötvös number  $Eo = \Delta\rho||\mathbf{g}||L^2/\sigma$ . We tested the values  $Eo = 10^3$ ,  $4 \times 10^3$ , and  $2.5 \times 10^4$ . See table 3.4 for the complete list of the parameters.

We show snapshots of the phase field in figures 3.10, 3.11 and 3.12. Figure 3.9 presents the evolution of the droplet mean radius in the three simulation. The one with the strongest gravity,  $Eo = 2.5 \times 10^4$ , noticeably differs from the two others: the droplets flow and coalesce much faster. Accordingly, at this value of  $Eo$ , the time evolution of the radius seems to tend towards a power law with an exponent above one.

We may interpret the result of this last simulation as the manifestation of the crossover due to gravity mentioned by ref. [24]. To make certain of this, it would be good to perform new simulations with a higher supersaturation to keep more droplets after the transient regime and thus obtain a better statistical average. Furthermore, testing intermediate values for  $Eo$  would allow us to estimate the crossover point. Finally, exploring longer times might reveal crossovers from the lower gravity values.

## 3.4 Conclusion

In this last chapter, we have proven the validity of the two-phase ternary material subset of the model as well as its two-phase flow subset by reproducing the analytical solutions of two well-known test cases.

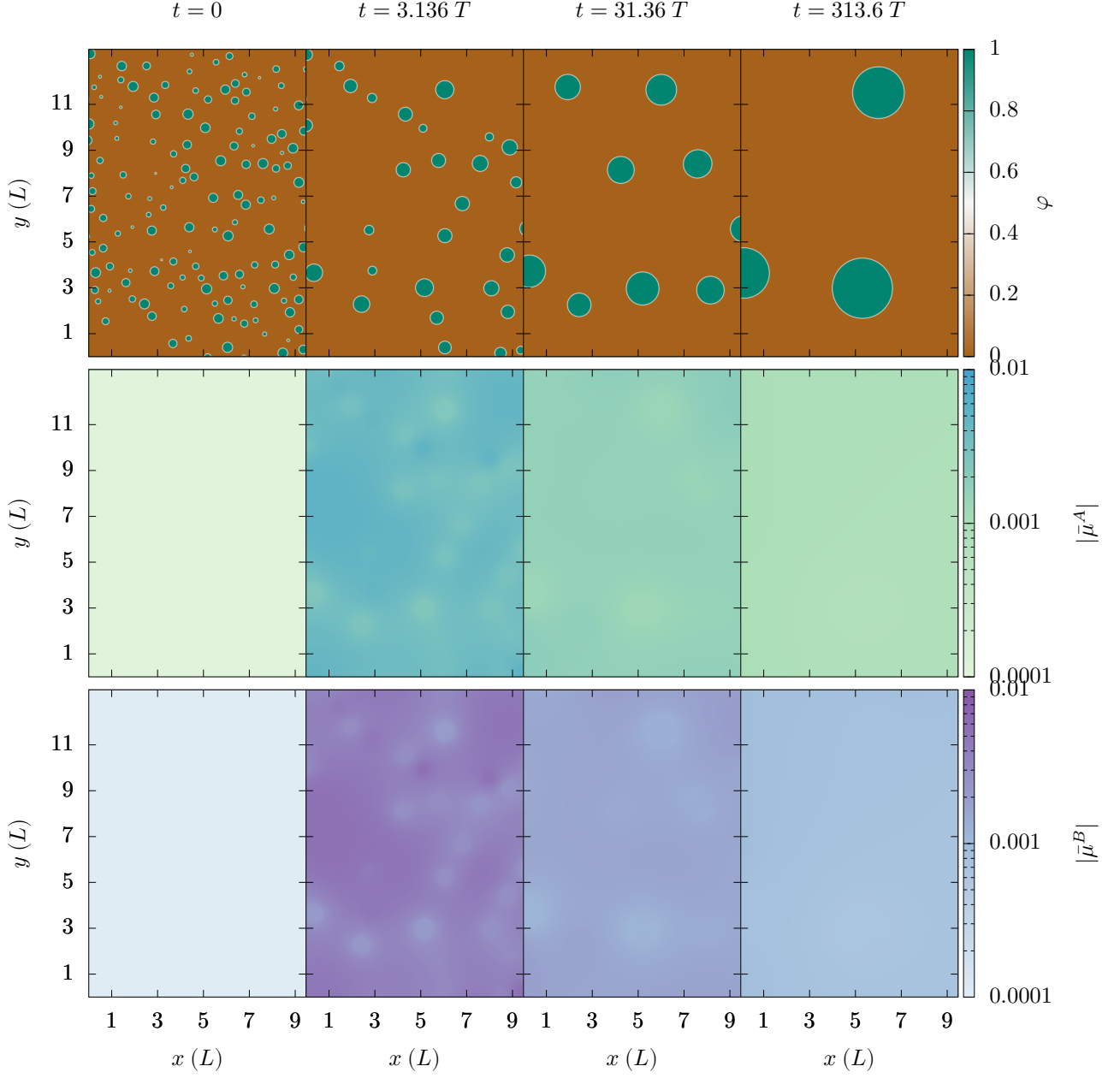


Figure 3.7: Snapshot pictures at different times of the flow-less 2D droplet growth simulation. Only a portion of the numerical domain is displayed, with a hundred out of the total of 2738 droplets. (Top) phase field. (Middle, bottom) absolute value of the chemical potentials (*ie.* departure from the reference equilibrium) in log scale. During the establishment of the droplet-matrix local equilibria, some of the smallest droplets disappear. Then, the ripening dynamics proceeds as expected: small droplets disappear and redistribute their components to the neighboring larger droplets, which grow. This redistribution can be seen on the chemical potential fields, for instance by the strong gradient created by the two small shrinking droplets in the upper half at  $t = 17.38 T$ , or the smaller gradients bridging the bigger droplets and their neighbors of similar size. At long times, the ripening dynamics slows down and the chemical potentials become more and more homogeneous. This homogeneous value is different from the equilibrium value  $\bar{\mu} = 0$  set at equilibrium: it actually matches the mean curvature of the droplets, following the Gibbs-Thomson condition.



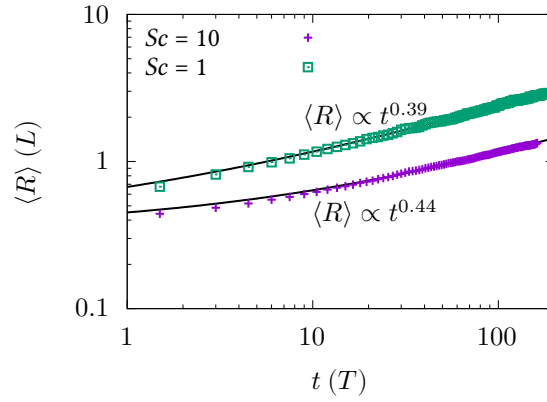


Figure 3.8: Evolution of the mean radius during two simulations of the growth of 2D droplets under a flow, one with Schmidt numbers around 1 in purple crosses and the other with Schmidt numbers of order 10 in green squares (refer to the text for the exact values). The best fitting power law is plotted for each case with a black line.

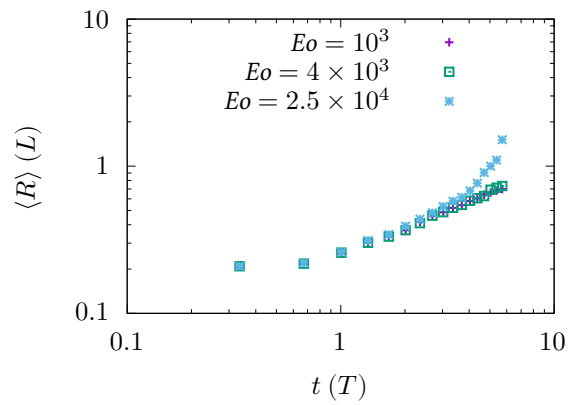


Figure 3.9: Time evolution of the mean radius during the simulation of the growth of 3D droplets accelerated by their buoyancy. The results are indicated for each tested value of the  $Eo$  number, see the key in the top left.

LBM	
lattice	D3Q19
domain	$[-16L, 16L] \times [-4L, 4L] \times [-4L, -4L]$ , $2048 \times 512 \times 512$ nodes
$\delta x$	$8/512 L = 0.015625 L$
$\delta t$	$2.1 \times 10^{-5} T$
Phase field	
$W$	$4\delta x \approx 1.565 \times 10^{-2} L$
$M_\varphi$	$1.2 L^2 \cdot T^{-1}$
$\lambda$	155.95
Free energy	
$\bar{K}_0$	1
$\bar{K}_1$	1
$\mathbf{c}_0^{\text{eq}}$	$(0.3 \ 0.3)^T$
$\mathbf{c}_1^{\text{eq}}$	$(0.4 \ 0.4)^T$
Chemical mobilities	
$\bar{M}_0^{AA}$	$1.0 L^2 \cdot T^{-1}$
$\bar{M}_0^{BB}$	$0.8 L^2 \cdot T^{-1}$
$\bar{M}_1^{AA}$	$1.0 L^2 \cdot T^{-1}$
$\bar{M}_1^{BB}$	$0.8 L^2 \cdot T^{-1}$
Flow	
$\nu_0$	$1.0 L^2 \cdot T^{-1}$
$\nu_1$	$1.0 L^2 \cdot T^{-1}$
	for $Eu = 10^3$ for $Eu = 4 \times 10^3$ for $Eu = 2.5 \times 10^4$
$\Delta\rho$	$1 \ \rho$ $4 \ \rho$ $25 \ \rho$
$\mathbf{g}$	$1 L \cdot T^{-2} \mathbf{e}_x$
$\sigma$	$10^{-3} \rho \cdot L^3 \cdot T^{-2}$
Droplets	
$\mathbf{c}_{\text{inv}}$	$(0.31 \ 0.31)^T$
$s$	0.08
$V_{\text{avg}} \pm \Delta V$	$(0.08 \pm 0.072) L^3$

Table 3.4: Numerical parameters for the 3D simulation of droplet growth with a buoyancy driven flow in a channel. The numerical length unit  $L$  is the average distance between two droplets at the initial time and the time unit  $T$  is the expected time until the start of the growth dynamics, see eq. (3.3.9).

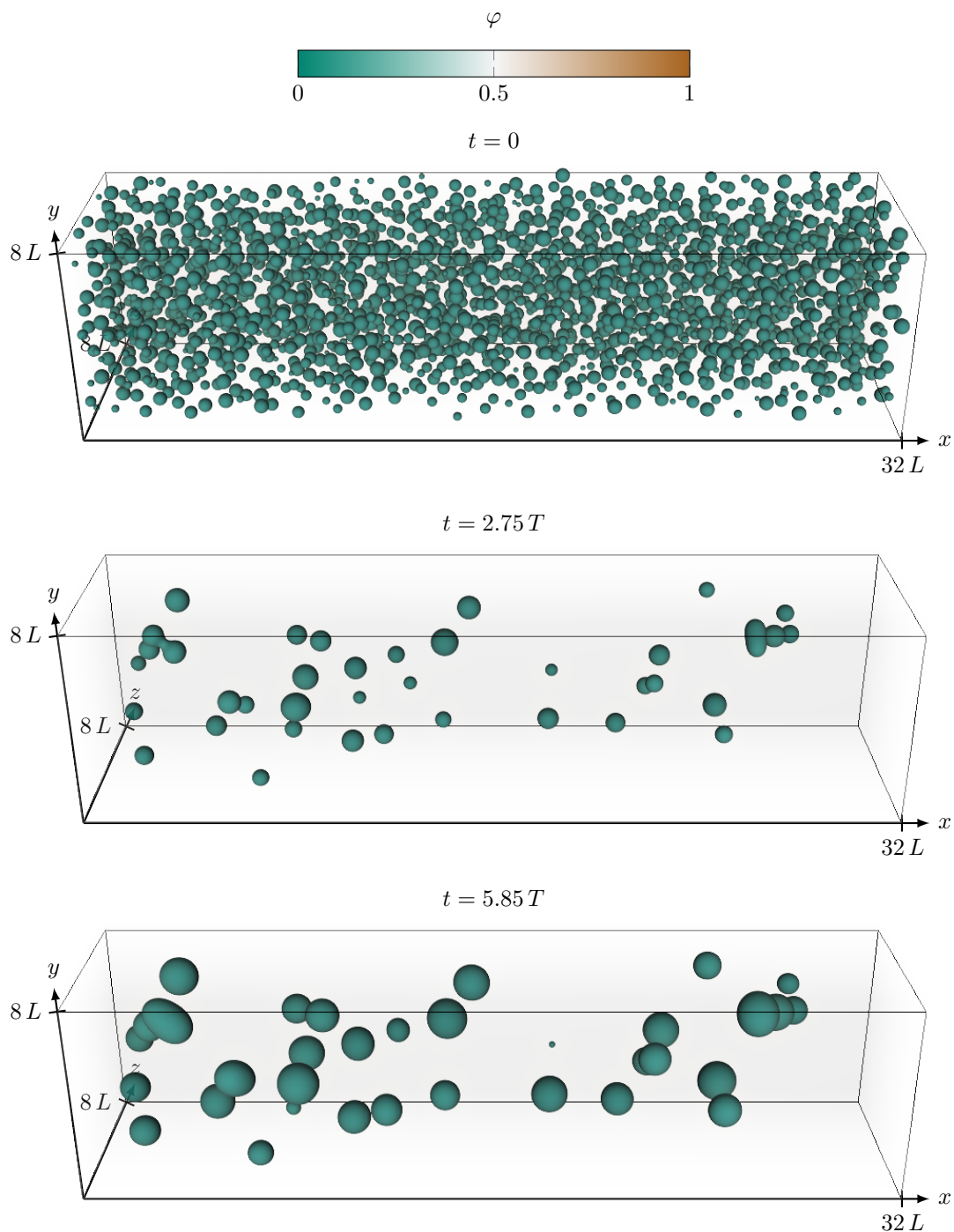


Figure 3.10: Snapshot visualisations of the phase field at multiple times during the 3D simulations of droplet ripening. A constant gravity toward  $+x$  displaces the droplets and accelerates growth and coalescence. The strength of the gravity is quantified with the Eötvös number  $Eo = \Delta\rho g L^2 / \sigma$ ; in this figure  $Eo = 10^3$ . There are 2035 droplets at initialization, and about 30 on the later times. The visualisation was done with the volume rendering capabilities of the visit [3] software. A transfer function makes the values under  $\varphi = 0.5$  transparent. The presented timesteps were obtained after approximately 22 hours of simulation using 16 Nvidia V100 GPUs on the Jean-Zay cluster.

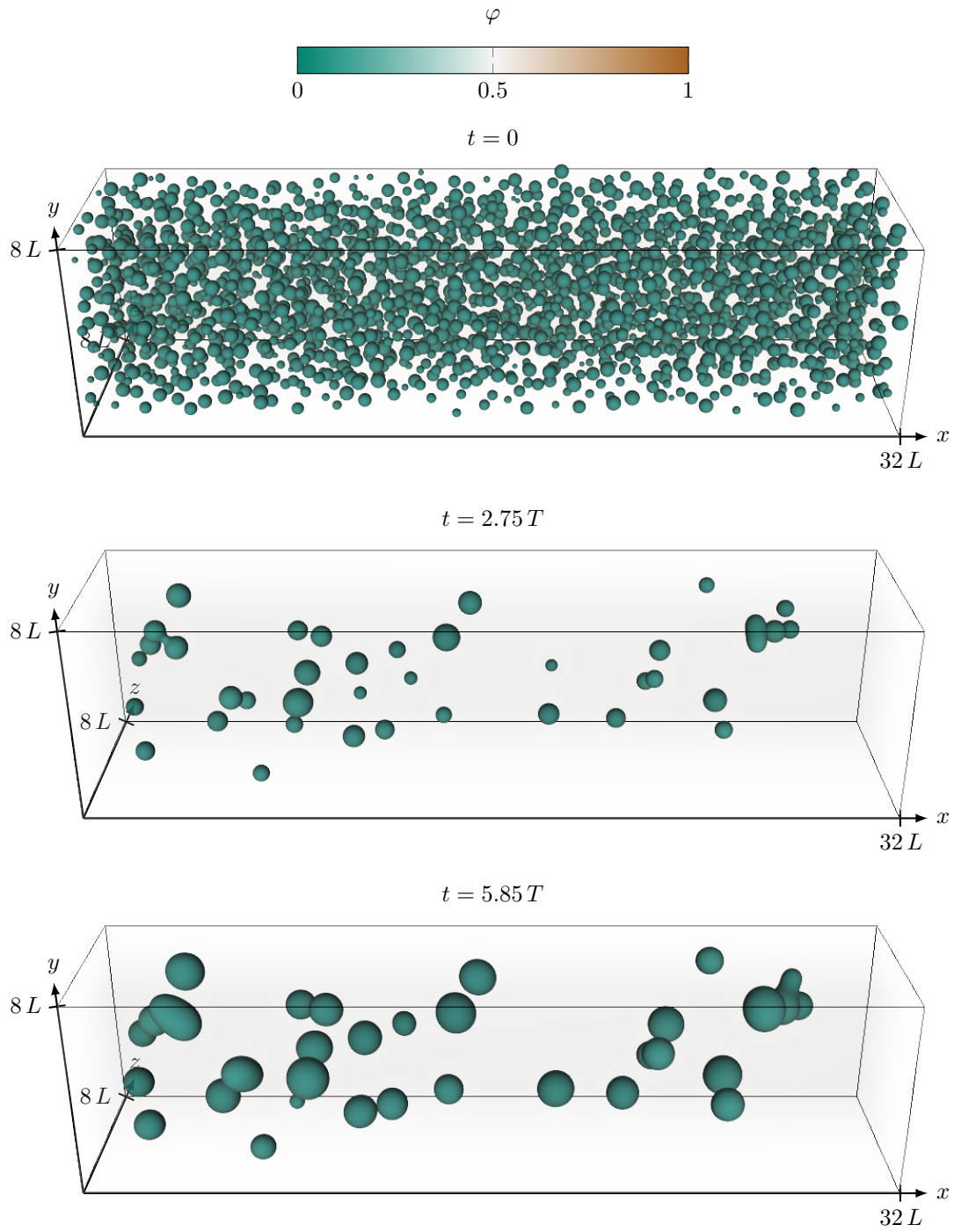


Figure 3.11: Visualisations for the droplet ripening simulation with  $Eo = 4 \times 10^3$ ; see fig. 3.10 for more details. Compared to the simulation at  $Eo = 10^3$ , the coalescence is only very slightly accelerated with only the rightmost droplet cluster being noticeably different at the latest time.

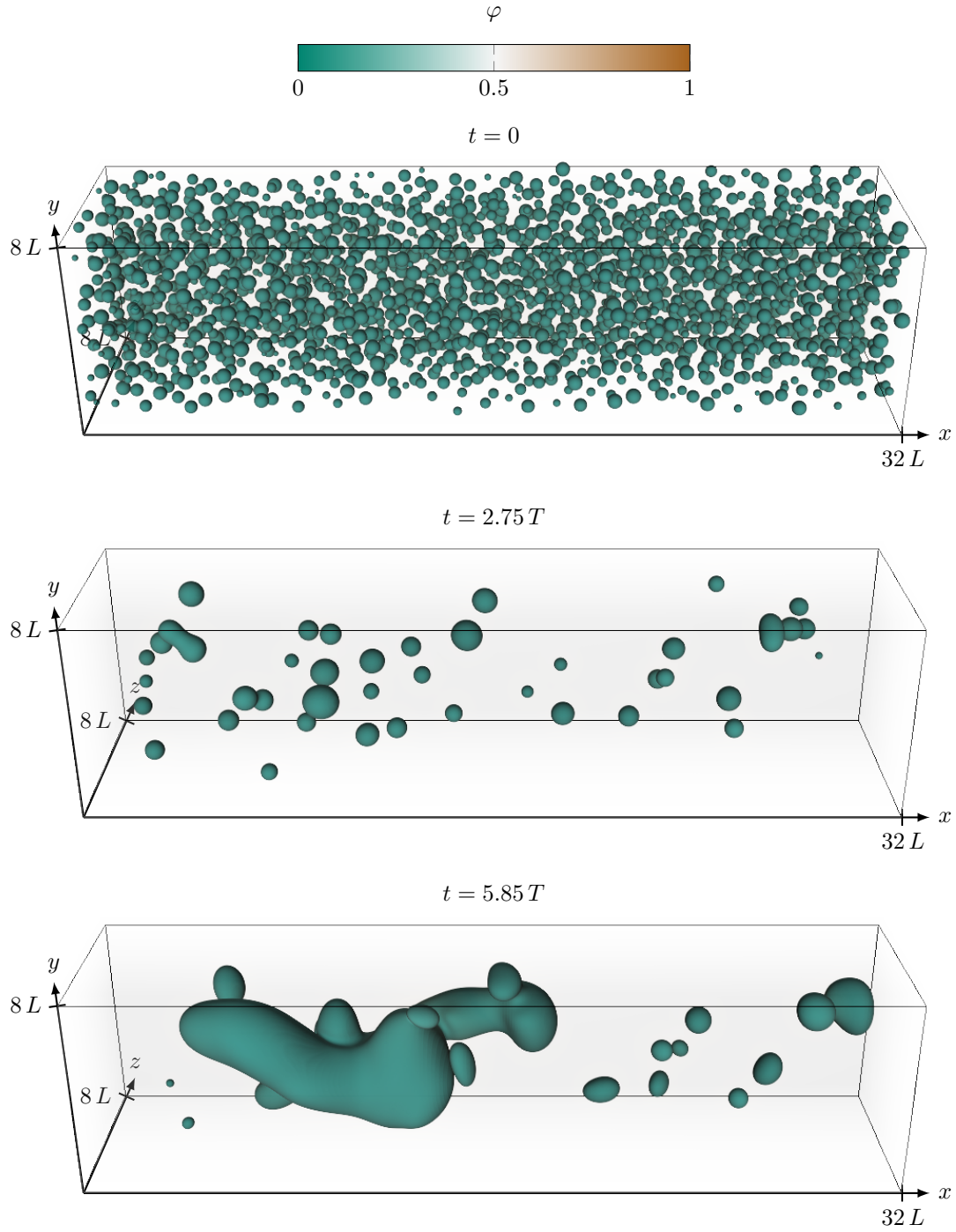


Figure 3.12: Visualisations for the droplet ripening simulation with  $Eo = 2.5 \times 10^4$ ; see fig. 3.10 for more details. Compared to the simulation at  $Eo = 10^3$  and  $Eo = 4 \times 10^3$ , the buoyancy noticeably accelerates the coalescence with the formation of large non-spherical aggregates of daughter phase.

This allowed us to proceed to simulations of droplet growth, a test case for the complete model and a basis for future comparisons to experimental observations of the ternary  $\text{Na}_2\text{O}-\text{SiO}_2-\text{MoO}_3$  nuclear glass. Because the model is by construction unable to produce spontaneous nucleations, we took care to formulate a detailed initialization scheme. During growth, we were able to match the power-law in time for the average droplet radius, with an exponent of  $1/3$  without flow and the departure from this value with a two-phase flow and a buoyancy-driven flow. 3D simulations on a multi-GPU cluster were conducted, attesting for the numerical efficiency of the model's implementation in LBM\_saclay.

We would hope next to be able to model the growth dynamics in the real  $\text{Na}_2\text{O}-\text{SiO}_2-\text{MoO}_3$  glass and not just in a fictitious idealized material as done in these simulations. In the following subsections, we will detail our current efforts toward this goal.

### 3.4.1 Opening: comparison to experiments

Refining the description of the  $\text{Na}_2\text{O}-\text{SiO}_2-\text{MoO}_3$  material would be done essentially through the model's physical parameters. Order of magnitudes estimates for the diffusion matrix  $\mathbf{D}$  may be obtained from the measurements of diffusion in borosilicate glasses conducted in the thesis of H. Pablo [21] [20]. This would in turn give estimates for the mobility matrix  $\bar{\mathbf{M}}$  once the matrix of second derivatives  $\bar{\mathbf{K}}$  is also determined. The fitting strategy of the  $\bar{\mathbf{K}}$  matrices from thermodynamic data was established and implemented. It is extensively detailed in the next subsection. Lastly, the surface tension  $\sigma$  is probably the most difficult parameter to obtain, but it may be possible to also estimate it using thermodynamic data [6].

In the previous paragraph, we mentioned borosilicate glasses. They are of particular interest for nuclear glasses and present a further opportunity of refinement: extending the model to a quaternary system with the addition of a boron oxide. The mathematical model in itself is easy to extend to any number of components. The difficulties lie in the determination of dynamical and thermodynamic properties of the more complex compound; the choice of a simplified ternary glass was essentially motivated by the existence of the  $\text{Na}_2\text{O}-\text{SiO}_2-\text{MoO}_3$  Calphad database at CEA.

But even without a complete refinement of the model and its parameters, we can already propose to compare the results of simulations to experimental observations. Work is in progress at the CEA Marcoule to set up a small glass furnace equipped with an endoscope which would allow observations of the bulk of the glass. Such experiments will typically operate at temperature around  $1110^\circ\text{C}$  and an oxide mixture with a few percent of  $\text{MoO}_3$  and the rest being split at 80%/20% between  $\text{SiO}_2$  and  $\text{Na}_2\text{O}$  respectively. This mixture sets the initial condition of the droplet growth simulations, and we will see that both the temperature and mixture will parametrize the fitting of the  $\bar{\mathbf{K}}$  matrices.

### 3.4.2 Coupling to the thermodynamic potential of the $\text{Na}_2\text{O}-\text{SiO}_2-\text{MoO}_3$ glass

To quantitatively describe the real nuclear glass, the parameters of the model must be fitted to the properties of the glass. In this subsection, we detail how we fit the free energy parameters in particular. These parameters are the matrices of second derivatives of the quadratic wells,  $\bar{\mathbf{K}}_0$ ,  $\bar{\mathbf{K}}_1$ , and the coexistence compositions of a reference tie-line,  $c_0^{\text{eq}}$ ,  $c_1^{\text{eq}}$ .

#### Fitting methodology

The coupling methodology is similar to the one presented in ref. [4], where the authors present a simple framework to couple a multi-component grand potential model to thermodynamic data. They do so by expanding the phase free energies as parabolic polynomials around a reference composition. We reiterate this method here and propose a practical implementation. This implementation, along with our model and the first droplet growth test cases, was presented at the CALPHAD 2022 conference [29].

Remark that the quadratic free energy wells as used in our modelling are equivalent to the second order Taylor expansion of a global free energy landscape  $F(\mathbf{c})$  around the extremities of a given tie line. More specifically, when considering the transformation of  $F(\mathbf{c})$  relative to the reference equilibrium  $F^*(\mathbf{c}) = F(\mathbf{c}) - \boldsymbol{\mu}^{\text{eq}} \cdot \mathbf{c}$ , one can verify that the expression for  $f_\pi^*(\mathbf{c})$  in eq. (1.3.18) exactly matches the expansion of  $F^*(\mathbf{c})$  around each coexistence composition  $\mathbf{c}_\pi^{\text{eq}}$  with

$$\left. \frac{\partial^2 F^*}{\partial \mathbf{c} \partial \mathbf{c}} \right|_{\mathbf{c}_\pi^{\text{eq}}} = \mathbf{K}_\pi, \quad \left. \frac{\partial F^*}{\partial \mathbf{c}} \right|_{\mathbf{c}_\pi^{\text{eq}}} = \boldsymbol{\mu}^{*\text{eq}} = \mathbf{0}, \quad F^*(\mathbf{c}_\pi^{\text{eq}}) = Q^*. \quad (3.4.1)$$

Given  $F(\mathbf{c})$  and a reference equilibrium, we propose to perform this expansion numerically by curve-fitting the functions  $f_\pi^*(\mathbf{c})$  against  $F^*(\mathbf{c})$  around the abscissas  $\mathbf{c}_\pi^{\text{eq}}$ . This will give the numerical values for the two  $\mathbf{K}_\pi$  matrices and for  $Q'$ . This last parameter is a constant energy offset, identical for both phases because of the tangent plane removal, and we are free to set it to 0 afterwards. We then strip the energy dimension as specified in sec. 1.3.3 to obtain the dimensionless matrices  $\bar{\mathbf{K}}_\pi$ .

### Extracting thermodynamic data with OpenCalphad

We will use thermodynamic data given by the Calphad method [13]. Calphad is a method commonly used in the material science community to numerically build the Gibbs energy profiles and the corresponding phase diagram of multi-component materials. There are also many examples in the literature of its use in conjunction with phase field modelling [14, 5, 4].

This thermodynamic landscape is reconstructed by fitting an elaborate model Gibbs energy against experimental measurements or simulations at the microscopic scale (e.g. molecular dynamics or density functional theory simulations). They are then exported as thermodynamic databases. Others may then query those databases to obtain thermodynamic data at a desired pressure, temperature and composition inventory. Database assessment and querying both use specialized software such as the open-source OpenCalphad [25] or the proprietary ThermoCalc and FactSage.

Here, as just users of the Calphad method, we may simply imagine it as the numerical function

$$(T, p, \mathbf{c})_{\text{global}} \rightarrow \{(G_\pi, \mathbf{c}_\pi^{\text{eq}}, \boldsymbol{\mu}^{\text{eq}}, s_\pi)\}_\pi \quad (3.4.2)$$

which, given the global thermodynamic variables (temperature, pressure and global composition inventory), yields the equilibrium thermodynamic data of all stable phases  $\pi$  (Gibbs energy, coexistence composition, chemical potentials and phase fraction). The modelling in terms of the Gibbs energy  $G$  is the convention taken by Calphad. We will propose that going from  $G$  to  $F$  is direct under the assumptions of a closed system, of constant pressure and of identical and constant molar volumes. This is because under the corresponding equation of state

$$V\mathcal{N} = V_m^A N^A + V_m^B N^B \quad (3.4.3)$$

the transformation  $F = G - pV$  only corresponds to a constant energy offset. In the above equation,  $V_m^A, V_m^B$  are the molar volume of each component species and  $\mathcal{N}$  is the Avogadro constant.

The Calphad method is used here with the OpenCalphad software to query a thermodynamic database for the  $\text{Na}_2\text{O}-\text{SiO}_2-\text{MoO}_3$  recently produced during the PhD thesis of S. Bordier at the CEA of Saclay's Département de Physico-Chimie [2]. The interested reader can refer to the cited manuscript for the details on its design.

To determine the reference tie-line, we give ourselves a certain global inventory of oxide composition  $\mathbf{c} = (c^{\text{SiO}_2}, c^{\text{Na}_2\text{O}})^T$ , a certain temperature  $T$  and a pressure  $p$  always taken as the atmospheric pressure of  $10^5$  pascals, all being consistent with experimental conditions. We ask OpenCalphad to compute the equilibrium at these conditions and if it is the desired liquid-liquid two-phase coexistence, the reference tie-line is obtained.

Input parameters		Outputs	
$c_{\text{inv}}$	$(0.7879 \quad 0.1921)^T$	$c_0^{\text{eq}}$	$(0.7970 \quad 0.1885)^T$
$T$	1152 °C	$c_1^{\text{eq}}$	$(0.009 \quad 0.4977)^T$
$p$	$10^5$ Pa	$\bar{K}_0$	(4.38, 5.49, 4.79)
		$\bar{K}_1$	(6.88, 25.7, -2.62)

Table 3.5: Input parameters and outputs of the example Calphad fitting procedure. Compositions vectors are given in the order  $(c^{\text{SiO}_2} \quad c^{\text{Na}_2\text{O}})^T$ . The symmetric matrices are given as the tuples  $(\bar{K}^{\text{SiO}_2 \text{ SiO}_2}, \bar{K}^{\text{Na}_2\text{O Na}_2\text{O}}, \bar{K}^{\text{SiO}_2 \text{ Na}_2\text{O}})$ .

The global free energy landscape  $F(c)$  is obtained with the same tools. In OpenCalphad, the mechanism that resolves the miscibility gaps and determines the phases at equilibrium is called the grid minimizer. Under an hypothesis of local equilibrium [26], we will assume that OpenCalphad calculations with this grid minimizer turned off (in which case the function (3.4.2) only returns a single “mixture” stable phase) are sufficient to obtain consistent Gibbs energy values for a global landscape of the compound’s free energy.

### Implementation and calculation example

In summary, the fitting methodology proceeds in two steps:

1. for a given temperature and global composition inventory, query the Calphad database for the corresponding equilibrium, *ie.* sample the numerical function (3.4.2). If it is the liquid-liquid phase coexistence of interest, this gives us the reference tie line with its endpoints  $c_\pi^{\text{eq}}$  and the reference chemical potentials  $\mu^{\text{eq}}$ .
2. Over a given discrete range of compositions  $c$ , execute local equilibria calculations with OpenCalphad to obtain the local free energy landscape  $F(c)$ . Apply the reference tangent plane removal (using the previous tie line calculation), the curve fit and the dimension removal to get  $\bar{K}_0, \bar{K}_1$ .

We implemented this method in a python program [16] using a python interface to OpenCalphad. The program also handles the necessary stoichiometry transformations: the thermodynamic database is written in terms of the chemical species (O, Si, Na, Mo) but our model is written in terms of the oxide compounds. The curve-fitting is done with the Levenberg-Marquardt least-squares algorithm [22, 7] implemented in the python library `scipy` [30] (`scipy.optimize.curve_fit`). The Jacobian of  $f'_\pi$  with respect to the coefficients of  $\bar{K}_\pi$  is given analytically. The curve fitting done by the program is parametrized by a radius  $R_{\text{fit}}$ . It constrains the points used in the two curve fits to the regions where  $(c - c_\pi^{\text{eq}})^2 < R_{\text{fit}}^2$ . The program verifies that the fitted  $\bar{K}_\pi$  matrices are positive definite.

We present an example of these calculations. Table 3.5 lists the input and outputs of the procedure, figure 3.13 the constructed free energy landscape, and figure 3.14 the fitted paraboloids along the tie line.

We then attempted to simulate the model with the obtained  $\bar{K}_\pi$  matrices. The simulation proved to be unstable and diverged after a few time steps. The reason is not yet clearly identified, but an idea might lie in the implicit diffusion matrices. This diffusion matrix is given in each phase  $\pi$  by

$$D_\pi = \bar{M}_\pi \bar{K}_\pi, \quad (3.4.4)$$

the product of the chemical mobility matrix and the matrix of the free energies’ second derivatives (or their dimensioned equivalents). The previous simulations used identity  $\bar{K}_\pi$  matrices and diagonal  $\bar{M}_\pi$



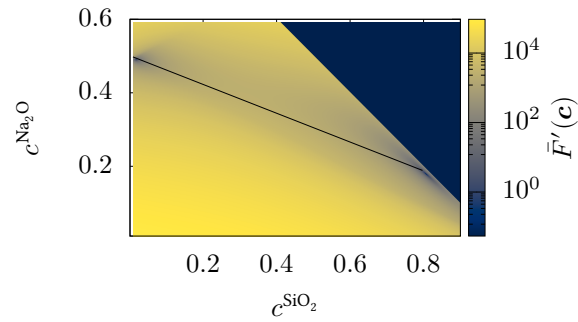


Figure 3.13: Global free energy landscape  $\bar{F}(\mathbf{c})$  (in log scale) obtained with local equilibria calculations with OpenCalphad. The reference tangent plane and the characteristic energy scale was removed. The reference tie-line obtained by the first equilibrium calculation at  $\mathbf{c}_{\text{inv}}$  is shown with a black line.

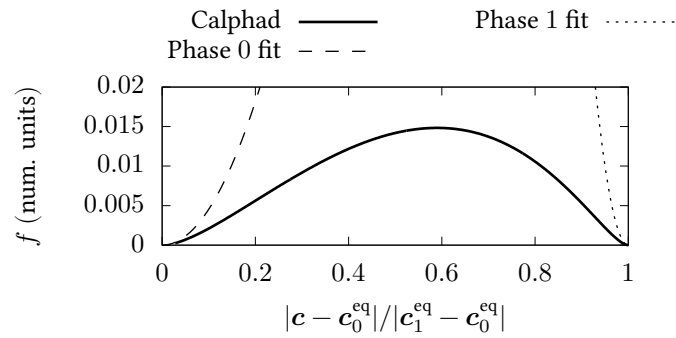


Figure 3.14: Projection of the dimensionless free energy landscape (solid line) and the fitted paraboloids  $\bar{f}'(\mathbf{c})$  (dashed and dotted lines) along the reference tie line.

	Matrix coefficients	Eigenvalues
$D_0$	$\begin{pmatrix} 4.38 & 4.79 \\ 3.822 & 4.392 \end{pmatrix}$	(0.1017 8.670)
$D_1$	$\begin{pmatrix} 6.88 & -2.62 \\ -2.096 & 20.56 \end{pmatrix}$	(6.490 20.95)

Table 3.6: Numerical values of the implicit diffusion matrices of the chemical diffusion equations when the mobility matrices are taken as  $\bar{M}_0 = \bar{M}_1 = \text{diag}(1.0, 0.8)$  and the free energy second derivatives matrices are taken as in tab. 3.5. All numerical values in this table are to read in the units  $L^2 \cdot T^{-1}$ , the characteristic diffusion squared length and inverse time.

matrices equal in both phases, e.g. the mobilities listed in table 3.3. The eigenvalues of the mobility and diffusion matrices were always within the same order of magnitude: typically  $1.0 L^2 \cdot T^{-1}$  for the A component eigenvalue and  $0.8 L^2 \cdot T^{-1}$  for the B component eigenvalue, with  $L$  and  $T$  the characteristic length and time units of the diffusive processes.

Using the same values for the  $\bar{M}_\pi$  matrices and the values of the  $\bar{K}_\pi$  matrices given by the Calphad curve fit gives the diffusion matrices listed in table 3.6. One can notice that the eigenvalues differ by two orders of magnitudes in each phase, or three orders across all phases and components. This may be relevant since the diffusion eigenvalues are expected to bound the numerical stability of the lattice Boltzmann scheme: three orders of magnitude across the diffusion eigenvalues might have restricted the stability range too much. Another remark is that despite the individual  $\bar{K}_\pi$  and  $\bar{M}_\pi$  matrices being symmetric positive definite, the individual  $\bar{D}_\pi$  are not (it is only the case if  $\bar{K}_\pi$  and  $\bar{D}_\pi$  commute).

We are not yet certain if this range of orders of magnitude is truly too restrictive or if the symmetry of the diffusion matrices are a hard requirement for the numerical stability. We still need to construct intermediary test values for both kind of matrices to answer these questions. However, it can be hard to build such test cases while keeping the mobility matrices diagonal; this is necessary to keep our diffusion equations uncoupled, and breaking this condition will require further work on the LBM discretization. In addition, if the  $\bar{M}_\pi$  and  $\bar{K}_\pi$  are to satisfy new constraints, we must also probably guarantee that the phase field interpolation also upholds these constraints in the interface. For now, we have only confirmed that the simulations are well-behaved and do not diverge when the  $\bar{K}_\pi$  matrices are taken as different but close multiples of the identity matrix.

## References

- [1] Robert F. Almgren. “Second-Order Phase Field Asymptotics for Unequal Conductivities.” In: *SIAM Journal on Applied Mathematics* 59.6 (1999), pp. 2086–2107. doi: 10.1137/S0036139997330027.
- [2] Sébastien Bordier. “Modélisation thermodynamique des phases insolubles dans les verres nucléaires : application à la vitrification du molybdène et des produits de fission platinoides.” 2015AIXM4339. PhD thesis. 2015.
- [3] Hank Childs et al. “VisIt: An End-User Tool For Visualizing and Analyzing Very Large Data.” In: *High Performance Visualization—Enabling Extreme-Scale Scientific Insight*. Oct. 2012, pp. 357–372. doi: 10.1201/b12985.
- [4] Abhik Choudhury, Michael Kellner, and Britta Nestler. “A method for coupling the phase-field model based on a grand-potential formalism to thermodynamic databases.” In: *Current Opinion in Solid State and Materials Science* 19.5 (2015), pp. 287–300. ISSN: 1359-0286. doi: <https://doi.org/10.1016/j.cossms.2015.03.003>.

- [5] J.-L. Fattebert, M.E. Wickett, and P.E.A. Turchi. “Phase-field modeling of coring during solidification of Au–Ni alloy using quaternions and CALPHAD input.” In: *Acta Materialia* 62 (2014), pp. 89–104. ISSN: 1359-6454. doi: <https://doi.org/10.1016/j.actamat.2013.09.036>.
- [6] Kasi Gajavalli and Romain Le Tellier. “Butler-based thermodynamic modeling of interfacial energies for in-vessel corium systems.” In: *Journal of Nuclear Materials* 569 (2022), p. 153935. ISSN: 0022-3115. doi: <https://doi.org/10.1016/j.jnucmat.2022.153935>.
- [7] Henri P. Gavin. *The Levenberg-Marquadt algorithm for nonlinear least squares curve-fitting problems*. <https://people.duke.edu/~hpgavin/ce281/lm.pdf>. Retrieved 28/03/2022. 2020.
- [8] D.W. Hahn and M.N. Özisik. *Heat Conduction*. Wiley, 2012. Chap. 12, pp. 452–495. ISBN: 9781118330111.
- [9] Hervé Henry and György Tegze. “Kinetics of coarsening have dramatic effects on the microstructure: Self-similarity breakdown induced by viscosity contrast.” In: *Phys. Rev. E* 100 (1 July 2019), p. 013116. doi: 10.1103/PhysRevE.100.013116.
- [10] Hervé Henry and György Tegze. “Self-similarity and coarsening rate of a convecting bicontinuous phase separating mixture: Effect of the viscosity contrast.” In: *Phys. Rev. Fluids* 3 (7 July 2018), p. 074306. doi: 10.1103/PhysRevFluids.3.074306.
- [11] J. Heulens, B. Blanpain, and N. Moelans. “Phase-field analysis of a ternary two-phase diffusion couple with multiple analytical solutions.” In: *Acta Materialia* 59.10 (2011), pp. 3946–3954. ISSN: 1359-6454. doi: 10.1016/j.actamat.2011.03.020.
- [12] V. I. Kalikmanov. “Classical Nucleation Theory.” In: *Nucleation Theory*. Dordrecht, 2013, pp. 17–41. ISBN: 978-90-481-3643-8. doi: 10.1007/978-90-481-3643-8\_3.
- [13] Larry Kaufman and Henry L. Bernstein. “Computer calculation of phase diagrams with special reference to refractory metals.” In: 1970. ISBN: 0-12-402050-X.
- [14] Sung S. Kim and T.H. Sanders. “Phase-field simulation of spinodal phase separation in the Na<sub>2</sub>O–SiO<sub>2</sub> glasses.” In: *Journal of Non-Crystalline Solids* 528 (Jan. 2020), p. 119591. doi: 10.1016/j.jnoncrysol.2019.119591.
- [15] Arka Lahiri, T. A. Abinandanan, and Abhik Choudhury. “Theoretical and Numerical Study of Growth in Multi-Component Alloys.” In: *Metallurgical and Materials Transactions A* 48 (10 Oct. 2017), pp. 4463–4476. ISSN: 1543-1940. doi: 10.1007/s11661-017-4215-6.
- [16] Romain Le Tellier and Werner Verdier. [https://www-git-cad.intra.cea.fr/DTN/sivit/these\\_werner\\_verdier/-/tree/werner](https://www-git-cad.intra.cea.fr/DTN/sivit/these_werner_verdier/-/tree/werner). GitLab intranet Cadarache. 2021.
- [17] I.M. Lifshitz and V.V. Slyozov. “The kinetics of precipitation from supersaturated solid solutions.” In: *Journal of Physics and Chemistry of Solids* 19.1 (1961), pp. 35–50. ISSN: 0022-3697. doi: [https://doi.org/10.1016/0022-3697\(61\)90054-3](https://doi.org/10.1016/0022-3697(61)90054-3).
- [18] P. Maugis et al. “Multiple interface velocity solutions for ternary biphasic infinite diffusion couples.” In: *Acta Materialia* 45.5 (1997), pp. 1941–1954. ISSN: 1359-6454. doi: 10.1016/S1359-6454(96)00321-7.
- [19] Keith O’Hara. *OptimLib: a lightweight C++ library of numerical optimization methods for nonlinear functions*. <https://github.com/kthohr/optim>. 2021.
- [20] H. Pablo et al. “Multicomponent diffusion in sodium borosilicate glasses.” In: *Journal of Non-Crystalline Solids* 478 (2017), pp. 29–40. ISSN: 0022-3093. doi: <https://doi.org/10.1016/j.jnoncrysol.2017.10.001>.

- [21] Hélène Pablo. “Diffusion chimique dans les verres borosilicates d’intérêt nucléaire.” 2017MNH0014. PhD thesis. 2017.
- [22] William H. Press et al. *Numerical Recipes 3rd Edition: The Art of Scientific Computing*. 3rd ed. USA: Cambridge University Press, 2007. Chap. 15-5, pp. 799–806. ISBN: 0521880688.
- [23] Hamed Ravash et al. “Three-dimensional phase-field study of grain coarsening and grain shape accommodation in the final stage of liquid-phase sintering.” In: *Journal of the European Ceramic Society* 37.5 (2017), pp. 2265–2275. ISSN: 0955-2219. DOI: <https://doi.org/10.1016/j.jeurceramsoc.2017.01.001>.
- [24] Eric D. Siggia. “Late stages of spinodal decomposition in binary mixtures.” In: *Phys. Rev. A* 20 (2 Aug. 1979), pp. 595–605. DOI: 10.1103/PhysRevA.20.595.
- [25] Bo Sundman et al. “The OpenCalphad thermodynamic software interface.” In: *Computational Materials Science* 125 (2016), pp. 188–196. ISSN: 0927-0256. DOI: <https://doi.org/10.1016/j.commatsci.2016.08.045>.
- [26] Vaishnvi Tiwari. “A consistent approach for coupling lumped-parameter and phase-field models for in-vessel corium to thermodynamic databases.” Theses. Université Paris Saclay (COMUE), Nov. 2019.
- [27] Werner Verdier. *Modèle à champ de phase pour verres ternaires diphasiques*. Note technique DES STMF/LMSF/NT/2021-67858 (CEA internal technical report). 2021.
- [28] Werner Verdier, Pierre Kestener, and Alain Cartalade. “Performance portability of lattice Boltzmann methods for two-phase flows with phase change.” In: *Computer Methods in Applied Mechanics and Engineering* 370 (2020), p. 113266. ISSN: 0045-7825. DOI: <https://doi.org/10.1016/j.cma.2020.113266>.
- [29] Werner Verdier et al. “Coupling a grand potential ternary phase field model to the thermodynamic landscape of the Na<sub>2</sub>O-SiO<sub>2</sub>-MoO<sub>3</sub> nuclear glass.” In: *CALPHAD XLIX* (Skogshem & Wijk, Lidingö, May 22–27, 2022). 2022.
- [30] Pauli Virtanen et al. “SciPy 1.0: Fundamental Algorithms for Scientific Computing in Python.” In: *Nature Methods* 17 (2020), pp. 261–272. DOI: 10.1038/s41592-019-0686-2.
- [31] K.G. Wang et al. “A comparison of theory and simulation with microgravity experiments on phase coarsening.” In: *Acta Materialia* 221 (2021), p. 117402. ISSN: 1359-6454. DOI: <https://doi.org/10.1016/j.actamat.2021.117402>.
- [32] Rafael Wiemker. “Total Euler Characteristic as a Noise Measure to aid Transfer Function Design.” In: *EuroVis - Short Papers*. 2013. ISBN: 978-3-905673-99-9. DOI: 10.2312/PE.EuroVisShort.EuroVisShort2013.097-101.
- [33] Ryo Yamada, Haruki Inubushi, and Munekazu Ohno. “Ostwald ripening under temperature gradient: A phase-field study.” In: *Journal of Applied Physics* 130.1 (2021), p. 015109. DOI: 10.1063/5.0055198.
- [34] Y. Q. Zu and S. He. “Phase-field-based lattice Boltzmann model for incompressible binary fluid systems with density and viscosity contrasts.” In: *Phys. Rev. E* 87 (4 Apr. 2013), p. 043301. DOI: 10.1103/PhysRevE.87.043301.

# Conclusion

## Summary

This thesis has set up a framework for the modelling and the simulation of the phase separation of a ternary nuclear glass in the nucleation and growth regime, like the one observed experimentally in the model  $\text{Na}_2\text{O}-\text{SiO}_2-\text{MoO}_3$  glass. The model relies on the phase field theory to produce a representation of the interface that is both thermodynamically consistent and numerically convenient. We have reinforced this thermodynamic aspect by extending a grand potential formalism to the case of the diffusion of three chemical species, and by deriving the associated Gibbs-Thomson condition acting at the interface with an asymptotic analysis. The Navier-Stokes equations were coupled to the phase field and chemical diffusion equations to account for the fluid flow during a liquid-liquid phase separation.

We exploited the simplicity of the diffuse interface model to formulate a parallel and highly efficient numerical implementation. This was done by discretizing our set of partial differential equations following the lattice Boltzmann method, a numerical technique particularly well adapted to the diffusion-type equations making up our model, and also easy to implement and very efficient on parallel computer architectures, including modern multi-GPU architectures on HPC clusters. To that goal, we have used and continued the development of `LBM_saclay`, a C++ simulation code with high portable performance enabled by the Kokkos library. This allowed us to carry out simulations on a desktop machine with a multithreaded CPU, a small multi-CPU cluster of our department, or the national IDRIS Jean-Zay multi-GPU cluster with a single codebase.

With these theoretical and numerical tools ready, we have conducted numerical simulations that first asserted the validity of the model and of its discretization by comparison of numerical results and known analytical solutions for specific test cases. We then built a specific test case, the diffusion-controlled growth of droplets, as a first comparison point to experimental observations of the real nuclear glass. Simulations proved to produce the expected power-law in time for average radius during the growth regime with an exponent dependent on the flow properties. A 3D simulation with a buoyancy-driven flow showed the onset of an additional crossover in the power law; the phenomenology of an accelerated coalescence of droplets due to their sedimentation, which may be of interest during experiments because of the presence of the relatively heavy molybdenum in the glass; and the high parallel efficiency achievable by our numerical simulations.

Our work thus yielded both theoretical and numerical progress, with the establishment of an original model, its discretization, its implementation under constraint of high performance, the identification of a test case relevant to the object of study and its simulation. We were also regularly involved in discussions with experimentalists of the CEA Marcoule to prepare applications close to the real nuclear glass. While this could not be achieved within the time frame of this thesis, we are confident that our model will be soon able to answer this challenge since we have proven that the growth phenomenology is coherently simulated and because we have laid out the methodology of coupling to the thermodynamics of the  $\text{Na}_2\text{O}-\text{SiO}_2-\text{MoO}_3$  compound.

## Openings

We have identified many possible extensions on almost every aspect of the model and its simulation, with most of them listed in the conclusion of each chapter. The most urgent point to examine further is the coupling to the available Calphad data of the  $\text{Na}_2\text{O}-\text{SiO}_2-\text{MoO}_3$  material. This involves inserting non-trivial matrices of free energy second derivatives (and possibly non-trivial matrices of chemical mobilities) which we have assessed to challenge the stability of our numerical scheme. Solving this issue will be a big step towards the description to the real glass.

Possible extensions on the phase field modelling would for example be a stronger formulation of the Navier-Stokes coupling by rederiving the associated equations from a free energy functional. The definition of an additional intensive thermodynamic field, the temperature, would also be interesting and relatively easy to implement, as it only consists of extending the Onsager formalism. We may also consider more complicated cases in the asymptotic expansion of the model, for instance by describing the errors (and possible corrections of these errors) due to asymmetric chemical mobilities, the asymptotic behaviour of the flow, and asserting if more elaborate interpolations are necessary with the previously mentioned matrices. On the numerical side, we may want to reinforce the stability of the LBM scheme by using a more elaborate collision operator; this could end up being necessary if measurements of the properties of the glass reveal high viscosity or diffusivity contrasts between the phases.

A very interesting modelling extension we have kept for last concerns the relaxation of the hypothesis of identical and constant molar volumes, which would notably create a back-coupling of the diffusion equations to the flow equations. In complement of the application to the real glass, this is one of the subjects of a new thesis currently starting which will continue the present work. Moreover, the LBM\_saclay code continues to be developed and extended by other students currently performing research with it.

# Acknowledgements

I wish to thank first my two thesis advisors. With their complementary expertise, their disponibility and their goodwill, Alain and Mathis were essential to this research and it has been a pleasure to work with them both. I also wish to thank the reviewers and the defense jury for taking the time to evaluate my work and for their valuable remarks and corrections.

Many thanks to the CEA researchers of the SIVIT project, notably Romain Le Tellier, Paul Fossati, Stéphane Gossé, Sophie Schuller and the researchers of the LDPV laboratory for their ongoing work on the observation furnace which will lead to an experimental application to my modelling. It was always very interesting and refreshing to visit the CEA Marcoule and get a glimpse of the industrial context of my work. I acknowledge the support of SIVIT's industrial partners, EDF and Orano. Thanks also to Pierre for his help on the HPC side and the very welcome advice and motivational support during my studies.

The LMSF was a wonderful workplace, and that was mainly because of my fellow PhD students and friends there. Big thanks to Clément, Mathis, Gabriel, Antonin, Aurore, Aymeric, Raksmy, Nathalie, Loïc, Jiayi and also to Nicolas and Andrew for dragging me out to do some sport; I never imagined I would do any martial art in my life, let alone pass a grade. It was also immensely satisfying and formative to participate in the training of interns and future PhD students: Pauline, Wissam, Téo, Hugo, Théo and also Capucine who is now working on the follow-up of my thesis.

Thank you Sébastien for organizing these evenings in Paris and the vacations in Auvergne, it is so nice to see and stay updated with everyone from Paris Diderot ! And thank you Julien for travelling all the way to the end of the RER B line for my defense.

Shout-outs to Kneg, Dagoth and many others kaeizuka players for the good games.

Thanks to mom and dad for their ever-present support and uncountably many other things. I think the few days spent in Bretagne with you were the best I had during the writing of this manuscript.

## Appendix A

# Asymptotic analysis of the two-phase three components model

The phase-field formalism is an alternative to the sharp-interface models for the description of systems with free interfaces. However, the implicitness of the interface means it is not possible to freely and directly choose the boundary condition that acts in it (in the following, we will name such a boundary condition an "interface condition").

Having explicit interface conditions is physically and mathematically desirable; as such, with the establishment of phase-field methods came a systematic way to draw an interface condition from the phase-field equations. This method, an asymptotic analysis, allows for the deduction of an equivalent sharp-interface formulation for a given phase-field model. These notes attempt to detail a framework for this analysis (in 3D space, for the sake of completeness).

A general outline of the asymptotic analysis is as follows:

1. the definition of an "outer" (far from the interface) and "inner" scale (close to the interface, and the definition of an asymptotic parameter  $\varepsilon$  as the ratio of both, qualifying the "thinness" of the interface.
2. The definition of a curvilinear system in the inner region so that the analysis may apply to any arbitrary interface shape. The differential operators  $\partial_t$  and  $\nabla$  must be given an expression in this system, and the curvatures describing the interface are expanded in the manner as in 1.
3. The expansion of the field variables and of the differential operators in terms of  $\varepsilon$  in both regions. In the inner region, the interface's geometry (curvature and velocity) are also expanded.
4. Once both the inner and outer expansions of the PDEs are laid out they are matched to each other using a set of relations known as the matching conditions. This matching will yield the interface conditions.

These notes will follow the above outline. Each step will be carried on the ternary model based on the grand potential with a mixed formulation without flow, a subset of the full model presented in sec. 1.3. We will write it

$$\tau \partial_t \varphi = W^2 \nabla^2 \varphi - f'_{\text{dw}}(\varphi) + \lambda p'(\varphi) (\omega_L(\mu^A, \mu^B) - \omega_R(\mu^A, \mu^B)), \quad (\text{A.0.1})$$

$$\partial_t c^\alpha = M^\alpha \nabla \cdot (q^\alpha(\varphi) \nabla \mu^\alpha), \quad (\text{A.0.2})$$

$$c^\alpha = -(\tilde{p}(1 - \varphi) \partial_\alpha \omega_L + \tilde{p}(\varphi) \partial_\alpha \omega_R). \quad (\text{A.0.3})$$

We used the same notation as in sec. 1.3 with some changes:



- the relaxation rate  $\tau = W^2/M_\varphi$  replaces the phase field mobility  $M_\varphi$ ,
- the two phases are identified with the indices  $L$  (“left phase”) and  $R$  (“right phase”) to avoid confusion with the latter expansion order indices,
- we will use exponent indices instead of vector notations for the component-space variables. The chemical mobility matrix is assumed to be diagonal with coefficients  $M^\alpha$  with  $\alpha = A, B$ ,
- in addition, the mobility coefficients of each phase and through the interface is written as an interpolation around a mean value  $M^\alpha$ , with the interpolation polynomial  $q^\alpha(\varphi)$ ,
- the quantities  $\omega_L, \omega_R, \mu^\alpha$  and  $M^\alpha$  are implicitly used in their dimensionless form. We have dropped the bar notation when removing the energy dimensions because we will use it instead for the non-dimensionalization proper to the asymptotic analysis,
- we write the derivative with respect the chemical potential  $\mu^\alpha$  as  $\partial/\partial\mu^\alpha = \partial_\alpha$ ,
- for the sake generality, we define two energy interpolation functions  $p(\varphi)$  and  $\tilde{p}(\varphi)$  even though the derivation of the model from a grand potential functional requires only one.

The asymptotics will show that this model reconstructs the general Gibbs-Thomson interface condition

$$\Delta\omega = -\delta K - \beta V_n, \quad (\text{A.0.4})$$

with  $\Delta\omega = \omega_L - \omega_R$ ,  $K$  the mean curvature of the interface,  $V_n$  its normal velocity, and  $\delta, \beta$  two coefficients that will be related to the phase field parameters and understood physically as the capillary length and the kinetic coefficient, respectively.

## A.1 Sharp- and thin-interface limit, rescaling

The first step in the asymptotic analysis is to define its expansion parameter  $\varepsilon$ . A first option is to define

$$\varepsilon = W/L \quad (\text{A.1.1})$$

with  $L$  the smallest characteristic length in the problem.

Karma and Rappel [6] proposed that the previous definition puts a numerical constraint too high on the limit  $\varepsilon \rightarrow 0$ . Thus, as an alternative to this “sharp-interface” limit, they instead introduce the “thin-interface” limit with

$$\varepsilon = WV_n/D \quad (\text{A.1.2})$$

with  $V_n$  the normal velocity of the interface and  $D$  a characteristic value for the diffusion coefficients in the model. Equivalently, this is  $\varepsilon = W/\ell_D$  with  $\ell_D = M/V_n$ , the length of the diffusion layer in the coupled model. Note that this definition supposes the existence of such  $V_n$  or  $\ell_D$ . This scale is intrinsic to the physical problem studied and not to the model itself. It might not even be properly defined: in the diffusion couple, the simplest setup possible of a two-phase problem, the interface velocity is unbounded at  $t = 0$ .

To reveal  $\varepsilon$  in the equations, we apply a diffusive rescaling: we measure lengths in units of  $\ell_D$  and time in units of  $t_D = \ell_D^2/D$ . This means defining the dimensionless differential operators

$$\bar{\nabla} = \ell_D \nabla = \varepsilon^{-1} W \nabla, \quad (\text{A.1.3})$$

$$\bar{\partial}_t = \frac{\ell_D^2}{D} \partial_t = \varepsilon^{-2} \frac{W^2}{D} \partial_t, \quad (\text{A.1.4})$$

and rewriting the model as

$$\varepsilon^2 \frac{D}{W^2} \tau \bar{\partial}_t \varphi = \varepsilon^2 \bar{\nabla}^2 \varphi - f'_{\text{dw}}(\varphi) + \lambda p'(\varphi) \Delta \omega, \quad (\text{A.1.5})$$

$$\varepsilon^2 \bar{\partial}_t c^\alpha = \varepsilon^2 \frac{M^\alpha}{D} \bar{\nabla} \cdot (q^\alpha(\varphi) \bar{\nabla} \mu^\alpha). \quad (\text{A.1.6})$$

The fraction  $D/W^2$  was simplified out of the diffusion equation. However, it is important to keep the  $\varepsilon^2$  in, so that both equations' orders stay coherent.

Later, Echebarria et. al. [3] argued that the thin-interface limit is not entirely coherent. The expansion parameter  $WV_n/D$  describes a limit of “small” interface velocity, but it does not capture the assumption of small curvature, necessary in section A.2. In addition, the fact that both the double-well term and the coupling term  $\lambda p'(\varphi)u$  fall at the same order can be questionable. Before the energy dimensions were stripped from the phase field equation, it was seen that the double-well term was of characteristic scale  $H$ , while a scale for the thermodynamic free energy offset between the phases at equilibrium,  $\Delta F_{th}$ , can be extracted from the coupling term. One can argue that the most rigorous asymptotic limit is the energy constraint

$$\frac{\Delta F_{th}}{H} \ll 1 \quad (\text{A.1.7})$$

ie. the dynamic issued from the thermodynamic functions should not disturb the double-well structure, responsible for the separation of phases. This is also consistent with the mathematical process of a perturbative calculation: knowing the solution of the phase field equation with a zero coupling term, we look for solutions with non-zero but asymptotically small coupling term by expanding around the zero coupling solution, translating (A.1.7) into

$$|\lambda \mu^\alpha| \ll 1. \quad (\text{A.1.8})$$

In summary, it is reasonable to expect an order of difference between the double-well and coupling term.

Coincidentally, this order of difference can appear in the sharp-interface limit. Instead of the previous rescaling, measure lengths in units of the capillary length  $\delta$ , a physical length intrinsic to the problem studied, time in units of  $\delta^2/D$ , and specify the expansion parameter as

$$\varepsilon = W/\delta. \quad (\text{A.1.9})$$

More importantly, remember that  $\lambda$  is defined as  $H/k$ , the ratio of the double-well height and a characteristic energy density scale  $k$  extracted from the free energy functions. We also know that  $H = 3\sigma/2W$ , meaning

$$\lambda = \frac{2}{3} \frac{kW}{\sigma} = \frac{2}{3} \frac{k\delta}{\sigma} \varepsilon. \quad (\text{A.1.10})$$

We can then increase the order in  $\varepsilon$  of the coupling term by a change of variable in  $\lambda$  or in the diffusion field  $u$ . Choose the former, with

$$\lambda^* = \frac{2}{3} \frac{k\delta}{\sigma} = \varepsilon^{-1} \lambda \quad (\text{A.1.11})$$

so that the dimensionless model becomes

$$\varepsilon^2 \frac{D}{W^2} \tau \bar{\partial}_t \varphi = \varepsilon^2 \bar{\nabla}^2 \varphi - f'_{\text{dw}}(\varphi) + \varepsilon \lambda^* p'(\varphi) \Delta \omega, \quad (\text{A.1.12})$$

$$\varepsilon^2 \bar{\partial}_t c^\alpha = \varepsilon^2 \frac{M^\alpha}{D} \bar{\nabla} \cdot (q^\alpha(\varphi) \bar{\nabla} \mu^\alpha). \quad (\text{A.1.13})$$

The change of variable (A.1.11) can feel unsatisfying, as it seemingly only serves to “artificially” increase the order of the coupling term. Furthermore, the expansion parameter (A.1.9) can be confusing, as  $\delta$  defines the asymptotic limit but will also be given an expression in terms of the phase field

parameters through the reconstructed Gibbs-Thomson interface condition. Ultimately, one must accept that these manipulations are only a mathematical convenience to fit the sharp-interface view with the real limit (A.1.7) on the energy scales: this way, one does not have to presuppose the form of the free energy functions to explicit the expansion parameter, and one can reuse the sharp-interface calculations as done in [1] (for example).

Note that  $\varepsilon$  is then not a conventional asymptotic parameter since  $\varepsilon \ll 1$  is not necessary (coherent with Karma and Rappel's thin interface limit), but it allows rewriting (A.1.8) as

$$\varepsilon |\lambda^* u| \ll 1. \quad (\text{A.1.14})$$

If we take for granted the reconstructed interface condition (A.0.4), we can give an order of magnitude for the l.h.s. of the previous relation:

$$\varepsilon \lambda^* u \sim \varepsilon (-\delta K - \beta V_n + W V_n / D), \quad (\text{A.1.15})$$

where the first two terms are the Gibbs-Thomson condition and the third term a dimensionless order of magnitude (Péclet number) of the diffusion inside the interface region. After substituting  $\varepsilon$  by its definition, the limit (A.1.14) becomes

$$WK + \frac{W V_n}{D} \left( \frac{\beta D}{\delta} + \frac{W}{\delta} \right) \ll 1. \quad (\text{A.1.16})$$

It is seen that the energy criterion then reduces to two constraints on  $W$ : the geometrical constraint of the interface width being much smaller than the radius of curvature, and a second thin-interface constraint on the interface being much more thin than the physical diffusion layer.

With this in mind, we will use the sharp-interface limit with  $\varepsilon = W/\delta$  in the rest of these notes.

## A.2 Inner region, curvilinear coordinates

To continue with the analysis, the physical space is split into two regions. The first region is the one inside the diffuse interface ; it is equivalent to the region close to the isocontour  $\{\hat{x} | \varphi(\hat{x}) = 1/2\}$  provided that the interface's radius of curvature is always much larger than  $W$  [4]. Additionally, "close" is understood as examining distances much closer than the radius of curvature of interface.

To follow the shape of the interface in the inner region, define the 3-dimesional orthogonal curvilinear coordinate system  $(r, s_1, s_2)$ , with  $r$  the normal signed distance to the interface and  $s_1, s_2$  the two tangential coordinates<sup>1</sup> along the interface (from some indeterminate origin). We take the convention that  $r$  is positive toward the  $\varphi = 1$  side, and note the unit vectors associated to each coordinate as  $\hat{n}, \hat{s}_1$  and  $\hat{s}_2$ .

### A.2.1 Scale factors and differential operators

With orthogonal coordinates, the spatial differential operators are redefined using their scale factors. In our case, these are

$$h_n = 1, \quad (\text{A.2.1})$$

$$h_{s_1} = |1 + \kappa_1 r|, \quad (\text{A.2.2})$$

$$h_{s_2} = |1 + \kappa_2 r|, \quad (\text{A.2.3})$$

---

<sup>1</sup>In the example model used here, a reference tangential direction can be defined by the diffusive flux  $-D\nabla u$  across the interface. It may be convenient to align  $\hat{s}_1$  or  $\hat{s}_2$  on this direction [2], but we chose not to do that here for generalization's sake and because our ternary model has two, possibly unaligned diffusive fluxes.

with  $\kappa_i$  the principal curvature along  $\hat{s}_i$ . These definitions can also be seen in [5] in the 2D case and with a different sign convention. For a generic function  $f(r, s_1, s_2)$  and vector  $\mathbf{a} = a_n \hat{n} + a_{s_1} \hat{s}_1 + a_{s_2} \hat{s}_2$ , the differential operators are

$$\nabla f = \frac{1}{h_n} \partial_r f \hat{n} + \frac{1}{h_{s_1}} \partial_{s_1} f \hat{s}_1 + \frac{1}{h_{s_2}} \partial_{s_2} f \hat{s}_2, \quad (\text{A.2.4})$$

$$\nabla \cdot \mathbf{a} = \frac{1}{h_n h_{s_1} h_{s_2}} \left[ \partial_r (h_{s_1} h_{s_2} a_n) + \partial_{s_1} (h_n h_{s_2} a_{s_1}) + \partial_{s_2} (h_n h_{s_1} a_{s_2}) \right], \quad (\text{A.2.5})$$

which expand to

$$\nabla f = \partial_r f \hat{n} + \frac{1}{|1 + \kappa_1 r|} \partial_{s_1} f \hat{s}_1 + \frac{1}{|1 + \kappa_2 r|} \partial_{s_2} f \hat{s}_2, \quad (\text{A.2.6})$$

$$\nabla \cdot \mathbf{a} = \partial_r a_n + \Delta r a_n + \frac{1}{|1 + \kappa_1 r|} \partial_{s_1} a_{s_1} + \frac{1}{|1 + \kappa_2 r|} \partial_{s_2} a_{s_2}. \quad (\text{A.2.7})$$

with  $\Delta r = (2\kappa_1 \kappa_2 + \kappa_1^2 + \kappa_2^2) / (|1 + \kappa_1 r| |1 + \kappa_2 r|)$  (also called the mean curvature in ref. [1]).

We will use these coordinates to describe regions close to the interface, at a distance much smaller than the radii of curvature. We write these limits as  $\kappa_1 |r| \ll 1$  and  $\kappa_2 |r| \ll 1$ , and with them, we can strip the absolute values from the scale factors and use the following Taylor series expansion for  $1/h_i$  with respect to  $\kappa_1 r$  and  $\kappa_2 r$ :

$$\frac{1}{(1 + \kappa_i r)^n} = 1 - n \kappa_i r + O(r^2) \quad i = 1, 2. \quad (\text{A.2.8})$$

We have stopped at the first order. The orders above are all  $O(r^2)$  and these terms will be ignored, the reason being is that they become high order terms ( $O(\varepsilon^3)$ ) when expanded.

Furthermore, the term  $\Delta r$  on the r.h.s. of eq. (A.2.7) can be simplified by considering the total and Gaussian curvature, respectively

$$K = \kappa_1 + \kappa_2, \quad (\text{A.2.9})$$

$$\Pi = \kappa_1 \kappa_2, \quad (\text{A.2.10})$$

with which it becomes

$$\Delta r = \frac{1}{r} \frac{Kr + 2\Pi r^2}{1 + Kr + \Pi r^2}. \quad (\text{A.2.11})$$

The previous limit implies  $Kr \ll 1$  and  $\Pi r^2 \ll 1$ . Using again a Taylor series on the second denominator (with respect to  $Kr$  and  $\Pi r^2$ ), the mean curvature is simplified as

$$\Delta r = K(1 - Kr) + 2\Pi r + O(r^2). \quad (\text{A.2.12})$$

The expansion was also done until the first order, and the  $O(r^2)$  terms removed (one can check that the removed first orders terms would've become  $-3\Pi K r^2 - 2\Pi^2 r^3$ ).

The expressions (A.2.6) and (A.2.7) for the spatial operators become

$$\nabla f = \partial_r f \hat{n} + \sum_{i=1,2} (1 - \kappa_i r) \partial_{s_i} f \hat{s}_i + O(r^2), \quad (\text{A.2.13})$$

$$\nabla \cdot \mathbf{a} = \partial_r a_n + [K(1 - Kr) + 2\Pi r] a_n + \sum_{i=1,2} (1 - \kappa_i r) \partial_{s_i} a_{s_i} + O(r^2). \quad (\text{A.2.14})$$

The interface is in movement with a velocity we will write  $\mathbf{V}$ . The Eulerian time derivative  $\partial_t$  is thus linked to the Lagrangian derivative  $D_t$  through

$$D_t = \partial_t + \mathbf{V} \cdot \nabla. \quad (\text{A.2.15})$$

### A.2.2 Stretched normal coordinate and diffusive scaling

The curvilinear coordinates are tied to the asymptotics by defining the stretched normal coordinate

$$\rho = \varepsilon^{-1}r \quad (\text{A.2.16})$$

and applying the diffusive scaling on all geometrical quantities, defining

$$\bar{\rho} = \rho/\ell_D = \varepsilon\rho/W, \quad (\text{A.2.17})$$

$$\bar{s}_i = s_i/\ell_D = \varepsilon s_i/W, \quad (\text{A.2.18})$$

$$\bar{\kappa}_i = \ell_D \kappa_i = \varepsilon^{-1}W\kappa_i, \quad (\text{A.2.19})$$

$$\bar{K} = \ell_D K = \varepsilon^{-1}WK, \quad (\text{A.2.20})$$

$$\bar{\Pi} = \ell_D^2 \Pi = \varepsilon^{-2}W^2\Pi, \quad (\text{A.2.21})$$

$$\bar{V}_n = \ell_D V_n/D, \quad (\text{A.2.22})$$

$$\bar{V}_{s_i} = \ell_D V_{s_i}/D. \quad (\text{A.2.23})$$

With those definitions and the expressions for the curvilinear differential operators (A.2.6), (A.2.7), (A.2.15), the scaled operators (A.1.3), (A.1.4) become

$$\bar{\nabla} f = \varepsilon^{-1} \partial_{\bar{\rho}} f \hat{n} + \sum_{i=1,2} \left\{ \partial_{\bar{s}_i} f - \varepsilon \bar{\kappa}_i \bar{\rho} \partial_{\bar{s}_i} f \right\} \hat{s}_i + O(\varepsilon^2) \quad (\text{A.2.24})$$

$$\bar{\nabla} \cdot \mathbf{a} = \varepsilon^{-1} \partial_{\bar{\rho}} a_n + \left( \bar{K} a_n + \sum_{i=1,2} \partial_{\bar{s}_i} a_{s_i} \right) + \varepsilon \left( [2\bar{\Pi} - \bar{K}^2] \bar{\rho} a_n - \sum_{i=1,2} \bar{\kappa}_i \bar{\rho} \partial_{\bar{s}_i} a_{s_i} \right) + O(\varepsilon^2) \quad (\text{A.2.25})$$

$$\partial_{\bar{t}} f = -\varepsilon^{-1} \bar{V}_n \partial_{\bar{\rho}} f - \sum_{i=1,2} \bar{V}_{s_i} \partial_{\bar{s}_i} f + D_{\bar{t}} f + \varepsilon \sum_{i=1,2} \bar{V}_{s_i} \bar{\kappa}_i \bar{\rho} \partial_{\bar{s}_i} f + O(\varepsilon^2) \quad (\text{A.2.26})$$

with  $D_{\bar{t}} = t_D D_t$ .

### A.3 Expansions and matching conditions

In the outer and inner region, the PDEs and their variables will be expanded separately with respect to  $\varepsilon$ . We will write  $\varphi_n$  and  $\Phi_n$  with  $n = 0, 1, 2, \dots$  the outer and inner phase field variable respectively;  $\mu_n^\alpha$  and  $\nu_n^\alpha$  the outer and inner chemical potentials; and  $c_n^\alpha$  and  $C_n^\alpha$  the outer and inner compositions. In the inner region, the curvatures  $\bar{K}_n$ ,  $\bar{\kappa}_{i,n}$  and  $\bar{\Pi}_n$  will also be expanded.

To obtain the interface condition, we will match both sets of PDEs using the matching conditions below, in the example of the phase field variables:

$$\lim_{\rho \rightarrow \pm\infty} \Phi_0(\rho, s) = \varphi_0(0^\pm, s), \quad (\text{A.3.1})$$

$$\Phi_1(\rho, s) \sim \varphi_1(0^\pm, s) + \rho \partial_r \varphi_0(0^\pm, s) \quad \text{as } \rho \rightarrow \pm\infty, \quad (\text{A.3.2})$$

$$\Phi_2(\rho, s) \sim \varphi_2(0^\pm, s) + \rho \partial_r \varphi_1(0^\pm, s) + \frac{1}{2} \rho^2 \partial_{rr} \varphi_0(0^\pm, s) \quad \text{as } \rho \rightarrow \pm\infty. \quad (\text{A.3.3})$$

We refer the reader the book by Fife [4] for their justification.

## A.4 Expansion and analysis of the ternary model

We remind below the PDE model studied:

$$\tau \partial_t \varphi = W^2 \nabla^2 \varphi - f'_{\text{dw}}(\varphi) + \lambda p'(\varphi)(\omega_L(\mu^A, \mu^B) - \omega_R(\mu^A, \mu^B)), \quad (\text{A.4.1})$$

$$\partial_t c^\alpha = M^\alpha \nabla \cdot (q^\alpha(\varphi) \nabla \mu^\alpha), \quad (\text{A.4.2})$$

$$c^\alpha = -(\tilde{p}(1 - \varphi) \partial_\alpha \omega_L + \tilde{p}(\varphi) \partial_\alpha \omega_R), \quad (\text{A.4.3})$$

As mentioned before, we assume the existence of a characteristic diffusion length scale  $\ell_D$  and we will define the characteristic diffusion time as  $t_D = \ell_D^2/D$ , here with  $D = \sqrt{M^A M^B}$ . With these, we can write right away the model in the outer region:

$$\partial_t c^\alpha_i = \frac{M^\alpha_{\{L,R\}}}{D} \bar{\nabla}^2 \mu^\alpha_i \quad \forall i = 0, 1, 2, \dots, \quad (\text{A.4.4})$$

$$c^\alpha_0 = -\partial_\alpha \omega_{\{L,R\}}, \quad (\text{A.4.5})$$

$$c^\alpha_1 = -\sum_{\beta=A,B} \mu^\beta_1 \partial_{\beta\alpha} \omega_{\{L,R\}}, \quad (\text{A.4.6})$$

with  $M^\alpha_{\{L,R\}} = M^\alpha q^\alpha(\{0, 1\})$ . The  $O(\varepsilon^2)$  order of the closure relation will not be useful in the calculations. In the outer region, where  $\varphi = 0$  or  $\varphi = 1$ , the phase field equation reduces to zero. The inner expansions are longer to detail and each order is presented in the following subsections.

### A.4.1 Phase-field $O(1)$

Take eq. (A.4.1) and substitute  $\varphi$  for its inner expansion  $\Phi_0 + \varepsilon \Phi_1 + \varepsilon^2 \Phi_2 + O(\varepsilon^3)$  (the same for  $\mu^\alpha$ ), and replace the differential operator with their dimensionless, expanded equivalents in the curvilinear coordinates as given by eqs. (A.2.24)–(A.2.26). After reassembling all the terms not proportional to  $\varepsilon$  or its powers, one is left with only

$$f'_{\text{dw}}(\Phi_0) = \partial_{\bar{\rho}\bar{\rho}} \Phi_0 \quad (\text{A.4.7})$$

telling us that the usual hyperbolic tangent profile

$$\Phi_0(\bar{\rho}) = \frac{1}{2}(1 + \tanh 2\bar{\rho}) \quad (\text{A.4.8})$$

is the zeroth-order solution in the inner region.

### A.4.2 Diffusion and closure $O(1)$

Doing the same on the diffusion equation (A.4.2) and on the closure relation (A.4.3) gives

$$\partial_{\bar{\rho}}(q^\alpha(\Phi_0) \partial_{\bar{\rho}} \nu^\alpha_0) = 0, \quad (\text{A.4.9})$$

$$C^\alpha_0 = -(\tilde{p}(1 - \Phi_0) \partial_\alpha \omega_L + \tilde{p}(\Phi_0) \partial_\alpha \omega_R). \quad (\text{A.4.10})$$

We'll infer from (A.4.9) that  $\nu^\alpha_0$  take constant values for all  $\bar{\rho}$ . The 0th order composition then interpolates between two constant values following (A.4.10). Matching to the outer variables using (A.3.1) tells us

$$\nu^\alpha_0 = \mu^\alpha_0(0^\pm, \bar{s}_1, \bar{s}_2), \quad (\text{A.4.11})$$

$$-\partial_\alpha \omega_{\{R,L\}}(\nu^A_0, \nu^B_0) = c^\alpha_0(0^\pm, \bar{s}_1, \bar{s}_2) = -\partial_\alpha \omega_{\{R,L\}}(\mu^A_0(0^\pm, \bar{s}_1, \bar{s}_2), \mu^B_0(0^\pm, \bar{s}_1, \bar{s}_2)), \quad (\text{A.4.12})$$

Note that since the leftmost term of (A.4.12) are constants, we can strip the dependence on the  $\bar{s}_i$  on the right terms. Those relations are consistent with the thermodynamic equilibrium of a multi-component system: the outer compositions left and right of the interface are given by identical slopes of  $\omega_0$  and  $\omega_1$ , *ie.* identical chemical potentials, at values  $\nu^A_0$  and  $\nu^B_0$ . Remark that since we study a ternary system, the phase co-existence tuple  $(\nu^A_0, \nu^B_0)$  is not unique and depends on the tie-line taken by the system in its phase diagram.

### A.4.3 Phase-field $O(\varepsilon)$

We now assemble all terms proportional to  $\varepsilon$  after the expansion. This gives

$$\mathcal{L}\Phi_1 + \lambda p'(\Phi_0)\Delta\omega_0 + (\bar{K}_0 + m\bar{V}_{n,0})\partial_{\bar{\rho}}\Phi_0 = 0 \quad (\text{A.4.13})$$

with the linear differential operator  $\mathcal{L} = \partial_{\bar{\rho}\bar{\rho}} - f''_{\text{dw}}(\Phi_0)$  and the notations  $\Delta\omega_i = \omega_0(\nu^A_i, \nu^B_i) - \omega_1(\nu^A_i, \nu^B_i)$  and  $m = \tau D/W^2$ . The solvability condition is

$$\Delta\omega_0(\nu^A_0, \nu^B_0) = -\frac{I}{\lambda J}\bar{K}_0 - \frac{Im}{\lambda J}\bar{V}_{n,0}, \quad (\text{A.4.14})$$

the expected Gibbs-Thomson condition at first order, with the integrals

$$I = \int_0^1 \partial_{\bar{\rho}}\Phi_0 d\Phi_0 = 2/3, \quad (\text{A.4.15})$$

$$J = \int_{-\infty}^{+\infty} \partial_{\bar{\rho}}(p(\Phi_0)) d\bar{\rho} = 1. \quad (\text{A.4.16})$$

Note here again the consistency with the thermodynamic equilibrium: for a static plane interface,  $\omega_L = \omega_R$  at the 0th order in  $\nu^\alpha$ , as in the common tangent plane construction. As for non-equilibrium, remember that the tuple  $(\nu^A_0, \nu^B_1)$  is constant but not unique, and thus the values of 0th order curvature and interface velocity will also depend on the choice of tie-line. The converse might be more intuitive: the system allows a spectrum of non-equilibrium thermodynamic states depending on curvature and speed of its interface.

For  $\Phi_1$ , we have then

$$\Phi_1 = \Delta\omega_0 \mathcal{L}^{-1} \left( \partial_{\bar{\rho}}\Phi_0 - \frac{I}{J}p'(\Phi_0) \right), \quad (\text{A.4.17})$$

which vanishes when using  $p(\varphi) = 3\varphi^2 - 2\varphi^3$ .

### A.4.4 Diffusion and closure $O(\varepsilon)$

$$\frac{M^\alpha}{D} \partial_{\bar{\rho}}(q^\alpha(\Phi_0)\partial_{\bar{\rho}}\nu^\alpha_1) = -\bar{V}_{n,0}\tilde{p}'(\Phi_0)(\partial_{\bar{\rho}}\Phi_0)\partial_\alpha\Delta\omega_0, \quad (\text{A.4.18})$$

$$C^\alpha_1 = \Phi_1\tilde{p}'(\Phi_0)\partial_\alpha\Delta\omega_0 - \sum_{\beta=A,B} \nu^\beta_1(\tilde{p}(1-\Phi_0)\partial_{\beta\alpha}\omega_L + \tilde{p}(\Phi_0)\partial_{\beta\alpha}\omega_R). \quad (\text{A.4.19})$$

Integrate (A.4.18) once,

$$q^\alpha(\Phi_0)\partial_{\bar{\rho}}\nu^\alpha_1 = \frac{A}{M^\alpha/D} - \frac{\bar{V}_{n,0}}{M^\alpha/D}\tilde{p}(\Phi_0)\partial_\alpha\Delta\omega_0, \quad (\text{A.4.20})$$

and twice

$$\nu_1^\alpha = \nu_*^\alpha + \frac{A}{M^\alpha/D} \int_0^{\bar{\rho}} \frac{d\sigma}{q^\alpha(\Phi_0(\sigma))} - \frac{\bar{V}_{n,0}}{M^\alpha/D} (\partial_\alpha \Delta\omega_0) \int_0^{\bar{\rho}} \frac{\tilde{p}(\Phi_0(\sigma))}{q^\alpha(\Phi_0(\sigma))} d\sigma, \quad (\text{A.4.21})$$

with  $A$  and  $\nu_*^\alpha$  two integrations constants (actually functions of  $\bar{s}_1$ ,  $\bar{s}_2$  and  $\bar{t}$ ).

Next, remember the expression for the far-field expansion of an integral

$$\int_0^a f(x) dx \sim a \lim_{x \rightarrow \pm\infty} f(x) + \int_0^{\pm\infty} \left( f(x) - \lim_{x \rightarrow \pm\infty} f(x) \right) dx + o(1) \quad \text{as } a \rightarrow \pm\infty. \quad (\text{A.4.22})$$

Thus, at  $\bar{\rho} \rightarrow \pm\infty$ , we have

$$\nu_1^\alpha(\bar{\rho}, \bar{s}, \bar{t}) \sim \begin{cases} \left( \frac{A - \bar{V}_{n,0} \partial_\alpha \Delta\omega_0}{M_R^\alpha/D} \right) \bar{\rho} + \left( \nu_*^\alpha + \frac{AG_+^\alpha + \bar{V}_{n,0}(\partial_\alpha \Delta\omega_0) \tilde{F}_+^\alpha}{M^\alpha/D} \right) + o(1) & \text{as } \bar{\rho} \rightarrow +\infty, \\ \left( \frac{A}{M_L^\alpha/D} \right) \bar{\rho} + \left( \nu_*^\alpha + \frac{AG_-^\alpha + (\partial_\alpha \Delta\omega_0) \bar{V}_{n,0} \tilde{F}_-^\alpha}{M^\alpha/D} \right) + o(1) & \text{as } \bar{\rho} \rightarrow -\infty, \end{cases} \quad (\text{A.4.23})$$

with the integrals

$$\begin{aligned} G_+^\alpha &= \int_0^{+\infty} \left( \frac{1}{q^\alpha(\Phi_0)} - \frac{1}{q^\alpha(1)} \right) d\bar{\rho}, & \tilde{F}_+^\alpha &= \int_0^{+\infty} \left( \frac{1}{q^\alpha(1)} - \frac{\tilde{p}(\Phi_0)}{q^\alpha(\Phi_0)} \right) d\bar{\rho} \\ G_-^\alpha &= \int_{-\infty}^0 \left( \frac{1}{q^\alpha(0)} - \frac{1}{q^\alpha(\Phi_0)} \right) d\bar{\rho}, & \tilde{F}_-^\alpha &= \int_{-\infty}^0 \frac{\tilde{p}(\Phi_0)}{q^\alpha(\Phi_0)} d\bar{\rho} \end{aligned} \quad (\text{A.4.24})$$

The asymmetries in the above equations is due to the range  $\varphi \in [0, 1]$  and won't matter in the end. The matching condition (A.3.2) then gives

$$\partial_{\bar{r}} \mu_0^\alpha(0^\pm) = \frac{2A - (1 \pm 1) \bar{V}_{n,0} \partial_\alpha \Delta\omega_0}{2M_{\{R,L\}}^\alpha/D}, \quad (\text{A.4.25})$$

$$\mu_1^\alpha(0^\pm) = \nu_*^\alpha + \frac{AG_\pm^\alpha + (\partial_\alpha \Delta\omega_0) \bar{V}_{n,0} \tilde{F}_\pm^\alpha}{M^\alpha/D}. \quad (\text{A.4.26})$$

Taking the difference of the two cases of (A.4.25) and using the previous matching relations (A.4.12), (A.4.11) to express  $\partial_\alpha \Delta\omega_0$  yields the 0th order of the conservation of the composition at the interface:

$$D \bar{V}_{n,0} (c_0^\alpha(0^-) - c_0^\alpha(0^+)) = -(M_L^\alpha \partial_{\bar{r}} \mu_0^\alpha(0^-) - M_R^\alpha \partial_{\bar{r}} \mu_0^\alpha(0^+)). \quad (\text{A.4.27})$$

Taking the sum gives an expression for  $A$ ,

$$A = \frac{1}{2D} (M_L^\alpha \partial_{\bar{r}} \mu_0^\alpha(0^-) + M_R^\alpha \partial_{\bar{r}} \mu_0^\alpha(0^+)) + \frac{1}{2} \bar{V}_{n,0} \partial_\alpha \Delta\omega_0. \quad (\text{A.4.28})$$

Finally, the difference of (A.4.26) is

$$M^\alpha (\mu_1^\alpha(0^-) - \mu_1^\alpha(0^+)) = DA(G_-^\alpha - G_+^\alpha) + D(\partial_\alpha \Delta\omega_0) \bar{V}_{n,0} (\tilde{F}_-^\alpha - \tilde{F}_+^\alpha), \quad (\text{A.4.29})$$

which after putting in the expressions above for  $\bar{V}_{n,0}$  and  $A$  becomes

$$\begin{aligned} &M^\alpha (c_0^\alpha(0^-) - c_0^\alpha(0^+)) (\mu_1^\alpha(0^-) - \mu_1^\alpha(0^+)) \\ &= \frac{1}{2} (G_-^\alpha - G_+^\alpha) (c_0^\alpha(0^-) - c_0^\alpha(0^+)) (M_L^\alpha \partial_{\bar{r}} \mu_0^\alpha(0^-) + M_R^\alpha \partial_{\bar{r}} \mu_0^\alpha(0^+)) \\ &\quad - \left( (\partial_\alpha \Delta\omega_0) (\tilde{F}_-^\alpha - \tilde{F}_+^\alpha) + \frac{1}{2} (G_-^\alpha - G_+^\alpha) \right) (M_L^\alpha \partial_{\bar{r}} \mu_0^\alpha(0^-) + M_R^\alpha \partial_{\bar{r}} \mu_0^\alpha(0^+)). \end{aligned} \quad (\text{A.4.30})$$



The jump in  $\mu^\alpha_1$  must vanish at the interface, giving the integral conditions

$$\tilde{F}_+^\alpha = \tilde{F}_-^\alpha \equiv \tilde{F}^\alpha, \quad (\text{A.4.31})$$

$$G_+^\alpha = G_-^\alpha \equiv G^\alpha. \quad (\text{A.4.32})$$

As for the closure relation (A.4.19), applying the matching condition (A.3.2) and comparing the terms not proportional to  $\bar{\rho}$  gives a simple expression for  $c^\alpha_1$  at the interface ,

$$c^\alpha_1(0^\pm) = \sum_\beta \mu^\beta_1(0^\pm) \partial_{\alpha\beta} \omega_{\{R,L\}}(0^\pm). \quad (\text{A.4.33})$$

If the jump in  $\mu^\alpha_1$  is zero, so is the jump in  $c^\alpha_1$ .

#### A.4.5 Phase-field $O(\varepsilon^2)$

$$\begin{aligned} & \mathcal{L}\Phi_2 + (\bar{K}_0 + m\bar{V}_{n,0})\partial_{\bar{\rho}}\Phi_1 + (2\bar{\Pi}_0 - \bar{K}_0^2)\bar{\rho}\partial_{\bar{\rho}}\Phi_0 \\ & + (\bar{K}_1 + m\bar{V}_{n,1})\partial_{\bar{\rho}}\Phi_0 - \frac{1}{2}\Phi_1^2 f_{\text{dw}}'''(\Phi_0) \\ & + \lambda\Phi_1 p''(\Phi_0)\Delta\omega_0 + \lambda p'(\Phi_0) \sum_\alpha \nu^\alpha_1 \partial_\alpha \Delta\omega_0 = 0 \end{aligned} \quad (\text{A.4.34})$$

Following [1], we split the solvability condition at this order in three parts.

**Anomalous curvature terms** Corresponds to the third term in (A.4.34) :

$$(2\bar{\Pi}_0 - \bar{K}_0^2) \int_{-\infty}^{+\infty} \bar{\rho} (\partial_{\bar{\rho}}\Phi_0)^2 d\bar{\rho}. \quad (\text{A.4.35})$$

Since  $\partial_{\bar{\rho}}\Phi_0^2$  is an even function of  $\bar{\rho}$ , this term cancels out.

**Anomalous thermodynamic terms** Corresponds to the terms proportional to  $\Phi_1$  and  $\partial_{\bar{\rho}}\Phi_1$ . They cancel out if  $\Phi_1$  is zero, following (A.4.17). Even if  $\Phi_1 \neq 0$ , it can be shown that the contribution of these terms amount to zero with just the assumption that  $p(\varphi)$  is an odd function of  $\bar{\rho}$  [1, sec. 4.5.2.].

**Anomalous kinetic terms** The terms left. To begin, look at the term proportional to  $\nu^\alpha_1$  and use (A.4.21)

$$\begin{aligned} & \lambda \int_{-\infty}^{+\infty} p'(\Phi_0) (\partial_{\bar{\rho}}\Phi_0) \sum_\alpha \nu^\alpha_1 (\partial_\alpha \Delta\omega_0) d\bar{\rho} \\ & = \lambda \int_{-\infty}^{+\infty} \sum_\alpha \left( \nu^\alpha_* + \frac{A}{M^\alpha/D} \int_0^{\bar{\rho}} \frac{d\sigma}{q^\alpha(\Phi_0(\sigma))} - \frac{\bar{V}_{n,0}(\partial_\alpha \Delta\omega_0)}{M^\alpha/D} \int_0^{\bar{\rho}} \frac{\tilde{p}(\Phi_0(\sigma))}{q^\alpha(\Phi_0(\sigma))} d\sigma \right) \\ & \quad \times (\partial_\alpha \Delta\omega_0) p'(\Phi_0) (\partial_{\bar{\rho}}\Phi_0) d\bar{\rho} \end{aligned} \quad (\text{A.4.36})$$

Compute the three integrals in order. The first is

$$\lambda \int_{-\infty}^{+\infty} \sum_\alpha \nu^\alpha_* (\partial_\alpha \Delta\omega_0) p'(\Phi_0) \partial_{\bar{\rho}}\Phi_0 d\bar{\rho} = \lambda J \sum_\alpha \nu^\alpha_* \partial_\alpha \Delta\omega_0. \quad (\text{A.4.37})$$

For the two other integrals, remark that

$$\int_{-\infty}^{+\infty} \left( \int_0^{\bar{\rho}} f(\sigma) d\sigma \right) \partial_{\bar{\rho}} p(\Phi_0) d\bar{\rho} = \int_0^{+\infty} (1 - p(\Phi_0)) f(\sigma) d\sigma - \int_{-\infty}^0 p(\Phi_0) f(\sigma) d\sigma. \quad (\text{A.4.38})$$

The second integral is

$$\begin{aligned} & \lambda A \sum_{\alpha} \frac{\partial_{\alpha} \Delta \omega_0}{M^{\alpha}/D} \int_{-\infty}^{+\infty} \left( \int_0^{\bar{\rho}} \frac{d\sigma}{q^{\alpha}(\Phi_0(\sigma))} \right) \partial_{\bar{\rho}} p(\Phi_0) d\bar{\rho} \\ &= \lambda A \sum_{\alpha} \frac{\partial_{\alpha} \Delta \omega_0}{M^{\alpha}/D} \left( \int_0^{+\infty} \frac{1 - p(\Phi_0)}{q^{\alpha}(\Phi_0)} d\bar{\rho} - \int_{-\infty}^0 \frac{p(\Phi_0)}{q^{\alpha}(\Phi_0)} d\bar{\rho} \right) \\ &= \lambda A \sum_{\alpha} \frac{\partial_{\alpha} \Delta \omega_0}{M^{\alpha}/D} (G_+^{\alpha} + F_+^{\alpha} - F_-^{\alpha}). \end{aligned} \quad (\text{A.4.39})$$

And the third integral is

$$\begin{aligned} & \lambda \bar{V}_{n,0} \sum_{\alpha} \frac{(\partial_{\alpha} \Delta \omega_0)^2}{M^{\alpha}/D} \int_{-\infty}^{+\infty} \left( \int_0^{\bar{\rho}} \frac{\tilde{p}(\Phi_0(\sigma))}{q^{\alpha}(\Phi_0(\sigma))} d\sigma \right) \partial_{\bar{\rho}} p(\Phi_0) d\bar{\rho} \\ &= \lambda \bar{V}_{n,0} \sum_{\alpha} \frac{(\partial_{\alpha} \Delta \omega_0)^2}{M^{\alpha}/D} \left( \int_0^{+\infty} \frac{(1 - p(\Phi_0)) \tilde{p}(\Phi_0)}{q^{\alpha}(\Phi_0)} d\bar{\rho} - \int_{-\infty}^0 \frac{p(\Phi_0) \tilde{p}(\Phi_0)}{q^{\alpha}(\Phi_0)} d\bar{\rho} \right) \\ &= \lambda \bar{V}_{n,0} \sum_{\alpha} \frac{(\partial_{\alpha} \Delta \omega_0)^2}{M^{\alpha}/D} (K_+^{\alpha} + K_-^{\alpha}), \end{aligned} \quad (\text{A.4.40})$$

with

$$\begin{aligned} K_+^{\alpha} &= \int_0^{+\infty} \frac{(1 - p(\Phi_0)) \tilde{p}(\Phi_0)}{q^{\alpha}(\Phi_0)} d\bar{\rho}, \\ K_-^{\alpha} &= - \int_{-\infty}^0 \frac{p(\Phi_0) \tilde{p}(\Phi_0)}{q^{\alpha}(\Phi_0)} d\bar{\rho}. \end{aligned} \quad (\text{A.4.41})$$

The final term proportional to  $\bar{K}_1 + m \bar{V}_{n,1}$  is the term expected to continue the Gibbs-Thomson condition. Putting it together with the other, we get the solvability condition

$$I \bar{K}_1 + Im \bar{V}_{n,1} + \lambda \sum_{\alpha} (\partial_{\alpha} \Delta \omega_0) \left( J \nu_*^{\alpha} + \frac{A(G_+^{\alpha} + F_+^{\alpha} - F_-^{\alpha}) - (\partial_{\alpha} \Delta \omega_0) \bar{V}_{n,0} (K_+^{\alpha} + K_-^{\alpha})}{M^{\alpha}/D} \right) = 0. \quad (\text{A.4.42})$$

Using the expression (A.4.26) for  $\mu^{\alpha}_1$  at the interface, we have

$$\begin{aligned} & \sum_{\alpha} (\partial_{\alpha} \Delta \omega_0) \frac{1}{2} (\mu^{\alpha}_1(0^+) + \mu^{\alpha}_1(0^-)) = - \frac{I}{J\lambda} \bar{K}_1 - \frac{Im}{J\lambda} \bar{V}_{n,1} \\ & - \sum_{\alpha} (\partial_{\alpha} \Delta \omega_0) \frac{A \left( \frac{1}{2} (G_+^{\alpha} - G_-^{\alpha}) + (F_+^{\alpha} - F_-^{\alpha}) \right) - (\partial_{\alpha} \Delta \omega_0) \bar{V}_{n,0} \left( K_+^{\alpha} + K_-^{\alpha} + \frac{1}{2} (\tilde{F}_+^{\alpha} + \tilde{F}_-^{\alpha}) \right)}{JM^{\alpha}/D}, \end{aligned} \quad (\text{A.4.43})$$

Using the previous integral conditions (A.4.31), (A.4.32) and the additional condition

$$F_+^{\alpha} = F_-^{\alpha}, \quad (\text{A.4.44})$$

we can write the equation above as the continuation of the Gibbs-Thomson condition:

$$\Delta\omega_1(\mu^A, \mu^B) = -\frac{I}{J\lambda}\bar{K}_1 - \frac{Im}{J\lambda}\bar{V}_{n,1} + \sum_{\alpha} \frac{(\partial_{\alpha}\Delta\omega_0)^2\bar{V}_{n,0}(K_+^{\alpha} + K_-^{\alpha} + \tilde{F}^{\alpha})}{JM^{\alpha}/D} \quad \text{on the interface.} \quad (\text{A.4.45})$$

We've also used (A.4.11) and the fact that

$$\Delta\omega_1(\nu^A, \nu^B) = \sum_{\alpha} \nu^{\alpha}_0 \partial_{\alpha} \Delta\omega_0(\nu^A, \nu^B) \quad (\text{A.4.46})$$

to make  $\Delta\omega_1(\mu^A, \mu^B)$  appear on the l.h.s. An additional error term proportional to  $K_+^{\alpha} + K_-^{\alpha}$  and  $\tilde{F}^{\alpha}$  appears.

#### A.4.6 Diffusion and closure $O(\varepsilon^2)$

$$\begin{aligned} \frac{M^{\alpha}}{D} & \left( \partial_{\bar{\rho}}(q^{\alpha}(\Phi_0)\partial_{\bar{\rho}}\nu^{\alpha}_2 + \Phi_1 q^{\alpha'}(\Phi_0)\partial_{\bar{\rho}}\nu^{\alpha}_1) + q^{\alpha}(\Phi_0)\bar{K}_0\partial_{\bar{\rho}}\nu^{\alpha}_1 + \sum_{i=1,2} \partial_{\bar{s}_i}(q^{\alpha}(\Phi_0)\partial_{\bar{s}_i}\nu^{\alpha}_0) \right) \\ & = -\bar{V}_{n,0}\partial_{\bar{\rho}}C^{\alpha}_1 - \bar{V}_{n,1}\partial_{\bar{\rho}}C^{\alpha}_0 - \sum_{i=1,2} \bar{V}_{s_i,0}\partial_{\bar{s}_i}C^{\alpha}_0 + D_{\bar{t}}C^{\alpha}_0 \end{aligned} \quad (\text{A.4.47})$$

$$\begin{aligned} C^{\alpha}_2 & = \left( \Phi_2 \tilde{p}'(\Phi_0) + \frac{1}{2} \Phi_1^2 \tilde{p}''(\Phi_0) \right) \partial_{\alpha} \Delta\omega_0 + \Phi_1 \tilde{p}'(\Phi_0) \sum_{\beta=A,B} \partial_{\beta\alpha} \Delta\omega_0 \\ & + \sum_{\beta=A,B} \nu^{\beta}_2 (\tilde{p}(1-\Phi_0)\partial_{\beta\alpha}\omega_l + \tilde{p}(\Phi_0)\partial_{\beta\alpha}\omega_r) \\ & + \frac{1}{2} \sum_{\beta,\gamma=A,B} \nu^{\beta}_1 \nu^{\gamma}_1 (\tilde{p}(1-\Phi_0)\partial_{\gamma\beta\alpha}\omega_l + \tilde{p}(\Phi_0)\partial_{\gamma\beta\alpha}\omega_r) \end{aligned} \quad (\text{A.4.48})$$

In the diffusion equation, express the derivative of  $C^{\alpha}_0$  with eq. (A.4.10) and use the result from eq. (A.4.20); then integrate and rearrange to get

$$\begin{aligned} M^{\alpha} q^{\alpha}(\Phi_0) \partial_{\bar{\rho}} \nu^{\alpha}_2 & = -M^{\alpha} \Phi_1 q^{\alpha'}(\Phi_0) \partial_{\bar{\rho}} \nu^{\alpha}_1 + DB - D\bar{K}_0 A \bar{\rho} + D\tilde{P}(\bar{\rho}) \bar{K}_0 \bar{V}_{n,0} \partial_{\alpha} \Delta\omega_0 \\ & - M^{\alpha} Q^{\alpha}(\bar{\rho}) \sum_{i=1,2} \partial_{\bar{s}_i \bar{s}_i} \nu^{\alpha}_0 - D\bar{V}_{n,0} C^{\alpha}_1 + Dp(\Phi_0) \bar{V}_{n,1} \partial_{\alpha} \Delta\omega_0 \\ & + \bar{\rho} D \left( \sum_{i=1,2} \bar{V}_{s_i,0} \partial_{\bar{s}_i} C^{\alpha}_0 - D_{\bar{t}} C^{\alpha}_0 \right), \end{aligned} \quad (\text{A.4.49})$$

with  $B$  an integration constant and

$$\tilde{P}(\bar{\rho}) = \int_0^{\bar{\rho}} \tilde{p}(\Phi_0(\sigma)) d\sigma, \quad (\text{A.4.50})$$

$$Q^{\alpha}(\bar{\rho}) = \int_0^{\bar{\rho}} q^{\alpha}(\Phi_0(\sigma)) d\sigma. \quad (\text{A.4.51})$$

Next, we write the far-field expansions before applying the matching conditions. The integrals above expands to

$$\tilde{P}(\bar{\rho}) \sim o(1) + \begin{cases} \bar{\rho} - \tilde{H}_+ & \text{as } \bar{\rho} \rightarrow +\infty, \\ -\tilde{H}_- & \text{as } \bar{\rho} \rightarrow -\infty, \end{cases} \quad (\text{A.4.52})$$

$$Q^\alpha(\bar{\rho}) \sim o(1) + \begin{cases} q^\alpha(1)\bar{\rho} - J_+ & \text{as } \bar{\rho} \rightarrow +\infty, \\ q^\alpha(0)\bar{\rho} - J_- & \text{as } \bar{\rho} \rightarrow -\infty, \end{cases} \quad (\text{A.4.53})$$

with

$$\begin{aligned} \tilde{H}_+ &= \int_0^{+\infty} (1 - \tilde{p}(\Phi_0)) d\bar{\rho}, & J_+ &= \int_0^{+\infty} (q^\alpha(1) - q^\alpha(\Phi_0)) d\bar{\rho}, \\ \tilde{H}_- &= \int_{-\infty}^0 \tilde{p}(\Phi_0) d\bar{\rho}, & J_- &= - \int_{-\infty}^0 (q^\alpha(0) - q^\alpha(\Phi_0)) d\bar{\rho}. \end{aligned} \quad (\text{A.4.54})$$

The second order diffusive flux then expands as

$$\begin{aligned} M_{\{R,L\}}^\alpha \partial_{\bar{\rho}} \nu^\alpha_2 &= \left\{ -AD\bar{K}_0 + \frac{1 \pm 1}{2} D\bar{K}_0 \bar{V}_{n,0} \partial_\alpha \Delta\omega_0 - \sum_{i=1,2} (M_{\{R,L\}}^\alpha \partial_{\bar{s}_i \bar{s}_i} \nu^\alpha_0 + D\bar{V}_{s_i} \partial_{\bar{s}_i} C^\alpha_0) \right. \\ &\quad \left. + DD_{\bar{t}} C^\alpha_0 - D\bar{V}_{n,0} \sum_{\beta=A,B} \left( \frac{A - \frac{1 \pm 1}{2} \bar{V}_{n,0} \partial_\beta \Delta\omega_0}{M^\beta/D} \right) \partial_{\beta\alpha} \omega_{\{R,L\}} \right\} \bar{\rho} \\ &\quad + \left\{ B - D\bar{K}_0 \bar{V}_{n,0} \tilde{H}_\pm + J_\pm M^\alpha \sum_{i=1,2} \partial_{\bar{s}_i \bar{s}_i} \nu^\alpha_0 \right. \\ &\quad \left. - D\bar{V}_{n,0} \sum_{\beta=A,B} \left( \nu_*^\beta + \frac{AG^\beta + \bar{V}_{n,0} \tilde{F}^\beta}{M^\beta/D} \right) \partial_{\beta\alpha} \omega_{\{R,L\}} + \frac{1 \pm 1}{2} D\bar{V}_{n,1} \partial_\alpha \Delta\omega_0 \right\} + o(1). \end{aligned} \quad (\text{A.4.55})$$

To write the above equation, we have used the fact that  $\Phi_1 \sim 0$  as  $\bar{\rho} \rightarrow \pm\infty$ , assumed the equalities of the  $G_\pm^\alpha$  and  $F_\pm^\alpha$  integrals, and used eqs. (A.4.19) and (A.4.21) to express  $C^\alpha_1$ .

Then, derive the second order matching condition (A.3.3) w.r.t.  $\bar{\rho}$  and match the  $O(1)$  parts to write the jump in diffusive flux at the interface

$$\begin{aligned} M_R^\alpha \partial_{\bar{r}} \mu^\alpha_1(0^+) - M_L^\alpha \partial_{\bar{r}} \mu^\alpha_1(0^-) &= -D\bar{K}_0 \bar{V}_{n,0} (\tilde{H}_+ - \tilde{H}_-) - M^\alpha (J_+ - J_-) \sum_{i=1,2} \partial_{\bar{s}_i \bar{s}_i} \nu^\alpha_0 \\ &\quad - D\bar{V}_{n,0} \sum_{\beta=A,B} \left( \nu_*^\beta + \frac{AG^\beta + \bar{V}_{n,0} \tilde{F}^\beta}{M^\beta/D} \right) \partial_{\beta\alpha} \Delta\omega_0 + D\bar{V}_{n,1} \partial_\alpha \Delta\omega_0. \end{aligned} \quad (\text{A.4.56})$$

The last two terms of the right-hand side can be rewritten using the previous results (A.4.12), (A.4.26) and (A.4.33) to reveal the first order conservation of the composition:

$$\begin{aligned} M_R^\alpha \partial_{\bar{r}} \mu^\alpha_1(0^+) - M_L^\alpha \partial_{\bar{r}} \mu^\alpha_1(0^-) &= -D\bar{K}_0 \bar{V}_{n,0} (\tilde{H}_+ - \tilde{H}_-) - M^\alpha (J_+ - J_-) \sum_{i=1,2} \partial_{\bar{s}_i \bar{s}_i} \nu^\alpha_0 \\ &\quad - D\bar{V}_{n,0} (c^\alpha_1(0^+) - c^\alpha_1(0^-)) - D\bar{V}_{n,1} (c^\alpha_0(0^+) - c^\alpha_0(0^-)) \end{aligned} \quad (\text{A.4.57})$$

The first two right terms are error terms, giving the last integral conditions  $\tilde{H}_+ = \tilde{H}_-$  and  $J_+ = J_-$ .

We will not investigate the closure relation (A.4.48), as it only serves to obtain intermediate results for calculations at order  $O(\varepsilon^3)$ .

### A.4.7 Summary

#### Gibbs-Thomson

Reassembling eqs. (A.4.14) and (A.4.45) gives the complete Gibbs-Thomson condition

$$\begin{aligned} \Delta\omega_0 + \varepsilon\Delta\omega_1 &= -\frac{I}{\lambda J}(\bar{K}_0 + \varepsilon\bar{K}_1) - \frac{Im}{\lambda J}(\bar{V}_{n,0} + \varepsilon\bar{V}_{n,1}) \\ &+ \varepsilon \sum_{\alpha} \frac{D(K_+^{\alpha} + K_-^{\alpha} + \tilde{F}^{\alpha})(\partial_{\alpha}\Delta\omega_0)^2}{JM^{\alpha}}\bar{V}_{n,0}. \end{aligned} \quad (\text{A.4.58})$$

Restore the physical dimensions (sec. A.2.2) to obtain

$$\Delta\omega_0 + \varepsilon\Delta\omega_1 = -\delta(K_0 + \varepsilon K_1) - \beta_0(V_{n,0} + \varepsilon V_{n,1}) - \beta_1 V_{n,0} \quad (\text{A.4.59})$$

with

$$\delta = \varepsilon^{-1} \frac{I}{J} \frac{W}{\lambda} = \frac{I}{J} \frac{W}{\lambda^*}, \quad (\text{A.4.60})$$

$$\beta_0 = \varepsilon^{-1} \frac{I}{J} \frac{\tau}{\lambda W} = \frac{I}{J} \frac{\tau}{\lambda^* W}, \quad (\text{A.4.61})$$

$$\beta_1 = - \sum_{\alpha} \frac{K_+^{\alpha} + K_-^{\alpha} + \tilde{F}^{\alpha}}{J} \frac{W(\partial_{\alpha}\Delta\omega_0)^2}{M^{\alpha}}. \quad (\text{A.4.62})$$

To write those results, we assumed the following integral conditions to be true,

$$\partial_{\bar{\rho}}\Phi_0 = \frac{I}{J}p'(\Phi_0), \quad (\text{A.4.63})$$

$$\tilde{F}_+^{\alpha} = \tilde{F}_-^{\alpha} \equiv \tilde{F}^{\alpha}, \quad (\text{A.4.64})$$

$$G_+^{\alpha} = G_-^{\alpha} \equiv G^{\alpha}, \quad (\text{A.4.65})$$

$$F_+^{\alpha} = F_-^{\alpha}. \quad (\text{A.4.66})$$

The integrals involved are

$$\begin{aligned} I &= \int_0^1 \partial_{\bar{\rho}}\Phi_0 d\Phi_0 = 2/3, & J &= \int_{-\infty}^{+\infty} \partial_{\bar{\rho}}(p(\Phi_0)) d\bar{\rho}, \\ \tilde{F}_+^{\alpha} &= \int_0^{+\infty} \left( \frac{1}{q^{\alpha}(1)} - \frac{\tilde{p}(\Phi_0)}{q^{\alpha}(\Phi_0)} \right) d\bar{\rho}, & \tilde{F}_-^{\alpha} &= \int_{-\infty}^0 \frac{\tilde{p}(\Phi_0)}{q^{\alpha}(\Phi_0)} d\bar{\rho}, \\ G_+^{\alpha} &= \int_0^{+\infty} \left( \frac{1}{q^{\alpha}(\Phi_0)} - \frac{1}{q^{\alpha}(1)} \right) d\bar{\rho}, & G_-^{\alpha} &= \int_{-\infty}^0 \left( \frac{1}{q^{\alpha}(0)} - \frac{1}{q^{\alpha}(\Phi_0)} \right) d\bar{\rho}, \\ F_+^{\alpha} &= \int_0^{+\infty} \left( \frac{1}{q^{\alpha}(1)} - \frac{p(\Phi_0)}{q^{\alpha}(\Phi_0)} \right) d\bar{\rho}, & F_-^{\alpha} &= \int_{-\infty}^0 \frac{p(\Phi_0)}{q^{\alpha}(\Phi_0)} d\bar{\rho}, \\ K_+^{\alpha} &= \int_0^{+\infty} \frac{(1-p(\Phi_0))\tilde{p}(\Phi_0)}{q^{\alpha}(\Phi_0)} d\bar{\rho}, & K_-^{\alpha} &= - \int_{-\infty}^0 \frac{p(\Phi_0)\tilde{p}(\Phi_0)}{q^{\alpha}(\Phi_0)} d\bar{\rho}. \end{aligned} \quad (\text{A.4.67})$$

#### Conservation of the composition

$$(V_{n,0}[c^{\alpha}_0]_-^+ + \varepsilon(V_{n,1}[c^{\alpha}_0]_-^+ + V_{n,0}[c^{\alpha}_1]_-^+)) = -[M^{\alpha}\partial_r(\mu^{\alpha}_0 + \varepsilon\mu^{\alpha}_1)]_-^+ + \varepsilon^{-1}E^{\alpha} \quad (\text{A.4.68})$$

with

$$E^{\alpha} = -W \left( K_0 V_0 (\tilde{H}_+ - \tilde{H}_-) + M^{\alpha} (J_+ - J_-) \sum_{i=1,2} \partial_{\bar{s}_i \bar{s}_i} \nu^{\alpha}_0 \right) \quad (\text{A.4.69})$$

#### A.4.8 Numerical application: symmetrical diffusion couple

We can now verify analytically the value of  $\lambda = 110$  estimated numerically in the simulation of a symmetrical diffusion couple carried out in sec. 3.2.2.

For these simulations, we have used the interpolation polynomials  $p(\varphi) = \tilde{p}(\varphi) = 3\varphi^2 - 2\varphi^3$  and  $q(\varphi) = 1$ . With this choice of interpolation functions, the integral constraints are satisfied and numerical values of the integrals are

$$\tilde{F}^\alpha = \frac{4 \ln 2 - 1}{16}, \quad (\text{A.4.70})$$

$$K_-^\alpha = \frac{-30 \ln 2 + 17}{120}, \quad (\text{A.4.71})$$

$$K_+^\alpha = \frac{19}{240}. \quad (\text{A.4.72})$$

$$(\text{A.4.73})$$

The free energy used were the usual paraboloids with the second derivatives matrices set to the identity. With these, the derivative of the difference of 0th-order grand potentials is

$$\partial_\alpha \Delta \omega_0 = c_L^{\text{eq},\alpha} - c_R^{\text{eq},\alpha}. \quad (\text{A.4.74})$$

The  $\beta_1$  term in the Gibbs-Thomson condition is then

$$\beta_1 = - \sum_\alpha \frac{19}{120} \frac{W(c_L^{\text{eq},\alpha} - c_R^{\text{eq},\alpha})^2}{M^{\alpha\alpha}}. \quad (\text{A.4.75})$$

To cancel  $\beta$  for  $M_\varphi$ ,  $M^{\alpha\alpha}$  and  $\Delta c^{\text{eq},\alpha}$  given, we have the condition on  $\lambda$

$$\lambda = \frac{80}{9} \frac{1}{M_\varphi} \left( \sum_\alpha \frac{\Delta m^{\alpha^2}}{M^\alpha} \right)^{-1} \quad (\text{A.4.76})$$

By cancelling  $\beta$ , one obtains the Gibbs-Thomson condition with no right-hand side as was supposed for the diffusion couple. Inserting the numerical values for each parameter listed in table 3.2 gives us a value of  $\lambda = 155.95$ , close the estimated value of 110. The analytical reconstruction of the Gibbs-Thomson condition is thus confirmed.

### A.5 Other differential operators in curvilinear coordinates

By making extensive use of Taylor series in  $\varepsilon$  and the base expressions of the gradient (A.2.6) and divergence (A.2.7), one can derive expressions for multiple dimensionless operators in the curvilinear

coordinates. Below are some of them:

$$\begin{aligned} \bar{\nabla}^2 f &= \varepsilon^{-2} \partial_{\bar{\rho}\bar{\rho}} f + \varepsilon^{-1} \bar{K} \partial_{\bar{\rho}} f + (2\bar{\Pi} - \bar{K}^2) \bar{\rho} \partial_{\bar{\rho}} f + \sum_{i=1,2} \partial_{\bar{s}_i \bar{s}_i} f \\ &\quad - \varepsilon \sum_{i=1,2} (\bar{\rho} \partial_{\bar{s}_i} \bar{\kappa}_i - 2\bar{\kappa}_i \bar{\rho} \partial_{\bar{s}_i \bar{s}_i} f) + O(\varepsilon^2) \end{aligned} \quad (\text{A.5.1})$$

$$\begin{aligned} \bar{\nabla} \cdot (F(f) \bar{\nabla} f) &= \varepsilon^{-2} \partial_{\bar{\rho}} (F(f) \partial_{\bar{\rho}} f) \\ &\quad + \varepsilon^{-1} F(f) \bar{K} \partial_{\bar{\rho}} f + F(f) (2\bar{\Pi} - \bar{K}^2) \bar{\rho} \partial_{\bar{\rho}} f + \sum_{i=1,2} \partial_{\bar{s}_i} (F(f) \partial_{\bar{s}_i} f) \\ &\quad - \varepsilon F(f) \sum_{i=1,2} (\bar{\rho} \partial_{\bar{s}_i} \bar{\kappa}_i - 2\bar{\kappa}_i \bar{\rho} \partial_{\bar{s}_i \bar{s}_i} f) + O(\varepsilon^2) \end{aligned} \quad (\text{A.5.2})$$

$$|\bar{\nabla} f|^n = (\partial_{\bar{\rho}} f)^n \left( \varepsilon^{-1} + \varepsilon \frac{n}{2} \sum_{i=1,2} \left( \frac{\partial_{\bar{s}_i} f}{\partial_{\bar{\rho}} f} \right)^2 \right) + O(\varepsilon^2) \quad (\text{A.5.3})$$

$$\frac{\bar{\nabla} f}{|\bar{\nabla} f|} = \left\{ 1 - \varepsilon^2 \frac{1}{2} \sum_i \left( \frac{\partial_{\bar{s}_i} f}{\partial_{\bar{\rho}} f} \right)^2 + O(\varepsilon^3) \right\} \hat{n} + \sum_{i=1,2} \left\{ \varepsilon \frac{\partial_{\bar{s}_i} f}{\partial_{\bar{\rho}} f} - \varepsilon^2 \bar{\rho} \bar{\kappa}_i \frac{\partial_{\bar{s}_i} f}{\partial_{\bar{\rho}} f} + O(\varepsilon^3) \right\} \hat{s}_i \quad (\text{A.5.4})$$

$$\begin{aligned} \bar{\nabla} \cdot \left( F(f) \frac{\bar{\nabla} f}{|\bar{\nabla} f|} \right) &= \varepsilon^{-1} F'(f) \partial_{\bar{\rho}} f + F(f) \bar{K} + \varepsilon \left( F(f) [2\bar{\Pi} - \bar{K}^2] \bar{\rho} \right. \\ &\quad \left. - F(f) \frac{1}{2} \sum_{i=1,2} \partial_{\bar{\rho}} \left[ \frac{\partial_{\bar{s}_i} f}{\partial_{\bar{\rho}} f} \right]^2 + F(f) \sum_{i=1,2} \partial_{\bar{s}_i} \frac{\partial_{\bar{s}_i} f}{\partial_{\bar{\rho}} f} - \frac{1}{2} F'(f) \sum_{i=1,2} \frac{(\partial_{\bar{s}_i} f)^2}{\partial_{\bar{\rho}} f} \right) + O(\varepsilon^2) \end{aligned} \quad (\text{A.5.5})$$

In the second and last expression,  $F$  is an arbitrary function of  $f$ .

## References

- [1] Robert F. Almgren. “Second-Order Phase Field Asymptotics for Unequal Conductivities.” In: *SIAM Journal on Applied Mathematics* 59.6 (1999), pp. 2086–2107. doi: 10.1137/S0036139997330027.
- [2] Arnoldo Badillo. “Quantitative phase-field modeling for boiling phenomena.” In: *Phys. Rev. E* 86 (4 Oct. 2012), p. 041603. doi: 10.1103/PhysRevE.86.041603.
- [3] Blas Echebarria et al. “Quantitative phase-field model of alloy solidification.” In: *Phys. Rev. E* 70 (6 Dec. 2004), p. 061604. doi: 10.1103/PhysRevE.70.061604.
- [4] Paul Fife. “Dynamics of Internal Layers and Diffusive Interfaces.” In: 1988. Chap. 1. Internal Layers, pp. 1–16. doi: 10.1137/1.9781611970180.ch1. eprint: <https://epubs.siam.org/doi/pdf/10.1137/1.9781611970180.ch1>.
- [5] R. Folch et al. “Phase-field model for Hele-Shaw flows with arbitrary viscosity contrast. II. Numerical study.” In: *Phys. Rev. E* 60 (2 Aug. 1999), pp. 1734–1740. doi: 10.1103/PhysRevE.60.1734.
- [6] Alain Karma and Wouter-Jan Rappel. “Quantitative phase-field modeling of dendritic growth in two and three dimensions.” In: *Phys. Rev. E* 57 (4 Apr. 1998), pp. 4323–4349. doi: 10.1103/PhysRevE.57.4323.

## Appendix B

# Two papers published during this thesis

We include in this appendix two papers written during the thesis. The first one, “Performance portability of lattice Boltzmann methods for two-phase flows with phase change” [3], publishes the result of a 5-month internship that preceded this thesis. It built a two-phase flow model based on the conservative Allen-Cahn equation for the simulation of a liquid-gas flow, in particular a film boiling test case. The evaporation at the interface was taken into account by a source term in the mass conservation of the Navier-Stokes equations and in the Allen-Cahn equation. This was the first appearance of the LBM\_saclay code and the paper presents some details of performance and implementation. Besides setting the base for the code and the typical LBM schemes implemented therein, this preliminary work also helped prepare the flow coupling of our two-phase three-component model; this coupling was transferred with little changes beyond the assumption of equal densities.

The second, “Grand-potential-based phase-field model of dissolution/precipitation: Lattice Boltzmann simulations of counter term effect on porous medium” [1], also presents simulations carried out with LBM\_saclay. It uses the mixed formulation grand potential framework to model a two-phase (solid-liquid) binary material with zero diffusion in the solid phase, and showcases the effect of the counter term on the diffusion in a domain akin to a porous medium. An asymptotic analysis is also presented in details.

Two other items of scientific production were also authored: an internal technical note at CEA [2] and an abstract and oral presentation at the CALPHAD 2022 conference in Stockholm, Sweden [4]. A third paper on the two-phase ternary model with flow and the effects of sedimentation on droplet growth is currently in writing.

## References

- [1] Téo Boutin, Werner Verdier, and Alain Cartalade. “Grand-potential-based phase-field model of dissolution/precipitation: Lattice Boltzmann simulations of counter term effect on porous medium.” In: *Computational Materials Science* 207 (2022), p. 111261. ISSN: 0927-0256. DOI: <https://doi.org/10.1016/j.commatsci.2022.111261>.
- [2] Werner Verdier. *Modèle à champ de phase pour verres ternaires diphasiques*. Note technique DES STMF/LMSF/NT/2021-67858 (CEA internal technical report). 2021.



- [3] Werner Verdier, Pierre Kestener, and Alain Cartalade. “Performance portability of lattice Boltzmann methods for two-phase flows with phase change.” In: *Computer Methods in Applied Mechanics and Engineering* 370 (2020), p. 113266. ISSN: 0045-7825. doi: <https://doi.org/10.1016/j.cma.2020.113266>.
- [4] Werner Verdier et al. “Coupling a grand potential ternary phase field model to the thermodynamic landscape of the Na<sub>2</sub>O-SiO<sub>2</sub>-MoO<sub>3</sub> nuclear glass.” In: *CALPHAD XLIX* (Skogshem & Wijk, Lidingö, May 22–27, 2022). 2022.

# Performance portability of lattice Boltzmann methods for two-phase flows with phase change

WERNER VERDIER<sup>a</sup>, PIERRE KESTENER<sup>b</sup>, ALAIN CARTALADE<sup>a,\*</sup>

<sup>a</sup>DES, ISAS, DM2S, STMF, LMSF, CEA, Université de Paris-Saclay, F-91191, Gif-sur-Yvette, France.

<sup>b</sup>DRF – Maison de la Simulation, CEA, Université de Paris-Saclay, F-91191, Gif-sur-Yvette, France.

## Abstract

Numerical codes using the lattice Boltzmann methods (LBM) for simulating one- or two-phase flows are widely compiled and run on graphical process units. However, those computational units necessitate to re-write the program by using a low-level language which is suited to those architectures (e.g. CUDA for GPU NVIDIA<sup>®</sup> or OpenCL). In this paper we focus our effort on the performance portability of LBM i.e. the possibility of writing LB algorithms with a high-level of abstraction while remaining efficient on a wide range of architectures such as multicores x86, GPU NVIDIA<sup>®</sup>, ARM, and so on. For such a purpose, implementation of LBM is carried out by developing a unique code, `LBM_saclay` written in the C++ language, coupled with the `Kokkos` library for performance portability in the context of High Performance Computing. In this paper, the LBM is used to simulate a phase-field model for two-phase flow problems with phase change. The mathematical model is composed of the incompressible Navier-Stokes equations coupled with the conservative Allen-Cahn model. Initially developed in the literature for immiscible binary fluids, the model is extended here to simulate phase change occurring at the interface between liquid and gas. For that purpose, a heat equation is added with a source term involving the time derivative of the phase field. In the phase-field equation a source term is added to approximate the mass production rate at the interface. Several validations are carried out to check step-by-step the implementation of the full model. Finally, computational times are compared on CPU and GPU platforms for the physical problem of film boiling.

## Keywords:

Lattice Boltzmann method, phase-field model, two-phase flows with phase change, performance portability, `Kokkos` library, `LBM_saclay`, conservative Allen-Cahn model.

## 1. Introduction

The Lattice Boltzmann Method (LBM) [1, 2] is a very attractive method to simulate problems involving fluid flows. Since more than ten years, numerical codes using that method are widely compiled and run on Graphical Process Units (GPU) [3–6]. The GPUs allow for a very high calculation throughput and they are particularly efficient for repetitive workloads with simple memory access patterns. These units were initially designed for image processing or graphics rendering, but LBM simulations can also benefit from their use, because the stages of streaming and collide are two simple (stencil-like) computational operations. Numerous works have demonstrated the efficiency of LBM on single GPU (e.g. [5]) and later on clusters of GPUs (e.g. [7, 8]). However, those computational units necessitate to re-write the code by using a low-level language which is suited to their specific architectures (e.g. CUDA for GPU NVIDIA<sup>®</sup> or OpenCL). In this paper we focus our effort on the performance portability of LBM i.e. the possibility of writing LBM algorithms with a high-level of abstraction, but by remaining efficient on a wide range of architectures such as multicores x86, GPU NVIDIA<sup>®</sup>, ARM, and so on.

The issue of performance portability has already been studied and implementation of numerical algorithms running on various architectures (GPU and so on) can be done by directive approaches (mostly OpenMP or OpenACC). Directive-based parallel programming solutions consist in decorating source code with comments that are interpreted by the compiler to derive the actual parallel code. They are useful when porting a legacy simulation code with a large number of lines, for which it is not reasonable to rewrite it from scratch. However, those programming models deal with computational patterns (for loops, reduction loops, ...) and do not provide tools for data or memory containers. Here we present an application of a more promising approach that uses a library-based solution which offers high-level abstract programming concepts and hardware agnostic solution for a better integration into C++ codes. Among libraries sharing the same goal of performance portability (like RAJA or SYCL), the `Kokkos` library [9] is used for simulating two-phase flows with LBM. `Kokkos` implements a programming model in C++ for writing performance portable applications targeting all major High Performance Computing (HPC) platforms. Programming tools provide abstractions for both parallel execution of code and

\*Corresponding author. Tel.: +33 (0)1 69 08 40 67

Email addresses: werner.verdier@cea.fr (WERNER VERDIER), pierre.kestener@cea.fr (PIERRE KESTENER), alain.cartalade@cea.fr (ALAIN CARTALADE)

data management, i.e. they provide memory containers (multidimensional arrays) where the actual memory layout will be chosen by the library during compilation. Directive-based solution does not provide such advanced features regarding memory. The Kokkos library can currently use OpenMP, Pthreads and CUDA as backend programming models. The library has already been applied to accelerate high-order mesh optimization in [10].

Because of its explicit scheme and local interactions, the LBM ideally exploits the massively parallel supercomputers based on either CPUs or GPUs or heterogeneous architectures. In this paper, we take advantage of those benefits to study two-phase flows. Several topical reviews exist in the literature for modeling two-phase flows in LBM framework [11, 12]. The main families of methods are the color-gradient method [13], the pseudo-potential method [14, 15], the free-energy method [16], and the phase-field method [17]. Most of approaches consider the interface as a diffuse zone (characterized by a thickness and a surface tension) which can be seen as a small region of transition between bulk phases. In pseudo-potential methods [14, 15] an additional force term is added in the Navier-Stokes equations to take into account an equation of state which is not the classical law of perfect gases [18]. In that case, the density plays the role of a phase index varying smoothly between densities of gas and liquid. Several recent applications use that method for simulating liquid-gas phase change [19, 20]. Another class of diffuse interface methods is the color-gradient model [13] for which two distribution functions are introduced for computation of each phase (red and blue). In those approaches, surface tension is derived from a recoloring step involving both distribution functions [21, 22]. The final approach that is commonly applied in the LBM literature is to capture the interfacial behavior through a phase-field equation. In this paper, we follow this latter method: the phase-field theory for two-phase flows [23]. The phase-field method is quite similar to the free-energy lattice Boltzmann method [16] in the sense that both models are thermodynamically consistent and can be derived from a free-energy functional. However, in the free-energy LB approach, the density gradient appears explicitly in the free-energy functional and the phase separation is described by a non-ideal equation of state. For that purpose, the equilibrium distribution function is modified to include a non-ideal thermodynamic pressure tensor. In this paper, both fluids are considered as quasi-incompressible, i.e. we assume that the incompressibility condition holds in the bulk phases except in the interfacial zone where the mass production rate  $\dot{m}'''$  acts. That mass production rate comes from the phase change between the gas and the liquid. A new function  $\phi$  is introduced to track the interfacial zone where the density varies.

Two main phase-field models for interface tracking between two immiscible fluids exist in literature: the first one is the Cahn-Hilliard (CH) model [17, 24, 25] which was extensively applied in LBM literature for simulating spinodal decomposition [26], buoyancy of bubbles [27], drop impact [28], Rayleigh-Taylor instability [29] and so on. The second one is a more recent model, called the conservative Allen-Cahn (CAC) model, which was first developed in [30] and derived in conservative form in [31]. The model became popular in the LB community [32–34] and several papers compare the Cahn-Hilliard and conservative Allen-Cahn models, e.g. [35] without LBM and [36] with LBM. In this work the CAC model is chosen for interface tracking in order to eliminate the curvature-driven interface motion which is implicitly contained in the CH equation (see Section 2). Moreover, the CAC model involves only a second-order derivative and does not require to compute the fourth-order derivative (Laplacian of chemical potential) which appears in the CH equation.

In this paper, we take advantage of the simplicity of LBM to develop a new portable code for simulating two phase flows with the coupled Navier-Stokes/conservative Allen-Cahn (NS/CAC) model. The new code, called `LBM_saclay`, targets all major HPC platforms such as multi-GPUs and multi-CPU. In this paper, we also check the capability of the NS/CAC model to simulate phase change problems in the vicinity of the critical temperature. Near the critical temperature, properties of each phase vary smoothly and the range of variation of those parameters remains small. Several fluid flow models of phase change have already been proposed in the literature with the Cahn-Hilliard equation [37, 38]. Following those references, the NS/CAC model is extended here by adding a source term in both the mass balance and the CAC equations. The source term involves the mass production rate  $\dot{m}'''$  occurring at the interface. In references [37, 38], the liquid is often considered at saturation temperature and its thermal conductivity is neglected. Under those assumptions,  $\dot{m}'''$  is calculated by a gradient operator (Fourier’s law) involving only the thermal conductivity of gas. Moreover, in order to avoid computing the temperature equation in liquid phase (because the thermal conductivity is neglected), a cut-off value of the phase-field is introduced beyond which the temperature equation will not be computed [38]. Here we propose an alternative way to calculate  $\dot{m}'''$  that avoids computing this gradient and avoids introducing this cut-off value. For that purpose,  $\dot{m}'''$  will be related to the normal interface velocity and expressed as a source term close to what is done in solidification models (section 2.3). Implementation of lattice Boltzmann methods will be checked step-by-step by considering separately solutions of the phase-field equation, the phase-field coupled successively with a fluid flow, and the phase-field coupled only with temperature for which the ratio of physical properties remain low. Finally, the aspects of two-phase flow, phase change and heat transfer are coupled to simulate the phenomena of film boiling [39].

This paper is organized as follows. Section 2 presents the continuous mathematical model based on the conservative Allen-Cahn equation which is extended to handle phase change. The model derivation will be reminded, as well as definition of the chemical potential and interpolation methods for kinematics viscosities and densities. Section 3 presents the Lattice Boltzmann schemes based on the Bhatnagar-Gross-Krook (BGK) collision operator for each equation. That collision operator is chosen because of its simplicity of implementation. Several improvements exist such as the two-relaxation-times (TRT) and the multiple-relaxation-times (MRT). Their benefits will be quickly discussed in that section. Computation of gradient and Laplacian operators that are involved in equations of phase-field and fluid flow will also be specified. Details on numerical implementation with the Kokkos library and various optimizations of LBM kernel will be discussed in Section

3.5. In Section 4, several basic code verifications are presented to check the implementation of each equation step-by-step. In Section 5, two purely qualitative simulations will be presented on the two-dimensional test case of film boiling. The first one will illustrate the capability of the model to simulate the detachment of bubbles on nodes and antinodes. The second one will illustrate the influence of the Jacob number on their detachment and shape. Here, we give a comparison of the code performance running on two architectures (CPU Intel and GPU NVIDIA®). Finally, Section 6 and three appendices will conclude this paper.

## 2. Two-phase flow with mass transfer

### 2.1. Phase change model

A single component fluid is considered, which can be either in a liquid ( $l$ ) or gas ( $g$ ) phase. The system is then composed with two incompressible fluids with constant densities  $\rho_l$  and  $\rho_g$ . A phase index  $\phi \equiv \phi(\mathbf{x}, t)$  is introduced which can vary between 0 and 1 with  $\phi = 0$  (respectively  $\phi = 1$ ) corresponding to fluid  $l$  (resp.  $g$ ) which is characterized by its density  $\rho_l$  (resp.  $\rho_g$ ) and its kinematic viscosity  $\nu_l$  (resp.  $\nu_g$ ). All other values of  $\phi$  represent the interfacial zone or a mixture of both fluids  $l$  and  $g$ . When  $0 < \phi < 1$ , the densities  $\rho(\phi)$  and the kinematic viscosities  $\nu(\phi)$  are respectively interpolated by

$$\rho(\phi) = \phi(\mathbf{x}, t)\rho_g + (1 - \phi(\mathbf{x}, t))\rho_l, \quad (1a)$$

$$\nu(\phi) = \frac{\nu_l \nu_g}{\phi(\mathbf{x}, t)\nu_l + (1 - \phi(\mathbf{x}, t))\nu_g}. \quad (1b)$$

Local densities depending on position and time are noted  $\tilde{\rho}_\chi$  (for  $\chi = g, l$ ) and write  $\tilde{\rho}_g(\mathbf{x}, t) = \rho_g\phi(\mathbf{x}, t)$  and  $\tilde{\rho}_l(\mathbf{x}, t) = (1 - \phi(\mathbf{x}, t))\rho_l$ . The total density writes  $\rho(\mathbf{x}, t) = \rho_g\phi(\mathbf{x}, t) + (1 - \phi(\mathbf{x}, t))\rho_l$ . The method of harmonic mean is used in this work to interpolate the viscosity (Eq. (1b)) for simulating flows with viscosity contrast ([29, Eq. (29c)]). A comparison of both interpolation methods (linear and harmonic mean) is presented on the double-Poiseuille flow in Section 4.1. The local velocity  $\mathbf{u}_\chi$  of each component  $\chi$  is related to the volume averaged velocity  $\mathbf{u}$ , the constant bulk density value  $\rho_\chi$ , and the volume diffusive flow rate  $\mathbf{j}_\chi$  by [28]  $\rho_\chi \mathbf{j}_\chi = \tilde{\rho}_\chi(\mathbf{u}_\chi - \mathbf{u})$  i.e.  $\tilde{\rho}_\chi \mathbf{u}_\chi = \tilde{\rho}_\chi \mathbf{u} + \rho_\chi \mathbf{j}_\chi$ . The mass balance equations for each phase  $g$  and  $l$  writes

$$\frac{\partial \tilde{\rho}_g}{\partial t} + \nabla \cdot (\tilde{\rho}_g \mathbf{u} + \rho_g \mathbf{j}_g) = +\dot{m}''', \quad (2a)$$

$$\frac{\partial \tilde{\rho}_l}{\partial t} + \nabla \cdot (\tilde{\rho}_l \mathbf{u} + \rho_l \mathbf{j}_l) = -\dot{m}''', \quad (2b)$$

where  $\dot{m}'''$  is the volumic production term (+) or sink term (−) due to phase change. Its physical dimension is  $M.L^{-3}.T^{-1}$  and its computation will be discussed in Section 2.3. In Eqs. (2a) and (2b), signs are chosen such as the phase change produces gas phase  $g$  to the detriment of liquid phase  $l$ . The mass flux relative to advection in each phase is  $\tilde{\rho}_\chi \mathbf{u}$ . In interfacial region, the mass flux  $\rho_\chi \mathbf{j}_\chi$  has a diffusive origin and results of a regular transition of composition between two phases. By expressing Eqs. (2a) and (2b) with respect to  $\phi(\mathbf{x}, t)$  and assuming that the fluxes  $\mathbf{j}_g$  and  $\mathbf{j}_l$  are identical and opposite,  $\mathbf{j} = \mathbf{j}_g = -\mathbf{j}_l$ , the following equations are obtained:

$$\frac{\partial \phi}{\partial t} + \nabla \cdot (\mathbf{u}\phi + \mathbf{j}) = +\frac{\dot{m}'''}{\rho_g}, \quad (3a)$$

$$\frac{\partial (1 - \phi)}{\partial t} + \nabla \cdot (\mathbf{u}(1 - \phi) - \mathbf{j}) = -\frac{\dot{m}'''}{\rho_l}, \quad (3b)$$

which after summing yield

$$\nabla \cdot \mathbf{u} = \dot{m}''' \left( \frac{1}{\rho_g} - \frac{1}{\rho_l} \right). \quad (4)$$

To derive the interface tracking equation, in references [28, 38] the flux  $\mathbf{j}$  is assumed to be given by the Cahn-Hilliard flux defined by  $\mathbf{j} = -M_\phi \nabla \mu_\phi$  where  $\mu_\phi$  is the chemical potential. In that case Eq. (3a) becomes the CH equation with a source term of production in the second member. The Navier-Stokes/Cahn-Hilliard (NS/CH) model is very popular for simulations of two-phase flow since more than twenty years (e.g. without LBM [17, 25] and [26–29] with LBM). However the chemical potential can be interpreted as the product of surface tension  $\sigma$  and curvature  $\kappa$  (see details in Section 2.2), and the CH equation imposes in its formulation a motion due to  $\sigma$  and  $\kappa$  even without coupling with a fluid flow. Here, in order to eliminate the curvature-driven interface motion inside the phase-field equation, we assume that the flux is defined by [30, 31]  $\mathbf{j} = -M_\phi (\nabla \phi - 4\phi(1 - \phi)\mathbf{n}/W)$  and Eq. (3a) becomes the conservative Allen-Cahn (CAC) model with a source term:

$$\frac{\partial \phi}{\partial t} + \nabla \cdot (\mathbf{u}\phi) = \nabla \cdot \left[ M_\phi \left( \nabla \phi - \frac{4}{W}\phi(1 - \phi)\mathbf{n} \right) \right] + \frac{\dot{m}'''}{\rho_g}. \quad (5)$$

In Eq. (5),  $M_\phi$  is the interface mobility,  $W$  is the diffuse interface width and

$$\mathbf{n} = \frac{\nabla\phi}{|\nabla\phi|} \quad (6)$$

is the unit normal vector at the interface directed from liquid toward gas. Eq. (5) is the Conservative version of Allen-Cahn (CAC) equation with a source term for modeling interface tracking with phase change. The accuracy of the phase-field simulations depends on two parameters: the interface thickness  $W$  and the mobility  $M_\phi$ . In reference [17, Sec. 5], a discussion is given regarding the numerical convergence of the phase-field method and the choice of those parameters in relation to the discretization step  $\delta x$ . For the Cahn-Hilliard equation, the mobility affects the thickness and perturbation magnitude of the chemical potential boundary layers. Here, for simulations of film boiling, preliminary sensitivity tests are performed on  $M_\phi$  and some details of its effects will be given in Section 5. The choice of  $\dot{m}'''$  will be discussed in Section 2.3. In the original paper [30], this equation is derived by assuming that the total advection velocity is composed of two terms: the external advective velocity  $\mathbf{u}$ , plus the normal velocity to the interface  $u_n \mathbf{n}$ . That velocity  $u_n$  is also defined as the sum of one term depending on the curvature  $\kappa$ , plus one independent of  $\kappa$ :  $u_n \mathbf{n} = (\bar{v} - M_\phi \kappa) \mathbf{n}$ . In the right-hand side of Eq. (5), the first term  $\nabla \cdot \mathbf{j}$  is an equivalent expression to the curvature term that is corrected with a “counter term”  $-M_\phi \kappa |\nabla\phi|$  [40], in order to cancel the curvature-driven interface motion. The derivation is reminded in Appendix A by using the usual definition of curvature  $\kappa = \nabla \cdot \mathbf{n}$  with  $\mathbf{n}$  defined by Eq. (6), and introducing the kernel function

$$\phi = \frac{1}{2} \left[ 1 + \tanh \left( \frac{2\zeta}{W} \right) \right] \quad (7)$$

in order to give an expression of  $|\nabla\phi|$  (see Eq. (A.7) in Appendix A):

$$|\nabla\phi| = \frac{4}{W} \phi(1 - \phi). \quad (8)$$

That choice of kernel function imposes bulk phases for  $\phi = 0$  and  $\phi = 1$ . Similar reasoning that cancels the curvature term can be found in [41] in order to eliminate effects of surface tension (inherent in phase-field models) for membranes embedded in a Newtonian fluid. Let us notice that in this work the standard convention  $0 \leq \phi \leq 1$  is used. Other conventions are possible, particularly when studying two-phase flow with high density ratio e.g.  $-\phi^* \leq \phi \leq \phi^*$  where  $\phi^*$  is defined by  $\rho_g$  and  $\rho_l$  (e.g. [27, Eq. (31)]). More generally, the inequality  $\phi_l \leq \phi \leq \phi_g$  can be chosen. In that case the kernel function (Eq. (7)) and the expression of  $|\nabla\phi|$  must change. Moreover the source term in Eq. (5) must be modified by (see [12, Eq. (188)]):  $\dot{m}'''(\phi_g/\rho_g - \phi_l/\rho_l)$ . Here, that expression is simplified to  $\dot{m}'''/\rho_g$  with the standard choice  $\phi_g = 1$  and  $\phi_l = 0$ .

The temperature equation is derived from the conservation law of total enthalpy  $\rho \mathcal{H}$  where  $\mathcal{H}$  is the enthalpy (physical dimension  $\text{E.M}^{-1}$  where E is used for Energy) as carried out in crystal growth simulations [42]:

$$\frac{\partial(\rho \mathcal{H})}{\partial t} + \nabla \cdot (\mathbf{u} \rho \mathcal{H}) = \nabla \cdot (\mathcal{K} \nabla T) \quad (9)$$

where the diffusive flux is given by the Fourier's law  $\mathbf{j}_T = -\mathcal{K} \nabla T$  with  $T$  being the temperature and  $\mathcal{K}$  the thermal conductivity (physical dimension  $\text{E.T}^{-1}.\text{L}^{-1}.\Theta^{-1}$ ). The enthalpy is defined by  $\mathcal{H} = C_p T + \phi \mathcal{L}$  where  $C_p$  is the specific heat ( $\text{E.M}^{-1}.\Theta^{-1}$ ) and  $\mathcal{L}$  is the latent heat of phase change ( $\text{E.M}^{-1}$ ). With this relation, enthalpies of liquid and gas are respectively equal to  $\mathcal{H}_l = C_p T$  for  $\phi = 0$  and  $\mathcal{H}_g = C_p T + \mathcal{L}$  for  $\phi = 1$ . With those notations and definitions the heat equation for temperature writes

$$\frac{\partial T}{\partial t} + \nabla \cdot (\mathbf{u} T) = \alpha \nabla^2 T - \frac{\mathcal{L}}{C_p} \left[ \frac{\partial \phi}{\partial t} + \nabla \cdot (\mathbf{u} \phi) \right], \quad (10)$$

where  $\alpha = \mathcal{K}/(\rho C_p)$  is the thermal diffusivity, the second term in the right-hand side of Eq. (10) is interpreted as the release (or production) of latent heat during the displacement of the interface. When  $\mathbf{u} = \mathbf{0}$  the movement of the interface is only due to phase change between liquid and gas. Solving only Eq. (5) and (10) must be equivalent to solve the Stefan problem of phase change (see validation of Section 4).

Finally, the complete model of two-phase flows with phase change writes:

$$\nabla \cdot \mathbf{u} = \dot{m}''' \left( \frac{1}{\rho_g} - \frac{1}{\rho_l} \right), \quad (11a)$$

$$\left[ \frac{\partial(\rho \mathbf{u})}{\partial t} + \nabla \cdot (\rho \mathbf{u} \mathbf{u}) \right] = -\nabla p + \nabla \cdot [\eta (\nabla \mathbf{u} + \nabla \mathbf{u}^T)] + \mathbf{F}_{tot}, \quad (11b)$$

$$\frac{\partial \phi}{\partial t} + \nabla \cdot (\mathbf{u} \phi) = \nabla \cdot \left[ M_\phi \left( \nabla \phi - \frac{4}{W} \phi(1 - \phi) \mathbf{n} \right) \right] + \frac{\dot{m}'''}{\rho_g}, \quad (11c)$$

$$\frac{\partial T}{\partial t} + \nabla \cdot (\mathbf{u} T) = \alpha \nabla^2 T - \frac{\mathcal{L}}{C_p} \left[ \frac{\partial \phi}{\partial t} + \nabla \cdot (\mathbf{u} \phi) \right]. \quad (11d)$$

Eqs. (11a) and (11b) are the Navier-Stokes equations for modeling two Newtonian and incompressible fluids. In those equations  $p$  is the pressure,  $\rho(\phi)$  is the density depending on the phase-field  $\phi$  and  $\eta(\phi)$  is the dynamic viscosity.  $\mathbf{F}_{tot}$  is the total force term defined as:

$$\mathbf{F}_{tot} = \mathbf{F}_s + \mathbf{F}_v \quad (12)$$

where  $\mathbf{F}_s$  is the surface tension force that is defined in the next subsection. The volumic force  $\mathbf{F}_v$  is the buoyancy force. Among different formulations of that force [43, Sec. 3.7], in this work the buoyancy is defined such as  $\mathbf{F}_v = (\rho_l - \rho(\phi))\mathbf{g}$  where  $\mathbf{g}$  is the constant acceleration due to the gravity. With that formulation, the gravity acts only on the gas phase for simulations of film boiling in Section 5.

## 2.2. Chemical potential and Cahn-Hilliard equation

The surface tension force  $\mathbf{F}_s$  is expressed here in its potential form [17]:

$$\mathbf{F}_s = \mu_\phi \nabla \phi \quad (13)$$

where  $\mu_\phi$  is the chemical potential which is defined as the change of free energy for a small variation of local composition of mixture:  $\mu_\phi = \delta \mathcal{F} / \delta \phi$ . When the free energy is defined such as  $\mathcal{F}(\phi) = \int_V [\mathcal{V}(\phi) + K |\nabla \phi|^2 / 2] dv$  with  $\mathcal{V}(\phi) = H\phi^2(1 - \phi)^2$ , the chemical potential writes

$$\mu_\phi = 4H\phi(\phi - 1) \left( \phi - \frac{1}{2} \right) - K \nabla^2 \phi. \quad (14)$$

The first term of the right-hand side of Eq. (14) is the derivative of  $\mathcal{V}(\phi)$  with respect to  $\phi$  and the second term comes from the gradient energy term. The double-well ensures minima at  $\phi = 0$  and  $\phi = 1$ . Coefficient  $H$  is the height of double-well and  $K$  is the gradient energy coefficient. It is well-known that the one-dimensional solution at equilibrium (i.e.  $\mu_\phi = 0$ ) of Eq. (14) is the hyperbolic tangent function defined by Eq. (7). A dimensional analysis of  $\mathcal{F}(\phi)$  indicates that  $H$  has the dimension of energy per volume unit, whereas  $K$  has the dimension of energy per length unit. In this formalism, the surface tension  $\sigma$  and the diffuse interface width  $W$  are proportional to the product and the ratio of both coefficients:

$$\sigma = \frac{1}{6} \sqrt{2KH} \quad \text{and} \quad W = \sqrt{\frac{8K}{H}} \quad (15a)$$

We also note that  $\sqrt{KH}$  is homogeneous to an energy per surface unit which corresponds to the physical dimension of surface tension. The term  $\sqrt{K/H}$  is homogeneous to a length as expected for the interface thickness. For the simulations of section 4, values of  $\sigma$  and  $W$  will be set and  $K$  and  $H$  will be derived by inverting those two relationships:

$$K = \frac{3}{2} W \sigma \quad \text{and} \quad H = 12 \frac{\sigma}{W}. \quad (15b)$$

Let us notice that, if we use Eqs. (14) and (15b), the surface tension force  $\mathbf{F}_s = \mu_\phi \nabla \phi$  can be written as  $\mu_\phi \nabla \phi = -(3/2)W\sigma [\nabla^2 \phi - 16\phi(1 - \phi)(1 - 2\phi)/W^2] \nabla \phi$ . The term inside the brackets is the curvature term  $\kappa |\nabla \phi|$  provided that the kernel function Eq. (7) is used for the second term (see Eq. (A.9) in Appendix A). In that case, the surface tension  $\sigma$  and the curvature  $\kappa$  appear explicitly in the definition of the chemical potential  $\mu_\phi$  and the surface tension force is  $\mathbf{F}_s = \mu_\phi \nabla \phi = -(3/2)W\sigma \kappa |\nabla \phi| \nabla \phi$ . Besides, if we set  $K = \varepsilon^2$  and  $H = 1/4$  in Eq. (15a), then we find  $(3/2)W = 6\sqrt{2}\varepsilon$ . The surface tension force is  $\mathbf{F}_s = -\sigma(6\sqrt{2}\varepsilon)(\nabla \cdot \mathbf{n}) |\nabla \phi| \nabla \phi$  which is the same relation in [44, Eq. (13)] provided that the kernel function Eq. (7) is applied for  $\kappa$ . As mentioned earlier, when the diffusive flux is proportional to the gradient of the chemical potential, then the evolution of  $\phi$  follows the Cahn-Hilliard equation:

$$\frac{\partial \phi}{\partial t} + \nabla \cdot (\mathbf{u} \phi) = \nabla \cdot (M_\phi \nabla \mu_\phi), \quad (16)$$

with  $\mu_\phi$  defined by Eq. (14). Compared to the standard CH equation, the main advantage of the conservative Allen-Cahn model lies in the computation of the right-hand side term. Indeed, the CH equation involves a fourth-order derivative because the flux is assumed to be proportional to gradient of chemical potential. A first Laplacian appears in Eq. (14) and a second one appears in the conservative equation Eq. (16). In the conservative Allen-Cahn equation (Eq. (11c)), only the second-order derivative is involved in its definition.

## 2.3. Production rate $\dot{m}'''$

### 2.3.1. Interface velocity of phase change

In sharp interface methods, the surface production rate  $\dot{m}'''$  (physical dimension  $\text{M.L}^{-2}.\text{T}^{-1}$ ) occurs on the separation area between liquid and gas. It is usually defined by [45, 46]  $\dot{m}''' = \rho_g(\mathbf{u}_g - \mathbf{V}_I) \cdot \mathbf{n} = \rho_l(\mathbf{u}_l - \mathbf{V}_I) \cdot \mathbf{n}$  where  $\mathbf{V}_I$  is the velocity of the interface, and  $\mathbf{u}_l$  and  $\mathbf{u}_g$  are respectively the velocities on liquid and gas sides. This relation is derived by integrating the mass conservation across the interface. Integration of the energy conservation yields an additional relation

on  $\dot{m}''$  which can be calculated in its simplest form by the difference of heat fluxes,  $\dot{m}'' = (\mathcal{K}\nabla T|_l - \mathcal{K}\nabla T|_g) \cdot \mathbf{n}/\mathcal{L}$ . The driving force of evaporation is the heat quantity which is transferred at the interface. In [38], the liquid is assumed to be at saturation temperature  $T_{sat}$  and in that case, only the heat quantity of the gas is considered and the temperature equation is solved only in the gas phase. Because of the diffuse interface, the rate  $\dot{m}''$  is transformed to a volumic quantity  $\dot{m}'''$  by  $\dot{m}''' = \dot{m}''|\nabla\phi| = \mathcal{K}\nabla T \cdot \nabla\phi/\mathcal{L}$  where  $\phi$  follows the Cahn-Hilliard equation. The model was extended in [47] to include the gradient of the vapor concentration at the liquid-vapor interface as the driving force for vaporization. The model [38] was also applied in [48] to simulate nucleate pool boiling, including the bubble growth on and periodic departure from a superheated wall. Several other popular mass transfer models are reviewed in [39, Section 4.2] for phase change simulations.

Here, we notice that the source term  $\dot{m}'''/\rho_g$  in Eq. (11c) can be identified as the normal velocity of the interface  $-\tilde{v}|\nabla\phi|$  (see Eq. (A.8) in Appendix A) i.e.  $\dot{m}'''/\rho_g = -\tilde{v}$  (because  $\dot{m}''' = \dot{m}''|\nabla\phi|$ ). In Eq. (11c), the total velocity is the sum of an external velocity  $\mathbf{u}$  plus the interface normal velocity. The latter has also been separated into one velocity depending on the curvature  $-M_\phi\kappa$  (which has been canceled) plus one velocity  $\tilde{v}$  independent of the curvature. That velocity is responsible for the displacement of the interface because of the phase change. Its expression can be approximated by [30, Eq. (A.5)]:

$$\tilde{v} = \frac{\alpha}{\mathcal{A}} \frac{\theta_I - \theta}{W}, \quad (17)$$

where  $\theta$  is the dimensionless temperature defined as  $\theta = (C_p/\mathcal{L})(T - T_{sat})$ ,  $\theta_I$  is the dimensionless interface temperature and  $\mathcal{A}$  is a constant of proportionality that will be specified in section 2.3.2. Finally, if the kernel function  $|\nabla\phi| = (4/W)\phi(1-\phi)$  is used (see Eq. (8)), the source term  $\dot{m}'''/\rho_g$  in Eq. (11c) takes the form

$$\frac{\dot{m}'''}{\rho_g} = -\tilde{v}|\nabla\phi| = -\frac{4\alpha}{\mathcal{A}W^2}(\theta_I - \theta)\phi(1-\phi). \quad (18)$$

### 2.3.2. Value of coefficient $\mathcal{A}$

In order to derive the value of  $\mathcal{A}$  in Eq. (18), we proceed by analogy with the model of phase change for solidification and crystallization [49]. First, Eq. (11c) with Eq. (18) are re-written in order to make appear the derivatives of the double-well potential  $f(\phi)$  and the interpolation function  $p(\phi)$ . Those functions are used in the solidification models derived from variational formulation based on the minimization of free energy [49]. The interface is tracked by Eq. (11c) by assuming that the movement due to curvature is cancelled. That equation can be re-written (see Appendix A):

$$\frac{\partial\phi}{\partial t} + \nabla \cdot (\mathbf{u}\phi) = M_\phi \left[ \nabla^2\phi - \frac{\nabla\phi \cdot \nabla|\nabla\phi|}{|\nabla\phi|} \right] - M_\phi\kappa|\nabla\phi| - \frac{4\alpha}{\mathcal{A}W^2}(\theta_I - \theta)\phi(1-\phi). \quad (19)$$

If the interface temperature is considered at saturation (i.e.  $\theta_I = 0$ ), the source term is simplified to  $(4\alpha/\mathcal{A}W^2)\theta\phi(1-\phi)$ . With the kernel function Eq. (7), the second term in the brackets writes (see Eq. (A.9))  $\nabla\phi \cdot \nabla|\nabla\phi|/|\nabla\phi| = (16/W^2)\phi(1-\phi)(1-2\phi)$ . That term is proportional to the derivative (with respect to  $\phi$ ) of a double-well potential defined by  $f(\phi) = H\phi^2(1-\phi)^2$  with  $H = 1$ , hence  $\nabla\phi \cdot \nabla|\nabla\phi|/|\nabla\phi| = (8/W^2)\partial f/\partial\phi$ . Besides if we set  $K \equiv \varepsilon^2$ , then the two relationships Eqs. (15b) with  $H = 1$  yields  $\varepsilon^2 = W^2/8$ . We also set  $M_\phi = \varepsilon^2/\mathcal{T}$  where  $\mathcal{T}$  is the kinetic time, then Eq. (19) becomes

$$\mathcal{T} \left[ \frac{\partial\phi}{\partial t} + \nabla \cdot (\mathbf{u}\phi) \right] = \varepsilon^2 \nabla^2\phi - \frac{\partial f}{\partial\phi} - \varepsilon^2\kappa|\nabla\phi| - \frac{4\mathcal{T}\alpha}{\mathcal{A}W^2}(\theta_I - \theta)\frac{\partial p}{\partial\phi}. \quad (20)$$

In the right-hand side of Eq. (20), the second term is the derivative of the double-well and the third term is the counter term. The last term is the coupling with temperature which involves the derivative (with respect to  $\phi$ ) of an interpolation function defined as  $p(\phi) = \phi^2/2 - \phi^3/3$ . The factor 4 comes from the choice  $a = 1/2$  in the kernel function (Eq. (A.6)) and we set  $W_0 = W/2$ . If we compare the coupling term of reference [49] with the last term of Eq. (20), we can identify

$$\lambda^* = \frac{\mathcal{T}\alpha}{\mathcal{A}W_0^2}, \quad (21)$$

where  $W_0^2 = W^2/4$  and  $\lambda$  is the coupling coefficient in solidification/crystallization phase-field models. The star of  $\lambda^*$  means it is the particular value of  $\lambda$  that cancels the kinetic coefficient in the Gibbs-Thomson condition recovered by the matched asymptotic analysis of the phase-field model. Hence, that coupling term (Eq. (21)) means this is the particular model of phase change which cancels the kinetic coefficient in the Gibbs-Thomson equation. Besides, the curvature term is also removed by the counter term  $-\varepsilon^2\kappa|\nabla\phi|$ . Finally, the coefficient  $\mathcal{A}$  is identified to the coefficient  $a_2$  in reference [49]. Its value is  $a_2 = 0.6267$  when the phase-field varies between  $-1 \leq \phi \leq +1$  and when the derivative of the interpolating function of temperature is  $p_\phi(\phi) = 1 - \phi^2$  (the index  $\phi$  indicates the derivative with respect to  $\phi$ ). In the present paper, the phase-field  $\phi$  varies between 0 and 1 and the derivative of the polynomial function is  $p_\phi = \phi(1-\phi)$ . Because of those differences, the value of  $\mathcal{A}$  must be computed from integrals obtained from the matched asymptotic expansion of the phase-field model. In Appendix B, details are given to obtain  $\mathcal{A} = 10/48 \approx 0.21$ , value that will be used for all simulations of this paper.

### 3. Lattice Boltzmann schemes

In this Section, we detail the lattice Boltzmann methods that are used to simulate the phase change model of Section 2 composed of Eqs (11a)–(11d) with Eq (13) for surface tension force and Eq. (18) for mass production rate. Simulations are performed by using three distribution functions  $\vartheta_i(\mathbf{x}, t) \equiv \vartheta_i$  for  $\vartheta = f, h, s$  where  $i = 0, \dots, N_{pop}$  and  $N_{pop}$  is the total number of moving directions  $\mathbf{e}_i$  on a lattice (defined below). The first distribution function  $f_i$  is used to recover the Navier-Stokes model (subsection 3.1); the second one  $g_i$  is used for the phase-field equation (subsection 3.2) and the last one  $s_i$  is used for the temperature equation (subsection 3.3). Each distribution function follows its own discrete lattice Boltzmann equation in which the collision term is considered with the Bhatnagar-Gross-Krook (BGK) approximation. That collision operator uses a unique relaxation parameter that is related to the diffusive parameter of the PDE (kinematic viscosity, mobility or diffusion coefficient). Several improvements exist such as the TRT [50] or MRT [51, 52] collision operators. They both use additional relaxation parameters (only one for TRT). With MRT, some of them can be related to physical parameters (e.g. anisotropic diffusion coefficient for transport equation) and the other ones control the stability of the algorithm when increasing the Reynolds number or Péclet number. Hence a wider range of parameters can be reached when simulations are performed with TRT and MRT. Let us mention that other alternatives exist in the literature (entropic, central moments, cumulants, ...) but an in-depth discussion of their benefits and drawbacks is out of the scope of this work. In Eq. (25), each discrete Boltzmann equation is expressed in terms of new variables  $\bar{f}_i$ ,  $\bar{g}_i$  and  $\bar{s}_i$ , each one of them being defined by an appropriate variable change [53] (see details in Appendix C):

$$\bar{\vartheta}_i = \vartheta_i + \frac{\delta t}{2\tau_\vartheta} (\vartheta_i - \vartheta_i^{eq}) - \frac{\delta t}{2} S_i^\vartheta \quad \text{for } \vartheta = f, h, s, \quad (22)$$

where  $\tau_\vartheta$  and  $S_i^\vartheta$  are respectively the collision time and the source term relative to the distribution function  $\vartheta$ ;  $\delta t$  is the time step and  $\vartheta_i^{eq}$  is the equilibrium distribution function. Two other notations are introduced:  $\bar{\tau}_\vartheta$  and  $\vartheta_i^*$ . The first one is the dimensionless collision rate that is defined by  $\bar{\tau}_\vartheta = \tau_\vartheta/\delta t$  for each  $\vartheta$ . The second one is the distribution function that is obtained after the stages of collision and streaming:  $\vartheta_i^* \equiv \vartheta_i(\mathbf{x} + \mathbf{c}_i \delta t, t + \delta t)$ . The use of this variable change (Eq. (22)) modifies the calculation of the zeroth-order moment  $\mathcal{M}_0^\vartheta$  of the distribution function  $\bar{\vartheta}_i$  by (see Appendix C)

$$\mathcal{M}_0^\vartheta = \sum_i \bar{\vartheta}_i + \frac{\delta t}{2} S_i^\vartheta \quad \text{for } \vartheta = f, h, s. \quad (23)$$

It is also useful to introduce the variable change for the equilibrium function (see Appendix C.1)

$$\bar{\vartheta}_i^{eq} = \vartheta_i^{eq} - \frac{\delta t}{2} S_i^\vartheta \quad \text{for } \vartheta = f, h, s, \quad (24)$$

so that, with all those notations, the lattice Boltzmann equation writes

$$\bar{\vartheta}_i^* = \bar{\vartheta}_i - \frac{1}{\bar{\tau}_\vartheta + 1/2} [\bar{\vartheta}_i - \bar{\vartheta}_i^{eq}] + S_i^\vartheta \delta t \quad (25)$$

for each distribution function  $\vartheta = f, h, s$ . Before defining the equilibrium distribution functions and source terms, several lattices are introduced. In this work, the D2Q9 lattice and three 3D lattices are used: D3Q7, D3Q15 and D3Q19 (Fig. 1). For D2Q9 the moving vectors are defined by  $\mathbf{e}_0 = (0, 0)$ ,  $\mathbf{e}_{1,3} = (\pm 1, 0)$ ,  $\mathbf{e}_{2,4} = (0, \pm 1)$ ,  $\mathbf{e}_{5,6} = (\pm 1, 1)$  and  $\mathbf{e}_{7,8} = (\mp 1, -1)$ . for 3D lattices, the moving vectors  $\mathbf{e}_i$  are defined such as  $\mathbf{e}_1 = (1, 0, 0)^T$ ,  $\mathbf{e}_2 = (0, 1, 0)^T$ , ...,  $\mathbf{e}_6 = (0, 0, -1)^T$  for D3Q7 (Fig. 1a). For D3Q15, additional diagonal vectors are defined such as (see Fig. 1b)  $\mathbf{e}_7 = (1, 1, 1)^T$ ,  $\mathbf{e}_8 = (-1, 1, 1)^T$ , ...,  $\mathbf{e}_{14} = (1, -1, -1)^T$ . Finally for D3Q19 (Fig. 1c):  $\mathbf{e}_{7,8} = (\pm 1, 1, 0)^T$ ,  $\mathbf{e}_{9,10} = (\pm 1, -1, -0)^T$ ,  $\mathbf{e}_{11,12} = (\pm 1, 0, 1)$ ,  $\mathbf{e}_{13,14} = (\pm 1, 0, -1)^T$ ,  $\mathbf{e}_{15,16} = (0, \pm 1, 1)^T$ ,  $\mathbf{e}_{17,18} = (0, \pm 1, -1)^T$ . For D3Q7  $N_{pop} = 6$ ,  $e^2 = 1/4$ ,  $w_0 = 1/4$  and  $w_{1,\dots,6} = 1/8$ . For D3Q15  $N_{pop} = 14$ ,  $e^2 = 1/3$ ,  $w_0 = 2/9$ ,  $w_{1,\dots,6} = 1/9$  and  $w_{7,\dots,14} = 1/72$ . For D3Q19  $N_{pop} = 18$ ,  $e^2 = 1/3$ ,  $w_0 = 1/3$ ,  $w_{1,\dots,6} = 1/18$  and  $w_{7,\dots,18} = 1/36$ . The standard notations will be used:  $\mathbf{c}_i = \mathbf{e}_i c$  with  $c = \delta x/\delta t$  where  $\delta x$  and  $\delta t$  are the space- and time-steps respectively and  $c_s^2 = c^2/3$ .

#### 3.1. Incompressible Navier-Stokes

Several lattice Boltzmann schemes exist for incompressible version of Navier-Stokes equations. The fully incompressible condition has already been proposed in literature but necessitates to solve an additional Poisson equation [54] or an additional predictor-corrector step [29]. Here we prefer to apply the artificial compressibility method [55] for which the solenoidal condition  $\nabla \cdot \mathbf{u} = 0$  is approximated by  $(1/\beta)\partial p/\partial t + \nabla \cdot \mathbf{u} = 0$  where  $\beta$  is the artificial compressibility coefficient. In LB framework, the method was derived in [56] with  $\beta = \rho_0 c_s^2$  where  $\rho_0$  is the constant density of bulk phase. The LB scheme writes

$$\bar{f}_i^* = \bar{f}_i - \frac{1}{\bar{\tau}_f + 1/2} [\bar{f}_i - \bar{f}_i^{eq}] + S_i^f \delta t, \quad (26a)$$

$$f_i^{eq} = w_i \left[ p + \rho(\phi) c_s^2 \left( \frac{\mathbf{c}_i \cdot \mathbf{u}}{c_s^2} + \frac{(\mathbf{c}_i \cdot \mathbf{u})^2}{2c_s^4} - \frac{\mathbf{u} \cdot \mathbf{u}}{2c_s^2} \right) \right], \quad (26b)$$



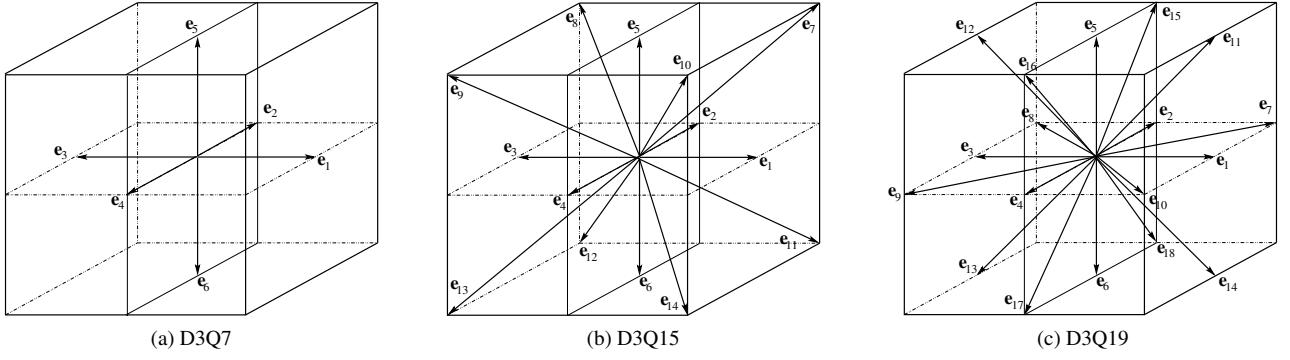


Figure 1: 3D lattices of LB scheme.

with  $\bar{f}_i^{eq} = f_i^{eq} - S_i^f \delta t / 2$  and  $\rho(\phi)$  is given by Eq. (1a). In Eq. (26a)  $\bar{\tau}_f$  is the collision rate which is related to the kinematic viscosity by  $\nu = \bar{\tau}_f c_s^2 \delta t$ . Hence, the collision rate is obtained by  $\bar{\tau}_f(\phi) = 3\nu(\phi)(\delta t / \delta x^2)$  with the kinematic viscosity  $\nu(\phi)$  interpolated by Eq. (1b). In Eq. (26a), the source term  $S_i^f$  contains contributions of external forces (involving  $\mathbf{F}_{tot}$ ) plus the production term in mass conservation (involving  $\dot{m}'''$ ):

$$S_i^f = \mathcal{F}_i^f + \mathcal{P}_i^f \quad (27a)$$

with [57]

$$\mathcal{F}_i^f = (\mathbf{c}_i - \mathbf{u}) \cdot [(\Gamma_i - w_i) \nabla \rho(\phi) c_s^2 + \Gamma_i \mathbf{F}_{tot}], \quad (27b)$$

$$\mathcal{P}_i^f = w_i \rho c_s^2 \dot{m}''' \left( \frac{1}{\rho_g} - \frac{1}{\rho_l} \right). \quad (27c)$$

In Eq. (27b),  $\mathbf{F}_{tot}$  is the external force defined by Eq. (12) and the function  $\Gamma_i \equiv \Gamma_i(\mathbf{u})$  is defined by:

$$\Gamma_i = w_i \left[ 1 + \frac{\mathbf{c}_i \cdot \mathbf{u}}{c_s^2} + \frac{(\mathbf{c}_i \cdot \mathbf{u})^2}{2c_s^4} - \frac{\mathbf{u} \cdot \mathbf{u}}{2c_s^2} \right]. \quad (27d)$$

After the stages of collision and streaming, the first-order moment (momentum) and the zeroth-order moment (pressure) are updated by [57]

$$\rho \mathbf{u} = \frac{1}{c_s^2} \sum_i \bar{f}_i \mathbf{c}_i + \frac{\delta t}{2} \mathbf{F}_{tot}, \quad (28a)$$

$$p = \sum_i \bar{f}_i + \frac{\delta t}{2} \left\{ \mathbf{u} \cdot \nabla \rho c_s^2 + \rho c_s^2 \dot{m}''' \left( \frac{1}{\rho_g} - \frac{1}{\rho_l} \right) \right\}. \quad (28b)$$

### 3.2. Conservative Allen-Cahn model

The lattice Boltzmann equation for the conservative Allen-Cahn model acts on the distribution function  $\bar{g}_i$ . The evolution equation is

$$\bar{g}_i^* = \bar{g}_i - \frac{1}{\bar{\tau}_g + 1/2} [\bar{g}_i - \bar{g}_i^{eq}] + S_i^g \delta t, \quad (29a)$$

$$g^{eq} = \phi \Gamma_i, \quad (29b)$$

with the variable change  $\bar{g}_i^{eq} = g^{eq} - \delta t S_i^g / 2$ . The mobility coefficient is related to the collision rate by  $M_\phi = \bar{\tau}_g c_s^2 \delta t$ . The source term  $S_i^g$  contains two contributions:

$$S_i^g = \mathcal{F}_i^g + \mathcal{P}_i^g, \quad (30a)$$

where the first one  $\mathcal{F}_i^g$  involves the counter term with the normal vector  $\mathbf{n}$  [34], and the second one  $\mathcal{P}_i^g$  involves the mass production term  $\dot{m}'''$ :

$$\mathcal{F}_i^g = \frac{4}{W} \phi (1 - \phi) w_i \mathbf{c}_i \cdot \mathbf{n} \quad \text{and} \quad \mathcal{P}_i^g = w_i \frac{\dot{m}'''}{\rho_g}. \quad (30b)$$

Let us notice that the scheme is equivalent (see Appendix C.2) to the lattice Boltzmann equation

$$\bar{g}_i^* = \bar{g}_i - \frac{1}{\bar{\tau}_g + 1/2} \left[ \bar{g}_i - \bar{g}_i^{eq, CAC} \right] + \mathcal{P}_i^g \delta t \quad (31a)$$

where only the source term  $\mathcal{P}_i^g$  appears in the source term and the equilibrium distribution function is redefined as [33]

$$g_i^{eq, CAC} = \phi \Gamma_i + M_\phi \frac{4}{W} \phi (1 - \phi) w_i \frac{\mathbf{c}_i \cdot \mathbf{n}}{c_s^2} \quad (31b)$$

with  $\bar{g}_i^{eq, CAC} = g_i^{eq, CAC} - \delta t \mathcal{P}_i^g / 2$ .

After the stages of collision and streaming, the new phase-field is obtained by the zeroth-order moment of  $\bar{g}_i$  which must be corrected with the production term:

$$\phi(\mathbf{x}, t) = \sum_i \bar{g}_i + \frac{\delta t}{2} \sum_i \mathcal{P}_i^g. \quad (32)$$

This relation holds for both formulations that use  $\bar{g}_i^{eq}$  and  $\bar{g}_i^{eq, CAC}$  because  $\sum_i \mathcal{F}_i^g \delta t / 2 = 0$ .

### 3.3. Temperature equation

The lattice Boltzmann scheme for temperature equation writes:

$$\bar{s}_i^* = \bar{s}_i - \frac{1}{\bar{\tau}_s + 1/2} \left[ \bar{s}_i - \bar{s}_i^{eq} \right] + \mathcal{S}_i^s \delta t \quad (33a)$$

$$s_i^{eq} = T \Gamma_i \quad (33b)$$

where the thermal diffusivity  $\alpha$  is related to the collision rate by  $\alpha = \bar{\tau}_s c_s^2 \delta t$ . The source term  $\mathcal{S}_i^s$  is defined such as:

$$\mathcal{S}_i^s = \mathcal{F}_i^s + \mathcal{P}_i^s \quad (33c)$$

where

$$\mathcal{F}_i^s = w_i \frac{\mathcal{L}}{C_p} \nabla \cdot (\mathbf{u} \phi) \quad \text{and} \quad \mathcal{P}_i^s = w_i \frac{\mathcal{L}}{C_p} \frac{\partial \phi}{\partial t} \quad (33d)$$

Finally, the new temperature is computed by

$$T = \sum_i \bar{s}_i - \frac{\delta t}{2} \frac{\mathcal{L}}{C_p} \left[ \frac{\partial \phi}{\partial t} + \nabla \cdot (\mathbf{u} \phi) \right]. \quad (34)$$

In Sections 4 and 5, simulations will be carried out with Dirichlet boundary conditions applied on temperature  $T$  and phase-field  $\phi$ . In order to impose such a condition, for example on temperature  $T_w$  on left boundary of a D2Q9 lattice, the unknown distribution functions  $\bar{s}_i|_{unknown}$  are updated with the anti bounce-back method [58]:  $\bar{s}_i|_{unknown} = -\bar{s}_{i'} + 2w_i T_w$  where  $i'$  is the opposite direction of  $i$ .

### 3.4. Computations of gradients and Laplacian

The unit normal vector  $\mathbf{n}$  and force term  $\mathbf{F}_s$  require computation of gradients. Moreover the chemical potential  $\mu_\phi$  necessitates to calculate the Laplacian of  $\phi$ . Gradients and Laplacian that are involved in definitions of  $\mathbf{n}$  (Eq. (6)) and  $\mu_\phi$  (Eq. (14)) are discretized by using the directional derivatives methods. The method has already demonstrated its performance for hydrodynamics problem in order to reduce parasitic currents for two-phase flow problem [28, 59, 60]. The directional derivative is the derivative along each moving direction on the lattice. Taylor's expansion at second-order of a differentiable scalar function  $\phi(\mathbf{x})$  at  $\mathbf{x} + \mathbf{e}_i \delta x$  and  $\mathbf{x} - \mathbf{e}_i \delta x$  yields the following approximation of directional derivatives:

$$\mathbf{e}_i \cdot \nabla \phi|_{\mathbf{x}} = \frac{1}{2\delta x} [\phi(\mathbf{x} + \mathbf{e}_i \delta x) - \phi(\mathbf{x} - \mathbf{e}_i \delta x)] \quad (35a)$$

The number of directional derivatives is equal to the number of moving direction  $\mathbf{e}_i$  on the lattice i.e.  $N_{pop}$ . The gradient is obtained by

$$\nabla \phi|_{\mathbf{x}} = 3 \sum_{i=1}^{N_{pop}} w_i \mathbf{e}_i (\mathbf{e}_i \cdot \nabla \phi|_{\mathbf{x}}). \quad (35b)$$

Intel CPUs	NVidia GPUs	ARM	IBM	AMD
Sandy/Ivy Bridge	Kepler	ThunderX	Blue gene Q	AMD CPUs
Haswell	Maxwell	ARMv8.0	Power7	
Skylake	Pascal	ARMv8.1	Power8	
Westmere CPUs	Volta		Power9	
Knights Landing/Corner Xeon Phi	Turing			
Broadwell Xeon E-class				

Table 1: List of architectures that are currently compatible with the `Kokkos` library.

The three components of the gradient  $\partial_x\phi$ ,  $\partial_y\phi$  and  $\partial_z\phi$  are obtained by calculating each directional derivative  $\mathbf{e}_i \cdot \nabla\phi|_{\mathbf{x}}$  and next, by calculating the moment of first-order  $\nabla\phi|_{\mathbf{x}}$ . For the calculation of  $\nabla^2\phi$ , all directions of propagation are taken into account by

$$(\mathbf{e}_i \cdot \nabla)^2\phi|_{\mathbf{x}} = \frac{1}{\delta x^2} [\phi(\mathbf{x} + \mathbf{e}_i\delta x) - 2\phi(\mathbf{x}) + \phi(\mathbf{x} - \mathbf{e}_i\delta x)]. \quad (36a)$$

The Laplacian is obtained by summing and weighting each term with

$$\nabla^2\phi|_{\mathbf{x}} = 3 \sum_{i=1}^{N_{pop}} w_i (\mathbf{e}_i \cdot \nabla)^2\phi|_{\mathbf{x}}. \quad (36b)$$

Other approximations exist [28, 61] such as the first-order and second-order upwind schemes (or biased differences) respectively defined by  $\mathbf{e}_i \cdot \nabla^{up1}\phi|_{\mathbf{x}} = [\phi(\mathbf{x} + \mathbf{e}_i\delta x) - \phi(\mathbf{x})]/\delta x$  and  $\mathbf{e}_i \cdot \nabla^{up2}\phi|_{\mathbf{x}} = [-\phi(\mathbf{x} + 2\mathbf{e}_i\delta x) + 4\phi(\mathbf{x} + \mathbf{e}_i\delta x) - 3\phi(\mathbf{x})]/(2\delta x)$ . Here, by simplicity, the central difference approximation is applied for all simulations even though that approximation fails to capture the velocity profiles in low density regions [62] and biased directional derivatives can fix that issue [2]. Those biased differences could be tested in future works with `LBM_saclay`.

### 3.5. Numerical implementation and kernel optimization

All LBM schemes of this Section were implemented in a new code called `LBM_saclay` written in C++. The main advantage of this new code is its portability targeting all major HPC platforms and especially those based on GPU- and CPU-architectures. Actually, `LBM_saclay` can run without modification on any architecture that `Kokkos` supports. The current compatibilities are indicated in [63] and summarized in Tab. 1. For more information, the reader can refer to the `Kokkos` documentation. Let us mention that the current support for AMD GPU is experimental through the C++ library `HIP` (Heterogeneous-Compute Interface for Portability) and it is planned to be supported at the end of 2020.

Two levels of parallelism are implemented in the code. The first one is the intra-node parallelism (shared memory) with the `Kokkos` library, an opensource C++ library with parallel algorithmic patterns and data containers. Specific commands of the `Kokkos` library optimize loops with `OpenMP`, `Pthreads` or `CUDA` during compilation. An example of using `Kokkos`' functionalities is presented on Fig. 2 to compute at each time-step the zeroth-order moment of a distribution function. The second level of parallelism is a standard domain decomposition performed with `MPI`: the full computational domain is cut into several sub-domains associated with each computational node (distributed memory).

When developing the code, several optimizations were implemented and compared in particular to enhance its performance on each architecture. The first way to consider the stages of collision and streaming is to “fuse” those two steps inside a single kernel, i.e. both stages are simply done in one single “for-loop” performed on the lattice nodes. The “fused” version does not require an intermediate memory load contrary to standard implementation for which both stages are well separated. However, the fused kernel contains more floating point operations per iteration of the “for-loop”. This is a drawback if the number of floating point operations becomes large enough to exhaust the amount of register memory available on the architecture (this number is significantly lower on GPU than on CPU). So, if the register memory is full, additional variables will be allocated in the external DRAM memory, generating additional traffic on the memory bus and degrading performance. For GPUs `NVIDIA`® and CPUs `Intel`® `Skylake`, best performance is obtained with the fused version.

Alternatively, two optimizations were tested which are well suited for `Intel`® `KNL` (`KNights Landing`) processors [64]: the first one is the “CSoA” optimization (Cluster of Structure of Array) i.e. for each line of the lattice, LBM nodes are stored in memory modulo  $M$  where typically  $M = 8$  and each line is padded to be a multiple of  $M$ . The access of data container is done with `data(iMem, j, k, ipop)` where `iMem` is computed from the physical node location `i`. The CSoA optimization improves vectorization and memory alignment for streaming stage but performance decreases for large domain on `D2Q9` lattice. The second optimization for `KNL` is “CSoA2”, i.e. the population index `ipop` of `data(i, j, k, ipop)` is interverted to `data(i, ipop, j, k)`, where `i, j, k` are indices of position. With this permutation, the memory locality is restored for the collision stage.

Comparisons were performed on a simplified diffusive problem. The CSoA2 optimization enhances performance on `KNL` processors, but on Fig. 3, we can see that it remains far below to that obtained on GPUs, even older generation GPUs (`K80`). Computational times are expressed in Million Lattice Updates per Second (MLUPS) as an effective metric measuring

```

class CalcMoment0_Functor {
public:
    CalcMoment0_Functor(/* ... */) { /* ... */};
    KOKKOS_INLINE_FUNCTION
    void operator()(const int& index) const {
        const int isize = /* Lattice's maximum x-axis index. */;
        const int jsize = /* Lattice's maximum y-axis index. */;
        const int npop = /* Lattice's direction count. */;
        int i, j;
        /* Maps the 1D dispatch index to the 2D node index. */
        index2coord(index, i, j, isize, jsize);
        if (j < jsize && i < isize) {
            double mom = 0;
            for (int k = 0; k < npop; ++k) {
                mom = mom + f(i, j, k);
            }
            density(i, j) = mom;
        }
    }

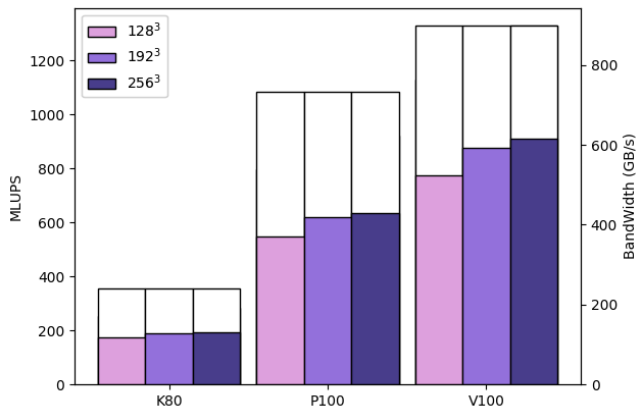
    // Multi-dimensional containers allocated on the CPU or GPU.
    Kokkos::View<double**, Device> density; /* 2 space dimensions. */
    Kokkos::View<double***, Device> f; /* 2 space dimensions, */
    /* + 1 velocity dimension */

};

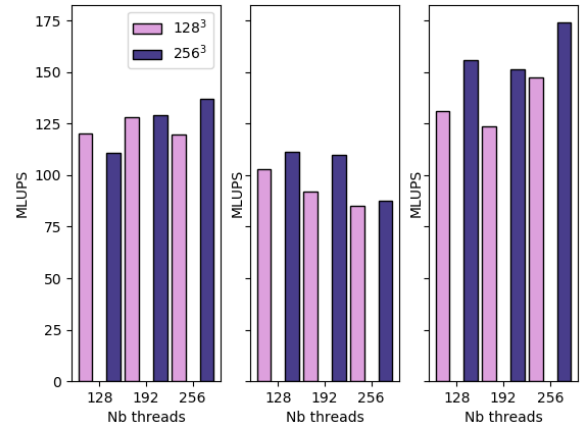
// Elsewhere in the code, the CalcMoment0_Functor's operator() can be
// dispatched by Kokkos.
CalcMoment0_Functor functor(/* ... */);
const int iter_count = isize*jsize;
Kokkos::parallel_for(iter_count, functor);

```

Figure 2: Example of using the Kokkos library to compute the zeroth-order moment of distribution function.



(a) Comparison of computational times for three NVIDIA<sup>®</sup> graphical cards: K80 (oldest), P100 and V100 (newest).



(b) Comparisons of computational times for three optimizations of LBM kernel for Intel<sup>®</sup> KNL: fused (left), CSoA (middle) and CSoA2 (right).

Figure 3: Computational times (in Million Lattice Updates Per Second – MLUPS) for a diffusive problem with a D3Q19 lattice. (a) GPU for three mesh sizes and (b) on CPU (Intel<sup>®</sup> KNL) for two mesh sizes.

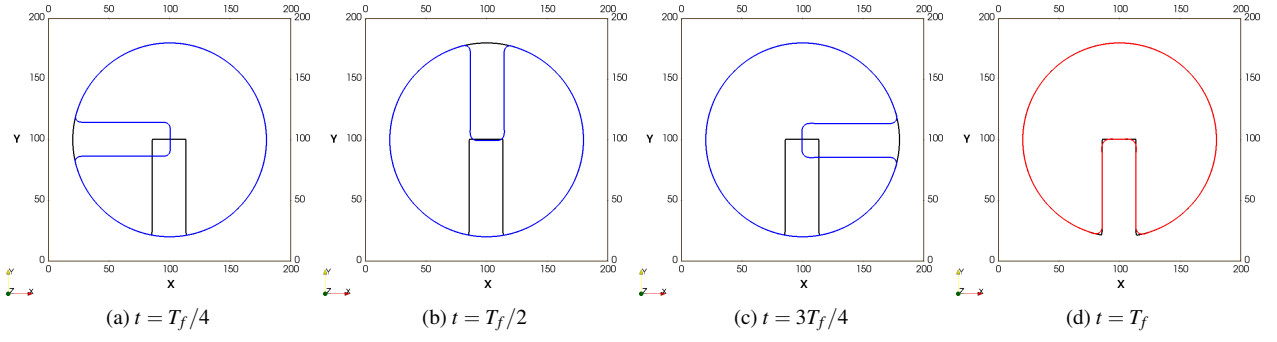


Figure 4: Zalesak's slotted disk with the conservative Allen-Cahn model.

the number of millions of node lattice update per seconds. That performance metric is used by node so that it is independent of the type of lattice (e.g. D3Q7, D3Q15, D3Q19). With that metric, a larger lattice will give a smaller MLUPS. In the rest of this paper, most of validations and simulations of Sections 4 and 5 are carried out on GPUs. In Section 5.3, comparisons of computational times on GPU and CPU will be presented on the test case of film boiling for two mesh sizes.

Finally, let us mention that all kernels (Navier-Stokes, phase-field and temperature equations) have been developed in 2D and in 3D. They all run in 3D separately. However, all coupling terms, i.e. the surface tension force (Eq. (13)), the chemical potential (Eq. (14)) and the advective term in Eq. (33d)) were developed and checked only in 2D. Hence, verification of couplings in Section 4 and film boiling simulations of Section 5 will be presented only in 2D. The three-dimensional extension of coupling terms is planned for future works.

#### 4. Code verifications

In this section, the numerical implementation of the LBM schemes of Section 3 is checked by comparison with well-known solutions. Validations are gathered into two parts in order to check implementations step-by-step. In subsection 4.1, verifications are done without phase change, i.e. by neglecting the temperature equation and by assuming that the mass transfer is zero ( $\dot{m}''' = 0$  in Eq. (11a) and (11c)). The conservative Allen-Cahn model, and the coupling with fluid flow are verified successively. In subsection 4.2, the phase change model is checked by considering the phase-field equation coupled with temperature. The LBM code is compared with an analytical solution of Stefan's problem with two different diffusivities.

##### 4.1. Verifications without phase change

We first compare implementation of the conservative Allen-Cahn model on two test cases: Zalesak's slotted disk and interface deformation inside a vortex. Next the coupling with Navier-Stokes model will be considered with the layered Poiseuille flow and the Laplace law.

###### 4.1.1. Verifications of the phase-field model

Two verifications of phase-field implementation are presented. In the first one, we check that the contour of a slotted disk is well conserved inside a rotating fluid [65]. In the second one, we check that the simulation retrieves a circle when an initial disk is deformed inside a vortex that changes its direction of rotation over time. For both simulations, the mesh is composed of  $201 \times 201 \times 3$  nodes with periodic boundary conditions applied on all faces, the time-step is  $\delta t = 10^{-4}$  and the space-step  $\delta x = 5 \times 10^{-3}$ .

**Zalesak's slotted disk.** Inside a domain of lengths  $L_x = L_y = 1$ , and  $L_z = 0.01$ , a disk is initialized at the center of the domain  $\mathbf{x}_c = (100, 100, 1)^T$  by  $\phi(\mathbf{x}, 0) = \left[ 1 + \tanh \left( (R - d_c) / \sqrt{2} W_0 \right) \right] / 2$  with  $d_c = \sqrt{(x - x_c)^2 + (y - y_c)^2 + (z - z_c)^2}$ ,  $W_0 = 2$  and  $R = 80$  l.u. (lattice units). The diffuse disk is slotted by imposing  $\phi(\mathbf{x}, 0) = 0$  if  $x_c - R/6 \leq x \leq x_c + R/6$  and  $y_c - 1.1R \leq y \leq y_c$ . Components of velocity are imposed by  $u_x(\mathbf{x}) = u_0(2y - 1)$ ,  $u_y(\mathbf{x}) = u_0(1 - 2x)$  and  $u_z(\mathbf{x}) = 0$ . The value of  $u_0$  is chosen such that the slotted disk performs one complete rotation at  $T_f = 4$ , i.e.  $u_0 = 0.7853975$  and both parameters of CAC model are set as  $M_\phi = 5 \times 10^{-4}$  and  $W = 6\delta x$ . The rotation of the slotted disk is presented on Fig. 4 where the interface position  $\phi = 1/2$  is superimposed to the initial condition at four times. At the final time of simulation  $t = T_f$  (Fig. 4d), the contour  $\phi = 0.5$  (red) is superimposed to the initial one (black) although the slot corners are slightly rounded.

**Vortex.** We study the deformation of an initial disk standing inside a 2D vortex. The three components of velocity are defined by  $u_x(\mathbf{x}) = -u_0 \cos[\pi(x - 0.5)] \sin[\pi(y - 0.5)]$ ,  $u_y(\mathbf{x}) = u_0 \sin[\pi(x - 0.5)] \cos[\pi(y - 0.5)]$  and  $u_z(\mathbf{x}) = 0$ . LB simulations are performed on a D3Q19 lattice for a 3D domain with a very small thickness in  $z$ -direction. The initial condition  $\phi(\mathbf{x}, 0)$  is defined by a full disk centered at  $\mathbf{x}_c = (100, 60, 1)^T$ , with  $W = 2$  and  $R = 40$  l.u. The initial condition ( $\phi = 0.5$ ) and streamlines for  $u_0 = 0.7853975$  are presented on Fig. 5a-(i). The rotation is directed counterclockwise. Parameters are

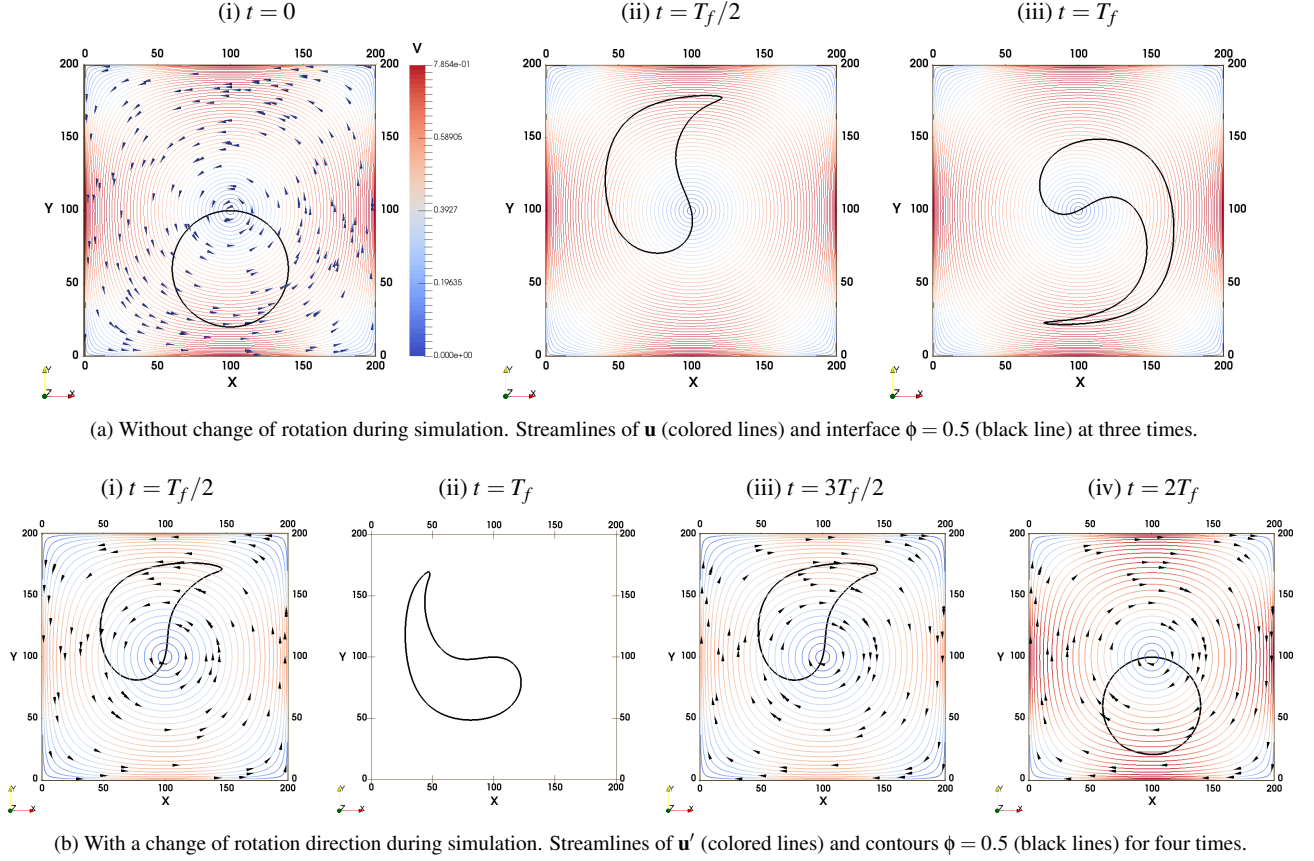


Figure 5: Deformation of an initial disk standing inside a vortex. (a) Without change of rotation during simulation. (b) With change of rotation.

$T_f = 4$ ,  $W = 6\delta x$  and  $M_\phi = 5 \times 10^{-4}$ . For  $t = T_f/2$  (Fig. 5a-(ii)) and  $t = T_f$  (Fig. 5a-(iii)) black contours  $\phi = 0.5$  are comparable to those presented in reference [32, Fig. 4]. Next, the velocity is changed during the simulation by multiplying  $\mathbf{u}(\mathbf{x})$  with a factor depending on time:  $\mathbf{u}'(\mathbf{x}, t) = \mathbf{u}(\mathbf{x}) \times \cos(\pi t/2T_f)$ . With the cosine function, the velocity  $\mathbf{u}'(\mathbf{x}, t)$  presents three stages during the simulation: when  $t < T_f$ , the direction of rotation is counterclockwise (Fig. 5b-(i)); when  $t = T_f$  the cosine function cancels the velocity  $\mathbf{u}'$  (Fig. 5b-(ii)); and when  $t > T_f$ , the sign changes and the direction of rotation becomes clockwise (Fig. 5b-(iii)). At the end of simulation  $t = 2T_f$ , we expect to find the shape of initial disk. That is what we observe on Fig. 5b-(iv) which confirms that the interface position  $\phi = 0.5$  is similar to the initial condition one (Fig. 5a-(i)).

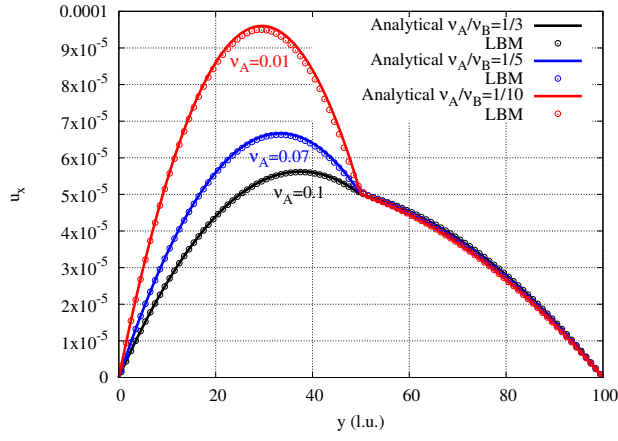
#### 4.1.2. Verifications of phase-field with fluid flow model

Two classical test cases are presented to check the coupling of phase-field equation and fluid flow model: the layered Poiseuille flow and the Laplace law.

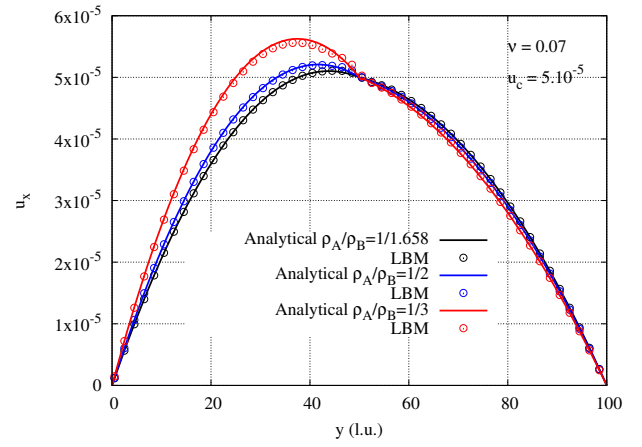
*Layered Poiseuille flow.* The Navier-Stokes implementation is checked with the analytical solution of a layered Poiseuille flow [29] for two fluids named A and B:

$$u_x(y) = \begin{cases} \frac{Gh^2}{2\eta_A} \left[ -\left(\frac{y}{h}\right)^2 - \frac{y}{h} \left( \frac{\eta_A - \eta_B}{\eta_A + \eta_B} \right) + \frac{2\eta_A}{\eta_A + \eta_B} \right] & (-h \leq y \leq 0) \\ \frac{Gh^2}{2\eta_B} \left[ -\left(\frac{y}{h}\right)^2 - \frac{y}{h} \left( \frac{\eta_A - \eta_B}{\eta_A + \eta_B} \right) + \frac{2\eta_B}{\eta_A + \eta_B} \right] & (0 \leq y \leq h) \end{cases} \quad (37)$$

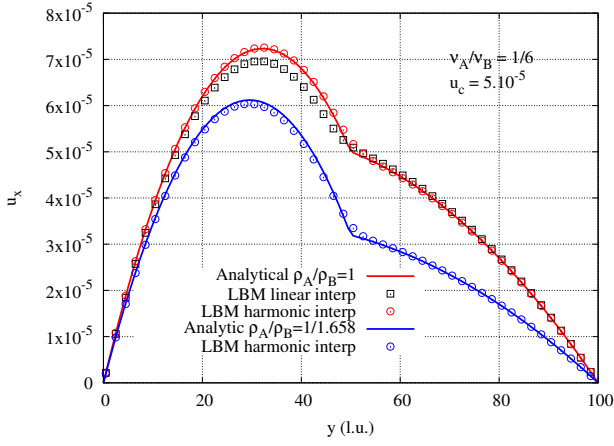
where  $\eta_A$  and  $\eta_B$  are the dynamic viscosities and  $2h$  is the channel width. The pressure gradient is defined by  $G = u_c(\eta_A + \eta_B)/h^2$  with  $u_c = 5 \times 10^{-5}$ . For the LB simulation, the mesh is composed of  $101 \times 101 \times 3$  nodes and the pressure gradient is replaced by a force term defined by  $\mathbf{F} = (G, 0, 0)^T$ . Periodic boundary conditions are set for all limits except for planes of normal vector directed in  $y$ -direction where no-slip conditions are imposed with the half bounce-back method. Two layers of different viscosity are defined as initial condition for  $\phi$ :  $\phi(\mathbf{x}, 0) = 0.5\{1 + \tanh[2(y - y_0)/W]\}$  where  $W = 6\delta x$  controls the slope of the hyperbolic tangent function and  $y_0 = (y_{\max} + y_{\min})/2$ . The mobility coefficient is  $M_\phi = 0.1$ . Comparisons between the LBM code and the analytical solution are presented for two cases. In the first one, the density is identical for both fluids ( $\rho_A = \rho_B = 1$ ) and three viscosity ratios are checked on Fig. 6a:  $\eta_B/\eta_A = 1/3, 1/5, 1/10$ . For the first ratio  $\nu_A = 0.1$  and  $\nu_B = 0.3$ ; for the second one  $\nu_A = 0.07$  and  $\nu_B = 0.35$  and for the third one  $\nu_A = 0.01$  and  $\nu_B = 0.1$ . For the second test case, the viscosity of each phase is set equal to  $\nu_A = \nu_B = 0.07$  and three density ratios are checked on Fig. 6b:  $\rho_A/\rho_B = 1/1.658, 1/2, 1/3$ . The ratio  $1/1.658$  is used in the simulations of film boiling as well as the viscosity ratio  $\nu_A/\nu_B = 1/6$ . In Fig. 6c this viscosity ratio is checked for two cases. In the first simulation (red curve), the density ratio is



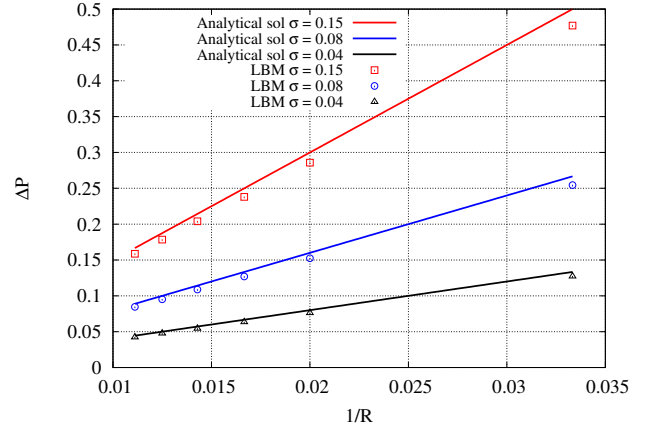
(a) Comparisons between LBM and the double-Poiseuille analytical solution for three viscosity ratios and  $\rho_A/\rho_B = 1$ .



(b) Comparisons between LBM and the double-Poiseuille analytical solution for three density ratios and  $v_A/v_B = 1$ .



(c) Red line – comparisons between two interpolation methods of viscosity: linear (black squares) and harmonic mean (red circles) defined by Eqs. (38) and (1b) respectively. Blue line – verification for  $\rho_A/\rho_B = 1/1.658$ .



(d) Laplace's law verification for three values of surface tension.

Figure 6: Verification of coupling between the phase-field equation and fluid flow model without phase change. (a) Double-Poiseuille flow with three viscosity ratios. (b) Double-Poiseuille for three density ratios. (c) Effect of linear interpolation and harmonic mean of viscosity. (d) Laplace law.

equal to one and the viscosity is interpolated by two methods: the linear (black squares) and the harmonic mean (red circles) defined by

$$v(\phi) = [1 - \phi(\mathbf{x}, t)]v_A + \phi(\mathbf{x}, t)v_B, \quad (38)$$

and Eq. (1b) respectively. The differences observed with the former method justify the choice of using the latter in the second simulation (blue curve) which combines both ratios of viscosity and density.

**Laplace law.** The two-dimensional Laplace law is checked by initializing a drop at the center of a square domain of length  $L_x = L_y = 2.56$  discretized with  $256 \times 256$  nodes. By varying the radius  $R$ , the difference between pressure inside the drop ( $p_{in}$ ) minus the pressure outside ( $p_{out}$ ) must vary proportionally with the surface tension  $\sigma$ :

$$p_{in} - p_{out} = \frac{\sigma}{R}. \quad (39)$$

In order to check that relationship, an initial drop of radius  $R$  and surface tension  $\sigma$  is initialized at the center of the domain ( $x_c = y_c = 1.28$ ). The density ratio  $\rho_g/\rho_l$  is set equal to two ( $\rho_g = 2, \rho_l = 1$ ) and the viscosities are identical for each phase:  $v_l = v_g = 0.04$ . The interface parameters are  $M_\phi = 0.04$  and  $W = 0.05 = 5\delta x$ . The LBM code is run with a time-step equal to  $\delta t = 10^{-4}$  until the stationary solution is obtained. At the end of simulation, the difference between numerical pressures  $\Delta p = p_{in} - p_{out}$  is plotted for three values of surface tension  $\sigma = 0.04, 0.08, 0.15$ . For each value of surface tension, six LBM simulations are run for six values of radius corresponding to each dot on Fig. 6d. On that plot, the slopes of LBM vary linearly and fit quite well to the Laplace law.

#### 4.2. Verifications with phase change: one-dimensional Stefan problem

In this section, we consider the problem of phase change without flow ( $\mathbf{u} = \mathbf{0}$ ). The objective is to validate the coupling between equations of phase-field and temperature. More precisely, we check the new approximation (Eq. (18)) of mass

production rate  $\dot{m}'''$  in the phase-field equation (Eq. (11c)) and the latent heat release in the temperature equation (Eq. (11d)), i.e. the source term  $-\partial\phi/\partial t$ . Validation is carried out with the Stefan problem for which several analytical solutions exist [66, Chapter 12]. Here we consider one of the most general one-dimensional problem where the three unknowns are the interface position varying with time  $x_I(t)$ , the liquid temperature  $T_l(x, t)$  and the gas temperature  $T_g(x, t)$ . Besides, the thermal diffusivities of each phase  $\alpha_l$  and  $\alpha_g$  can be different. The one-dimensional domain  $]0, \infty[$ , is initially filled with gas with constant temperature  $T_g(x, t)|_{x>0, t=0} = T_\infty$  that is greater than the saturation temperature  $T_{sat}$ . The left wall  $x = 0$  is maintained at  $T_w$  for  $t \geq 0$ . As a result, condensation starts at the boundary  $x = 0$  and the liquid-gas interface propagates in the positive direction. At  $x \rightarrow \infty$ , the temperature is kept at  $T_\infty$ .

*Analytical solutions.* The mathematical formulation of this problem writes [66, Section 12-3]

$$\frac{\partial T_l}{\partial t} = \alpha_l \frac{\partial^2 T_l}{\partial x^2} \quad (40a)$$

for  $0 < x < x_I(t)$ , with the left boundary condition imposed at  $T_l(x, t)|_{x=0} = T_w$ . The evolution of the gas phase is formulated as

$$\frac{\partial T_g}{\partial t} = \alpha_g \frac{\partial^2 T_g}{\partial x^2} \quad (40b)$$

for  $x_I(t) < x < \infty$  with  $T_g(x \rightarrow \infty, t) = T_\infty$ , with the initial condition  $T_g(x, t = 0) = T_\infty$  and boundary condition  $T_g(x \rightarrow \infty, t) = T_\infty$ . Interfacial conditions are specified by

$$T_l(x, t)|_{x=x_I(t)} = T_g(x, t)|_{x=x_I(t)} = T_I, \quad (40c)$$

$$\mathcal{K}_l \frac{\partial T_l}{\partial x} \Big|_{x=x_I(t)} - \mathcal{K}_g \frac{\partial T_g}{\partial x} \Big|_{x=x_I(t)} = \rho \mathcal{L} \frac{dx_I(t)}{dt}. \quad (40d)$$

In Eq. (40d),  $\mathcal{K}_l$  and  $\mathcal{K}_g$  are the thermal conductivities of each phase. We consider identical specific heat  $C_p^l = C_p^g = C_p$  and we set  $C_p = 1$ ,  $\mathcal{L} = 1$  and  $\rho = 1$ . Solutions of interface position and temperature profiles [66, p. 469] are

$$x_I(t) = 2\xi\sqrt{\alpha_l t}, \quad (41a)$$

$$\theta_l(x, t) = \theta_w + (\theta_I - \theta_w) \frac{\text{erf}(x/2\sqrt{\alpha_l t})}{\text{erf}(\xi)}, \quad (41b)$$

$$\theta_g(x, t) = \theta_\infty + (\theta_I - \theta_\infty) \frac{\text{erfc}(x/2\sqrt{\alpha_g t})}{\text{erfc}(\xi\sqrt{\alpha_l/\alpha_g})}, \quad (41c)$$

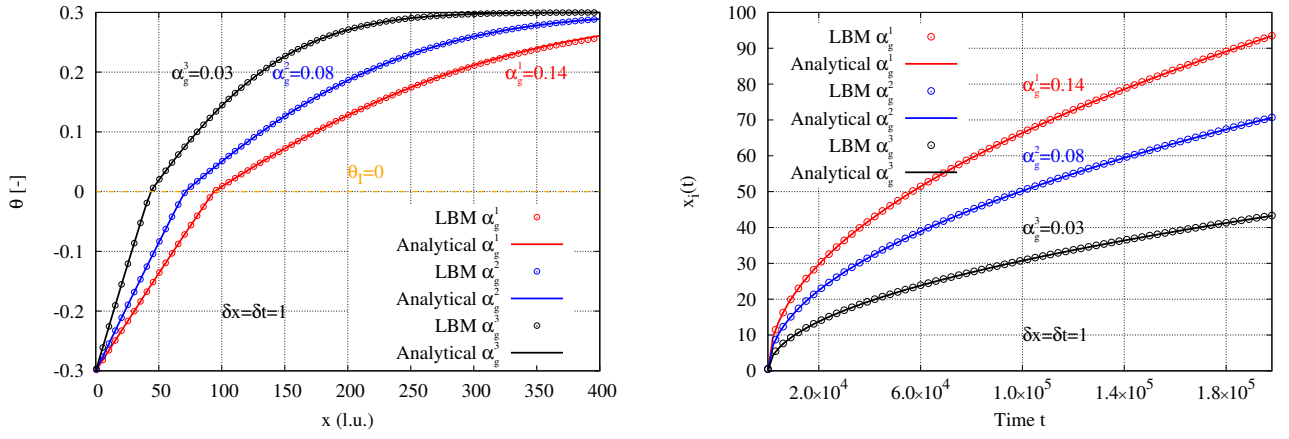
where the temperatures are re-written in dimensionless form with  $\theta = C_p(T - T_{sat})/\mathcal{L}$ . When  $\theta = 0$  the temperature of system is at saturation temperature  $T_{sat}$  and when  $\theta > 0$  (resp.  $\theta < 0$ ), the system is superheated (resp. undercooled). In Eqs. (41a)–(40d),  $\xi$  is solution of the transcendental equation

$$\frac{e^{-\xi^2}}{\text{erf}(\xi)} + \left(\frac{\alpha_g}{\alpha_l}\right)^{1/2} \frac{\theta_I - \theta_\infty}{\theta_I - \theta_w} \frac{e^{-\xi^2(\alpha_l/\alpha_g)}}{\text{erfc}(\xi\sqrt{\alpha_l/\alpha_g})} = -\frac{\xi\sqrt{\pi}}{\theta_w} \quad (41d)$$

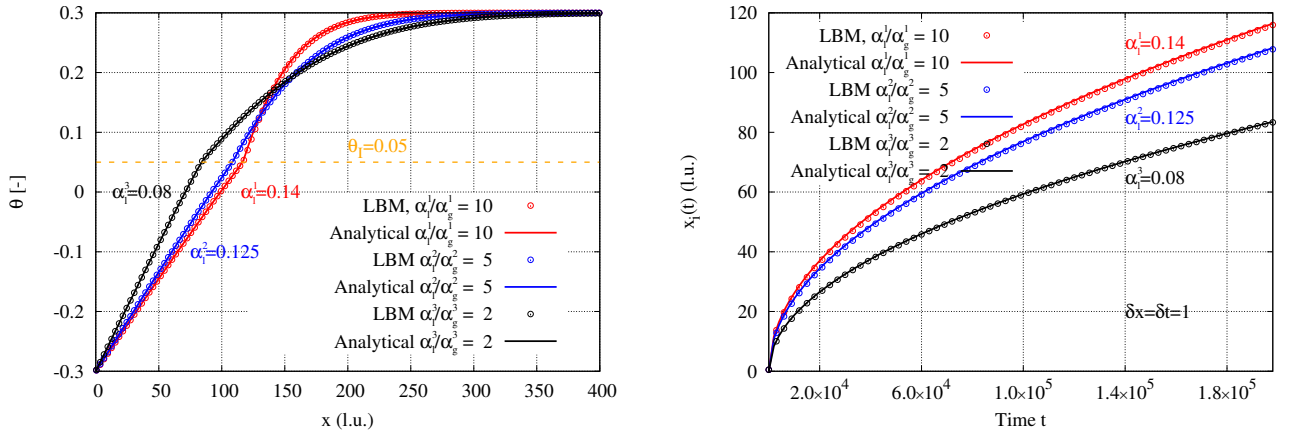
where  $\theta_w$  in the right-hand side is the Stefan number defined by  $St = C_p(T_w - T_{sat})/\mathcal{L}$ . Those solutions are compared with LBM\_saclay, first with identical thermal diffusivities  $\alpha_l = \alpha_g$  and an interface temperature  $\theta_I$  equals to zero. The second validation considers three ratios of diffusivity  $\alpha_l^j/\alpha_g^j$  (for  $j = 1, 2, 3$ ) with an interface temperature which is different of the saturation one ( $\theta_I \neq 0$ ).

*Data entry of LBM simulations.* For LBM simulations, the two-dimensional D2Q9 lattice is used for the temperature and phase-field equations. The LBM computational domain is  $[\ell_x, L_x] \times [\ell_y, L_y] = [0, 512] \times [0, 32]$  which is discretized by  $N_x \times N_y = 512 \times 32$  nodes i.e.  $\delta x = 1$ . The time-step is also set to  $\delta t = 1$ . Boundary conditions are periodic for  $s_i$  and  $g_i$  at  $\ell_y$  and  $L_y$  (bottom and top walls respectively) and Dirichlet boundary conditions are applied on left ( $x = \ell_x$ ) and right ( $x = L_x$ ) walls by anti-bounceback method on  $g_i$  and  $s_i$ . For phase-field, the Dirichlet boundary conditions are  $\phi(x, t)|_{x=\ell_x} = 0$  and  $\phi(x, t)|_{x=L_x} = 1$ . For the temperature equation, they are  $\theta(x, t)|_{x=\ell_x} = \theta_w$  and  $\theta(x, t)|_{x=L_x} = \theta_\infty$ . The temperature is initialized with  $\theta(x, 0) = \theta_\infty$  for  $0 < x \leq L_x$  and the phase-field with  $\phi(x, 0) = 0.5[1 + \tanh(2x/W)]$ . The mobility parameter is  $M_\phi = 0.08$ , the interface thickness is  $W = 3\delta x$ .





(a) Comparisons for three values of thermal diffusivity:  $\alpha_g^1 = 0.14$  (red),  $\alpha_g^2 = 0.125$  (blue) and  $\alpha_g^3 = 0.08$  (black). Left:  $x$ -profiles of temperature  $\theta$  at the end of simulation  $t_f = 2 \times 10^5$ . Right: evolution of interface position  $x_I(t)$  tracked by  $\phi = 1/2$ . The temperature interface is  $\theta_I = 0$ .



(b) Comparisons for three ratios  $\alpha_l^j/\alpha_g^j = 10, 5, 2$  for  $j = 1, 2, 3$  with  $\alpha_l^1 = 0.14$  (red),  $\alpha_l^2 = 0.125$  (blue) and  $\alpha_l^3 = 0.08$  (black). Left:  $x$ -profiles of temperature  $\theta$  at the end of simulation  $t_f = 2 \times 10^5$ . Right: evolution of interface position  $x_I(t)$  tracked by  $\phi = 1/2$ . The temperature interface is  $\theta_I = 0.05$ .

Figure 7: Comparisons between LBM (dots) and analytical solution of Stefan problem (solid lines). (a) With  $\alpha_l/\alpha_g = 1$  and  $\theta_I = 0$ . (b) With  $\alpha_l/\alpha_g \neq 1$  and  $\theta_I \neq 0$ .

**Validations for  $\alpha_l/\alpha_g = 1$  and  $\theta_I = 0$ .** Before considering the more general case  $\alpha_l/\alpha_g \neq 1$  and  $\theta_I \neq 0$ , we assume that thermal diffusivities are the same in liquid and gas ( $\alpha_l = \alpha_g = \alpha$ ) and the interface temperature is at saturation ( $\theta_I = 0$ ). In that case, whatever the diffusivity value  $\alpha$ , the solution of the transcendental equation (Eq. (41d)) depends only on  $\theta_w$  and  $\theta_\infty$ . With  $\theta_w = -0.3$  and  $\theta_\infty = 0.3$ , its solution is  $\xi = 0.280680$ . Comparisons between analytical solutions and LBM simulations are presented on Fig. 7a for three values of thermal diffusivity  $\alpha_g^j = 0.14, 0.08, 0.03$  with  $j = 1, 2, 3$ . LBM temperature profiles are superimposed with the analytical solution (Eqs. (41b) and (41c)) at the final time of simulation  $t_f = 2 \times 10^5$  (Fig. 7a, left). Successive positions of vapor/liquid interface also fit with the analytical solution (Fig. 7a, right) for three values of thermal diffusivity.

**Validations for  $\alpha_l/\alpha_g \neq 1$  and  $\theta_I \neq 0$ .** Now we consider a more general case for which the diffusivities of liquid and gas can be different. Three ratios are simulated  $\alpha_l^j/\alpha_g^j = 10, 5, 2$  for  $j = 1, 2, 3$  with  $\alpha_l^1 = 0.14$ ,  $\alpha_l^2 = 0.125$  and  $\alpha_l^3 = 0.08$ . Same values of  $\theta_w = -0.3$  and  $\theta_\infty = 0.3$  are kept, and the interface temperature is now equal to  $\theta_I = 0.05$ . For those values, the corresponding solutions of the transcendental equation are  $\xi^1 = 0.349635$ ,  $\xi^2 = 0.343882$  and  $\xi^3 = 0.331864$ . For LBM simulations, all numerical values are identical except for interface temperature and diffusivities of each phase. As confirmed by temperature profiles (Fig. 7b, left) and the evolution of interface position (Fig. 7b, right), the model of phase change is well adapted to simulate the phase change problem with different diffusivities in each phase and an interface temperature not equal to zero. Finally this test case validates the approximation of the mass production rate  $\dot{m}'''$  defined by Eq. (18) and implementation of LBM for the phase-field and temperature equations.

## 5. Simulations of film boiling

Film boiling is a classical problem of two-phase flows with phase change. It has already been simulated with a lot of different numerical techniques (see [39] for a recent review) for studying the effect of geometries such as an horizontal

Liquid and gas properties			Interface properties		Other parameters	
	Liquid	Gas	Parameter	Value	Parameter	Value
Density	$\rho_l = 1.658$	$\rho_g = 1$	Surface tension	$\sigma = 5 \times 10^{-3}$	Gravity	$g_y = 4$
Kinematic viscosity	$\nu_l = 3 \times 10^{-3}$	$\nu_g = 5 \times 10^{-4}$	Interface temp.	$\theta_l = 0$	Bottom temp.	$\theta_{y=\ell_y} = 0.025$
Thermal diffusivity	$\alpha_l = 2.5 \times 10^{-4}$	$\alpha_g = 2.5 \times 10^{-3}$	Mobility	$M_\phi = 1.7 \times 10^{-3}$	Top temp.	$\theta_{y=L_y} = 0$
			Interface width	$W = 5 \times 10^{-3}$	Latent/specific heat	$\mathcal{L}/C_p = 1$

Table 2: Parameters for film boiling simulations.

cylinder [67] or for studying the effect of an electric field [68]. With the lattice Boltzmann method, several simulations use the Cahn-Hilliard model or the pseudo-potential method (respectively in [69, 70, and references therein]). Here we present the capability of the conservative Allen-Cahn equation with a production rate defined by Eq. (18) to simulate that problem. In section 5.1, the physical configuration is reminded; in section 5.2 one simulation of bubbles detachment on nodes and anti-nodes is detailed; in section 5.3, indications will be given on computational times for two mesh sizes:  $1024^2$  for GPU and CPU and  $4096 \times 3072$  for multi-GPUs.

### 5.1. Physical configuration

Inside a two-dimensional domain  $\Omega = \Pi_{v=x,y}[\ell_v, L_v]$ , a thin film of gas of height  $y_0$  is initialized near the bottom wall  $y = \ell_y$  which is heated by applying a constant temperature  $\theta|_{y=\ell_y} = \theta_w$ . The liquid is above the thin film and the gravity acts downward  $\mathbf{g} = (0, -g_y)^T$ . On the top wall  $y = L_y$ , the temperature is imposed at saturation and the phase-field is equal to  $\phi = +1$  (i.e. gas phase). The left and right walls are periodic. If the interface is destabilized by an initial condition defined by

$$y = y_0 + y_1 \sin\left(\frac{2\pi x}{\lambda}\right), \quad (42)$$

where  $y_1$  and  $\lambda$  are respectively the amplitude and the wavelength of the perturbation, then we can observe bubbles of gas that grow, detach and rise in the domain, provided that the wavelength of perturbation  $\lambda$  is greater than a critical value  $\lambda_c$  defined by

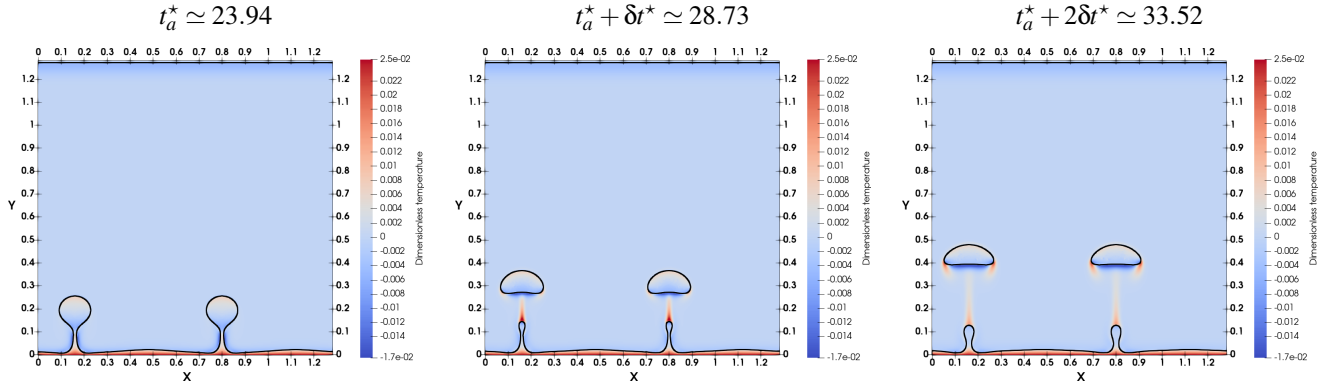
$$\lambda_s = \sqrt{\frac{\sigma}{(\rho_l - \rho_g)g_y}}, \quad \lambda_c = 2\pi\lambda_s. \quad (43)$$

The thermal-hydrodynamics of this problem is controlled by several dimensionless numbers: the Grashof number  $Gr = \rho_g g_y (\rho_l - \rho_g) \lambda_s^3 / \rho_g^2 \nu_g^2$ , the Prandtl number  $Pr = \nu_g / \alpha_g$  and the Jacob number  $Ja = C_p (T_w - T_{sat}) / \mathcal{L}$ . Moreover the solution is sensitive to parameters that are involved in Eq. (42). Several sensitivity simulations on parameters of the initial condition can be found in [71].

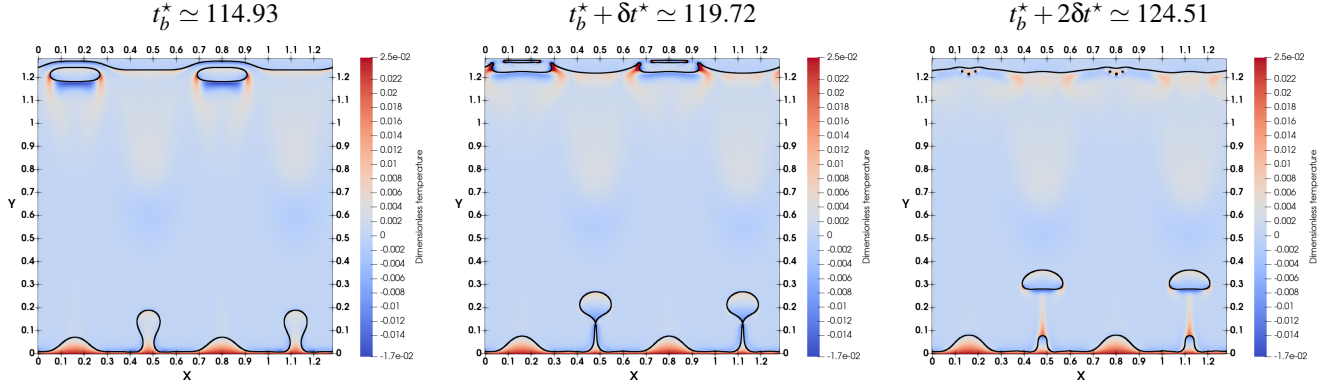
Simulations of film boiling with `LBM_saclay` are first carried out inside a two-dimensional domain  $\Omega = [0, 1.28]^2$  which is discretized with  $N_x \times N_y = 1024 \times 1024$  nodes. The space- and time-steps are respectively equal to  $\delta x = 1.25 \times 10^{-3}$  and  $\delta t = 7.5 \times 10^{-5}$ . The D2Q9 lattice is used for all distribution functions  $f_i$ ,  $g_i$  and  $s_i$ . For parameters of Table 2, the value of critical wavelength is  $\lambda_c = 2\pi\lambda_s = 0.2738$ , with  $\lambda_s = 4.358 \times 10^{-2}$ . The Jacob number is  $Ja = 0.025$ , the Prandtl  $Pr = 0.2$  and the Grashof number is  $Gr = 871.38$ .

### 5.2. Simulation of bubble detachment on nodes and antinodes

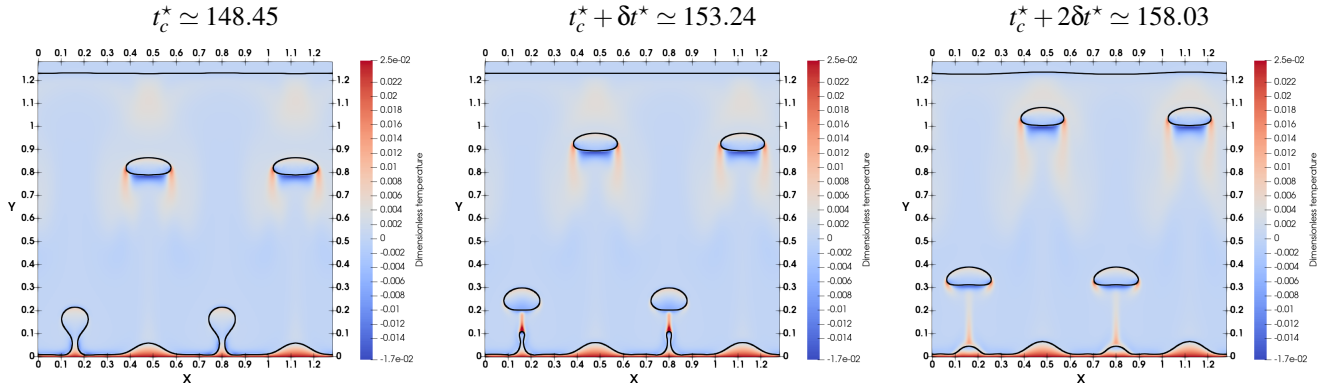
We present one simulation for which the interface is initialized by Eq. (42) with  $y_0 = 0.03$ ,  $y_1 = 0.015$  and  $\lambda = 0.64$ . The choice  $\lambda = 0.64$  was done after one first preliminary simulation which was performed with  $\lambda = 0.32 (> \lambda_c = 0.2738)$  to check detachment of bubbles. For  $\lambda = 0.64$ , the maximum value of  $y$  is  $y_{max} = 0.045$  for two positions  $x_{y_{max}}^{(1)} = 0.16$  and  $x_{y_{max}}^{(2)} = 0.8$ . Its minimum value is  $y_{min} = 0.015$  for two positions  $x_{y_{min}}^{(1)} = 0.48$  and  $x_{y_{min}}^{(2)} = 1.12$ . Positions  $x_{y_{max}}^{(1),(2)}$  are called “nodes” and  $x_{y_{min}}^{(1),(2)}$  are called “anti-nodes”. Here, we present one simulation to observe detachment of bubbles alternatively on nodes and anti-nodes. Actually, it is what we observe on Figs. 8a–8c which present the temperature fields and the iso-values  $\phi = 1/2$  (black line) at several dimensionless times. The dimensionless time is defined by  $t^* = t/t_s$  where  $t_s = \sqrt{\lambda_s/g_y} = 0.1044$ . At the early stage of simulation (Fig. 8a), we can observe that the detachment of bubbles occurs on nodes. Later during the simulation (Fig. 8b), the bubbles that are emitted on nodes coalesce on the top on the domain, while two other bubbles grow and are detached from anti-nodes. Finally (Fig. 8c), the cycle is repeated periodically: bubbles emitted at anti-nodes coalesce and new bubbles on nodes detach and rise. Streamlines and velocity magnitude corresponding to the last time  $t^* \simeq 158.03$  are presented on Fig. 8d. In Table 2, the mobility was set to  $M_\phi = 1.7 \times 10^{-3}$  after a sensitivity analysis. If  $M_\phi$  is too low, the authors have observed the appearance of parasitic bubbles in the liquid phase. The mobility coefficient is directly related to the relaxation time  $\tau_g$  and the algorithm can be unstable if its value is too low. It is expected that a wider range of parameter  $M_\phi$  could be reached with the TRT or MRT collisions operators.



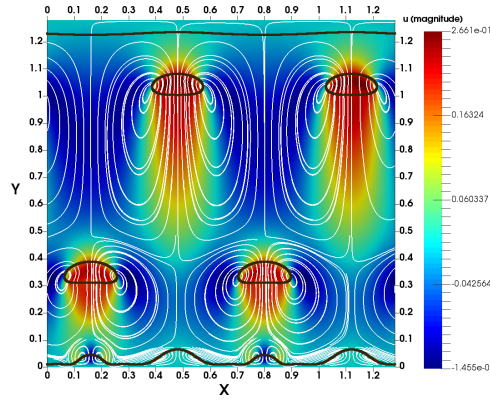
(a) Detachment of bubbles occurs on nodes at the early stage of the simulation.



(b) Coalescence is observed at the top of the domain for bubbles detached from nodes. It is also observed a detachment of bubbles at anti-nodes.



(c) Later during the simulation, bubbles are detached on nodes, the cycle is pursued periodically.



(d) Streamlines (white lines) and interface  $\phi = 1/2$  (black lines) superimposed on the velocity magnitude (colored field) at  $t^* \approx 158.03$ .

Figure 8: Simulation of film boiling for  $Ja = 0.025$ . Interface position  $\phi = 1/2$  superimposed on temperature field and for several dimensionless times of simulation. Three successive times from (a)  $t_a^* \approx 23.94$ , (b)  $t_b^* \approx 114.93$  and (c)  $t_c^* \approx 148.45$  with  $\delta t^* = 4.79$ .

### 5.3. Computational times

A first comparison of computational times between GPUs and CPUs has been indicated in Section 3.5, but only for a diffusive problem. For a single- and double-Poiseuille flow of Section 4.1, the computational times on a  $100 \times 100$  lattice are respectively 56 MLUPS and 38 MLUPS. Those computations have been performed on a computer equipped of one AMD CPU processor (Ryzen 5 2600, 3.4GHz with 12 threads). The MLUPS are higher for the single-phase because the algorithm requires much less floating points computations. There is neither Allen-Cahn equation nor intermediate gradient to update for a single-phase flow. However, let us note that the MLUPS for two distribution functions are higher than half of the value obtained with only one (i.e. 28 MLUPS), which indicates a good code optimization by resolving the phase-field equation.

Simulation of diffusion or single-phase flow requires only one distribution and the double-Poiseuille flow requires two distribution functions. The film boiling simulation requires three Lattice Boltzmann equations with three distribution functions and the computation of additional gradients. In that case, to complete  $5.33 \times 10^5$  time iterations on a computational domain of  $1024^2$  nodes, the simulation took 1h56m (80.96 MLUPS) on a single GPU NVIDIA® K80. The same simulation took 12h57m (11.97 MLUPS) on 16-cores Intel® Xeon® CPU E5-2630 v3 2.40GHz. The computation on GPU is quicker than on CPU as expected after the preliminary diffusion simulation of section 3.5. The ratio is 6.7 times in favor of GPU compared to CPU. Next, the full grid ( $1024^2$  nodes) is decomposed in four sub-domains composed of  $256 \times 1024$  nodes, each one of them being taken in charge by one GPU. The simulation took 38 minutes (249.99 MLUPS) to perform the same number of time iterations on four parallel GPUs. The computational time is divided by a factor three compared to a single GPU. Finally, the computational domain is increased to  $\Omega = [0, 5.12] \times [0, 3.84]$  and discretized by  $N_x \times N_y = 4096 \times 3072$  nodes, i.e. the mesh size is twelve times bigger than the previous one. The initial condition is slightly modified to

$$y = y_0 + y_1 \sum_{i=1}^{16} \sin\left(\frac{2\pi x}{\lambda_i}\right) \quad (44)$$

where the interface position  $y$  is perturbed with several modes  $\lambda_i$  which are randomly picked, uniformly distributed between  $0.5\lambda_c \leq \lambda_i \leq 1.5\sqrt{3}\lambda_c$ . We simulate two values of wall temperature  $\theta_w = 0.025$  and  $\theta_w = 0.1$  corresponding to Jacob numbers respectively equal to  $Ja = 0.025$  and  $Ja = 0.1$ . All other values of physical parameters remain identical (Table 2). A comparison on shapes of bubbles is given at  $t^* = 95.78$  on Fig. 9. When the Jacob number has the value of Section 5.2, discrete bubbles are released periodically from the initial condition (Fig. 9a). When the Jacob number is increased to 0.1, long vapor jets are observed below bubbles (Fig. 9b). That observation is consistent with those simulated with other techniques and even observed on experiments cited in [39, Sec 5.1.2 and Fig. 9]. The simulation took 80 minutes (713 MLUPS) on 8 parallel GPUs to complete  $5.33 \times 10^5$  time iterations.

## 6. Conclusion

In this paper, the LBM implementation of two-phase flows was revisited by improving two main points. The first one focuses on the model formulation of phase change and the second one focuses on the portability of the code on various platforms. The interface is tracked by the conservative Allen-Cahn model with a source term involving a mass production rate at the interface. In this work, that source term is simplified compared to approaches of literature, and the approximation avoids to calculate the gradients of temperature numerically. The model is able to simulate two phases of different thermal diffusivities with an interface temperature which is not necessarily at saturation. The phase-field model is coupled with the incompressible Navier-Stokes model where a source term was added in the mass balance equation. The source term is defined as the product of mass production rate times one term inversely proportional to densities. An additional equation on temperature completes the model. The time derivative of phase-field appears in the source term of that equation. It is interpreted as the release or absorption of latent heat at the interface.

The Lattice Boltzmann schemes for all equations are implemented in a new C++ code coupled with the Kokkos library for its performance portability. The new code, called LBM\_saclay, can be run with good performance on several architectures such as Graphical Process Units (GPUs), Central Process Units (CPUs) and even multi-GPUs and multi-CPUs. Indeed, two levels of parallelism are developed inside the code. The first one uses Kokkos for intra-node parallelism, whereas MPI takes in charge the domain decomposition. Preliminary comparisons between GPUs and CPUs were carried out on a simple diffusive problem. As expected from literature, those tests show clearly that best performance is obtained with GPU compared to CPU (Skylake or KNL) even for best optimization of LBM kernels (CSOa2) which has been developed for Intel Skylake. Here, comparisons were performed with the same C++ source code. No low-level language (CUDA or OpenCL) was used for GPUs.

Numerical implementation was checked with several test cases to validate step-by-step the full model of fluid flows with phase change. The conservative Allen-Cahn equation is validated with two test cases: (i) Zalesak's slotted disk and (ii) interface deformation inside a vortex. The coupling with Navier-Stokes equations is also checked with two test cases: the layered Poiseuille flow and Laplace law. Next, the coupling between equations of phase-field and temperature were compared to the most general one-dimensional analytical solution of the Stefan problem. Comparisons were done first by assuming identical thermal diffusivities, and next by using various ratios of diffusivities with an interface temperature that is different of the saturation one. The full model was simulated on the test case of film boiling on one GPU and one multicore CPU for two mesh sizes. Computational times are clearly in favor of GPUs. Finally, the film boiling problem is simulated with 8 parallel GPUs for mesh size that is twelve times bigger than the previous one.

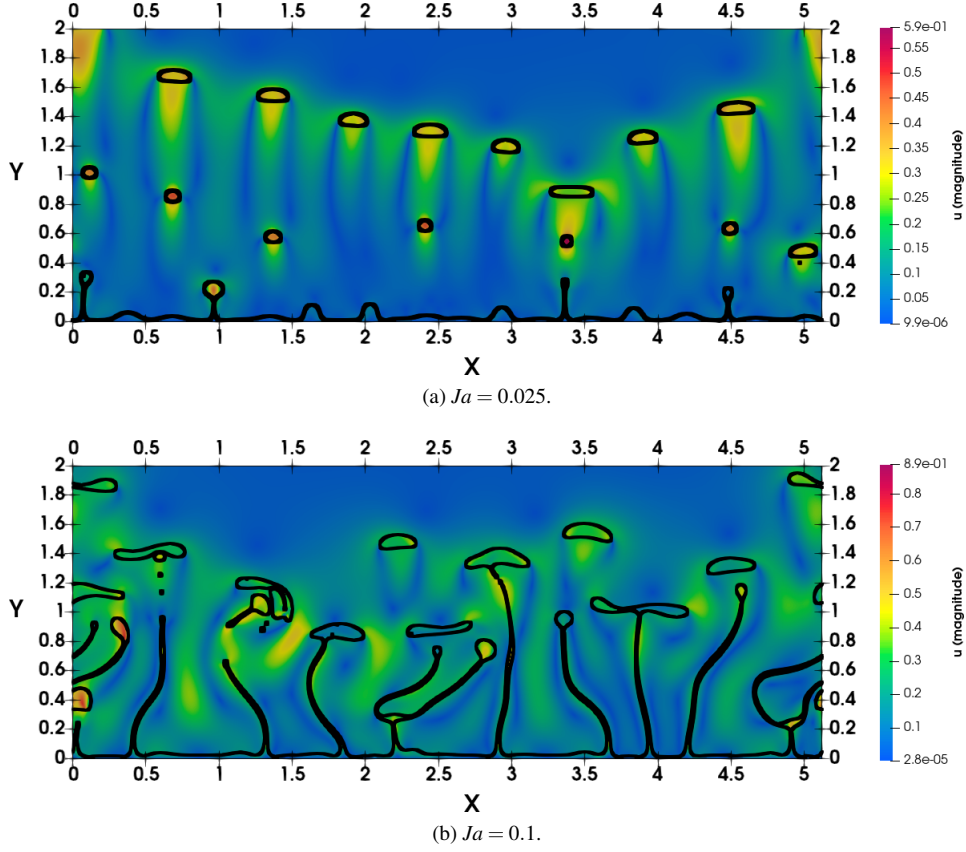


Figure 9: Velocity magnitude (colored field) and interface position  $\phi = 1/2$  (black lines) at  $t^* = 95.78$  for (a)  $Ja = 0.025$  and (b)  $Ja = 0.1$ .

In this paper, foundations have been laid for improving performance of lattice Boltzmann simulations in a context of quick evolution of HPC platforms. In the future, a three-dimensional extension of the coupling terms is planned. Next `LBM_saclay` could be enriched with other models requiring interface tracking such as crystal growth and demixing of ternary fluids. Besides, the range of physical parameters could be increased and the code stability could be enhanced by using alternative collision operators such as those based on the Two-Relaxation-Times and Multiple-Relaxation-Times.

## Acknowledgments

We would like to thank MATHIS PLAPP for the insightful discussions on theoretical aspects of phase-field models.

## Appendix A. Removal of the driven-curvature interface motion in Eq. (5)

In this Appendix, the derivation of first term in the right-hand side of Eq. (5) is reminded. The advection of phase index  $\phi$  writes

$$\frac{\partial \phi}{\partial t} + \mathbf{V} \cdot \nabla \phi = 0. \quad (\text{A.1})$$

If the total velocity  $\mathbf{V}$  is defined as the sum of an external advective velocity  $\mathbf{u}$  of an incompressible fluid plus a normal velocity of the interface  $v_n \mathbf{n}$ , then  $\mathbf{V} \cdot \nabla \phi = \mathbf{u} \cdot \nabla \phi + v_n |\nabla \phi|$ . For the second term, we have used the definition of normal vector  $\mathbf{n} = \nabla \phi / |\nabla \phi|$ . If the normal velocity  $v_n$  is also assumed to be separated into one term,  $-M_\phi \kappa$ , depending on the curvature  $\kappa$  and another one,  $\tilde{v}$  independent on  $\kappa$  then:  $v_n |\nabla \phi| = -M_\phi \kappa |\nabla \phi| + \tilde{v} |\nabla \phi|$  and Eq. (A.1) writes:

$$\frac{\partial \phi}{\partial t} + \nabla \cdot (\mathbf{u} \phi) = M_\phi \kappa |\nabla \phi| - \tilde{v} |\nabla \phi|. \quad (\text{A.2})$$

For solidification problems,  $\tilde{v}$  is the coupling with temperature equation and ensures that the Gibbs-Thomson condition is well recovered. A discussion on  $\tilde{v}$  is presented at the end of this appendix. The next stage of the derivation is to cancel the driven-curvature interface motion  $M_\phi \kappa |\nabla \phi|$ , without setting  $M_\phi = 0$ , but by adding a supplementary counter term:

$M_\phi \kappa |\nabla \phi| - M_\phi \kappa |\nabla \phi| = S(\phi)$ . The purpose is to transform an hyperbolic-type PDE into a parabolic-type PDE by expanding  $\kappa$  in the first term with its definition  $\kappa = \nabla \cdot \mathbf{n} = \nabla \cdot (\nabla \phi / |\nabla \phi|)$  in order to obtain an expression involving the laplacian of  $\phi$ :

$$S(\phi) = M_\phi \left[ \nabla^2 \phi - \frac{\nabla \phi \cdot \nabla |\nabla \phi|}{|\nabla \phi|} \right] - M_\phi \kappa |\nabla \phi|. \quad (\text{A.3})$$

The main advantage of this formulation (Eq. (A.3)) is that, for a plane interface, i.e.  $\kappa = 0$ , the equilibrium solution of  $S(\phi) = 0$  is an hyperbolic tangent. By using the definition of  $\mathbf{n}$ , Eq. (A.3) becomes  $S(\phi) = M_\phi [\nabla^2 \phi - \mathbf{n} \cdot \nabla |\nabla \phi|] - M_\phi |\nabla \phi| \nabla \cdot \mathbf{n}$ , i.e. Eq. (A.2) becomes

$$\frac{\partial \phi}{\partial t} + \nabla \cdot (\mathbf{u}\phi) = M_\phi [\nabla^2 \phi - \mathbf{n} \cdot \nabla |\nabla \phi| - |\nabla \phi| \nabla \cdot \mathbf{n}] - \tilde{v} |\nabla \phi| \quad (\text{A.4})$$

which, after the straightforward manipulation  $-\mathbf{n} \cdot \nabla |\nabla \phi| - |\nabla \phi| \nabla \cdot \mathbf{n} = -\nabla \cdot (|\nabla \phi| \mathbf{n})$  yields

$$\frac{\partial \phi}{\partial t} + \nabla \cdot (\mathbf{u}\phi) = \nabla \cdot [M_\phi (\nabla \phi - |\nabla \phi| \mathbf{n})] - \tilde{v} |\nabla \phi|. \quad (\text{A.5})$$

For calculating  $|\nabla \phi|$ , the following kernel function is used

$$\phi = \frac{1}{2} \left[ 1 + \tanh \left( \frac{\zeta}{aW} \right) \right], \quad (\text{A.6})$$

where  $\zeta$  is the normal coordinate of the interface,  $a$  controls the slope of the hyperbolic tangent and  $W$  is the interface width. The above kernel function ensures an hyperbolic tangent profile at equilibrium. It is consistent with the profile obtained in a thermodynamically derived phase-field model, such as the one used for computation of chemical potential (Eq. (14)) with bulk phases  $\phi = 0$  and  $\phi = 1$ . The normal derivative of Eq. (A.6) leads to

$$|\nabla \phi| = \frac{\partial \phi}{\partial \zeta} = \frac{2}{aW} \phi(1 - \phi). \quad (\text{A.7})$$

Finally by setting  $a = 1/2$  the conservative Allen-Cahn equation with a source term is

$$\frac{\partial \phi}{\partial t} + \nabla \cdot (\mathbf{u}\phi) = \nabla \cdot \left[ M_\phi \left( \nabla \phi - \frac{4}{W} \phi(1 - \phi) \mathbf{n} \right) \right] - \tilde{v} \frac{4}{W} \phi(1 - \phi). \quad (\text{A.8})$$

Eq. (A.8) is the Allen-Cahn equation for which the curvature-driven displacement of the interface has been canceled with a counter term. Let us notice that, if  $\tilde{v}$  is chosen such as  $\tilde{v} = \alpha(\theta_I - \theta)/(\mathcal{A}W)$  then  $\tilde{v} |\nabla \phi| \approx -(4\alpha/\mathcal{A}W^2)(\theta_I - \theta)\phi(1 - \phi)$  can be used in Eq. (A.8) for the problem of phase change. The release or absorption of latent heat at the interface is taken into account in the temperature equation by the time derivative of  $\phi$ . If the physical problem necessitates a curvature-driven interface motion, the curvature term must be kept in the Allen-Cahn equation and then only the first term in the right-hand side of Eq. (A.3) appears in the derivation. With  $a = 1/2$ , the term  $\nabla \phi \cdot \nabla |\nabla \phi| / |\nabla \phi|$  is equal to

$$\frac{\nabla \phi \cdot \nabla |\nabla \phi|}{|\nabla \phi|} = \frac{\partial^2 \phi}{\partial \zeta^2} = \frac{16}{W^2} \phi(1 - \phi)(1 - 2\phi) \quad (\text{A.9})$$

The curvature-driven term writes

$$M_\phi \kappa |\nabla \phi| = M_\phi \left[ \nabla^2 \phi - \frac{16}{W^2} \phi(1 - \phi)(1 - 2\phi) \right]. \quad (\text{A.10})$$

## Appendix B. Numerical value of coefficient $\mathcal{A}$

When the matched asymptotic expansions are carried out on the one-dimensional phase-field model, the coefficient  $\mathcal{A}$  is defined by four integrals  $\mathcal{J}$ ,  $\mathcal{I}$ ,  $\mathcal{G}$  and  $\mathcal{U}$  by (e.g. [49, Eq. (59)]):

$$\mathcal{A} = \frac{\mathcal{G} + \mathcal{I}\mathcal{U}}{2\mathcal{J}}, \quad (\text{B.1})$$

with

$$\mathcal{J} = \int_{-\infty}^{\infty} d\zeta (\partial_\zeta \phi_0)^2, \quad \mathcal{I} = \int_{-\infty}^{\infty} d\zeta (\partial_\zeta \phi_0) p_\phi^0, \quad \mathcal{G} = \int_{-\infty}^{\infty} d\zeta (\partial_\zeta \phi_0) p_\phi^0 \int_0^\zeta d\zeta' h^0, \quad \text{and} \quad \mathcal{U} = \int_{-\infty}^0 d\zeta h^0. \quad (\text{B.2})$$

In Eq. (B.2), the functions  $\phi_0$ ,  $p_\phi^0$  and  $h^0$  of our model are defined such as

$$\phi_0 = \frac{1}{2} \left[ 1 + \tanh \left( \frac{2\zeta}{W} \right) \right], \quad p_\phi^0 = \phi_0(1 - \phi_0), \quad \text{and} \quad h^0 = \phi_0 \quad (\text{B.3})$$

Those integrals can be computed analytically and yield a numerical value provided that the interface width  $W$  is set. Here, to be consistent with the rescaling of space and the analysis performed in [49], it is enough to set  $W = 2\sqrt{2}$ , and the integrals are:

$$\mathcal{J} = \frac{1}{3\sqrt{2}}, \quad \mathcal{J} = \frac{1}{6}, \quad \mathcal{G} = -\frac{(12\ln 2 - 10)}{72\sqrt{2}}, \quad \text{and} \quad \mathcal{U} = \frac{\ln 2}{\sqrt{2}}. \quad (\text{B.4})$$

Finally Eq. (B.1) yields

$$\mathcal{A} = \frac{10}{48} \cong 0.20833. \quad (\text{B.5})$$

## Appendix C. Discrete lattice Boltzmann equations

In this Appendix, the variable change for the discrete lattice Boltzmann equation is reminded in Appendix C.1. In Appendix C.2, we will show that, for CAC model, the formulation with a source term is equivalent to the formulation with a modification of the equilibrium distribution function.

### Appendix C.1. Variable change for discrete lattice Boltzmann equation

The discrete lattice Boltzmann equation with an external force or source term  $S_i^\vartheta$  can be written with the BGK collision term:

$$\frac{\partial \vartheta_i}{\partial t} + \mathbf{c}_i \cdot \nabla \vartheta_i = -\frac{\vartheta_i - \vartheta_i^{eq}}{\tau_\vartheta} + S_i^\vartheta. \quad (\text{C.1})$$

In what follows, the calculations will be performed by setting  $\vartheta \equiv f$ ,  $S_i^\vartheta = S_i^f = S_i$  and  $\tau_\vartheta \equiv \tau$  but the variable change derivation holds also for  $\vartheta \equiv h$  and  $\vartheta \equiv s$ . Terms that are evaluated at position  $\mathbf{x}$  and time  $t$  are noted  $f_i \equiv f_i(\mathbf{x}, t)$ ,  $f_i^{eq} \equiv f_i^{eq}(\mathbf{x}, t)$  and  $S_i \equiv S_i(\mathbf{x}, t)$ , whereas terms evaluated at position  $\mathbf{x} + \mathbf{c}_i \delta t$  and time  $t + \delta t$  are noted with a star:  $f_i^* \equiv f_i(\mathbf{x} + \mathbf{c}_i \delta t, t + \delta t)$ ,  $f_i^{*eq} \equiv f_i^{eq}(\mathbf{x} + \mathbf{c}_i \delta t, t + \delta t)$  and  $S_i^* \equiv S_i(\mathbf{x} + \mathbf{c}_i \delta t, t + \delta t)$ . With those notations, integration of Eq. (C.1) over  $t$  and  $t + \delta t$  yields:

$$f_i^* = f_i - \frac{\delta t}{2\tau} (f_i^* - f_i^{*eq}) - \frac{\delta t}{2\tau} (f_i - f_i^{eq}) + \frac{\delta t}{2} S_i^* + \frac{\delta t}{2} S_i \quad (\text{C.2})$$

where the trapezoidal rule was applied for the right-hand side of Eq. (C.1). In this expression, the natural variable change for implicit terms is

$$\bar{f}_i^* = f_i^* + \frac{\delta t}{2\tau} (f_i^* - f_i^{*eq}) - \frac{\delta t}{2} S_i^*. \quad (\text{C.3})$$

The same variable change is used for  $\bar{f}_i$ :

$$\bar{f}_i = f_i + \frac{\delta t}{2\tau} (f_i - f_i^{eq}) - \frac{\delta t}{2} S_i. \quad (\text{C.4})$$

By inverting the latter relation in order to express  $f_i$  with respect to  $\bar{f}_i$ , we obtain:

$$f_i = \frac{2\tau}{2\tau + \delta t} \left( \bar{f}_i + \frac{\delta t}{2\tau} f_i^{eq} + \frac{\delta t}{2} S_i \right). \quad (\text{C.5})$$

With Eqs. (C.3) and (C.5), Eq. (C.2) becomes

$$\bar{f}_i^* = \bar{f}_i - \frac{\delta t}{\tau + \delta t/2} \left( \bar{f}_i - f_i^{eq} + \frac{\delta t}{2} S_i \right) + \delta t S_i \quad (\text{C.6})$$

At this stage, if we define a new variable change

$$\bar{f}_i^{eq} = f_i^{eq} - \frac{\delta t}{2} S_i, \quad (\text{C.7})$$

then Eq. (C.6) is equivalent to

$$\bar{f}_i^* = \bar{f}_i - \frac{\delta t}{\tau + \delta t/2} (\bar{f}_i - \bar{f}_i^{eq}) + \delta t S_i. \quad (\text{C.8})$$

Without using the previous variable change for  $f_i^{eq}$ , Eq. (C.6) is equivalent to

$$\bar{f}_i^* = \bar{f}_i - \frac{\delta t}{\tau + \delta t/2} (\bar{f}_i - f_i^{eq}) + \frac{\tau \delta t}{\tau + \delta t/2} S_i, \quad (C.9)$$

where only the factor in front of the source term is modified.

By introducing the dimensionless collision rate which is defined by  $\bar{\tau} = \tau/\delta t$ , Eq. (C.8) finally writes

$$\bar{f}_i^* = \bar{f}_i - \frac{1}{\bar{\tau} + 1/2} (\bar{f}_i - \bar{f}_i^{eq}) + \delta t S_i, \quad (C.10)$$

or alternatively,

$$\bar{f}_i^* = \bar{f}_i - \frac{1}{\bar{\tau} + 1/2} (\bar{f}_i - f_i^{eq}) + \frac{\bar{\tau} \delta t}{\bar{\tau} + 1/2} S_i. \quad (C.11)$$

In Section 3, Eq. (C.10) is the starting point for each lattice Boltzmann equation. The variable change Eq. (C.4) leads to the calculation of the zeroth-order moment:

$$\mathcal{M}_0 = \sum_i \bar{f}_i + \frac{\delta t}{2} \sum_i S_i \quad (C.12)$$

### Appendix C.2. Equivalence of lattice Boltzmann formulations for the Allen-Cahn equation

The purpose of this Appendix is to prove the equivalence between the source term and the modification of the equilibrium distribution function. The lattice Boltzmann scheme for the conservative Allen-Cahn equation is (Eq. (29a) with  $S_i^g$  defined by Eq. (30a)):

$$\bar{g}_i^* = \bar{g}_i - \frac{1}{\bar{\tau}_g + 1/2} [\bar{g}_i - \bar{g}_i^{eq}] + \mathcal{P}_i^g \delta t + \mathcal{F}_i^g \delta t \quad (C.13)$$

with the mobility coefficient defined by  $M_\phi = \bar{\tau}_g c_s^2 \delta t$ . By using the definition of  $\bar{g}_i^{eq}$  for  $\bar{g}_i^{eq} = \phi \Gamma_i - \delta t \mathcal{P}_i^g/2 - \mathcal{F}_i^g \delta t/2$  and gathering the term  $\mathcal{F}_i^g \delta t$  inside the bracket, we obtain

$$\bar{g}_i^* = \bar{g}_i - \frac{1}{\bar{\tau}_g + 1/2} \left[ \bar{g}_i - \phi \Gamma_i - \mathcal{F}_i^g \bar{\tau}_g \delta t + \frac{\delta t}{2} \mathcal{P}_i^g \right] + \mathcal{P}_i^g \delta t \quad (C.14)$$

Next, the collision rate is replaced by its mobility  $\bar{\tau}_g = M_\phi/(c_s^2 \delta t)$ :

$$\bar{g}_i^* = \bar{g}_i - \frac{1}{\bar{\tau}_g + 1/2} \left[ \bar{g}_i - \phi \Gamma_i - \mathcal{F}_i^g \frac{M_\phi}{c_s^2} + \frac{\delta t}{2} \mathcal{P}_i^g \right] + \mathcal{P}_i^g \delta t \quad (C.15)$$

Finally, if we use the definition of  $\mathcal{F}_i^g$  given by Eq. (30b), the Allen-Cahn equilibrium distribution function  $\bar{g}_i^{eq,CAC}$  can be defined by [33]

$$g_i^{eq,CAC} = \phi \Gamma_i + M_\phi \frac{4}{W} \phi(1-\phi) w_i \frac{\mathbf{c}_i \cdot \mathbf{n}}{c_s^2} \quad (C.16)$$

and the alternative lattice Boltzmann equation is

$$\bar{g}_i^* = \bar{g}_i - \frac{1}{\bar{\tau}_g + 1/2} [\bar{g}_i - \bar{g}_i^{eq,CAC}] + \mathcal{P}_i^g \delta t \quad (C.17)$$

with  $\bar{g}_i^{eq,CAC} = g_i^{eq,CAC} - \mathcal{P}_i^g \delta t/2$  with  $\mathcal{P}_i^g$  defined by Eq. (30b).

## References

- [1] T. Krueger, H. Kusumaatmaja, A. Kuzmin, O. Shardt, G. Silva, E. Viggien, The Lattice Boltzmann Method: Principles and Practice, Graduate Texts in Physics, Springer, 2016.
- [2] Z. Guo, C. Shu, Lattice Boltzmann Method and Its Applications in Engineering, WORLD SCIENTIFIC, 2013. doi:10.1142/8806.
- [3] W. Li, X. Wei, A. Kaufman, Implementing lattice Boltzmann computation on graphics hardware, The Visual Computer 19 (7) (2003) 444–456. doi:10.1007/s00371-003-0210-6.
- [4] J. Tölke, Implementation of a Lattice Boltzmann kernel using the Compute Unified Device Architecture developed by nVIDIA, Computing and Visualization in Science 13 (1) (2008) 29. doi:10.1007/s00791-008-0120-2.
- [5] F. Kuznik, C. Obrecht, G. Rusaouen, J.-J. Roux, LBM based flow simulation using GPU computing processor, Computers & Mathematics with Applications 59 (7) (2010) 2380–2392. doi:10.1016/j.camwa.2009.08.052.
- [6] H. Zhou, G. Mo, F. Wu, J. Zhao, M. Rui, K. Cen, GPU implementation of lattice Boltzmann method for flows with curved boundaries, Computer Methods in Applied Mechanics and Engineering 225-228 (2012) 65–73. doi:10.1016/j.cma.2012.03.011.



- [7] C. Obrecht, F. Kuznik, B. Tourancheau, J.-J. Roux, Multi-GPU implementation of the lattice Boltzmann method, *Computers & Mathematics with Applications* 65 (2) (2013) 252 – 261, special Issue on Mesoscopic Methods in Engineering and Science (ICMMES-2010, Edmonton, Canada). doi:10.1016/j.camwa.2011.02.020.
- [8] M. Januszewski, M. Kostur, Sailfish: A flexible multi-gpu implementation of the lattice boltzmann method, *Computer Physics Communications* 185 (9) (2014) 2350 – 2368. doi:10.1016/j.cpc.2014.04.018.
- [9] H. C. Edwards, C. R. Trott, D. Sunderland, Kokkos: Enabling manycore performance portability through polymorphic memory access patterns, *Journal of Parallel and Distributed Computing* 74 (12) (2014) 3202 – 3216. doi:10.1016/j.jpdc.2014.07.003.
- [10] J. Eichstädt, M. Green, M. Turner, J. Peiró, D. Moxey, Accelerating high-order mesh optimisation with an architecture-independent programming model, *Computer Physics Communications* 229 (2018) 36 – 53. doi:10.1016/j.cpc.2018.03.025.
- [11] H. Huang, M. Sukop, X.-Y. Lu, *Multiphase Lattice Boltzmann Methods. Theory and Application*, Wiley & Sons, 2015.
- [12] Q. Li, K. Luo, Q. Kang, Y. He, Q. Chen, Q. Liu, Lattice Boltzmann methods for multiphase flow and phase-change heat transfer, *Progress in Energy and Combustion Science* 52 (2016) 62 – 105. doi:10.1016/j.peccs.2015.10.001.
- [13] A. K. Gunstensen, D. H. Rothman, S. Zaleski, G. Zanetti, Lattice Boltzmann model of immiscible fluids, *Phys. Rev. A* 43 (1991) 4320–4327. doi:10.1103/PhysRevA.43.4320.
- [14] X. Shan, H. Chen, Lattice Boltzmann model for simulating flows with multiple phases and components, *Phys. Rev. E* 47 (1993) 1815–1819. doi:10.1103/PhysRevE.47.1815.
- [15] X. Shan, H. Chen, Simulation of nonideal gases and liquid-gas phase transitions by the lattice Boltzmann equation, *Phys. Rev. E* 49 (1994) 2941–2948. doi:10.1103/PhysRevE.49.2941.
- [16] M. R. Swift, E. Orlandini, W. R. Osborn, J. M. Yeomans, Lattice boltzmann simulations of liquid-gas and binary fluid systems, *Phys. Rev. E* 54 (1996) 5041–5052. doi:10.1103/PhysRevE.54.5041.
- [17] D. Jacqmin, Calculation of Two-Phase Navier-Stokes Flows Using Phase-Field Modeling, *Journal of Computational Physics* 155 (1999) pp. 96–127. doi:10.1006/jcph.1999.6332.
- [18] P. Yuan, L. Schaefer, Equations of state in a lattice Boltzmann model, *Physics of Fluids* 18 (2006) 042101. doi:10.1063/1.2187070.
- [19] X. Li, P. Cheng, Lattice Boltzmann simulations for transition from dropwise to filmwise condensation on hydrophobic surfaces with hydrophilic spots, *International Journal of Heat and Mass Transfer* 110 (2017) 710 – 722. doi:10.1016/j.ijheatmasstransfer.2017.03.033.
- [20] M. Li, C. Huber, Y. Mu, W. Tao, Lattice Boltzmann simulation of condensation in the presence of noncondensable gas, *International Journal of Heat and Mass Transfer* 109 (2017) 1004 – 1013. doi:10.1016/j.ijheatmasstransfer.2017.02.046.
- [21] S. Leclaire, M. Reggio, J.-Y. Trépanier, Numerical evaluation of two recoloring operators for an immiscible two-phase flow lattice boltzmann model, *Applied Mathematical Modelling* 36 (5) (2012) 2237 – 2252. doi:10.1016/j.apm.2011.08.027.
- [22] S. Leclaire, N. Pellerin, M. Reggio, J.-Y. Trépanier, Enhanced equilibrium distribution functions for simulating immiscible multiphase flows with variable density ratios in a class of lattice boltzmann models, *International Journal of Multiphase Flow* 57 (2013) 159 – 168. doi:10.1016/j.ijmultiphaseflow.2013.07.001.
- [23] D. Anderson, G. McFadden, A. Wheeler, Diffuse-interface methods in fluid mechanics, *Annual Reviews of Fluid Mechanics* 30 (1998) pp. 139–165.
- [24] J. Cahn, J. Hilliard, Free Energy of a Nonuniform System. I. Interfacial Free Energy, *Journal of Chemical Physics* 28 (2) (1958) pp. 258–267.
- [25] D. Jasnow, J. Viñals, Coarse-grained description of thermo-capillary flow, *Physics of Fluids* 8 (3) (1996) pp. 660–669. doi:10.1063/1.868851.
- [26] V. Kendon, M. Cates, I. Pagonabarraga, J.-C. Desplat, P. Bladon, Inertial effects in three-dimensional spinodal decomposition of a symmetric binary fluid mixture: a lattice Boltzmann study, *Journal of Fluid Mechanics* 440 (2001) pp. 147–203. doi:10.1017/S0022112001004682.
- [27] H. Zheng, C. Shu, Y. Chew, A lattice boltzmann model for multiphase flows with large density ratio, *Journal of Computational Physics* 218 (2006) pp. 353–371. doi:10.1016/j.jcp.2006.02.015.
- [28] T. Lee, L. Liu, Lattice Boltzmann simulations of micron-scale drop impact on dry surfaces, *Journal of Computational Physics* 229 (2010) 8045–8063. doi:10.1016/j.jcp.2010.07.007.
- [29] Y. Q. Zu, S. He, Phase-field-based lattice Boltzmann model for incompressible binary fluid systems with density and viscosity contrasts, *Phys. Rev. E* 87 (2013) 043301. doi:10.1103/PhysRevE.87.043301.
- [30] Y. Sun, C. Beckermann, Sharp interface tracking using the phase-field equation, *Journal of Computational Physics* 220 (2) (2007) 626 – 653. doi:10.1016/j.jcp.2006.05.025.
- [31] P.-H. Chiu, Y.-T. Lin, A conservative phase field method for solving incompressible two-phase flows, *Journal of Computational Physics* 230 (1) (2011) 185 – 204. doi:10.1016/j.jcp.2010.09.021.
- [32] M. Geier, A. Fakhari, T. Lee, Conservative phase-field lattice Boltzmann model for interface tracking equation, *Phys. Rev. E* 91 (2015) 063309. doi:10.1103/PhysRevE.91.063309.
- [33] A. Fakhari, D. Bolster, L.-S. Luo, A weighted multiple-relaxation-time lattice Boltzmann method for multiphase flows and its application to partial coalescence cascades, *Journal of Computational Physics* 341 (2017) 22 – 43. doi:10.1016/j.jcp.2017.03.062.
- [34] T. Mitchell, C. Leonardi, A. Fakhari, Development of a three-dimensional phase-field lattice Boltzmann method for the study of immiscible fluids at high density ratios, *International Journal of Multiphase Flow* 107 (2018) 1 – 15. doi:10.1016/j.ijmultiphaseflow.2018.05.004.
- [35] D. Lee, J. Kim, Comparison study of the conservative Allen–Cahn and the Cahn–Hilliard equations, *Mathematics and Computers in Simulation* 119 (2016) 35 – 56. doi:10.1016/j.matcom.2015.08.018.
- [36] H. L. Wang, Z. H. Chai, B. C. Shi, H. Liang, Comparative study of the lattice Boltzmann models for Allen–Cahn and Cahn–Hilliard equations, *Phys. Rev. E* 94 (2016) 033304. doi:10.1103/PhysRevE.94.033304.
- [37] Z. Dong, W. Li, Y. Song, Lattice Boltzmann Simulation of Growth and Deformation for a Rising Vapor Bubble Through Superheated Liquid, *Numerical Heat Transfer, Part A: Applications* 55 (4) (2009) 381–400. doi:10.1080/10407780902720718.
- [38] H. Safari, M. H. Rahimian, M. Krafczyk, Extended lattice Boltzmann method for numerical simulation of thermal phase change in two-phase fluid flow, *Phys. Rev. E* 88 (2013) 013304. doi:10.1103/PhysRevE.88.013304.
- [39] C. R. Kharangate, I. Mudawar, Review of computational studies on boiling and condensation, *International Journal of Heat and Mass Transfer* 108 (2017) 1164 – 1196. doi:10.1016/j.ijheatmasstransfer.2016.12.065.
- [40] R. Folch, J. Casademunt, A. Hernández-Machado, L. Ramírez-Piscina, Phase-field model for Hele–Shaw flows with arbitrary viscosity contrast. I. Theoretical approach, *Phys. Rev. E* 60 (1999) 1724–1733. doi:10.1103/PhysRevE.60.1724.
- [41] D. Jamet, C. Misbah, Thermodynamically consistent picture of the phase-field model of vesicles: Elimination of the surface tension, *Phys. Rev. E* 78 (2008) 041903. doi:10.1103/PhysRevE.78.041903.
- [42] R. Kobayashi, Modeling and numerical simulations of dendritic crystal growth, *Physica D: Nonlinear Phenomena* 63 (3) (1993) 410 – 423. doi:10.1016/0167-2789(93)90120-P.
- [43] L. Amaya-Bower, T. Lee, Single bubble rising dynamics for moderate Reynolds number using Lattice Boltzmann Method, *Computers & Fluids* 39 (7) (2010) 1191 – 1207. doi:10.1016/j.compfluid.2010.03.003.
- [44] J. Kim, A continuous surface tension force formulation for diffuse-interface models, *Journal of Computational Physics* 204 (2) (2005) 784 – 804. doi:10.1016/j.jcp.2004.10.032.
- [45] J. Delhay, Jump conditions and entropy sources in two-phase systems. Local instant formulation, *International Journal of Multiphase Flow* 1 (3) (1974) 395 – 409. doi:10.1016/0301-9322(74)90012-3.
- [46] D. Juric, G. Tryggvason, Computations of boiling flows, *International Journal of Multiphase Flow* 24 (3) (1998) 387–410. doi:10.1016/

- [47] H. Safari, M. H. Rahimian, M. Krafczyk, Consistent simulation of droplet evaporation based on the phase-field multiphase lattice boltzmann method, *Phys. Rev. E* 90 (2014) 033305. doi:10.1103/PhysRevE.90.033305.
- [48] Amirhosein Begmohammadi, Mohsen Farhadzadeh, Mohammad Hassan Rahimian, Simulation of pool boiling and periodic bubble release at high density ratio using lattice Boltzmann method, *International Communications in Heat and Mass Transfer* 61 (2015) 78 – 87. doi:10.1016/j.icheatmasstransfer.2014.12.018.
- [49] A. Karma, W.-J. Rappel, Quantitative phase-field modeling of dendritic growth in two and three dimensions, *Physical Review E* 57 (4) (1998) pp. 4323–4349. doi:10.1103/PhysRevE.57.4323.
- [50] I. Ginzburg, Equilibrium-type and link-type lattice Boltzmann models for generic advection and anisotropic-dispersion equation, *Advances in Water Resources* 28 (11) (2005) 1171 – 1195. doi:10.1016/j.advwatres.2005.03.004.
- [51] D. D’Humières, Generalized Lattice-Boltzmann Equations, 1992, pp. 450–458, *prog. Astronaut. Aeronaut.* 59. doi:10.2514/5.9781600866319.0450.0458.
- [52] D. d’Humières, I. Ginzburg, M. Krafczyk, P. Lallemand, L.-S. Luo, Multiple-relaxation-time lattice Boltzmann models in three dimensions, *Phil. Trans. R. Soc. Lond. A* 360 (2002) pp. 437–451. doi:10.1098/rsta.2001.0955.
- [53] X. He, S. Chen, G. D. Doolen, A Novel Thermal Model for the Lattice Boltzmann Method in Incompressible Limit, *Journal of Computational Physics* 146 (1) (1998) 282 – 300. doi:10.1006/jcph.1998.6057.
- [54] T. Inamuro, T. Ogata, S. Tajima, N. Konishi, A lattice Boltzmann method for incompressible two-phase flows with large density differences, *Journal of Computational Physics* 198 (2) (2004) 628 – 644. doi:10.1016/j.jcp.2004.01.019.
- [55] A. J. Chorin, A numerical method for solving incompressible viscous flow problems, *Journal of Computational Physics* 2 (1) (1967) 12 – 26. doi:10.1016/0021-9991(67)90037-X.
- [56] X. He, L.-S. Luo, Lattice Boltzmann Model for the Incompressible Navier-Stokes Equation, *Journal of Statistical Physics* 88 (3/4) (1997) pp. 927–944.
- [57] M. Mohammadi-Shad, T. Lee, Phase-field lattice Boltzmann modeling of boiling using a sharp-interface energy solver, *Phys. Rev. E* 96 (2017) 013306. doi:10.1103/PhysRevE.96.013306.
- [58] I. Ginzburg, Generic boundary conditions for lattice Boltzmann models and their application to advection and anisotropic dispersion equations, *Advances in Water Resources* 28 (11) (2005) 1196 – 1216. doi:10.1016/j.advwatres.2005.03.009.
- [59] T. Lee, P. Fischer, Eliminating parasitic currents in the lattice Boltzmann equation method for non ideal gases, *Physical Review E* 74 (2006) 046709. doi:10.1103/PhysRevE.74.046709.
- [60] T. Lee, Effects of incompressibility on the elimination of parasitic currents in the lattice Boltzmann equation method for binary fluids, *Computers and Mathematics with Applications* 58 (2009) pp. 987–994. doi:10.1016/j.camwa.2009.02.017.
- [61] T. Lee, C.-L. Lin, A stable discretization of the lattice boltzmann equation for simulation of incompressible two-phase flows at high density ratio, *Journal of Computational Physics* 206 (1) (2005) 16 – 47. doi:10.1016/j.jcp.2004.12.001.
- [62] A. Fakhari, T. Mitchell, C. Leonardi, D. Bolster, Improved locality of the phase-field lattice-Boltzmann model for immiscible fluids at high density ratios, *Phys. Rev. E* 96 (2017) 053301. doi:10.1103/PhysRevE.96.053301.
- [63] Compatibilities of Kokkos library. Web link accessible on 12 May 2020: <https://github.com/kokkos/kokkos/wiki/Compiling>.
- [64] E. Calore, A. Gabbana, S. F. Schifano, R. Tripiccone, Early Experience on Using Knights Landing Processors for Lattice Boltzmann Applications, in: R. Wyrzykowski, J. Dongarra, E. Deelman, K. Karczewski (Eds.), *Parallel Processing and Applied Mathematics*, Springer International Publishing, Cham, 2018, pp. 519–530. doi:10.1007/978-3-319-78024-5\_45.
- [65] S. T. Zalesak, Fully multidimensional flux-corrected transport algorithms for fluids, *Journal of Computational Physics* 31 (3) (1979) 335 – 362. doi:doi.org/10.1016/0021-9991(79)90051-2.
- [66] D. Hahn, M. Özisik, *Heat Conduction*. Third Edition, Wiley & Sons, 2012.
- [67] A. Esmaceli, G. Tryggvason, A front tracking method for computations of boiling in complex geometries, *International Journal of Multiphase Flow* 30 (7) (2004) 1037 – 1050, a Collection of Papers in Honor of Professor G. Yadigaroglu on the Occasion of his 65th Birthday. doi:10.1016/j.ijmultiphaseflow.2004.04.008.
- [68] V. Pandey, G. Biswas, A. Dalal, Effect of superheat and electric field on saturated film boiling, *Physics of Fluids* 28 (5) (2016) 052102. doi:10.1063/1.4948545.
- [69] A. Begmohammadi, M. Rahimian, M. Farhadzadeh, M. A. Hatani, Numerical simulation of single- and multi-mode film boiling using lattice Boltzmann method, *Computers & Mathematics with Applications* 71 (9) (2016) 1861 – 1874. doi:10.1016/j.camwa.2016.02.033.
- [70] A. Hu, D. Liu, 2D Simulation of boiling heat transfer on the wall with an improved hybrid lattice Boltzmann model, *Applied Thermal Engineering* 159 (2019) 113788. doi:10.1016/j.applthermaleng.2019.113788.
- [71] N. K. Singh, B. Premachandran, Numerical investigation of film boiling on a horizontal wavy wall, *International Journal of Heat and Mass Transfer* 150 (2020) 119371. doi:10.1016/j.ijheatmasstransfer.2020.119371.

# Grand-potential-based phase-field model of dissolution/precipitation: lattice Boltzmann simulations of counter term effect on porous medium

TÉO BOUTIN<sup>a</sup>, WERNER VERDIER<sup>a</sup>, ALAIN CARTALADE<sup>a,\*</sup>

<sup>a</sup> Université Paris-Saclay, CEA, Service de Thermo-hydraulique et de Mécanique des Fluides, 91191, Gif-sur-Yvette, France.

## Abstract

Most of the lattice Boltzmann methods simulate an approximation of the sharp interface problem of dissolution and precipitation. In such studies the curvature-driven motion of interface is neglected in the Gibbs-Thomson condition. In order to simulate those phenomena with or without curvature-driven motion, we propose a phase-field model which is derived from a thermodynamic functional of grand-potential. Compared to the free energy, the main advantage of the grand-potential is to provide a theoretical framework which is consistent with the equilibrium properties such as the equality of chemical potentials. The model is composed of one equation for the phase-field  $\phi$  coupled with one equation for the chemical potential  $\mu$ . In the phase-field method, the curvature-driven motion is always contained in the phase-field equation. For canceling it, a counter term must be added in the  $\phi$ -equation. For reason of mass conservation, the  $\mu$ -equation is written with a mixed formulation which involves the composition  $c$  and the chemical potential. The closure relationship between  $c$  and  $\mu$  is derived by assuming quadratic free energies for the bulk phases. The anti-trapping current is also considered in the composition equation for simulations with null solid diffusion. The lattice Boltzmann schemes are implemented in `LBM_saclay`, a numerical code running on various High Performance Computing architectures. Validations are carried out with analytical solutions representative of dissolution and precipitation. Simulations with or without counter term are compared on the shape of porous medium characterized by microtomography. The computations have run on a single GPU-V100.

## Keywords:

Phase-field model, Grand-potential, Lattice Boltzmann method, Dissolution/Precipitation, porous media, `LBM_saclay` code.

## 1. Introduction

The Lattice Boltzmann Equation (LBE) [1] is an attractive method to simulate flow and transport phenomena in several areas of science and engineering. Because of its local collision term and its ease of implementation of the bounce-back method, the LBE has been extensively applied in porous media literature for simulating two-phase flows and transport at pore scale [2, 3, 4] (see [5] for a recent review). When the surface of separation  $\Gamma_{sl}$  between solid ( $s$ ) and liquid ( $l$ ) does not depend on time, it is sufficient to identify the nodes located at the interface and to apply the bounce-back method. However, when physico-chemical processes occur on the surface of solid, such as those involved in matrix dissolution or pore clogging, it is necessary to consider the free-boundary problem because the interface position  $\Gamma_{sl}(t)$  is now a function of time. The general sharp interface model of dissolution and precipitation without fluid flows writes:

$$\frac{\partial c}{\partial t} = D_{\Phi} \nabla^2 c \quad \text{in } \Gamma_{\Phi}(t) \quad (1a)$$

$$(c - c_s) v_n = -D_l \nabla c \cdot \mathbf{n}|_l + D_s \nabla c \cdot \mathbf{n}|_s \quad \text{on } \Gamma_{sl}(t) \quad (1b)$$

$$G(c) = -d_0 \kappa - \beta v_n \quad \text{on } \Gamma_{sl}(t) \quad (1c)$$

Eq. (1a) is the mass conservation of solute in bulk domains  $\Gamma_{\Phi}(t)$  (where  $\Phi = s, l$ ),  $c$  is the composition,  $D_{\Phi}$  is the diffusion coefficient of liquid ( $\Phi = l$ ) and solid ( $\Phi = s$ ). Although  $D_s$  is supposed to be zero in most of the dissolution studies, two diffusion coefficients  $D_l$  and  $D_s$  are considered for mathematical reasons. In Section 2.4, we will see the necessity of using an anti-trapping current in the phase-field model when  $D_s = 0$ . Two conditions hold at the interface  $\Gamma_{sl}(t)$ . The first one (Eq. (1b)) is the balance of advective and diffusive fluxes where  $v_n$  is the normal velocity of interface. In that equation the right-hand side is the difference of diffusive fluxes between liquid and solid,  $\mathbf{n}$  is the unit normal vector of interface pointing into the liquid, and  $c_s$  is the composition of the solid phase. The second interface equation (Eq. (1c)) is the Gibbs-Thomson condition that relates the driving force  $G(c)$  (left-hand side) to the interface motion (right-hand side). In literature, the most common form of  $G(c)$  is proportional to the difference between the interface composition  $c_i$  and the solid composition  $c_s$ :  $G(c) \propto (c_i - c_s)$ . Two terms contribute to the interface motion: the first one is the curvature-driven motion  $-d_0 \kappa$  where  $\kappa$  is the curvature and  $d_0$  is a capillary length coefficient. The second term is the normal velocity  $-\beta v_n$  where  $\beta$  is a kinetic coefficient representing the dissipation of energy.

In literature, the lattice Boltzmann methods often simulate an approximation of that sharp interface problem. In [6], the equilibrium distribution functions are designed to fulfill the mass conservation at the interface (Eq. (1b)). However, the method only simulates an approximation of the Gibbs-

\*Corresponding author. Tel.: +33 (0)1 69 08 40 67

Email addresses: teo.boutin@cea.fr (TÉO BOUTIN),  
werner.verdier@cea.fr (WERNER VERDIER),  
alain.cartalade@cea.fr (ALAIN CARTALADE)

Thomson condition because the curvature term is neglected ( $-d_0\kappa = 0$ ). For instance in [7], Eq. (1c) is replaced by an evolution equation of the volume fraction of solid: the time variation of the mineral volume  $V$  is related to the reaction flux by  $\partial_t V = -V_m A(c - c_s)$  [7, Eq. (5)] where  $V_m$  is the molar volume of mineral and  $A$  is the product of solid area times a kinetic coefficient. The model has been applied recently in [8] for studying the influence of pore space heterogeneity on mineral dissolution. When the surface tension of the material can be neglected, then the assumption  $-d_0\kappa = 0$  hold. But in most cases  $-d_0\kappa \neq 0$  and the accurate position of interface  $\Gamma_{sl}(t)$  must be computed while maintaining the two conditions Eqs (1b)-(1c) at each time-step.

Alternative methods exist for simulating the interface tracking problem. In the “phase-field method”, a phase index  $\phi \equiv \phi(\mathbf{x}, t)$  is introduced to describe the solid matrix if  $\phi = 0$  (solid) and the pore volume if  $\phi = 1$  (liquid). The phase index varies continuously between those two extreme values ( $0 \leq \phi \leq 1$ ) i.e. the method considers the interface as a diffuse zone. That diffuse interface is characterized by a diffusivity coefficient  $M_\phi$  and an interface width  $W$ . The interface, initially a surface, becomes a volumic region of transition between liquid and solid. The model is composed of two coupled Partial Derivative Equations (PDEs) defined on the whole computational domain. The first equation describes the dynamics of the phase-field  $\phi$  and the second one describes the dynamics of composition  $c \equiv c(\mathbf{x}, t)$ . Those two PDEs recover the sharp interface problem Eqs. (1a)–(1c) when  $W \rightarrow 0$ . The Gibbs-Thomson condition Eq. (1c) is replaced by the phase-field equation which contains implicitly the curvature term  $-d_0\kappa$ . By “implicitly” we mean that the phase-field models always include the curvature-driven motion when they derive from a double-well potential.

Various phase-field models have already been proposed for simulating the processes of precipitation and dissolution [9, 10, 11, 12]. The main feature of those works is the model derivation from a free energy functional  $\mathcal{F}[\phi, c]$ . The phase-field models that derive from such a functional have been successfully applied for solid/liquid phase change such as those encountered in crystal growth (e.g. [13] for pure substance and [14, 15] for dilute binary mixture). For those applications, the functional  $\mathcal{F}[\phi, T]$  depends on the phase-field  $\phi$  and the temperature  $T$ , which is an intensive thermodynamic variable. In spite of those successes for solid/liquid phase change, an issue occurs for models involving composition. The composition is an extensive thermodynamic quantity and the models do not necessarily insure the equality of chemical potentials at equilibrium. In order to fulfill that condition, the Kim-Kim-Suzuki (KKS) model [16] introduces two fictitious compositions  $c_s(\mathbf{x}, t)$  and  $c_l(\mathbf{x}, t)$  in addition to the global composition  $c(\mathbf{x}, t)$ . The two PDEs are formulated in  $\phi$  and  $c$  and the source term of  $\phi$  depends on  $c_s$  and  $c_l$ . With a Newton method, those two compositions are explicitly computed inside the interface by imposing the equality of chemical potential [17, p. 126]. That model has been applied for dissolution in [10, 12].

A formulation based on the grand-potential thermodynamic functional  $\Omega[\phi, \mu]$  avoids that supplementary numerical stage. That approach, proposed in [18], yields a phase-

field model that is totally equivalent to the KKS model. That theoretical framework contains the construction of common tangent and insures the equality of chemical potential at equilibrium. In the same way as they are derived from  $\mathcal{F}[\phi, c]$ , the PDEs are established by minimizing  $\Omega[\phi, \mu]$ . Hence, we retrieve the same features in the definition of  $\Omega$ . The density of grand-potential is composed of two terms. The first one, noted  $\omega_{int}(\phi, \nabla\phi)$ , contains the standard double-well potential and the gradient energy term of the interface. The second one, noted  $\omega_{bulk}(\phi, \mu)$  is an interpolation of bulk grand-potentials  $\omega_\phi(\mu)$ . Those latter come from the Legendre transform of free energy densities  $f_\phi(c)$ . The main dynamical variables of  $\Omega$  are the phase-field  $\phi$  and the chemical potential  $\mu \equiv \mu(\mathbf{x}, t)$ . The chemical potential is the conjugate variable to  $c$ , and like temperature, it is an intensive thermodynamic quantity. Whereas it is inappropriate to make an analogy between  $T$  and  $c$  when deriving models, an analogy can be done between  $T$  and  $\mu$ . Thus, the asymptotics are quite similar for establishing the equivalence between the sharp interface models and the phase-field ones. That theoretical framework is already extended to study multi-component phase transformation [19]. It has been applied for dendritic electro-deposition in [20]. The capability of grand-potential phase-field models to simulate spinodal decomposition is presented in [21]. In reference [22] effects are presented of introducing elasticity with different interpolation schemes in the grand-potential framework.

Contrary to solidification, the curvature term  $-d_0\kappa$  is often neglected in models of dissolution and precipitation. For instance in [9], the Gibbs-Thomson condition simply relates the normal velocity  $v_n$  proportionally to  $(c_i - c_s)$ . In [10] the normal velocity is only equal to the Tafel’s equation [10, Eqs. (2)-(3)]. In [11], the curvature term appears in the sharp interface model but the coefficient in front of the curvature is considered very small. However, the curvature-driven motion plays a fundamental role in the Ostwald ripening [23]. The Ostwald ripening is the dissolution of matter that occurs at regions with small radius of curvature. After diffusion of solute through the liquid, a re-precipitation occurs at regions with larger radius of curvature. The phenomenon originates from the difference of chemical potentials between solid grains of different sizes which is proportional to the surface tension and inversely proportional to the radius (i.e. the curvature  $\kappa$ ). The larger grains are energetically more favorable than smaller ones which disappear in favor of bigger ones. The same process occurs for two-phase systems composed of two immiscible liquids. The drop of pressure is proportional to the ratio of the surface tension over the radius (Laplace’s law). The smallest droplets disappear whereas the larger ones growth.

As already mentioned, that motion is always contained in the phase-field model. If it is undesired in the simulations, it is necessary to add a counter term  $-M_\phi\kappa|\nabla\phi|$  in the phase-field equation as proposed in the pioneer work [24]. The counter term has been included for interface tracking in the Allen-Cahn equation in reference [25]. For two-phase flows a “conservative Allen-Cahn” equation has been formulated in [26] and coupled with the incompressible Navier-Stokes equations. For dissolution, the same term has been con-

sidered in the phase-field equation of [9]. Here, the effect of the counter term is presented on the dissolution of a 2D porous medium. That term has an impact on the shape of the porous medium and the heterogeneity of composition inside the solid phase.

In this paper, we derive in Section 2 a phase-field model based on the grand-potential functional for simulating the processes of dissolution and precipitation. In Section 2.1, the phase-field equation is presented without counter term  $-M_\phi \kappa |\nabla \phi|$  for keeping the curvature-driven motion. Next, in Section 2.2, the counter term is included in the phase-field equation which is reformulated in conservative form. Although the second main dynamical variable is the chemical potential  $\mu$ , we use in this work a mixed formulation between the composition  $c$  and the chemical potential  $\mu$  (Section 2.3). The reason of this choice is explained by a better mass conservation when simulating the model. For the sake of simplicity, the link to a thermodynamic database is not considered in this work. The grand-potential densities of each bulk phase derive from two analytical forms of free energy densities. We assume they are quadratic with different curvatures  $\epsilon_l$  and  $\epsilon_s$  for each parabola (Section 2.3). Next, Section 2.4 is dedicated to a discussion about the relationships of phase-field parameters  $W$ ,  $\lambda$  and  $M_\phi$  with the sharp interface parameters, the capillary length  $d_0$  and the kinetic coefficient  $\beta$ . Those relationships will give indications to set the coupling parameter  $\lambda$  in the simulations.

The model is implemented in `LBM_saclay`, a numerical code running on various High Performance Computing architectures. With simple modifications of compilation flags, the code can run on CPUs (Central Process Units) or GPUs (Graphics Process Units) [27]. The LBM schemes of phase-field model are presented in Section 3. A special care is taken for canceling diffusion in solid phase and accounting for the anti-trapping current. Validations are carried out in Section 4. LBM results are compared with analytical solutions for precipitation and next for dissolution. The first case is performed for  $D_s \simeq D_l$  (Section 4.1) to show the discontinuity of composition on each side of interface. The second one presents for  $D_s = 0$  (Section 4.2) the impact of anti-trapping current on the profiles of composition. Finally, in Section 5, we present the dissolution of a porous medium characterized by microtomography. Two simulations compare the effect of the counter term on the composition and the shape of porous medium.

## 2. Phase-field model of dissolution/precipitation

The purpose of this Section is to present the phase-field model of dissolution and precipitation. Its derivation introduces a great quantity of mathematical notations. The reason is inherent to the whole methodology: the *diffuse interface method*, which originates from *out-of-equilibrium thermodynamics*, recovers the *sharp-interface model* through the *matched asymptotic expansions*. Each keyword introduces its own mathematical notations. All those relative to physical modeling are summarized in Tab. 1.

In Section 2.1, we remind the theoretical framework of grand-potential  $\Omega$ , and we present the general evolution equations on  $\phi$  and  $\mu$ . Section 2.2 reminds the equilibrium prop-

erties of the phase-field equation and introduces the counter term for canceling the curvature-driven motion. Equations on  $\phi$  and  $\mu$  require the densities of grand-potential for each phase  $\omega_s(\mu)$  and  $\omega_l(\mu)$ . In Section 2.3 their expressions are derived from analytical forms of free energies  $f_s(c)$  and  $f_l(c)$ . The phase-field model will be re-written with a mixed formulation between  $\mu$  and  $c$  with the compositions of coexistence and the equilibrium chemical potential. Finally, in Section 2.4 a discussion will be done regarding the links between phase-field model and free-boundary problem.

### 2.1. General equations on $\phi$ and $\mu$ in the grand-potential theoretical framework

The grand-potential  $\Omega[\phi, \mu]$  is a thermodynamic functional which depends on the phase-field  $\phi \equiv \phi(\mathbf{x}, t)$  and the chemical potential  $\mu \equiv \mu(\mathbf{x}, t)$ , two functions of position  $\mathbf{x}$  and time  $t$ . In comparison,  $\phi(\mathbf{x}, t)$  and the composition  $c(\mathbf{x}, t)$  are two main dynamical variables of free energy  $\mathcal{F}[\phi, c]$ . The functional of grand-potential contains the contribution of two terms:

$$\Omega[\phi, \mu] = \int_V [\omega_{int}(\phi, \nabla \phi) + \omega_{bulk}(\phi, \mu)] dV \quad (2)$$

The first term inside the brackets is the grand-potential density of interface  $\omega_{int}(\phi, \nabla \phi)$  which is defined by the contribution of two terms depending respectively on  $\phi$  and  $\nabla \phi$ :

$$\omega_{int}(\phi, \nabla \phi) = H\omega_{dw}(\phi) + \frac{\zeta}{2} |\nabla \phi|^2. \quad (3)$$

In Eq. (3), the first term is the double-well potential  $\omega_{dw}(\phi)$  and  $H$  is its height. The second term is the gradient energy term which is proportional to the coefficient  $\zeta$ . A quick dimensional analysis shows that the physical dimension of  $H$  is an energy per volume unit ( $[E].[L]^{-3}$ ) and  $\zeta$  has the dimension of energy per length unit ( $[E].[L]^{-1}$ ). Those two contributions are identical for models that are formulated with a free energy functional  $\mathcal{F}[\phi, c]$ . The mathematical form of the double-well used in this work will be specified in Section 2.2.

In Eq. (2), the second term  $\omega_{bulk}(\phi, \mu)$  interpolates the grand-potential densities of each bulk phase  $\omega_s(\mu)$  and  $\omega_l(\mu)$  by:

$$\omega_{bulk}(\phi, \mu) = p(\phi)\omega_l(\mu) + [1 - p(\phi)]\omega_s(\mu) \quad (4)$$

where  $p(\phi)$  is an interpolation function. It is sufficient to define it (see Section 2.4) as a monotonous function such as  $p(0) = 0$  and  $p(1) = 1$  in the bulk phases with null derivatives (w.r.t.  $\phi$ )  $p'(0) = p'(1) = 0$ . In this work we choose

$$p(\phi) = \phi^2(3 - 2\phi) \quad (5a)$$

and its derivative w.r.t.  $\phi$  is

$$p'(\phi) = 6\phi(1 - \phi) \quad (5b)$$

With that convention, if  $\phi = 0$  then  $\omega_{bulk}(\mu) = \omega_s(\mu)$  and if  $\phi = 1$  then  $\omega_{bulk}(\mu) = \omega_l(\mu)$ .

In this paper, we work with the dimensionless composition  $c(\phi, \mu)$  describing the local fraction of one chemical



## Nomenclature of physical modeling

Symbol	Definition	Dimension	Description
<b>Thermodynamics</b>			
$\Omega[\phi, \mu]$		[E]	Grand-potential functional
$\mu(\mathbf{x}, t)$		[E].[mol] <sup>-1</sup>	Chemical potential
$C(\phi, \mu)$		[mol].[L] <sup>-3</sup>	Global concentration depending on $\phi$ and $\mu$
$\omega_{int}(\phi, \nabla\phi)$	Eq. (3)	[E].[L] <sup>-3</sup>	Grand-potential density of interface
$\omega_{dw}(\phi)$	see Tab. 2	[-]	Double-well potential of minima $\phi_s$ and $\phi_l$
$\omega_{bulk}(\phi, \mu)$	Eq. (4)	[E].[L] <sup>-3</sup>	Interpolation of bulk grand-potential density
$V_m$		[L] <sup>3</sup> .[mol] <sup>-1</sup>	Molar volume
$\chi$	$= \partial C(\phi, \mu) / \partial \mu$	[mol] <sup>2</sup> .[L] <sup>-3</sup> .[E] <sup>-1</sup>	Generalized susceptibility
$\Phi$		[-]	Index for bulk phases: solid $\Phi = s$ and liquid $\Phi = l$
$\mathcal{M}_\phi$		[L] <sup>3</sup> .[E] <sup>-1</sup> .[T] <sup>-1</sup>	Mobility coefficient of the interface
$\phi_0(\mathbf{x})$		[-]	Hyperbolic tangent solution
$\zeta$		[E].[L] <sup>-1</sup>	Coefficient of gradient energy term
$H$		[E].[L] <sup>-3</sup>	Height of double-well function
$\sigma$	$= (1/6)\sqrt{2\zeta H}$	[E].[L] <sup>-2</sup>	Surface tension
$f_\Phi(c)$		[E].[L] <sup>-3</sup>	Free energy density of bulk phases
$m_\Phi$		[-]	Compositions for which $f_\Phi$ is minimum
$\omega_\Phi(\mu)$	$= f_\Phi - \mu C$	[E].[L] <sup>-3</sup>	Grand-potential density of each bulk phase
$\varepsilon_\Phi$		[E].[L] <sup>-3</sup>	Curvature of quadratic free energies
$\mathcal{E}$	$= \sqrt{\varepsilon_l \varepsilon_s}$	[E].[L] <sup>-3</sup>	Reference volumic energy for dimensionless quantities
$\Delta f^{min}$	$= f_s^{min} - f_l^{min}$	[E].[L] <sup>-3</sup>	Difference of minimum values of free energy densities
$\overline{\omega}_\Phi$	$= \omega_\Phi / \mathcal{E}$	[-]	Dimensionless grand-potential of bulk phases
$\overline{f}_\Phi$	$= f_\Phi / \mathcal{E}$	[-]	Dimensionless free energy densities
<b>Phase-field model</b>			
$\phi(\mathbf{x}, t)$		[-]	Phase-field $\phi_s \leq \phi \leq \phi_l$
$\phi_s, \phi_l$		[-]	values of $\phi(\mathbf{x}, t)$ in bulk phases: $\phi_s = 0$ and $\phi_l = 1$
$W$	$= \sqrt{8\zeta/H}$	[L]	Interface width of $\phi$ -equation
$M_\phi$	$= \mathcal{M}_\phi \zeta$	[L] <sup>2</sup> .[T] <sup>-1</sup>	Diffusivity of $\phi$ -equation
$\lambda$	$= 8\mathcal{E}/H$	[-]	Coupling coefficient of $\phi$ -equation
$\mathbf{n}(\mathbf{x}, t)$	$= \nabla\phi /  \nabla\phi $	[-]	Unit normal vector of interface
$c(\phi, \mu)$	$= V_m C(\phi, \mu)$	[-]	Global composition depending on $\phi$ and $\mu$
$\bar{\mu}(\mathbf{x}, t)$	$= \mu / (\mathcal{E} V_m)$	[-]	Dimensionless chemical potential
$\bar{\mu}^{eq}$	$= \Delta \bar{f}^{min} / \Delta m$	[-]	Equilibrium chemical potential of interface Eq. (29a)
$c_\Phi^{co}$		[-]	Coexistence (or equilibrium) compositions of each phase
$c^{co}(\phi)$	Eq. (29b)	[-]	Interpolation of coexistence compositions $c_s^{co}$ and $c_l^{co}$
$D_\Phi$		[L] <sup>2</sup> .[T] <sup>-1</sup>	Diffusion coefficient of solid ( $\Phi = s$ ) and liquid ( $\Phi = l$ )
$p(\phi)$	see Tab. 2	[-]	Interpolation function of derivative zero for $\phi = 0$ and $\phi = 1$
$h(\phi)$	see Tab. 2	[-]	Interpolation function for $c(\phi, \mu)$
$q(\phi)$	see Tab. 2	[-]	Interpolation function for diffusion coefficients
$\mathcal{S}_\phi(\phi, \bar{\mu})$	Eq. (25)	[-]	Source term of phase-field equation
$\kappa(\mathbf{x}, t)$	$= \nabla \cdot \mathbf{n}$	[L] <sup>-1</sup>	Curvature
$-M_\phi \kappa  \nabla\phi $		[T] <sup>-1</sup>	Phenomenological counter term
$\mathbf{j}_{at}(\mathbf{x}, t)$	Eq. (32)	[L].[T] <sup>-1</sup>	Phenomenological anti-trapping current
$a$	1/4	[-]	Coefficient of anti-trapping current
<b>Sharp interface</b>			
$v_n$	$= \mathbf{v} \cdot \mathbf{n}$	[L].[T] <sup>-1</sup>	Normal velocity of interface
$d_0$	Eq. (36a)	[L]	Capillary length in Gibbs-Thomson condition Eq. (35c)
$\beta_\Phi$	Eq. (36b)	[L] <sup>-1</sup> .[T]	Kinetic coefficients in Gibbs-Thomson condition for $\Phi = s, l$
$q_s$	$= D_s / D_l$	[-]	Ratio of diffusion
$\varepsilon$	$= W / d_0$	[-]	Small parameter of asymptotic expansions
$\mathcal{I}_\Phi, \tilde{\mathcal{I}}_\Phi, \mathcal{G}_\Phi, \mathcal{H}_\Phi$	See Tab. 3	[-]	Integrals (part 1) of interpolation functions (for $\Phi = s, l$ )
$\mathcal{I}, \mathcal{H}, \mathcal{J}_\Phi$	See Tab. 3	[-]	Integrals (part 2)
$\mathbb{E}_1, \mathbb{E}_2, \mathbb{E}_3$			Error terms derived from the asymptotic analysis

Table 1: Main mathematical symbols with their physical dimensions. Unit convention: energy [E], length [L], time [T] and mole [mol].

species and varying between zero and one. It is related to the concentration  $C(\phi, \mu)$  (physical dimension  $[\text{mol}]/[\text{L}]^{-3}$ ) by  $c(\phi, \mu) = V_m C(\phi, \mu)$  where  $V_m$  is the molar volume of  $([\text{L}]^3/[\text{mol}]^{-1})$ . For both chemical species, the molar volume is assumed to be constant and identical. In the rest of this paper  $V_m$  will appear in the equations for reasons of physical dimension, but it will be considered equal to  $V_m = 1$  for all numerical simulations.

The concentration  $C$  is now a function of  $\phi$  and  $\mu$ . It is related to the grand-potential by [18]  $C(\phi, \mu) = -\delta\Omega/\delta\mu = -\partial\omega_{\text{bulk}}(\phi, \mu)/\partial\mu$ . The application of that relationship with  $\omega_{\text{bulk}}(\phi, \mu)$  defined by Eq. (4) yields:

$$C(\phi, \mu) = p(\phi) \left[ -\frac{\partial\omega_l(\mu)}{\partial\mu} \right] + [1 - p(\phi)] \left[ -\frac{\partial\omega_s(\mu)}{\partial\mu} \right] \quad (6)$$

The concentration  $C(\phi, \mu)$  is defined by an interpolation of derivatives of  $\omega_s(\mu)$  and  $\omega_l(\mu)$  w.r.t.  $\mu$ . Each derivative defines the concentration of bulk phase  $C_s(\mu) = -\partial\omega_s(\mu)/\partial\mu$  and  $C_l(\mu) = -\partial\omega_l(\mu)/\partial\mu$ .

In Eq. (4), the grand-potential densities of each bulk phase  $\omega_l(\mu)$  and  $\omega_s(\mu)$  are defined by the Legendre transform of free energy densities  $f_s(c)$  and  $f_l(c)$ :

$$\omega_\Phi(\mu) = f_\Phi(c) - \mu C \quad \text{for} \quad \Phi = s, l \quad (7)$$

where  $\mu = \partial f_\Phi / \partial C$ . Finally, the phase-field equations are obtained from the minimization of the grand-potential functional  $\Omega[\phi, \mu]$ . The most general PDEs write (see [18, Eq. (43) and Eq. (47)]):

$$\frac{\partial\phi}{\partial t} = \mathcal{M}_\phi \left\{ \zeta \nabla^2 \phi - H \omega'_{dw}(\phi) - p'(\phi) [\omega_l(\mu) - \omega_s(\mu)] \right\} \quad (8a)$$

$$\chi(\phi, \mu) \frac{\partial\mu}{\partial t} = \nabla \cdot [\mathcal{D}(\phi, \mu) \chi(\phi, \mu) \nabla \mu] - p'(\phi) \left[ \frac{\partial\omega_s(\mu)}{\partial\mu} - \frac{\partial\omega_l(\mu)}{\partial\mu} \right] \frac{\partial\phi}{\partial t} \quad (8b)$$

Eq. (8a) is the evolution equation on  $\phi(\mathbf{x}, t)$  which tracks the interface between solid and liquid. The phase-field equation is derived from  $\partial_t \phi = -\mathcal{M}_\phi \delta\Omega/\delta\phi$  where  $\mathcal{M}_\phi$  is a coefficient of dimension  $[\text{L}]^3/[\text{E}]^{-1}/[\text{T}]^{-1}$ . The equilibrium properties of that equation are reminded in Section 2.2. The derivative of the double-well function w.r.t.  $\phi$  is noted  $\omega'_{dw} = \partial\omega_{dw}/\partial\phi$ . Compared to the model of reference [18], we notice the opposite sign of the last term because our convention is  $\phi = 0$  for solid and  $\phi = 1$  for liquid. In the reference,  $\phi = 1$  is solid and  $\phi = -1$  is liquid and the interpolation function  $p(\phi)$  is opposite. In order to reveal the diffusivity coefficient  $M_\phi = \mathcal{M}_\phi \zeta$  of dimension  $[\text{L}]^2/[\text{T}]^{-1}$ , the coefficient  $\zeta$  can be put in factor of the right-hand side. In that case, the second term is multiplied by  $H/\zeta$  whereas the last term is divided by  $\zeta$ .

Eq. (8b) is the evolution equation on chemical potential  $\mu(\mathbf{x}, t)$ . It is obtained from the conservation equation  $\partial_t C(\phi, \mu) = -\nabla \cdot \mathbf{j}_{diff}$  where the diffusive flux is given by  $\mathbf{j}_{diff} = -\mathcal{D}(\phi, \mu) \chi(\phi, \mu) \nabla \mu$ . The time derivative term has been expressed by the chain rule  $\partial C(\phi, \mu)/\partial t = (\partial C/\partial \mu) \partial \mu/\partial t +$

$(\partial C/\partial \phi) \partial \phi/\partial t$ . The function  $\chi(\phi, \mu)$ , called the generalized susceptibility, is defined by the partial derivative of  $C(\phi, \mu)$  with respect to  $\mu$ . For most general cases, the coefficient  $\mathcal{D}(\phi, \mu)$  is the diffusion coefficient which depends on  $\phi$  and  $\mu$ . Here we assume that the diffusion coefficients  $D_s$  and  $D_l$  are only interpolated by  $\phi$ , i.e.  $\mathcal{D}(\phi, \mu) \equiv \mathcal{D}(\phi)$ . Actually, in section 2.3, that equation on  $\mu$  will be transformed back to an equation on  $C$  (or  $c$ ) for reasons of mass conservation in simulations. Eq. (6) will be used to supply a relationship between  $\mu$  and  $c$ .

For simulating Eqs. (8a) and (8b), it is necessary to define the grand-potential densities of each bulk phase  $\omega_s(\mu)$  and  $\omega_l(\mu)$ . They both derive from Legendre transforms (Eq. (7)) which require the knowledge of free energy densities  $f_s(c)$  and  $f_l(c)$ . The free energy densities  $f_s(c)$  and  $f_l(c)$  depend on the phase diagram of chemical species (or materials), the temperature and the number of species involved in the process (binary or ternary mixtures). When the model is implemented in a numerical code coupled with a thermodynamic database, those values are updated at each time step of computation. A method for coupling a phase-field model based on the grand-potential with a thermodynamic database is proposed in [28]. A coupling of a phase-field model with the “thermodynamics advanced fuel international database” is presented in [29] with OpenCalphad [30, 31]. In this work, we assume in Section 2.3 that the densities of free energies  $f_s(c)$  and  $f_l(c)$  are quadratic.

The variational formulation based on the grand-potential yields to evolution equations on  $\phi$  and  $\mu$  (Eqs. (8a)-(8b)). Two ingredients are missing in those equations: the first one is the counter term  $-M_\phi \kappa |\nabla \phi|$  and the second one is the anti-trapping current  $\mathbf{j}_{at}$ . In our work, both are not contained in the definition of grand-potential  $\Omega[\phi, \mu]$  and have no variational origin. The counter term has been derived in [24]. It is used in the phase-field equation (Section 2.2.2) to make vanish the curvature-driven motion. The anti-trapping current has been derived in [32]. It is used in the chemical potential equation (Section 2.3.4) to cancel spurious effects at interface when the diffusion is supposed to be null in the solid. Their use is justified by the matched asymptotic expansions carried out on the phase-field model. The links between the phase-field model and the free-boundary problem will be discussed in Section 2.4.

## 2.2. Equilibrium properties of phase-field equation

The phase-field equation Eq. (8a) has the same structure as those derived from functionals of free energy. Hence, the equilibrium properties such as the hyperbolic tangent solution  $\phi_0$ , the interface width  $W$  and the surface tension  $\sigma$  remain the same. Those equilibrium properties are reminded in Section 2.2.1 with one particular choice of double-well potential  $\omega_{dw}(\phi)$ . This is done for two reasons. The phase-field equation is written with “thermodynamic” parameters  $\zeta$ ,  $H$  and  $\mathcal{M}_\phi$ . The phase-field equation is re-written with “macroscopic” parameters  $M_\phi$ ,  $W$  and the dimensionless coupling coefficient  $\lambda$  because they are directly related to the capillary length  $d_0$  and kinetic coefficient  $\beta$  of sharp interface model. The equilibrium properties are also necessary for introducing in Section 2.2.2 the kernel function  $|\nabla \phi| = 4\phi(1-\phi)/W$  and the counter term  $-M_\phi \kappa |\nabla \phi|$ .

### 2.2.1. Hyperbolic tangent solution $\phi_0$ , width $W$ and surface tension $\sigma$

When the system is at equilibrium, the construction of common tangent hold and the chemical potential is identical in both phases of value  $\mu^{eq}$ . The construction of common tangent is mathematically equivalent to  $\omega_s(\mu^{eq}) = \omega_l(\mu^{eq})$ . When the two phases are at equilibrium, we define the corresponding compositions of coexistence (or equilibrium) by  $c_s^{co} = c_l(\mu^{eq})$  and  $c_l^{co} = c_l(\mu^{eq})$  for solid and liquid respectively. Hence, the last term proportional to  $p'(\phi)$  in Eq. (8a) vanishes at equilibrium and the time derivative is zero ( $\partial\phi/\partial t = 0$ ). We recognize the standard equilibrium equation for the interface  $\zeta \nabla^2 \phi - H \omega'_{dw} = 0$  i.e. in one dimension  $\zeta d^2\phi/dx^2 - H d\omega/d\phi = 0$ . After multiplying by  $d\phi/dx$ , the first term is the derivative  $d/dx$  of  $(d\phi/dx)^2$  and the second term becomes a derivative of the double-well w.r.t.  $x$ . After gathering those two terms inside the same brackets, it yields:

$$\frac{d}{dx} \left[ \left( \frac{d\phi}{dx} \right)^2 - \frac{2H}{\zeta} \omega_{dw} \right] = 0 \quad (9)$$

In this work we define the double-well by

$$\omega_{dw}(\phi) = \phi^2(1-\phi)^2 \quad (10a)$$

for which the two minima are  $\phi_s = 0$  and  $\phi_l = +1$  and its derivative w.r.t.  $\phi$  is:

$$\omega'_{dw}(\phi) = 2\phi(1-\phi)(1-2\phi) \quad (10b)$$

For that form of double-well, the solution of Eq. (9) is the usual hyperbolic tangent function

$$\phi_0(x) = \frac{1}{2} \left[ 1 + \tanh \left( \frac{2x}{W} \right) \right] \quad (11)$$

where the interface width  $W$  and the surface tension  $\sigma$  are defined by

$$W = \sqrt{\frac{8\zeta}{H}} \quad \text{and} \quad \sigma = \frac{1}{6} \sqrt{2\zeta H} \quad (12a)$$

We can check that the square root of the ratio  $\zeta/H$  is homogeneous to a length as expected for the physical dimension of the width  $W$ . Moreover, the square root of the product  $\zeta H$  is homogeneous to an energy per surface unit as expected for the surface tension  $\sigma$ . The two relationships Eq. (12a) can be easily inverted to yield

$$\zeta = \frac{3}{2} W \sigma \quad \text{and} \quad H = 12 \frac{\sigma}{W} \quad (12b)$$

From Eq. (12b), the ratio  $H/\zeta$  is equal to  $8/W^2$ . Hence, the factor in front of the double-well in Eq. (8a) can be replaced by  $8/W^2$  and the factor of the last term is once again expressed with  $W^2$  i.e.  $1/\zeta = 8/(W^2 H)$ .

As a matter of fact, the double-well function Eq. (10a) is a special case of other popular choices of double-well. For example in two-phase flows of immiscible fluids, the double-well is  $\omega_{dw}(\phi) = (\phi_l - \phi)^2(\phi - \phi_s)^2$  [33] with  $\phi_s \leq \phi \leq \phi_l$  for which the two minima are  $\phi_l$  and  $\phi_s$ . For that form of double-well, the equilibrium solution is  $\phi_0(x) = 0.5[\phi_l + \phi_s + (\phi_l - \phi_s) \tanh(2x/W)]$ , the surface tension is  $\sigma = (1/6)(\phi_l - \phi_s)^3 \sqrt{2\zeta H}$  and the interface width is  $W =$

$[1/(\phi_l - \phi_s)] \sqrt{8\zeta/H}$ . Eqs. (11) and (12a) can be recovered by setting  $\phi_l = 1$  and  $\phi_s = 0$ . Another popular choice of double-well is  $\omega_{dw}(\phi) = (\phi^* - \phi)^2(\phi + \phi^*)^2$  [34] for which the two minima are  $\pm\phi^*$ . Once again, that double-well function is a particular case of the previous one by setting  $\phi_l = \phi^*$  and  $\phi_s = -\phi^*$ . The equilibrium solution writes  $\phi_0(x) = \phi^* \tanh(2x/W)$ , the surface tension is  $\sigma = (4\phi^{*3}/3) \sqrt{2\zeta H}$  and the interface width  $W = (1/\phi^*) \sqrt{2\zeta/H}$ . In this work the choice of Eq. (10a) is done by simplicity.

### 2.2.2. Removing the curvature-driven motion in Eq. (8a)

Another useful relationship that derives from Eq. (9) is the kernel function  $|\nabla\phi|$ . The square root of the term inside the brackets yields  $|\nabla\phi| = (4/W) \sqrt{\omega_{dw}}$  where the coefficient  $2H/\zeta$  was replaced by the interface width  $W$  with Eq. (12b) ( $2H/\zeta = 16/W^2$ ). Thus, with a double-well function defined by Eq. (10a), the kernel function writes:

$$|\nabla\phi| = \frac{4}{W} \phi(1-\phi) \quad (13)$$

For canceling the curvature-driven interface motion, a counter term  $-M_\phi \kappa |\nabla\phi|$  is simply added in the right-hand side of the phase-field equation. The counter term is proportional to the interface diffusivity  $M_\phi$ , the curvature  $\kappa$  and the kernel function  $|\nabla\phi|$ . The curvature is defined by  $\kappa = \nabla \cdot \mathbf{n}$  where  $\mathbf{n}$  is the unit normal vector of the interface

$$\mathbf{n} = \frac{\nabla\phi}{|\nabla\phi|} \quad (14)$$

In Section 2.4.3, we check that adding such a counter term in the phase-field equation cancels the curvature motion  $-d_0 \kappa$  in the Gibbs-Thomson equation. In order to write the phase-field equation in a more compact form, we remark that the second term involving the derivative of the double-well is equivalent to

$$-\frac{8M_\phi}{W^2} \omega'_{dw}(\phi) = -M_\phi \mathbf{n} \cdot \nabla |\nabla\phi| \quad (15a)$$

provided that the kernel function Eq. (13) is used for  $|\nabla\phi|$ . If the counter term  $-M_\phi \kappa |\nabla\phi|$  is added in the right-hand side of Eq. (8a) then

$$-\frac{8M_\phi}{W^2} \omega'_{dw}(\phi) - M_\phi \kappa |\nabla\phi| = -M_\phi \mathbf{n} \cdot \nabla |\nabla\phi| - M_\phi (\nabla \cdot \mathbf{n}) |\nabla\phi| \quad (15b)$$

where the definition of the curvature  $\kappa = \nabla \cdot \mathbf{n}$  has been applied for the second term. The right-hand side of Eq. (15b) is  $-M_\phi \nabla \cdot [|\nabla\phi| \mathbf{n}]$  and by using the kernel function  $|\nabla\phi| = (4/W) \phi(1-\phi)$  the phase-field equation writes

$$\frac{\partial\phi}{\partial t} = M_\phi \nabla \cdot \left[ \nabla\phi - \frac{4}{W} \phi(1-\phi) \mathbf{n} \right] - \frac{8M_\phi}{W^2 H} p'(\phi) \Delta\omega \quad (16)$$

where  $\Delta\omega = \omega_l(\mu) - \omega_s(\mu)$ . In simulations of Sections 4 and 5 two versions of the phase-field equation are used: Eq. (8a) when the curvature-driven motion is desired and Eq. (16) when that motion is undesired. When the source term of that equation is null, and when an advective term  $\nabla \cdot (\mathbf{u}\phi)$  is considered, Eq. (16) is the conservative Allen-Cahn equation that is applied for interface tracking of two immiscible fluids [26, 35].



### 2.3. Phase-field model derived from quadratic free energies

The source terms of Eqs. (8a) and (8b) contain the bulk densities of grand-potential  $\omega_l(\mu)$  and  $\omega_s(\mu)$ . They need to be specified. Here, we work with analytical expressions which define explicitly  $\omega_l$  and  $\omega_s$  as functions of  $\mu$ . The main advantage of that choice is to simplify their expressions by involving several scalar parameters representative of the thermodynamics. The densities of grand-potential are defined by the Legendre transform of free energy densities  $f_s(c)$  and  $f_l(c)$ . In [18], several choices for  $f_\Phi(c)$  are proposed in order to relate the grand-potential framework to the well-known models derived from free energy. The simplest phenomenological approximation is a quadratic free energy for each phase  $\Phi = s$  and  $\Phi = l$ :

$$f_\Phi(c) = \frac{\epsilon_\Phi}{2}(c - m_\Phi)^2 + f_\Phi^{\min} \quad \text{for } \Phi = s, l \quad (17)$$

where  $\epsilon_\Phi$ , of physical dimension  $[E].[L]^{-3}$ , are the curvature of each parabola and  $m_\Phi$  are two values of composition for which  $f_\Phi(c)$  are minimum of values  $f_\Phi^{\min}$ . In other words, when the phase diagram (i.e. the free energy versus composition) is available, it presents two regions (one for each phase) of smallest free energy  $f_\Phi^{\min}$  corresponding to the composition  $m_\Phi$ . Eq. (17) means that each region is approximated by one parabola, where  $\epsilon_\Phi$  is a parameter for improving the curvature fit around each minimum. As a comparison, the well-known Cahn-Hilliard equation is derived from one single double-well potential. The Cahn-Hilliard model is a fourth-order equation where the variable plays the roles of interface tracking and composition. Here, the single double-well is approximated by two separated parabolas. The advantage of that splitting is to facilitate the thermodynamical fit around each minima by using two functions with their own parameters. The double-well  $\omega_{dw}$ , defined in  $\omega_{int}$  (Eq. (3)), is used for tracking the interface between the bulk phases. With that approach, the parameters of  $\omega_{int}$  control the interface properties (width and surface tension) whereas the parameters of  $f_\Phi$  control the thermodynamics. As a drawback, the compositions of solid and liquid must not be initialized too far from each composition  $m_\Phi$ . In particular, the spinodal decomposition cannot be simulated without modification of the model. Let us emphasize that the compositions  $m_\Phi$  do not correspond to the coexistence compositions  $c_\Phi^{co}$  (also called compositions of equilibrium). When a binary system is considered with  $\epsilon_s = \epsilon_l$ , the construction of common tangent yields a simple relationship between  $m_\Phi$  and  $c_\Phi^{co}$  (see Section 2.3.2). But this is not true for more general cases, in particular for a system with two phases and three components.

In this Section, all terms of Eqs. (8a) and (8b) involving  $\omega_\Phi$  are simplified with the hypothesis of Eq. (17). First, Section 2.3.1 deals with the difference of grand-potential densities  $\omega_l(\mu) - \omega_s(\mu)$  which will be written with the dimensionless chemical potential  $\bar{\mu}$  and the thermodynamical parameters  $\epsilon_\Phi$ ,  $m_\Phi$  and  $f_\Phi^{\min}$  of Eq. (17). Section 2.3.2 introduces the coexistence compositions  $c_\Phi^{co}$  of interface and the equilibrium chemical potential  $\bar{\mu}^{eq}$ . The difference  $\omega_l(\mu) - \omega_s(\mu)$  will be re-expressed with  $c_\Phi^{co}$ ,  $\bar{\mu}$  and  $\bar{\mu}^{eq}$ . In Section 2.3.3 the composition equation is re-written with a mixed

formulation between  $c(\phi, \mu)$  and  $\bar{\mu}$ , and in Section 2.3.4 the anti-trapping current  $\mathbf{j}_{at}$  will be formulated as a function of  $c_\Phi^{co}$ . Finally, the complete model is summarized in Section 2.3.5.

#### 2.3.1. Difference of grand-potential densities in $\phi$ -equation

We start with the difference  $\omega_l(\mu) - \omega_s(\mu)$  where the chemical potential is defined by  $\mu = \partial f_\Phi / \partial C = V_m \partial f_\Phi / \partial c$  (for  $\Phi = s, l$ ). By inverting those relationships to obtain  $c$  as a function of  $\mu$ , the Legendre transforms of each bulk phase yield the grand-potential densities as function of  $\mu$  (see intermediate steps in [18]):

$$\omega_\Phi(\mu) = -\frac{\mu^2}{2V_m^2\epsilon_\Phi} - \frac{\mu}{V_m}m_\Phi + f_\Phi^{\min} \quad \text{for } \Phi = s, l \quad (18)$$

Before going further we set  $\Delta f^{\min} = f_s^{\min} - f_l^{\min}$  and we define the quantity  $\mathcal{E} = \sqrt{\epsilon_s \epsilon_l}$  (dimension  $[E].[L]^{-3}$ ) for introducing the dimensionless quantities  $\bar{\omega}_\Phi$ ,  $\bar{\mu}$  and  $\Delta \bar{f}^{\min}$  by  $\omega_\Phi = \bar{\omega}_\Phi \mathcal{E}$  (with  $\Phi = s, l$ ),  $\mu = \bar{\mu} V_m \mathcal{E}$  and  $\Delta f^{\min} = \mathcal{E} \Delta \bar{f}^{\min}$ . With those reduced variables, the difference  $\Delta \bar{\omega} = \bar{\omega}_l(\bar{\mu}) - \bar{\omega}_s(\bar{\mu})$  writes

$$\mathcal{E} \Delta \bar{\omega} = \mathcal{E} \left[ \frac{(\epsilon_l - \epsilon_s)}{\sqrt{\epsilon_l \epsilon_s}} \frac{\bar{\mu}^2}{2} - (m_l - m_s) \bar{\mu} - \Delta \bar{f}^{\min} \right] \quad (19)$$

Finally, if we define the dimensionless coefficient of coupling by  $\lambda = 8\mathcal{E}/H$ , the last term of Eq. (8a) writes

$$-\frac{8M_\phi \mathcal{E}}{W^2 H} p'(\phi) \Delta \bar{\omega} = -\frac{\lambda M_\phi}{W^2} \mathcal{S}_\phi(\phi, \bar{\mu}) \quad (20)$$

where for future use we have set  $\mathcal{S}_\phi(\phi, \bar{\mu}) \equiv \mathcal{S}_\phi$  defined by:

$$\mathcal{S}_\phi = p'(\phi) \left[ \frac{(\epsilon_l - \epsilon_s)}{\sqrt{\epsilon_l \epsilon_s}} \frac{\bar{\mu}^2}{2} - (m_l - m_s) \bar{\mu} - \Delta \bar{f}^{\min} \right] \quad (21)$$

When the free energies are quadratic, the coupling term of Eq. (8a) becomes Eq. (20) with  $\mathcal{S}_\phi(\phi, \bar{\mu})$  defined by Eq. (21). The dimensionless chemical potential  $\bar{\mu}$  appears explicitly in that equation.

#### 2.3.2. Coexistence compositions and chemical potential of equilibrium

In Eq. (21),  $m_s$  and  $m_l$  are two specific values of  $c$  for which the quadratic free energies  $f_s$  and  $f_l$  are minimum. A close link exists between  $m_\Phi$  and the coexistence (or equilibrium) compositions  $c_\Phi^{co}$ . Two relationships allow deriving them: the first one is the equality of chemical potential  $\mu^{eq}$ :

$$\mu^{eq} = V_m \left. \frac{\partial f_s}{\partial c} \right|_{c=c_s^{co}} = V_m \left. \frac{\partial f_l}{\partial c} \right|_{c=c_l^{co}} \quad (22a)$$

and the second one is the equality of grand-potential densities

$$\omega_s(\mu^{eq}) = \omega_l(\mu^{eq}). \quad (22b)$$

The graphical representation of Eq. (22b) is the standard construction of common tangent. When the curvature of

each parabola are identical  $\varepsilon_s = \varepsilon_l = \varepsilon$ , Eq. (22a) yields  $\bar{\mu}^{eq} = c_s^{co} - m_s = c_l^{co} - m_l$  and Eq. (22b) yields

$$\bar{\mu}^{eq} = \frac{\Delta \bar{f}^{min}}{\Delta m} \quad (23)$$

where  $\Delta m = m_s - m_l$  and  $\Delta \bar{f}^{min}$  has been defined in Section 2.3.1. Finally, those two conditions yield two simple relationships between  $c_\Phi^{co}$  and the parameters  $m_\Phi$  and  $\bar{f}_\Phi^{min}$ :

$$c_l^{co} = m_l + \frac{\Delta \bar{f}^{min}}{\Delta m} \quad (24a)$$

$$c_s^{co} = m_s + \frac{\Delta \bar{f}^{min}}{\Delta m} \quad (24b)$$

In the binary case this couple of coexistence compositions is unique, and the mathematical model can be re-defined with  $c_\Phi^{co}$  and  $\bar{\mu}^{eq}$ . More precisely in Eq. (21),  $m_l$  and  $m_s$  are replaced with  $c_l^{co}$  and  $c_s^{co}$  by using Eqs. (24a)-(24b). In addition, the ratio  $\Delta \bar{f}^{min}/\Delta m$  is simply replaced by  $\bar{\mu}^{eq}$ . The source term simplifies to

$$\mathcal{S}_\Phi = p'(\phi)(c_s^{co} - c_l^{co})(\bar{\mu} - \bar{\mu}^{eq}) \quad (25)$$

Here the source term has been formulated with  $c_s^{co}$  and  $c_l^{co}$  provided that  $\varepsilon_s = \varepsilon_l = \varepsilon$ . If  $\varepsilon_s \neq \varepsilon_l$  the relationships between  $m_\Phi$  and  $c_\Phi^{co}$  are more complicated because they are solutions of second degree equations. That case will be studied in a future work. Finally, we can relate the compositions  $c(\phi, \bar{\mu})$  to the chemical potential  $\bar{\mu}$ . By using the definition  $C_\Phi(\mu) = c_\Phi(\mu)/V_m$  and the dimensionless notation  $\bar{\mu} = \mu/V_m \mathcal{E}$ , we obtain  $c_l(\bar{\mu}) = \bar{\mu}(\varepsilon_s/\varepsilon_l)^{1/2} + m_l$  and  $c_s(\bar{\mu}) = \bar{\mu}(\varepsilon_l/\varepsilon_s)^{1/2} + m_s$ . Those relationships will be useful in Section 4.

### 2.3.3. Mixed formulation and closure relationship between $c(\phi, \bar{\mu})$ and $\bar{\mu}$ in $c$ -equation

Even though the equation on chemical potential (Eq. (8b)) could be directly simulated, we prefer using a mixed formulation that involves both variables  $c$  and  $\bar{\mu}$ . The time derivative is expressed with  $c$  and the flux is expressed with  $\bar{\mu}$ . The advantage of such a formulation, inspired from [36, p. 62], is explained by a better mass conservation. With the chain rule, the PDE on  $\mu$  (Eq. (8b)) is transformed back to the diffusion equation  $\partial C/\partial t = \nabla \cdot [\chi(\phi, \mu) \mathcal{D}(\phi, \mu) \nabla \mu]$ . Although, the diffusion coefficient is a function of  $\mu$  in general cases, here we assume that it is only a function of  $\phi$  i.e.  $\mathcal{D}(\phi) = D_l \phi + (1 - \phi) D_s$ . It is relevant to define  $\mathcal{D}(\phi) = D_l q(\phi)$  with  $q(\phi) = \phi + (1 - \phi)(D_s/D_l)$  because the interpolation function  $q(\phi)$  appears naturally during the asymptotic analysis of Section 2.4 when switching to a dimensionless timescale. In addition, the coefficient  $\chi(\phi, \mu)$  is defined by  $\chi = \partial C(\phi, \mu)/\partial \mu$  where  $C$  is defined by Eq. (27) when the free energies are quadratic. When  $\varepsilon_s = \varepsilon_l = \mathcal{E}$  that coefficient is simply equal to  $\chi = 1/V_m \mathcal{E}$  (see Eq. (27)). Finally, with  $C(\phi, \mu) = c(\phi, \mu)/V_m$  and  $\mu = \bar{\mu} V_m \mathcal{E}$ , the composition equation writes:

$$\frac{\partial c}{\partial t} = \nabla \cdot [D_l q(\phi) \nabla \bar{\mu}] \quad (26)$$

The closure equation between  $\bar{\mu}$  and  $c(\phi, \mu)$  is simply obtained with Eqs. (6) and (18) for expressing the composition  $c(\phi, \mu)$ . In Eq. (6), the interpolation function  $p(\phi)$  can be replaced by another one  $h(\phi)$ . The form of  $h(\phi)$  is discussed below. The closure equation writes:

$$c(\phi, \mu) = h(\phi) m_l + [1 - h(\phi)] m_s + \left\{ h(\phi) \frac{1}{V_m \varepsilon_l} + [1 - h(\phi)] \frac{1}{V_m \varepsilon_s} \right\} \mu \quad (27)$$

Next, by inverting Eq. (27), we find a relationship that relates the dimensionless chemical potential  $\bar{\mu} = \mu/V_m \mathcal{E}$  to compositions  $c(\phi, \mu)$ ,  $m_s$  and  $m_l$ :

$$\bar{\mu} = \frac{\sqrt{\varepsilon_s \varepsilon_l}}{\varepsilon_s h(\phi) + \varepsilon_l [1 - h(\phi)]} \left\{ c(\phi, \bar{\mu}) - h(\phi) m_l - [1 - h(\phi)] m_s \right\} \quad (28)$$

Once again, when  $\varepsilon_s = \varepsilon_l$  that closure can be re-expressed with  $c_s^{co}$ ,  $c_l^{co}$  and  $\bar{\mu}^{eq}$ . In that case, the factor of Eq. (28) is equal to one, and we replace  $m_l$  and  $m_s$  by Eqs. (24a)-(24b) to obtain:

$$\bar{\mu} = \bar{\mu}^{eq} + c(\phi, \bar{\mu}) - c^{co}(\phi) \quad (29a)$$

where:

$$c^{co}(\phi) = c_l^{co} h(\phi) + c_s^{co} [1 - h(\phi)] \quad (29b)$$

is the interpolation of coexistence compositions.

A special care must be taken for choosing the interpolation functions  $q(\phi)$  in Eq. (26) and  $h(\phi)$  in Eq. (28). Indeed, the matched asymptotic expansions show that  $q(\phi)$  and  $h(\phi)$  are involved in several pairs of integrals. Each pair of integrals must have identical values for canceling the spurious terms arising from expansions. The particular choices  $h(\phi) = \phi$  and  $q(\phi) = \phi + (1 - \phi) q_s$  with  $q_s = D_s/D_l$  fulfill those requirements. More details are given in Section 2.4. When  $D_s = 0$ , the interpolation function  $q(\phi)$  is simply equal to  $\phi$ .

### 2.3.4. Anti-trapping current $\mathbf{j}_{at}$ in Eq. (8b)

The anti-trapping current has been proposed in [32] in order to counterbalance spurious solute trapping when  $D_s = 0$  or when the ratio of diffusivities  $D_s/D_l$  is very small. The anti-trapping current is introduced for phenomenological reasons in the mass balance equation and justified by carrying out the matched asymptotic expansions. An alternative justification for this current has been proposed in [37, 38]. Thus, with anti-trapping current, the model becomes equivalent to the free-boundary problem without introducing other thin interface effects [14]. In the framework of grand-potential, the anti-trapping current is defined by [18]:

$$\mathbf{j}_{at} = a(\phi) W \left[ \frac{\partial \omega_l(\mu)}{\partial \mu} - \frac{\partial \omega_s(\mu)}{\partial \mu} \right] \frac{\partial \phi}{\partial t} \mathbf{n} \quad (30)$$

This current is proportional to the velocity  $(\partial_t \phi)$  and the thickness  $W$  of the interface. It is normal to the interface

and points from solid to liquid. The coefficient  $a$  is used as a degree of freedom to remove the spurious terms arising from the matched asymptotic expansions. The coefficient  $a(\phi)$  depends on the choice of interpolation functions in the phase-field model. For our choice it is sufficient to set  $a = 1/4$  to fulfill the equality of integrals (see Section 2.4.2 for more details). When the quadratic free energies are used, the term inside the brackets is simplified by deriving Eq. (19) w.r.t.  $\bar{\mu}$ . Using the dimensionless quantities, the anti-trapping current writes:

$$\mathbf{j}_{at} = \frac{1}{4}W \left[ -\frac{\varepsilon_s - \varepsilon_l}{\sqrt{\varepsilon_s \varepsilon_l}} \bar{\mu} + m_s - m_l \right] \frac{\partial \phi}{\partial t} \mathbf{n} \quad (31)$$

When  $\varepsilon_s = \varepsilon_l$ , the first term inside the brackets is zero. The coefficients  $m_s$  and  $m_l$  are expressed with the coexistence compositions (Eqs. (24a)-(24b)) and the anti-trapping writes:

$$\mathbf{j}_{at} = \frac{1}{4}W (c_s^{co} - c_l^{co}) \frac{\partial \phi}{\partial t} \mathbf{n} \quad (32)$$

The impact of that anti-trapping current will be emphasized in Section 4.2. The chemical potentials and compositions will be compared on one case of dissolution with  $D_s = 0$ .

### 2.3.5. Summary of the phase-field model

The complete phase-field model is composed of two coupled PDEs which write:

$$\frac{\partial \phi}{\partial t} = M_\phi \nabla^2 \phi - \frac{8M_\phi}{W^2} \omega'_{dw}(\phi) - \frac{\lambda M_\phi}{W^2} \mathcal{S}_\phi(\phi, \bar{\mu}) \quad (33a)$$

$$\frac{\partial c}{\partial t} = \nabla \cdot \left[ D_l q(\phi) \nabla \bar{\mu} - \mathbf{j}_{at}(\phi, \bar{\mu}) \right] \quad (33b)$$

where the source term  $\mathcal{S}_\phi(\phi, \bar{\mu})$  is re-written below for convenience:

$$\mathcal{S}_\phi(\phi, \bar{\mu}) = p'(\phi)(c_s^{co} - c_l^{co})(\bar{\mu} - \bar{\mu}^{eq}) \quad (33c)$$

In  $c$ -equation, the anti-trapping current  $\mathbf{j}_{at}$  is defined by Eq. (32).

The chemical potential  $\bar{\mu}$  appears inside the  $\phi$ -equation through the source term (Eq. (33c)). It also appears in the  $c$ -equation through the laplacian term and the anti-trapping current  $\mathbf{j}_{at}$ . The closure equation between  $\bar{\mu}$  and  $c$  is given by Eqs. (29a)-(29b). The derivatives  $p'(\phi)$  and  $\omega'_{dw}(\phi)$  of interpolation function and double-well have been defined by Eqs. (10b) and (5b). All functions depending on  $\phi$  are summarized in Tab. 2.

The phase-field equation Eq. (33a) includes the curvature-driven motion (see Section 2.4.1). In order to cancel it, the following PDE is solved for simulations:

$$\frac{\partial \phi}{\partial t} = M_\phi \nabla \cdot \left[ \nabla \phi - \frac{4}{W} \phi(1 - \phi) \mathbf{n} \right] - \frac{\lambda M_\phi}{W^2} \mathcal{S}_\phi(\phi, \bar{\mu}) \quad (34)$$

In that equation the counter term  $-M_\phi \kappa |\nabla \phi|$  has been included in the first term of the right-hand side.

Several scalar parameters appear in that model. The  $\phi$ -equation involves the diffusivity coefficient  $M_\phi$ , the interface width  $W$ , and the coupling parameter  $\lambda$ . Those three

parameters have a close link with the capillary length  $d_0$  and the kinetic coefficient  $\beta$  of the Gibbs-Thomson condition. Their relationships will be discussed in Section 2.4.1. They will indicate us how to set their values for simulations.

The model also requires providing the triplet of values  $(c_s^{co}, c_l^{co}, \bar{\mu}^{eq})$ . The phase-field model can simulate the dissolution processes as well as the precipitation ones. The difference lies in the sign of  $(c_s^{co} - c_l^{co})(\bar{\mu} - \bar{\mu}^{eq})$  in the source term  $\mathcal{S}_\phi$ . If we suppose that  $\bar{\mu}(\mathbf{x}, 0) = \bar{\mu}^{eq}$  in the solid with  $D_s = 0$ , then the processes of dissolution or precipitation depend on the choice of the initial condition for the liquid phase. For instance, in the simulations of Sections 4 and 5, with the convention  $c_s^{co} - c_l^{co} > 0$ , the dissolution process occurs when  $\bar{\mu}(\mathbf{x}, 0) < \bar{\mu}^{eq}$  in the liquid whereas the precipitation occurs when  $\bar{\mu}(\mathbf{x}, 0) > \bar{\mu}^{eq}$ . In terms of composition, the dissolution occurs when the composition of liquid is lower than its coexistence value:  $c(\mathbf{x}, 0) < c_l^{co}$ . The precipitation process occurs if its value is greater:  $c_l^{co} < c(\mathbf{x}, 0) < c_s^{co}$ .

## 2.4. Discussion on the matched asymptotic expansions

The equivalence between the phase-field model and the free-boundary problem is classically established with the method of ‘‘matched asymptotic expansions’’ [39, 40]. The method has been presented for solid/liquid phase change for identical conductivity in the solid and the liquid in [13], and for unequal conductivity in [41, 42]. That approach considers the ratio  $\varepsilon = W/d_0$  as small parameter of expansion where  $d_0$  is the capillary length. This choice of  $\varepsilon$  yields a correction of second order on the kinetic coefficient  $\beta$ . That correction makes possible to cancel  $\beta$ , if desired, by choosing appropriately the parameters  $\lambda$ ,  $W$  and  $M_\phi$  of the phase-field model. Based on that analysis, the anti-trapping current was derived in [32].

The matched asymptotic expansions have been applied in [14] for dilute binary mixture with anti-trapping current and  $D_s = 0$ . In [15] the analysis has been done for coupling with temperature. The case  $D_s \neq 0$  with anti-trapping current has been studied in [43]. In reference [44] the method has been applied to investigate the impact of one additional term in the phase-field equation which is derived from a variational formulation. Finally, the method has been applied recently for coupling with fluid flow in [45]. A pedagogical presentation of that method can be found in the Appendix of [17] which takes into account the anti-trapping current with  $D_s = 0$ .

### 2.4.1. Results of the asymptotic analysis

In this paper, the details of the matched asymptotic expansions are presented in Appendix A (equations of order  $\varepsilon^0$ ,  $\varepsilon^1$  and  $\varepsilon^2$  and their respective solutions  $\phi_j$  and  $\bar{\mu}_j$  for  $0 \leq j \leq 2$ ). The stages and the results remain essentially the same as those already published in [14] and [17, Appendix A]. In those references, the analyses are carried out in the theoretical framework of free energy with anti-trapping current and  $D_s = 0$ . In this Section, we focus the discussion on the main assumptions and results (Section 2.4.1). In our model, the use of grand-potential simplifies the source term analysis (see Appendix A). Two modifications have also an influence on the relationships relating the phase-field parameters to the interface conditions. The first one is our choice

Description	Functions	Derivatives
Double-well potential of minima $\phi_s = 0$ and $\phi_l = +1$	$\omega_{dw}(\phi) = \phi^2(1-\phi)^2$	$\omega'_{dw}(\phi) = 2\phi(1-\phi)(1-2\phi)$
Interpolation of coupling in Eq. (33a)	$p(\phi) = \phi^2(3-2\phi)$	$p'(\phi) = 6\phi(1-\phi)$
Interpolation of $c(\phi, \bar{\mu})$	$h(\phi) = \phi$	$h'(\phi) = 1$
Equilibrium solution	$\phi_0(x) = \frac{1}{2} [1 + \tanh(\frac{2x}{W})]$	$\frac{\partial \phi_0}{\partial x} = \frac{4}{W} \phi_0(1-\phi_0)$
Interpolation of bulk diffusivities	$\mathcal{D}(\phi) = D_l q(\phi)$	
Interpolation of $q(\phi)$	$q(\phi) = \phi + (1-\phi) \frac{D_s}{D_l}$	

Table 2: All functions depending on  $\phi$  in this work.

of interpolation functions (Tab. 2) which impact the coefficient  $a(\phi)$  of the anti-trapping current  $\mathbf{j}_{at}$ . The second one concerns the counter term  $-M_\phi \kappa |\nabla \phi|$  for canceling the curvature-driven motion. Those two modifications are discussed respectively in Sections 2.4.2 and 2.4.3.

In Appendix A, the phase-field model is expanded with anti-trapping  $\mathbf{j}_{at}$  with  $\epsilon_s = \epsilon_l$  and  $D_s \neq D_l$ . By setting  $\partial_n \bar{\mu}|_l = \partial_n c|_l$  and  $q_s \partial_n \bar{\mu}|_s = \partial_n c|_s$ , the equivalent sharp interface model writes for  $\Phi = s, l$ :

$$\frac{\partial c}{\partial t} = D_\Phi \nabla^2 c \quad (35a)$$

$$D_l \partial_n c|_l - D_s \partial_n c|_s = -v_n \Delta c^{co} - \mathbb{E}_2 \Delta \mathcal{H} - \mathbb{E}_3 \Delta \mathcal{J} \quad (35b)$$

$$(\bar{\mu}_\Phi - \bar{\mu}^{eq}) \Delta c^{co} = -d_0 \kappa - \beta_\Phi v_n + \mathbb{E}_1 [\Delta \tilde{\mathcal{F}} - \Delta \mathcal{G}_\Phi] \Delta c^{co} \quad (35c)$$

Eq. (35a) is the mass balance for each bulk phase and Eqs. (35b)-(35c) are the two interface conditions, respectively the mass conservation (or Stefan condition) and the Gibbs-Thomson condition.

The right-hand sides of the last two equations contain three error terms:  $\mathbb{E}_1$  in Eq. (35c) and  $\mathbb{E}_2, \mathbb{E}_3$  in Eq. (35b). The accurate form of those error terms are written in Appendix A. The  $\mathbb{E}$ -terms are multiplied by integrals defined in Tab. 3:  $\Delta \mathcal{H} = \mathcal{H}_l - \mathcal{H}_s$ ,  $\Delta \mathcal{J} = \mathcal{J}_l - \mathcal{J}_s$  in Eq. (35b) and  $\Delta \tilde{\mathcal{F}} = \tilde{\mathcal{F}}_l - \tilde{\mathcal{F}}_s$ ,  $\Delta \mathcal{G}_\Phi = \mathcal{G}_l - \mathcal{G}_\Phi$  in Eq. (35c). The integrals vanish with an appropriate choice of interpolation functions  $p(\phi)$ ,  $h(\phi)$  and  $q(\phi)$ . Those summarized in Tab. 2 fulfill the requirements  $\mathcal{H}_l = \mathcal{H}_s$  and  $\mathcal{J}_l = \mathcal{J}_s$ . For satisfying the conditions  $\mathcal{F}_l = \mathcal{F}_s$  and  $\mathcal{G}_l = \mathcal{G}_s$ , we must also consider identical diffusivities for each phase (i.e.  $q_s = D_s/D_l = 1$ ). When  $D_s = 0$ , the discussion with anti-trapping current (i.e.  $a(\phi_0) \neq 0$  in Tab. 3) is detailed in Section 2.4.2.

As expected, the term in the left-hand side of the Gibbs-Thomson condition (Eq. (35c)), appears in the source term  $\mathcal{S}_\phi$  of  $\phi$ -equation (Eq. (33c)). Let us emphasize that the index  $\Phi$  appears in Eq. (35c) because the condition is not necessarily the same for each side of the interface: the kinetic coefficient  $\beta_l$  can be different of  $\beta_s$  (see Eqs. (A.25a) and (A.25b) in Appendix A.3.5). More precisely, the capillary length  $d_0$  and the kinetic coefficient  $\beta_\Phi$  are related to  $W$ ,  $\lambda$  and  $M_\phi$  of the phase-field equation by:

$$d_0 = \mathcal{J} \frac{W}{\lambda} \quad (36a)$$

$$\beta_\Phi = \frac{W \mathcal{J}}{M_\phi \lambda} \left[ 1 - \lambda \frac{M_\phi}{D_l} \frac{\mathcal{K} + \mathcal{F}_\Phi}{\mathcal{J}} (\Delta c^{co})^2 \right] \quad (36b)$$

The two different values of  $\beta_s$  and  $\beta_l$  come from the integral  $\mathcal{F}_\Phi$  in Eq. (36b). A single value  $\beta_l = \beta_s = \beta$  is obtained provided that  $\mathcal{F}_l = \mathcal{F}_s = \mathcal{F}$ . The integrals  $\mathcal{F}_\Phi$ ,  $\mathcal{J}$  and  $\mathcal{K}$  of Eqs. (36a)-(36b) are defined in Tab. 3.

For validations of Section 4, the comparisons between the numerical simulations of phase-field model and the analytical solutions of Stefan's problem are carried out by considering  $\beta = 0$ . The particular value of  $\lambda$  that fulfills that requirement is noted  $\lambda^*$  and writes:

$$\lambda^* = \frac{D_l}{M_\phi (\Delta c^{co})^2} \frac{\mathcal{J}}{\mathcal{K} + \mathcal{F}} \quad (37)$$

Finally, Eq. (36a) relates the capillary length  $d_0$  to the interface width  $W$  and the coupling coefficient  $\lambda$ . The counter term  $-M_\phi \kappa |\nabla \phi|$  must be considered in the phase-field equation when  $d_0$  is negligible in the Gibbs-Thomson Eq. (35c). The capillary length  $d_0$  is directly related to the surface tension  $\sigma$ . Indeed, from its definition Eq. (12a), we have  $\sigma = (1/6) \sqrt{2\zeta H}$  and we use the relationships  $1/\zeta = 8/(W^2 H)$  and  $H = 2\mathcal{E}/\lambda$  to find  $\sigma = [(2/3)W/\lambda] \mathcal{E}$ . The term inside the brackets is Eq. (36a) with  $\mathcal{J} = 2/3$  i.e.  $\sigma = d_0 \mathcal{E}$ . If the surface tension of the system can be neglected, then the counter term must be considered in  $\phi$ -equation. Its impact is illustrated in the simulation of Section 5.

#### 2.4.2. Analysis of anti-trapping current $\mathbf{j}_{at}$ in $c$ -equation

When  $q_s = D_s/D_l \neq 1$ , the model does not satisfy the conditions  $\mathcal{F}_l = \mathcal{F}_s$  and  $\mathcal{G}_l = \mathcal{G}_s$  (see Tab. 3 with  $a(\phi_0) = 0$ ). The reason is that the diffusive behavior is not symmetric anymore inside the interface. Adding an anti-trapping current  $\mathbf{j}_{at}$  (Eq. (30) inside the composition equation becomes necessary to correct this asymmetry. In the most general cases, the coefficient  $a(\phi)$  is a function of  $\phi$  which adds a supplementary freedom degree in the model to cancel  $\Delta \mathcal{F}$ . In this work, the asymptotic expansions were performed with  $\mathbf{j}_{at}$  in order to determine the correct form of  $a(\phi)$ . From Tab. (3) we can see that  $a(\phi)$  is involved in three integrals  $\mathcal{F}_l$ ,  $\mathcal{F}_s$  and  $\mathcal{K}$ . Computing the integrals with the functions  $p(\phi) = \phi^2(3-2\phi)$ ,  $h(\phi) = \phi$  and  $q(\phi) = \phi + (1-\phi)q_s$  yields  $a = (1-q_s)/4$ . When  $D_s = 0$ , that condition simplifies to  $a = 1/4$ . Another way to derive that value is to consider that the integrands of condition  $\mathcal{F}_l = \mathcal{F}_s$  (see Tab. 3) must be identical to those of condition  $\mathcal{H}_l = \mathcal{H}_s$  yielding the relationship  $[h(\phi_0) - a(\phi_0) \partial \phi_0 / \partial \xi] / q(\phi_0) = h(\phi_0)$ . The value  $a = 1/4$  directly arises from that equality (see Appendix A.4). When  $q_s \neq 1$ , the condition  $\mathcal{G}_l = \mathcal{G}_s$  cannot be satisfied with the current model, even with the anti-trapping current. However, the spurious term  $\mathbb{E}_1$  in Eq. (35c) vanishes when  $D_s = 0$ . Finally, the sharp interface model is



Integral	Value	Integral	Value
$\mathcal{I} = \int_{-\infty}^{\infty} (\partial_{\xi} \phi_0)^2 d\xi$	$\frac{2}{3}$	$\mathcal{K} = \int_{-\infty}^{\infty} \left\{ \partial_{\xi} p(\phi_0) \int_0^{\xi} \left[ \frac{h(\phi_0) - a(\phi_0) \partial_{\xi} \phi_0}{q(\phi_0)} \right] dx \right\} d\xi$	$\frac{31 - 30 \ln 2}{150}$
$\mathcal{F}_l = \int_0^{\infty} \left[ 1 - \frac{h(\phi_0) - a(\phi_0) \partial_{\xi} \phi_0}{q(\phi_0)} \right] d\xi$	$\frac{\ln 2}{4}$	$\mathcal{F}_s = \int_{-\infty}^0 \left[ \frac{h(\phi_0) - a(\phi_0) \partial_{\xi} \phi_0}{q(\phi_0)} \right] d\xi$	$\frac{\ln 2}{4}$
$\tilde{\mathcal{F}}_l = \int_0^{\infty} \left[ 1 - \frac{p(\phi_0)}{q(\phi_0)} \right] d\xi$	$\frac{\ln(2) - 1}{4}$	$\tilde{\mathcal{F}}_s = \int_{-\infty}^0 \frac{p(\phi_0)}{q(\phi_0)} d\xi$	$\frac{\ln(2) + 1}{4}$
$\mathcal{G}_l = \int_0^{\infty} \left[ \frac{1}{q(\phi_0)} - 1 \right] d\xi$	$\left[ \frac{1}{q_s} - 1 \right] \frac{\ln(q_s + 1)}{4}$	$\mathcal{G}_s = \int_0^{\infty} \left[ \frac{1}{q(\phi_0)} - \frac{1}{q_s} \right] d\xi$	$\left[ \frac{1}{q_s} - 1 \right] \frac{\ln(q_s + 1) - \ln(q_s)}{4}$
$\mathcal{H}_l = \int_0^{\infty} [1 - h(\phi_0)] d\xi$	$\frac{\ln 2}{4}$	$\mathcal{H}_s = \int_{-\infty}^0 h(\phi_0) d\xi$	$\frac{\ln 2}{4}$
$\mathcal{J}_l = \int_0^{\infty} [q(\phi_0) - 1] d\xi$	$-\frac{\ln 2}{4}$	$\mathcal{J}_s = \int_0^{\infty} [q(\phi_0) - q_s] d\xi$	$-\frac{\ln 2}{4}$

Table 3: Definition of integrals involved in Eqs. (35b), (35c), (36a) and (36b). Their values are computed with  $q_s = 0$  (except  $\mathcal{G}_l$  and  $\mathcal{G}_s$  discussed in Appendix A.4) and the interpolation functions defined in Tab. 2. Here  $\xi = x/W$  and  $\phi_0$  is defined by Eq. (11).

recovered for  $D_s = D_l$  and when  $D_s = 0$  with anti-trapping. When  $D_s/D_l \sim 1$ , the error term  $\mathbb{E}_1 \Delta \mathcal{G}_{\Phi}$  remains very small as confirmed by Section 4.1.

#### 2.4.3. Analysis of counter term $-M_{\Phi} \kappa |\nabla \phi|$ in $\phi$ -equation

The references [24] and [46] have proved that adding the counter term  $-M_{\Phi} \kappa |\nabla \phi|$  cancels the curvature motion  $-d_0 \kappa$  in the Gibbs-Thomson condition. As a matter of fact, the curvature-driven term  $-d_0 \kappa$  arises from the asymptotic expansions of standard  $\phi$ -equation (Eq. (33a)). More precisely it arises from the expansion of two terms: the laplacian term and the double-well one. In references [24] and [46] such an analysis has been performed directly by adding  $-M_{\Phi} \kappa |\nabla \phi|$  to those two terms.

Here, the phase-field equation (Eq. (34)) differs slightly of  $\phi$ -equations of those references. It has been reformulated in Section 2.2.2 by using the kernel function  $|\nabla \phi| = (4/W) \sqrt{\omega_{dw}}$  (Eq. (13)) and the chain rule of the divergence operator. The manipulations made to obtain Eq. (34) conserves the structure of order zero of the phase-field equation and the Gibbs-Thomson condition. The results of the asymptotic expansions of Eq. (34) were found to be equivalent to those of the previous references: the equation guarantees canceling the curvature motion of the interface.

### 3. Lattice Boltzmann methods

The phase-field model of section 2.3.5 is implemented in LBM\_saclay, a 3D numerical code written in C++ language. The main advantage of this code is its portability on all major HPC architectures (especially GPUs and CPUs). It has already been used to study two-phase flows with phase change in the framework of the phase-field method in reference [27]. Section 3.1 introduces the main notations and the lattice. The LBM schemes for  $\phi$ -equation are presented in Section 3.2 and those for  $c$ -equation in Section 3.3.

#### 3.1. LBM notations

Several standard lattices have already been implemented in top-level files of LBM\_saclay. The two-dimensional lattices are D2Q5 and D2Q9 and the three-dimensional ones are D3Q7, D3Q15 and D3Q19. The lattice speed is  $s = \delta x / \delta t$  where  $\delta x$  and  $\delta t$  are respectively the space- and time-steps.

Among all those lattices, we only use in this work the standard D2Q9 one. It is defined by nine directions of displacement, each one of them is indexed by  $k = 0, \dots, N_{pop}$  with  $N_{pop} = 8$ . The nine vectors are  $\mathbf{e}_0 = (0, 0)^T$ ,  $\mathbf{e}_1 = (1, 0)^T$ ,  $\mathbf{e}_2 = (0, 1)^T$ ,  $\mathbf{e}_3 = (-1, 0)^T$ ,  $\mathbf{e}_4 = (0, -1)^T$ ,  $\mathbf{e}_5 = (1, 1)^T$ ,  $\mathbf{e}_6 = (-1, 1)^T$ ,  $\mathbf{e}_7 = (-1, -1)^T$  and  $\mathbf{e}_8 = (1, -1)^T$ . The lattice velocities are defined by  $\xi_k = s \mathbf{e}_k$  and the lattice weights are  $w_0 = 4/9$ ,  $w_{1,\dots,4} = 1/9$  and  $w_{5,\dots,8} = 1/36$ . The lattice coefficient is noted  $\xi_s^2 = s^2/3$ .

On that lattice, two distribution functions  $g_k(\mathbf{x}, t)$  and  $h_k(\mathbf{x}, t)$  are defined, for updating respectively the phase-field  $\phi(\mathbf{x}, t)$  and the composition  $c(\mathbf{x}, t)$  at each time-step. No distribution function is introduced for the chemical potential  $\bar{\mu}(\mathbf{x}, t)$ . Here  $\bar{\mu}$  is simply an additional macroscopic field which is kept in memory for updating  $c(\mathbf{x}, t)$ . A LBM using  $\bar{\mu}$  as main variable instead of  $c$  could have been possible. Indeed, the mathematical form of Eq. (8b) is similar to the supersaturation equation of reference [47]. But here, we use  $c$  as main computational variable for reason of mass conservation.

The evolution of distribution functions  $g_k$  and  $h_k$  obeys the “discrete velocity lattice Boltzmann equations” with a collision approximated by the BGK operator. With that form of collision, each distribution function relaxes toward an equilibrium  $g_k^{eq}$  and  $h_k^{eq}$  proportionally to collision times  $\tau_g$  and  $\tau_h$ . For each LBE, the source terms are noted  $\mathcal{G}_k$  and  $\mathcal{H}_k$ . The space and time discretizations are performed by method of characteristics. The BGK collision operators and the source terms are integrated with the trapezoidal rule, a method of second-order accuracy. In order to keep an explicit algorithm, the variable changes of  $g_k$  and  $h_k$  are defined by  $\tilde{g}_k = g_k + (\delta t / 2 \tau_g)(g_k - g_k^{eq}) - \mathcal{G}_k(\delta t / 2)$  and  $\tilde{h}_k = h_k + (\delta t / 2 \tau_h)(h_k - h_k^{eq}) - \mathcal{H}_k(\delta t / 2)$ . The ratios  $\tau_g / \delta t$  and  $\tau_h / \delta t$  are the dimensionless collision rates respectively noted  $\bar{\tau}_g$  and  $\bar{\tau}_h$ . All details of that variable change can be found in [27, Appendix C].

#### 3.2. LBM for $\phi$ -equation

The lattice Boltzmann method for the phase-field equation acts on the distribution function  $\tilde{g}_k$ . The evolution equation is:

$$\tilde{g}_k^* = \tilde{g}_k - \frac{1}{\bar{\tau}_g + 1/2} [\tilde{g}_k - \tilde{g}_k^{eq}] + \mathcal{G}_k \delta t \quad (38)$$

## Nomenclature for lattice Boltzmann

Symbol	Definition	Dimension	Description
$\mathbf{e}_k$	Sec. 3.1	[−]	Vectors of displacement on the lattice
$k$	$0 \leq k \leq N_{pop}$	[−]	Index for each direction of propagation
$N_{pop}$	$N_{pop} = 8$ for D2Q9	[−]	Total number directions
$\delta x$		[L]	Spatial discretization
$\delta t$		[T]	Time discretization
$s$	$= \delta x / \delta t$	[L].[T] <sup>−1</sup>	Lattice speed
$\xi_k$	$= s \mathbf{e}_k$	[L].[T] <sup>−1</sup>	Velocities associated to the vectors of displacement
$\xi_s^2$	$= s^2 / 3$	[L] <sup>2</sup> .[T] <sup>−2</sup>	Lattice coefficient
$g_k(\mathbf{x}, t), h_k(\mathbf{x}, t)$		[−]	Distribution function for $\phi$ and for $c$
$g_k^{eq}, h_k^{eq}$	Eq. (39) and Eq. (46)	[−]	Equilibrium distribution functions in LBE for $g_k$ and $h_k$
$\bar{\tau}_g, \bar{\tau}_h$		[−]	Collision rate in LBE for $g_k$ and $h_k$
$\mathcal{G}_k, \mathcal{H}_k$	Eq. (40) and Eq. (47)	[T] <sup>−1</sup>	Source terms in LBE for $g_k$ and $h_k$
$w_k$		[−]	Weights (constant) for each LBE
$\gamma$	$\bar{\tau}_h = 3\delta t / (\gamma \delta x^2)$	[L] <sup>−2</sup> .[T]	Parameter related to $\bar{\tau}_h$ in LBE for $h_k$

Table 4: Main mathematical symbols for the lattice Boltzmann schemes (LBE: lattice Boltzmann equation).

where  $\tilde{g}_k^* \equiv \tilde{g}_k(\mathbf{x} + \xi_k \delta t, t + \delta t)$  and the variable change  $\tilde{g}_k^{eq} = g_k^{eq} - \delta t \mathcal{G}_k / 2$  has been used. The equilibrium distribution function  $g_k^{eq}$  is defined by:

$$g_k^{eq} = \phi w_k \quad (39)$$

for which its moments are  $\phi$  (moment of order zero),  $\mathbf{0}$  (order one) and  $\phi \mathbf{I}$  (order two) where  $\mathbf{I}$  is the identity tensor of second-order. The diffusivity coefficient is related to the collision rate by  $M_\phi = \bar{\tau}_g \xi_s^2 \delta t$ . The source term  $\mathcal{G}_k$  contains two contributions:

$$\mathcal{G}_k = w_k (\mathcal{G}^{st} + \mathcal{G}^{curv}) \quad (40)$$

The first one  $\mathcal{G}^{st}$  involves the source term  $\mathcal{S}_\phi(\phi, \bar{\mu})$  defined by Eq. (41a). The second one  $\mathcal{G}^{curv}$  is either equal to the double-well term  $\mathcal{G}^{dw}$  or equal to the counter term  $\mathcal{G}_k^{ct}$ . The three source terms are defined by:

$$\mathcal{G}^{st} = -\frac{\lambda M_\phi}{W^2} \mathcal{S}_\phi(\phi, \bar{\mu}) \quad (41a)$$

$$\mathcal{G}^{dw} = -\frac{8M_\phi}{W^2} \omega'_{dw}(\phi) \quad (41b)$$

$$\mathcal{G}_k^{ct} = \frac{4}{W} \phi (1 - \phi) \xi_k \cdot \mathbf{n} \quad (41c)$$

The choice between  $\mathcal{G}^{dw}$  or  $\mathcal{G}_k^{ct}$  depends on the curvature-driven motion term i.e. the version of the phase-field equation we wish to simulate. For simulating Eq. (33a), the curvature term must contain the double-well  $\omega_{dw}(\phi)$ . In that case  $\mathcal{G}^{curv}$  is equal to Eq. (41b). If the curvature-driven motion is undesired, the term must involve the kernel function  $|\nabla \phi| = (4/W) \phi (1 - \phi)$  with the normal vector  $\mathbf{n}$ . In that case  $\mathcal{G}^{curv}$  is equal to Eq. (41c).

After the stages of collision and streaming, the new phase-field is obtained by the zeroth-order moment of  $\tilde{g}_k$  which must be corrected with the source term  $\mathcal{G}_k$ :

$$\phi = \sum_k \tilde{g}_k + \frac{\delta t}{2} \sum_k \mathcal{G}_k. \quad (42)$$

The unit normal vector  $\mathbf{n}$  requires the computation of gradients of  $\phi$ . The gradients are discretized by using the method of directional derivatives. The method has already demonstrated its performance in hydrodynamics in order to reduce parasitic currents for two-phase flow problems [48, 49]. The directional derivative is the derivative along each moving direction on the lattice. The Taylor expansions at second-order of a differentiable scalar function  $\phi(\mathbf{x})$  at  $\mathbf{x} + \mathbf{e}_k \delta x$  and  $\mathbf{x} - \mathbf{e}_k \delta x$  yields the following approximation of directional derivatives:

$$\mathbf{e}_k \cdot \nabla \phi|_{\mathbf{x}} = \frac{1}{2\delta x} [\phi(\mathbf{x} + \mathbf{e}_k \delta x) - \phi(\mathbf{x} - \mathbf{e}_k \delta x)] \quad (43a)$$

The number of directional derivatives is equal to the number of moving directions  $\mathbf{e}_k$  on the lattice i.e.  $N_{pop}$ . The gradient is obtained by:

$$\nabla \phi|_{\mathbf{x}} = 3 \sum_k w_k \mathbf{e}_k (\mathbf{e}_k \cdot \nabla \phi|_{\mathbf{x}}). \quad (43b)$$

The two components of gradient  $\partial_x \phi$  and  $\partial_y \phi$  are computed by the moment of first-order of each directional derivative  $\mathbf{e}_k \cdot \nabla \phi|_{\mathbf{x}}$ .

### 3.3. LBM for $c$ -equation

The basic LB algorithm for composition equation works on a new distribution function  $h_k$ . The specificity of Eq. (33b) is the mixed formulation between  $c$  and  $\bar{\mu}$ . The closure relationship is given by Eq. (28). The equilibrium distribution  $h_k^{eq}$  must be designed such as its moment of zeroth-order is  $c$  and its moment of second-order is  $\mathbf{I} \bar{\mu}$ . That equation is quite close to the Cahn-Hilliard (CH) equation with a simpler closure (Eq. (28)) which does not involve the laplacian of  $c$  (case of CH equation). The numerical scheme can be inspired from what is done for CH equation for two-phase flows of two immiscible fluids [34, 50]. For anti-trapping current  $\mathbf{j}_{at}$ , the methods are the same as those presented in [47] for crystal growth applications of binary mixture.

In the usual BGK operator, the diffusion coefficient  $\mathcal{D}(\phi)$  is related to the relaxation time  $\bar{\tau}_h(\phi)$  with the relationship

$\mathcal{D}(\phi) = (1/3)\bar{\tau}_h(\phi)\delta x^2/\delta t$ . However, the interpolation of diffusion  $\mathcal{D}(\phi) = D_l\phi$  means that the diffusion is null in the solid phase. In that case, the relaxation time would be equal to 0 leading to the occurrence of instabilities in the algorithm. In order to overcome the instability, the diffusive term is reformulated with the chain rule by  $\nabla[\mathcal{D}(\phi)\bar{\mu}] = \mathcal{D}(\phi)\nabla\bar{\mu} + \mathcal{D}'(\phi)\bar{\mu}\nabla\phi$  with  $\mathcal{D}'(\phi) = D_l$ . Eq. (33b) becomes:

$$\frac{\partial c}{\partial t} + \nabla \cdot [\bar{\mu}\mathcal{D}'(\phi)\nabla\phi] + \nabla \cdot \mathbf{j}_{at} = \nabla^2 [\mathcal{D}(\phi)\bar{\mu}] \quad (44)$$

Moreover, the laplacian term is reformulated as  $\nabla^2 [\mathcal{D}(\phi)\bar{\mu}] = (1/\gamma)\nabla^2 [\gamma\mathcal{D}(\phi)\bar{\mu}]$  where  $\gamma$  is a supplementary parameter allowing a better control of the relaxation rate. When the parameters  $M_\phi$  and  $\mathcal{D}(\phi)$  presents a ratio of several order of magnitude, it is useful to set  $\gamma = 1/M_\phi$ . The stability condition of the relaxation rates will be the same for both LBE. The discrete lattice Boltzmann equation writes

$$\tilde{h}_k^* = \tilde{h}_k - \frac{1}{\bar{\tau}_h + 1/2} [\tilde{h}_k - \tilde{h}_k^{eq}] + \mathcal{H}_k\delta t \quad (45)$$

where  $\tilde{h}_k^* \equiv \tilde{h}_k(\mathbf{x} + \boldsymbol{\xi}_k\delta t, t + \delta t)$  and  $\tilde{h}_k^{eq} = h_k^{eq} - \mathcal{H}_k\delta t/2$ . The equilibrium distribution function writes:

$$h_k^{eq} = \begin{cases} c(\phi, \bar{\mu}) - (1 - w_0)\gamma\mathcal{D}(\phi)\bar{\mu}(\mathbf{x}, t) & \text{if } k = 0 \\ w_k\gamma\mathcal{D}(\phi)\bar{\mu}(\mathbf{x}, t) & \text{if } k \neq 0 \end{cases} \quad (46)$$

The first line of Eq. (46) corresponds to a moment of order zero that is equal to  $c$ . The second line corresponds to a second-order moment equal to  $\mathcal{D}(\phi)\bar{\mu}$ . The anti-trapping current  $\mathbf{j}_{at}$  and the term  $\mathcal{D}'(\phi)\bar{\mu}\nabla\phi$  appear in the source term  $\mathcal{H}_k \equiv \mathcal{H}_k(\mathbf{x}, t)$  defined by:

$$\mathcal{H}_k = \gamma w_k \boldsymbol{\xi}_k \cdot [\bar{\mu}\mathcal{D}'(\phi)\nabla\phi + \mathbf{j}_{at}(\phi, \bar{\mu})] \quad (47)$$

The relaxation rate  $\bar{\tau}_h$  is related to  $\gamma$  by  $\bar{\tau}_h = 3\delta t/(\gamma\delta x^2)$ . After the stages of collision and streaming the composition  $c(\phi, \bar{\mu})$  is updated by:

$$c = \sum_k \tilde{h}_k \quad (48)$$

The moment of zeroth-order of Eq. (47) is null. For this reason,  $\mathcal{H}_k$  does not appear in the calculation of  $c$ . Once the new composition is known, the chemical potential  $\bar{\mu}$  is computed by Eq. (29a) and used in equilibrium function (Eq. (46)). The anti-trapping current  $\mathbf{j}_{at}$  is computed by Eq. (32) where the normal vector  $\mathbf{n}$  and the time derivative  $\partial\phi/\partial t$  are required. The normal vector has already been computed in Section 3.2. The time derivative of  $\phi$  is computed by an explicit Euler scheme of first-order. Hence, the LBE on  $\tilde{h}_k$  must be solved after the LBE on  $\tilde{g}_k$ . At first time-step the term  $\partial\phi/\partial t$  in Eq. (31) is obtained by  $\phi(\mathbf{x}, \delta t) - \phi(\mathbf{x}, t = 0)/\delta t$  where  $\phi(\mathbf{x}, t = 0)$  is the initial condition and  $\phi(\mathbf{x}, \delta t)$  is the phase-field after the first time-step.

Another formulation is possible for  $\mathbf{j}_{at}$  and  $\bar{\mu}\mathcal{D}'(\phi)\nabla\phi$ . They could have been included inside an alternative equilibrium distribution function  $h_k^{eq,alt}$  with  $\mathcal{H}_k = 0$ . In that case, the scheme writes

$$\tilde{h}_k^* = \tilde{h}_k - \frac{1}{\bar{\tau}_h + 1/2} [\tilde{h}_k - h_k^{eq,alt}] \quad (49a)$$

with  $h_k^{eq,alt}$  defined by

$$h_k^{eq,alt} = \begin{cases} c(\phi, \bar{\mu}) - (1 - w_0)\gamma\mathcal{D}(\phi)\bar{\mu} & \text{if } k = 0 \\ w_k \left[ \gamma\mathcal{D}(\phi)\bar{\mu} + \frac{\boldsymbol{\xi}_k \cdot (\mathbf{j}_{at} + \bar{\mu}\mathcal{D}'\nabla\phi)}{\xi_s^2} \right] & \text{if } k \neq 0 \end{cases} \quad (49b)$$

The computational stages for  $\bar{\mu}$  and  $\mathbf{j}_{at}$  remain the same as those presented above.

#### 4. Validations

The implementation of lattice Boltzmann schemes is validated with several analytical solutions. The solutions are obtained from the classical Stefan's problem. We present one case of precipitation in Section 4.1 for  $D_l \simeq D_s$  and one case of dissolution in Section 4.2 for  $D_s = 0$ . The domain is one-dimensional with  $x$  varying between  $[-L_x, L_x]$  where  $L_x = 0.25$ . The initial configuration states an interface position located at  $x_i(0) = 0$  with a solid phase on the left side (interval  $[-L_x, 0]$ ) and a liquid phase on the right side (interval  $]0, L_x]$ ). For the phase-field model, the first test is simulated without anti-trapping. Next, the second one is simulated successively with and without  $\mathbf{j}_{at}$  to present its impact on the profiles of composition and chemical potential. For each validation, the relative  $L^2$ -errors, defined by  $\|\vartheta^{LBM} - \vartheta^{as}\|_2 / \|\vartheta^{as}\|_2$ , are indicated in the caption of figures. The function  $\vartheta$  corresponds to  $c$  or  $\bar{\mu}$ . The errors are computed only over the range shown on each graph and the superscript *as* means "analytical solution".

The LBM simulations are carried out on a 2D computational domain varying between  $[-L_x, L_x] \times [\ell_y, L_y]$  with  $\ell_y = 0$  and  $L_y = 0.0036$ . The D2Q9 lattice is used with  $N_x \times N_y$  nodes with  $N_x = 5000$  and  $N_y = 36$ . The space- and time-steps are  $\delta x = 10^{-4}$  and  $\delta t = 5 \times 10^{-9}$ . The initial conditions for  $\phi$ -equation and  $c$ -equation are two hyperbolic tangent functions:  $\phi(x, 0)$  is initialized by Eq. (11) and  $c(x, 0)$  by

$$c(x, 0) = \frac{1}{2} \left[ c_l^\infty + c_s^\infty + (c_l^\infty - c_s^\infty) \tanh\left(\frac{2x}{W}\right) \right] \quad (50)$$

where  $c_s^\infty$  and  $c_l^\infty$  are the compositions of bulk far from interface. For horizontal walls at  $y = 0$  and  $y = L_y$ , the boundary conditions are periodic. For vertical walls at  $x = \pm L_x$ , the boundary conditions are imposed with the bounce-back method. A preliminary test was carried out to check that solutions of both  $\phi$ -equations (Eqs. (33a) and (34)) are identical on that one-dimensional case.

##### 4.1. Validation with $D_l \simeq D_s$

We first check the LBM implementation with two coefficients of diffusion:  $D_s = 0.9$  and  $D_l = 1$ . The analytical solution of such a problem can be found in [51, Chap. 12]. However, in that reference, the mathematical formulation of this problem is done by using the temperature as main variable. The equivalent intensive quantity in our model is the chemical potential. The validations using that quantity will

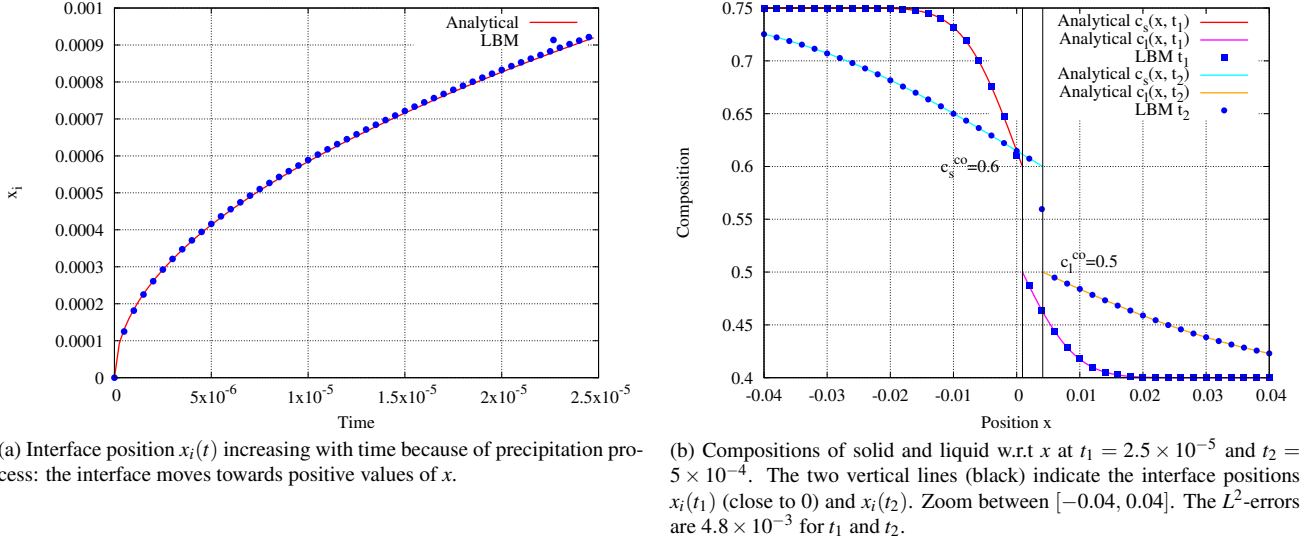


Figure 1: Analytical solutions Eqs. (52a)–(52c) (lines) compared to LBM (symbols) for one case of precipitation with  $D_s = 0.9$  and  $D_l = 1$ . The system is initialized with an interface located at  $x = 0$ . The solid and liquid are respectively on left- and right-side.

be presented in next section. Here, we prefer use the solutions of reference [52] which are written in terms of compositions. The numerical implementation must reproduce correctly the discontinuity of compositions at interface.

In [52], the solutions are derived for a ternary case. For binary case, the transcendental equation reduces to:

$$-\frac{1}{2}\alpha\Delta m^2 = \Delta\bar{f}^{min}[u_s(-\alpha) + u_l(\alpha)] + \Delta m[(m_s - c_s^\infty)u_s(-\alpha) + (m_l - c_l^\infty)u_l(\alpha)] \quad (51a)$$

where the function  $u_\Phi(\alpha)$  is defined by

$$u_\Phi(\alpha) = \sqrt{\frac{D_\Phi}{\pi}} \frac{e^{-\alpha^2/4D_\Phi}}{\text{erfc}(\alpha/2\sqrt{D_\Phi})} \quad \text{for } \Phi = s, l \quad (51b)$$

The compositions far from the interface are  $c_s^\infty = 0.75$  and  $c_l^\infty = 0.4$ . For  $m_s = 0.2$ ,  $m_l = 0.1$ ,  $\Delta m = 0.1$  and  $\Delta\bar{f}^{min} = 0.04$ , the root of the transcendental equation is  $\alpha = 0.184841$ . The three solutions are the interface position  $x_i(t)$ , the composition of solid  $c_s(x, t)$  and the composition of liquid  $c_l(x, t)$ . The interface position writes as a function of  $\alpha$  and  $t$ :

$$x_i(t) = \alpha\sqrt{t} \quad (52a)$$

Since  $\alpha > 0$ , the interface moves from  $x_i(0) = 0$  towards positive values of  $x$ , meaning that a precipitation process occurs. The two analytical solutions in the solid and the liquid write:

$$c_s^{as}(x, t) = c_s^\infty + (c_s^{co} - c_s^\infty) \frac{\text{erfc}[-x/2\sqrt{D_s t}]}{\text{erfc}[-\alpha/2\sqrt{D_s}]} \quad (52b)$$

$$c_l^{as}(x, t) = c_l^\infty + (c_l^{co} - c_l^\infty) \frac{\text{erfc}[x/2\sqrt{D_l t}]}{\text{erfc}[\alpha/2\sqrt{D_l}]} \quad (52c)$$

where Eq. (52b) is defined for  $x \in [-L_x, x_i(t)[$  and Eq. (52c) for  $x \in ]x_i(t), L_x]$ . On the whole domain, the composition  $c$  is discontinuous at interface  $x_i(t)$ , of value  $c_s^{co} = 0.6$  on solid side and  $c_l^{co} = 0.5$  on liquid side. From those values, each profile of composition diffuses until  $c_s^\infty$  for  $x \rightarrow -L_x$  and  $c_l^\infty$  for  $x \rightarrow L_x$ .

The simulations are performed without anti-trapping current. The interpolation of diffusion coefficients is simply done by  $\mathcal{D}(\phi) = \phi D_l + (1 - \phi) D_s$ . In  $\phi$ -equation the parameters are  $M_\phi = 1.2$ ,  $W = 1.2 \times 10^{-3}$  and  $\lambda^* = 277$ . The comparisons between the analytical solutions and the LBM simulation are presented on Fig. 1. As expected from the theory, the interface position  $x_i(t)$  is an increasing function of time (Fig. 1a). On the profiles of composition (Fig. 1b), the jump on each side of the interface is also well-reproduced by the numerical model. The coexistence values  $c_s^{co} = 0.6$  and  $c_l^{co} = 0.5$  remain the same at two times  $t_1 = 2.5 \times 10^{-5}$  and  $t_2 = 5 \times 10^{-4}$ . The LBM simulations fit perfectly with the analytical solutions.

The two solutions Eqs. (52b)–(52c) can be easily expressed in terms of chemical potential  $\bar{\mu}_s^{as}(x, t)$  and  $\bar{\mu}_l^{as}(x, t)$ . For instance, we add  $-m_s$  on both sides of Eq. (52b) and add  $m_s - m_s$  inside the term  $(c_s^{co} - c_s^\infty)$ . Thanks to Eqs. (24a)–(24b) we obtain  $(c_s^{co} - c_s^\infty) \equiv (\bar{\mu}^{eq} - \bar{\mu}_s^\infty)$  for solid and  $(c_l^{co} - c_l^\infty) \equiv (\bar{\mu}^{eq} - \bar{\mu}_l^\infty)$  for liquid. When expressed in terms of chemical potential, the solution does not present a jump at interface  $x_i(t)$ . The single value is  $\bar{\mu}^{eq}$  and each profile diffuse from that value until  $\bar{\mu}_s^\infty$  when  $x \rightarrow -L_x$  (solid) and  $\bar{\mu}_l^\infty$  when  $x \rightarrow L_x$  (liquid). The next section presents a validation using  $\bar{\mu}$  as main variable for discussing the analogy with temperature and comparing with solidification problems.

#### 4.2. Validation with $D_s = 0$ : effect of anti-trapping current

The analytical solution of the one-sided diffusion is presented in [51, Sec. 12-1]. Now a direct analogy is done between the temperature of that reference and the chemical potential of our model. The two solutions are  $x_i(t)$ , the interface position, and  $\bar{\mu}_l^{as}(x, t)$  the chemical potential of liquid.



The chemical potential of solid is set equal to the equilibrium value  $\bar{\mu}^{eq} = 0.4$ . Its value remains constant during the simulation because  $D_s = 0$ . The transcendental equation of that problem writes:

$$\alpha e^{\alpha^2} \operatorname{erfc}(\alpha) + \frac{(\bar{\mu}^{eq} - \bar{\mu}_l^\infty)}{(c_s^{co} - c_l^{co})\sqrt{\pi}} = 0 \quad (53)$$

where  $\alpha$  is the root of this equation, and  $\bar{\mu}_l^\infty$  is the value of chemical potential far from the interface. By analogy with problems of phase change (solidification or melting), the equilibrium chemical potential  $\bar{\mu}^{eq}$  plays the role of melting temperature. The term  $\Delta c^{co} = c_s^{co} - c_l^{co}$  can be compared to the latent heat. For phase change problems, that quantity is released (resp. absorbed) at interface during solidification (resp. melting). Here for our convention  $c_s^{co} > c_l^{co}$ , the quantity  $\Delta c^{co}$  is released at interface during dissolution and absorbed during precipitation. Finally, the quantity  $\chi = 1$  plays the role of specific heat.

In Eq. (53), the dissolution or precipitation processes can occur depending on the sign of second term. We keep  $c_s^{co} = 0.6$  and  $c_l^{co} = 0.5$  (i.e.  $\Delta c^{co} > 0$ ), and we set  $\bar{\mu}_l^\infty = 0.3$  meaning that  $\bar{\mu}^{eq} - \bar{\mu}_l^\infty > 0$ . The root of this equation is equal to  $\alpha = -0.357835$ . The interface position  $x_i(t)$  is a function of  $\alpha$ ,  $t$  and  $D_l$  which writes:

$$x_i(t) = 2\alpha\sqrt{D_l t} \quad (54a)$$

Since  $\alpha < 0$ , the interface position moves from  $x_i(0) = 0$  towards negative values of  $x$ , meaning that a dissolution process occurs. The chemical potential of liquid is

$$\bar{\mu}_l^{as}(x, t) = \bar{\mu}_l^\infty + (\bar{\mu}^{eq} - \bar{\mu}_l^\infty) \frac{\operatorname{erfc}[x/2\sqrt{D_l t}]}{\operatorname{erfc}(\alpha)} \quad (54b)$$

for  $x \in [x_i(t), L_x]$ . In the liquid,  $\bar{\mu}_l^{as}(x, t)$  diffuses from the equilibrium value  $\bar{\mu}^{eq}$  at the interface until  $\bar{\mu}_l^\infty$  when  $x \rightarrow L_x$ . In the solid, the chemical potential  $\bar{\mu}_s^{as}(x, t)$  is constant of value  $\bar{\mu}^{eq}$  for  $x \in [-L_x, x_i(t)]$ .

For LBM simulations, the parameters of  $\phi$ -equation are  $W = 5 \times 10^{-3}$ ,  $\lambda^* = 230$  and  $M_\phi = 1.2$ . In  $c$ -equation, the diffusion is interpolated by  $\mathcal{D}(\phi) = \phi D_l$  and the anti-trapping current is considered. The initial condition of composition is imposed by Eq. (50) with  $c_l^\infty = \bar{\mu}_l^\infty + m_l = 0.4$  and  $c_s^\infty = \bar{\mu}_s^\infty + m_s = 0.6$  with  $m_s = 0.2$  and  $m_l = 0.1$ . The comparisons between the analytical solutions and the LBM simulation are presented in Fig. 2. Compared to the previous section, now the curve of the interface position decreases with time (Fig. 2a) because the dissolution process occurs. The results of LBM are in good agreement with the analytical solutions for three times  $t_1 = 5 \times 10^{-5}$ ,  $t_2 = 2.5 \times 10^{-4}$  and  $t_3 = 5 \times 10^{-4}$  (Fig. 2b).

The anti-trapping effect is compared on the profiles of composition and chemical potential (Fig. 3). For composition, the analytical solution can be derived from Eq. (54b) by adding  $m_l$  on both sides and by adding and subtracting  $m_l$  inside  $(\bar{\mu}^{eq} - \bar{\mu}_l^\infty)$ . We obtain:

$$c_l^{as}(x, t) = c_l^\infty + (c_l^{co} - c_l^\infty) \frac{\operatorname{erfc}[x/2\sqrt{D_l t}]}{\operatorname{erfc}(\alpha)} \quad (55a)$$

where  $c_l^{co} = \bar{\mu}^{eq} + m_l = 0.5$ . In the solid phase, the composition is a constant of value  $c_s(x, t) = \bar{\mu}^{eq} + m_s = 0.6$  corresponding to its value of coexistence  $c_s^{co}$ . The compositions  $c_l^{as}(x, t)$  and  $c_s(x, t)$  are plotted with dashed lines on Fig. 3a.

The LBM simulations are carried out successively with and without anti-trapping current. The profiles of composition are reported on Fig. 3a at  $t = 10^{-4}$  (symbols). Without anti-trapping, the theory cannot provide a value of  $\lambda^*$  because the phase-field model is not strictly equivalent to the sharp interface one (see Section 2.4). Hence, the value of  $\lambda^* = 500$  is chosen such as the displacement of the interface is close to the analytical solution. The simulation corresponds to the best fit that is possible to obtain when  $D_s = 0$  and  $\mathbf{j}_{at} = \mathbf{0}$  in  $c$ -equation (squares on Fig. 3a). On that figure, the semi-analytical solution (*sas*) is plotted for comparison:

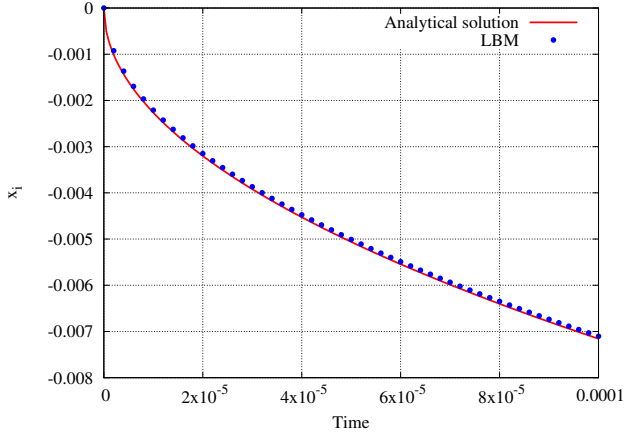
$$c^{sas}(\phi) = c_l^{as}(x, t)\phi(x, t) + c_s[1 - \phi(x, t)] \quad (55b)$$

The *sas*-solution corresponds to an interpolation of  $c_l^{as}(x, t)$  and  $c_s$  with  $\phi$ . When  $\mathbf{j}_{at}$  is not considered in  $c$ -equation, the compositions fit well far from the interface. However, inside the interface region, the compositions are over-estimated on the solid side whereas they are under-estimated on the liquid side. On the interval  $[-L_x, x_i(t)]$  (solid), the profile slightly oscillates above the composition of coexistence. That oscillation is more visible when we plot the chemical potential (Fig. 3b). That lack of accuracy slows down the displacement of interface compared to the analytical solution Eq. (54a).

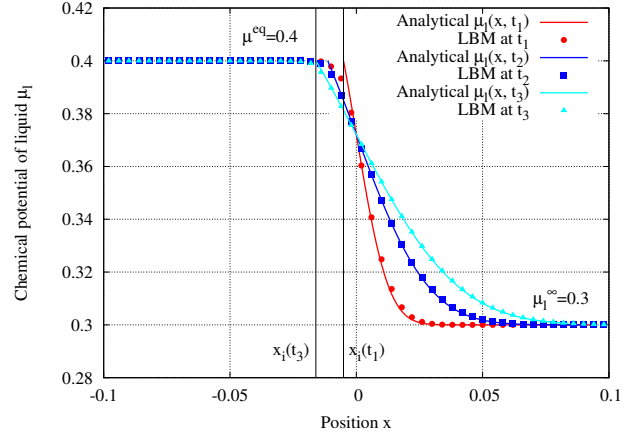
## 5. Dissolution of porous medium: counter term effect

In Section 4, the initial conditions of  $\phi$  and  $c$  are defined by two hyperbolic tangent functions. Here, the phase-field is initialized with an input datafile which comes from the characterization of a 3D porous sample with X-ray tomography. The datafile contains  $256 \times 256 \times 236$  rows with three indices of position ( $x$ ,  $y$  and  $z$ ) and one additional index describing the solid (value 0) or the pore (value 255). For simulating the dissolution, we assume that the poral volume is filled with a solute of smaller composition than the coexistence composition of liquid. A two-dimensional slice of size  $256 \times 256$  has been extracted from the datafile and rescaled to  $1024 \times 1024$  nodes covering a square of size  $[0, 1]^2$  ( $\delta x \simeq 9.76 \times 10^{-4}$ ). The time-step of discretization is  $\delta t = 5 \times 10^{-7}$ . The type of all boundary conditions is zero flux.

For the parameters of  $\phi$ -equation, the diffusivity is  $M_\phi = 1.2$  and the interface width is set equal to  $W = 0.02$  (i.e.  $\sim 20\delta x$ ). The value of coupling coefficient  $\lambda^* = 230$  (corresponding to  $\beta = 0$ ) is computed by using Eq. (37) with values of  $\mathcal{H}$ ,  $\mathcal{F}$  and  $\mathcal{J} = 2/3$  defined in Tab. 3. For  $c$ -equation, the coexistence compositions of solid and liquid are respectively equal to  $c_s^{co} = 0.6$  and  $c_l^{co} = 0.5$  ( $\Delta c^{co} = 0.1$ ) and the chemical potential of equilibrium is  $\bar{\mu}^{eq} = 0.4$ . The diffusion coefficients are zero in the solid ( $D_s = 0$ ) and one in the liquid ( $D_l = 1$ ). The anti-trapping current  $\mathbf{j}_{at}$  is used in the simulations.

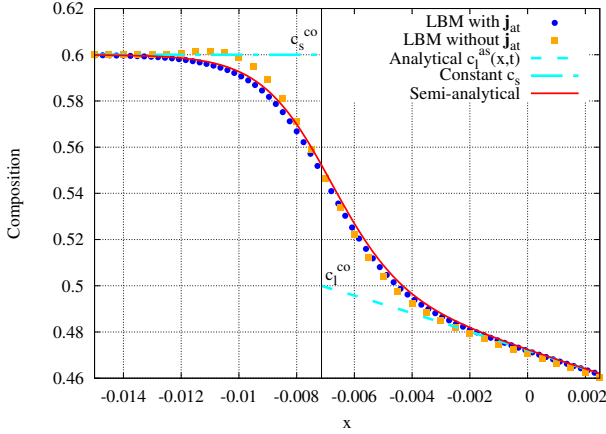


(a) Interface position  $x_i(t)$  decreasing with time because of dissolution process: the interface moves towards negative values of  $x$ .

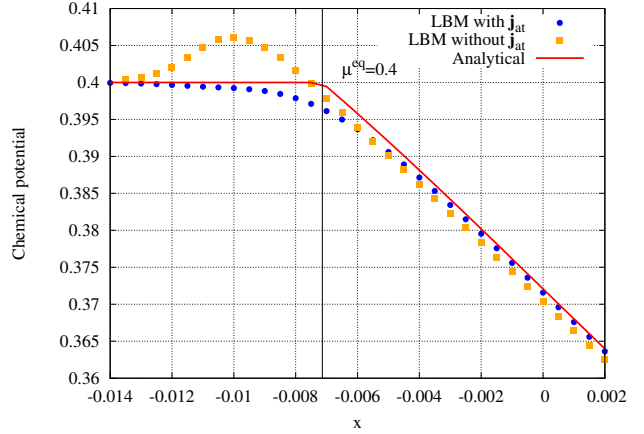


(b) Chemical potential  $\bar{\mu}_l$  w.r.t.  $x$  for three times  $t_1 = 5 \times 10^{-5}$  (red),  $t_2 = 2.5 \times 10^{-4}$  (blue) and  $t_3 = 5 \times 10^{-4}$  (cyan). The  $L^2$ -errors decrease with time:  $1.6 \times 10^{-3}$  for  $t_1$ ,  $7.2 \times 10^{-4}$  for  $t_2$  and  $5.4 \times 10^{-4}$  for  $t_3$ . The two vertical lines (black) indicate the interface positions at  $x_i(t_1)$  and  $x_i(t_3)$ .

Figure 2: Analytical solutions Eqs. (54a), (54b), (55a) (lines) compared with LBM (symbols) for a case of dissolution with  $D_s = 0$  and  $D_l = 1$ . The anti-trapping current  $\mathbf{j}_{at}$  is considered in the simulation. The system is initialized with an interface located at  $x = 0$ . The solid and liquid are respectively on left- and right-side.



(a) Profiles of composition compared between LBM (symbols), analytical (dashed line) and semi-analytical solutions (solid lines). The  $L^2$ -errors are  $3.6 \times 10^{-3}$  with anti-trapping and  $4.8 \times 10^{-3}$  without.



(b) Profiles of chemical potential compared between LBM (symbols) and analytical solution (line). The  $L^2$ -errors are  $3.5 \times 10^{-3}$  with anti-trapping and  $6.8 \times 10^{-3}$  without.

Figure 3: LB simulations with (dots) and without (squares)  $\mathbf{j}_{at}$  in  $c$ -equation. Comparison on profiles of composition (Fig. 3a) and chemical potential (Fig. 3b). Zoom between  $[-0.015, 0.002]$  at  $t = 10^{-4}$ .

The phase-field is simply initialized at  $t_0 = 0$  with two discontinuous values: for solid  $\phi(\mathbf{x}_s, t_0) = \phi_s = 0$  and for liquid  $\phi(\mathbf{x}_l, t_0) = \phi_l = 1$ . The composition of the solid phase  $c(\mathbf{x}_s, t_0)$  is set equal to the coexistence composition of solid  $c_s^{co}$ . For liquid, the initial condition is below its coexistence composition:  $c(\mathbf{x}_l, t_0) = 0.4 < 0.5$ . Those initializations are presented on Fig. 4a for  $\phi$  and Fig. 4b for  $c$ . On both figures, three squares are sketched for comparing the evolution of small pores which are enclosed inside the solid.

With those initial conditions, the dissolution process occurs until the composition of the liquid phase is equal to  $c_l^{co}$ . Two simulations are compared. In the first one, the  $\phi$ -equation is Eq. (34) which accounts for the counter term  $-M_\phi \kappa |\nabla \phi|$ . In the second one, the curvature-driven motion is possible because the  $\phi$ -equation is Eq. (33a). For both simulations, a diffuse interface replaces at first time-steps the initial discontinuity between the solid and liquid phases.

The code ran 70 seconds on a single GPU (Volta 100) until the steady state is reached after  $10^4$  time steps.

The results are presented in Fig. 5 for three times:  $t_1 = 10^2 \delta t$  (left),  $t_2 = 10^3 \delta t$  (middle) and  $t_f = 10^4 \delta t$  (right). At first sight, the difference concerns the shapes of the solid phase at the end of simulations. When the counter term is considered, the interface is much more irregular (Fig. 5a-right) than that obtained without counter term (Fig. 5b-right). The reason is that, with counter term, the interface motion is only caused by differences of composition in liquid and solid. The dissolution occurs in isotropic way until the equilibrium is reached. Without counter term, the irregularities of solid disappear because of the curvature-driven motion. Finally, the shape of the solid phase is much smoother.

For both simulations, when the steady state is reached, the composition of liquid phase is equal to the coexistence

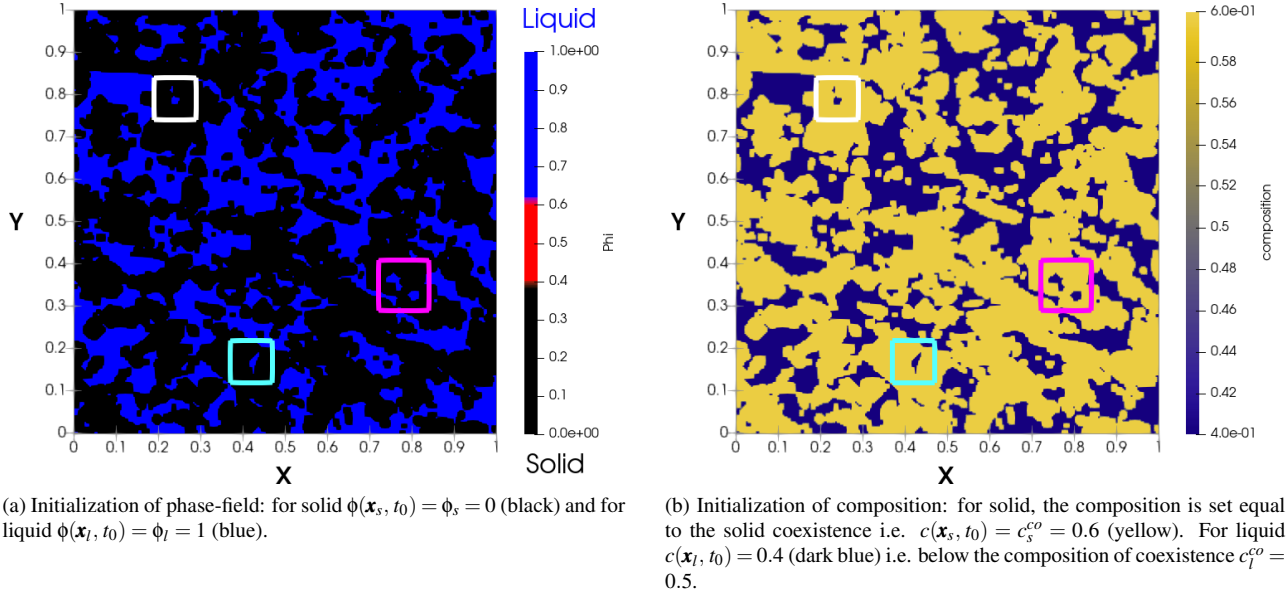


Figure 4: Positions  $\mathbf{x}_s$  and  $\mathbf{x}_l$  of datafile used to define the initial conditions for  $\phi$  (Fig. 4a) and  $c$  (Fig. 4b). Three squares are sketched for comparing the evolution of small pores enclosed inside the solid.

composition of liquid  $c(\mathbf{x}_l, t_f) = c_l^{co}$  (gray areas in the right figures of 5c and 5d). However, the composition inside the solid phase is different. When the curvature-driven motion is canceled, the composition  $c(\mathbf{x}_s, t_f)$  is homogeneous of value  $c_s^{co}$  (see Fig. 5c-right). When that motion is taken into account, the solid composition  $c(\mathbf{x}_s, t_f)$  is heterogeneous as revealed by the presence of areas of composition lower than  $c_s^{co}$  (gray areas inside squares in Fig. 5d-right). Those areas correspond to solid phases as confirmed by Fig. 5b-right.

That heterogeneity of composition is explained by the curvature-driven motion occurring when the counter term is not considered in  $\phi$ -equation. That interface motion makes disappear the small pores embedded in the solid phase. For instance at  $t_1$ , the small one inside the white square has disappeared (Fig. 5b-left) and the pore inside the cyan square has almost disappeared (red dot). That same pore has fully disappeared at  $t_2$  (Fig. 5b-middle) and one of the two pores inside the magenta square has also disappeared. At last both of them have disappeared at  $t_f$  (Fig. 5b-right). With counter term, all those pores still exist at the end of simulation (Fig. 5a-right).

With the curvature-driven motion a special area which is initially liquid ( $\phi = 1$ ) may become solid ( $\phi = 0$ ) even though the local composition  $c(\mathbf{x}_l, t)$  is not greater than  $c_l^{co}$ . That curvature motion acts like a precipitation process. For those areas, the diffusion coefficient changes from  $D_l$  to  $D_s = 0$  meaning that the diffusion process does not occur anymore. The value of composition is “frozen” explaining why small islands of lower composition are embedded in the solid phase.

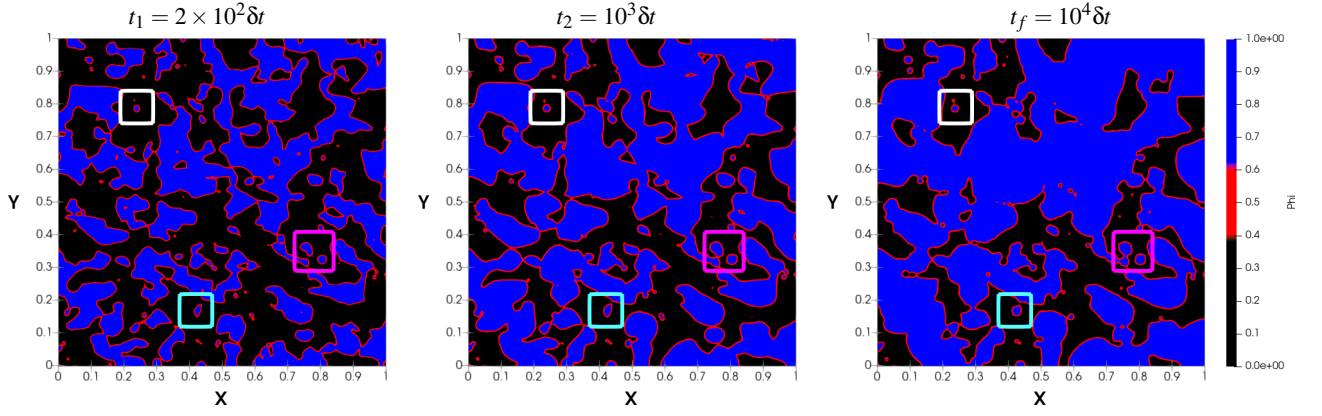
An in-depth physical analysis is based on the Gibbs-Thomson condition Eq. (35c) i.e.  $\bar{\mu} = \bar{\mu}^{eq} - d_0 \kappa$  (with  $\beta = 0$ ). When two phases coexist, the interface will move towards the position where the chemical potential  $\bar{\mu}$  is closer to  $\bar{\mu}^{eq}$ . In the first case, the counter term cancels the motion  $d_0 \kappa$  whereas in the second case that motion exists. In our simu-

lations  $\bar{\mu}(\mathbf{x}_s, t) = \bar{\mu}^{eq} = 0.4$  in the solid and  $\bar{\mu}(\mathbf{x}_l, t) = 0.3$  in the liquid. For small pores trapped in the solid, the interface will move towards the liquid phase and the physical process acts like precipitation. The interface disappears because it is the unique way to reach the equilibrium value  $\bar{\mu}^{eq}$ . On the contrary, for outgrowths, the curvature is opposite and the interface will move towards the solid phase, dissolution occurs.

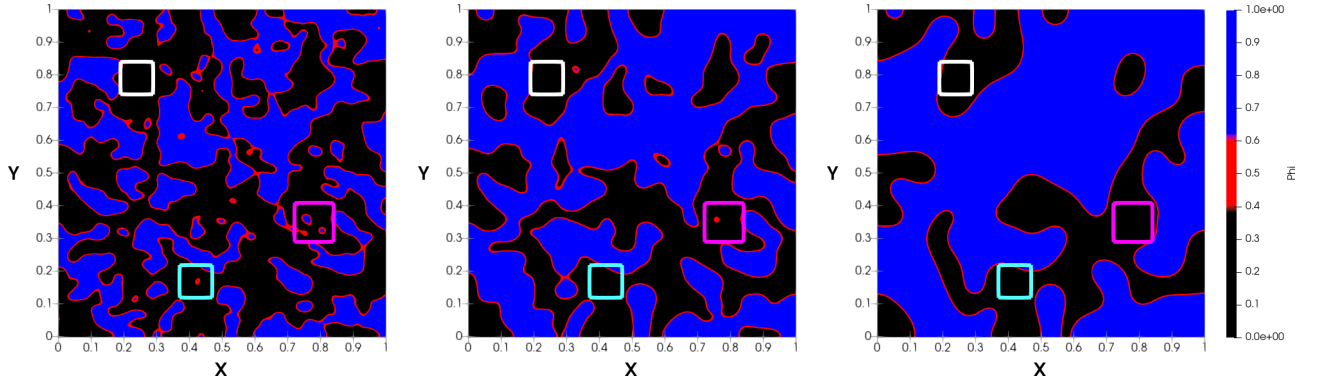
## 6. Conclusion

In this work we have presented a phase-field model of dissolution and precipitation. Its main feature lies in its derivation which is based on the functional of grand-potential  $\Omega[\phi, \mu]$ . In that theoretical framework, the phase-field  $\phi$  and the chemical potential  $\mu$  are the two main dynamical variables. In models based on free energy,  $\phi$  and the composition  $c$  are the two main variables. The benefits of using the grand-potential are twofold. First, for models based on free-energy, two additional conditions must be solved inside the diffuse zone in order to ensure the equality of chemical potential at interface. In grand-potential theory, it is not necessary because the model includes that assumption in its formulation. Second, the chemical potential is an intensive thermodynamic quantity like temperature so that many analogies can be done with solidification problems. Hence, the analytical solutions of the Stefan problem can be used for validation by comparing directly the temperature and the chemical potential. Besides, the matched asymptotic expansions can be directly inspired from those already performed for solidification problems. The phase-field model is composed of two PDEs. The first equation computes the evolution of the interface position  $\phi$ . The second one is a mixed formulation using the composition and chemical potential. Although that equation requires a closure relationship between  $c$  and  $\mu$ , that formulation improves the mass conservation.

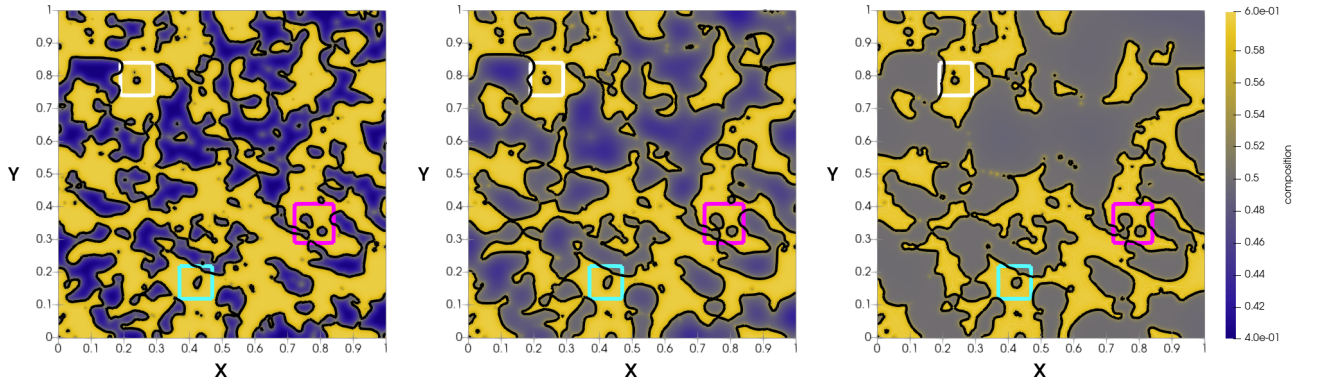




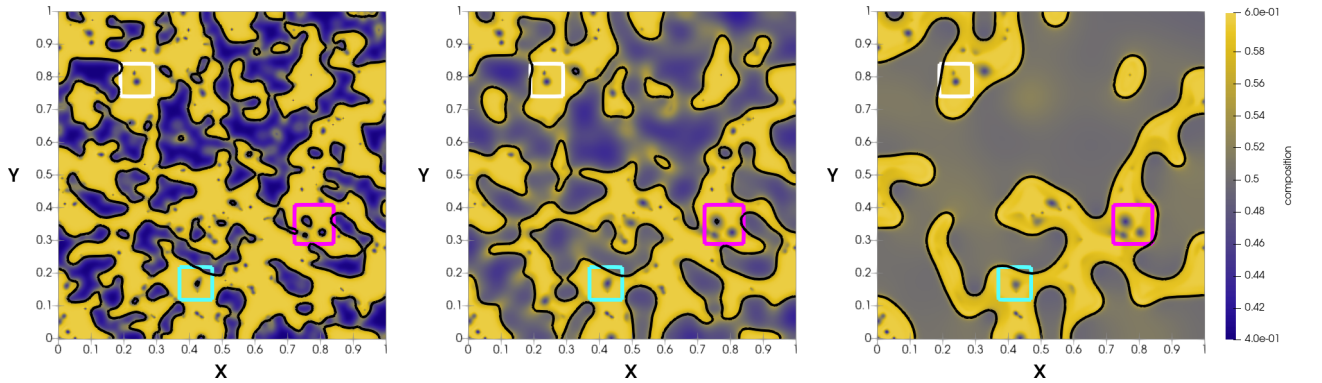
(a) Evolution of the phase-field when the counter term is considered in  $\phi$ -equation.



(b) Phase-field at same time steps without counter term. Because of the curvature-driven motion the final shape of solid is smoother and the small pores inside the squares have disappeared.



(c) Fields of composition at same time steps with counter term in  $\phi$ -equation. At final time the composition is homogeneous in the solid phase of value  $c_s^{co}$ .



(d) Fields of composition without counter term at same time steps. The composition of solid is heterogeneous because the small pores have disappeared and the diffusion is zero. Several areas of smaller composition than  $c_s^{co}$  are trapped in the solid phase (e.g. inside the squares).

Figure 5: Dissolution of porous medium simulated by a phase-field model based on the grand-potential. Snapshots of phase-field and composition at  $t_1 = 2 \times 10^2 \delta t$  (left),  $t_2 = 10^3 \delta t$  (middle) and final time of simulation  $t_f = 10^4 \delta t$  (right). Two simulations are carried out: in Figs. 5a and 5c the  $\phi$ -equation is Eq. (34) whereas in Figs. 5b and 5d the  $\phi$ -equation is Eq. (33a). The iso-contour  $\phi = 0.5$  (black line) is super-imposed on Figs. 5c and 5d.

In many simulations of dissolution or precipitation, two main hypotheses are often considered. First, the interface is assumed to move because of chemical reactions, which is often considered by a kinetics of first-order. That assumption means that the curvature-driven motion is neglected in the Gibbs-Thomson condition. In the phase-field theory, that motion is always contained in the  $\phi$ -equation. In order to cancel it, a counter term  $-M_\phi \kappa |\nabla \phi|$  must be added in  $\phi$ -equation. The second hypothesis is the diffusion that is neglected in the solid phase. In that case, the anti-trapping current  $j_{at}$  must be considered in  $c$ -equation. Those two terms are not contained in the functional of grand-potential, they are added for phenomenological reasons. Without them, the phase-field model is not equivalent to the sharp interface model because several spurious terms arise from the matched asymptotic expansions.

The model has been implemented with lattice Boltzmann schemes in the `LBM_saclay` code. The one-dimensional validations have been carried out with two analytical solutions of the Stefan problem. The test cases present one process of precipitation with  $D_s \simeq D_l$  and another one of dissolution for  $D_s = 0$ . The first one is performed without anti-trapping and compares the profiles of composition. The jump of composition is well-reproduced by the model at interface. The diffusive behavior is also perfectly fitted for each phase. The second test emphasizes the analogy with problems of solidification (or melting) where the equilibrium chemical potential  $\mu^{eq}$  plays the role of melting temperature and  $\Delta c^{co}$  is compared to the latent heat. For that test, the use of anti-trapping current avoids the oscillations of algorithm and improves the accuracy of composition profiles.

Finally, the numerical model has been applied for simulating the dissolution process of a porous medium. The rock sample has been characterized by X-ray microtomography. The datafile has been used for defining the initial conditions for  $\phi$  and  $c$ . Two simulations have compared the impact of counter term on the shape of solid. When the counter term is not considered in  $\phi$ -equation, the curvature-driven motion makes disappear small areas of liquid trapped inside the solid phase. The main consequence of that effect, acting like precipitation, is the heterogeneity of composition inside the solid phase. When the counter term is taken into account, the solid/liquid interface is much more irregular and the composition is homogeneous inside the solid phase.

The grand-potential densities  $\omega_\phi$  of each phase are defined by the Legendre transform of free energy densities  $f_\phi$ . In this work, the main assumption is that  $f_s$  and  $f_l$  are defined by two parabolas with identical curvature  $\epsilon_s = \epsilon_l$ . That hypothesis simplifies the link between the thermodynamic parameters  $m_\phi$ ,  $\epsilon_\phi$  and  $\bar{f}_\phi^{min}$  and the properties of equilibrium i.e. the coexistence compositions  $c_s^{co}$ ,  $c_l^{co}$ , and the equilibrium chemical potential  $\mu^{eq}$ . Nevertheless, for real materials the thermodynamics does not fulfill necessarily that condition. An in-depth study with  $\epsilon_s \neq \epsilon_l$  is planned for future work for binary and ternary mixtures.

## Acknowledgments

The authors wish to thank MATHIS PLAPP for the insightful discussions on 1) the theoretical framework of grand-

potential and 2) the asymptotic expansions of phase-field model. They also acknowledge the Genden project (number R0091010339) for computational resources of supercomputer Jean-Zay (IDRIS, France).

## Appendix A. Matched asymptotic expansions

The starting point of this Appendix is the phase-field model composed of Eqs. (33a)–(33c). The analysis is performed into two main stages. First, the whole computational domain is divided into two regions. The first region is located far from the interface (bulk phases) and called the “outer domain”. The second region is the diffuse interface and called the “inner domain”. In Appendix A.1, we define the dimensionless variables and the matching conditions between both regions. Next, we present the analysis of the outer domain in Appendix A.2 and the inner domain in Appendix A.3. Finally a discussion is carried out in Appendix A.4 to remove the error terms.

### Appendix A.1. Main definitions

#### Appendix A.1.1. Outer domain and inner domain

The unknown are  $\phi^{out}$ ,  $\mu^{out}$ ,  $c^{out}$  for the outer domain, and  $\phi^{in}$ ,  $\mu^{in}$ ,  $c^{in}$  for the inner domain. They are expanded as power of a small parameter  $\epsilon \ll 1$ :

$$\begin{aligned} \phi^{out} &\simeq \phi_0^{out} + \epsilon \phi_1^{out} + \epsilon^2 \phi_2^{out}, & \phi^{in} &\simeq \phi_0^{in} + \epsilon \phi_1^{in} + \epsilon^2 \phi_2^{in} \\ c^{out} &\simeq c_0^{out} + \epsilon c_1^{out} + \epsilon^2 c_2^{out}, & c^{in} &\simeq c_0^{in} + \epsilon c_1^{in} + \epsilon^2 c_2^{in} \\ \mu^{out} &\simeq \mu_0^{out} + \epsilon \mu_1^{out} + \epsilon^2 \mu_2^{out}, & \mu^{in} &\simeq \mu_0^{in} + \epsilon \mu_1^{in} + \epsilon^2 \mu_2^{in} \end{aligned}$$

The small parameter of expansions is defined by  $\epsilon = W/d_0$ , where  $d_0 = W/(\alpha\lambda)$  is the capillary length, and  $\alpha$  is a parameter to be determined. The two coefficients  $D_l$  and  $d_0$  define a characteristic speed  $v_c = D_l/d_0 = \epsilon D_l/W$ , and a characteristic time  $t_c = d_0^2/D_l = d_0/v_c$ . For the expansions, we also assume  $1/\kappa \sim d_0$  i.e.  $W\kappa \sim \epsilon$ . In the phase-field equation, the coefficient  $\lambda$  is replaced by  $\epsilon/\alpha$ . Finally, we define the following dimensionless quantities: the interface speed  $\bar{v}_n = v_n/v_c$ , the interface curvature  $\bar{\kappa} = d_0\kappa$ , the time  $\bar{t} = t/t_c$ , the spatial coordinate  $\bar{\mathbf{x}} = \mathbf{x}/d_0$ , and the dimensionless diffusivity  $\bar{D} = D_l/M_\phi$ . Finally  $q_s = D_s/D_l$  is the ratio of diffusion coefficients.

For each domain, the model is re-written with the curvilinear coordinates  $r$  and  $s$ , where  $r$  is the signed distance to the level line  $\phi = 0.5$ , and  $s$  the arc length along the interface. The dimensionless coordinates are also defined by:  $\eta = r/d_0$  and  $\bar{s} = s/d_0$ . The spatial operators (divergence, gradient, laplacian) and the time derivatives are also expressed in this new system of coordinates, and next expanded in power of  $\epsilon$ . Finally, the terms of same order are gathered and the solutions of all orders can be calculated with appropriate boundary conditions: the “matching conditions”.

#### Appendix A.1.2. Matching conditions

The matching conditions are established by comparing the limits of inner variables far from the interface with the limits of outer variables near the interface. For that purpose we define  $\xi = r/W$ , a “stretched” normal coordinate in

the inner region. Let us notice that the curvilinear coordinates  $r$  and  $s$  have been made dimensionless by introducing  $\eta = r/d_0$  and  $\bar{s} = s/d_0$  in the outer domain, we observe that  $\eta/\xi = \varepsilon \ll 1$ . This motivates us to compare the limits of inner variables when  $\xi \rightarrow \pm\infty$  with the limits of outer variables when  $\eta \rightarrow 0^\pm$ . For the phase-fields  $\phi_0^{in}$  and  $\phi_0^{out}$ , we define the matching conditions:

$$\lim_{\xi \rightarrow +\infty} \phi_0^{in} = \lim_{\eta \rightarrow 0^+} \phi_0^{out} \quad \text{and} \quad \lim_{\xi \rightarrow -\infty} \phi_0^{in} = \lim_{\eta \rightarrow 0^-} \phi_0^{out}$$

For the chemical potentials  $\mu_j^{in}$  and  $\mu_j^{out}$  ( $0 \leq j \leq 2$ ), the matching conditions are:

$$\begin{aligned} \lim_{\xi \rightarrow \pm\infty} \mu_0^{in} &= \mu_0^{out}(0^\pm) \\ \lim_{\xi \rightarrow \pm\infty} \mu_1^{in} &= \mu_1^{out}(0^\pm) + \partial_\eta \mu_0^{out}(0^\pm) \xi \\ \lim_{\xi \rightarrow \pm\infty} \partial_\xi \mu_2^{in} &= \partial_\eta \mu_1^{out}(0^\pm) + \partial_\eta^2 \mu_0^{out}(0^\pm) \xi \end{aligned}$$

where  $\mu_j^{out}(0^\pm) = \lim_{\eta \rightarrow 0^\pm} \mu_j^{out}$  for  $j = 0, 1$  and  $\partial_\eta \mu_0^{out}(0^\pm) = \lim_{\eta \rightarrow 0^\pm} \partial_\eta \mu_0^{out}$ .

#### Appendix A.2. Analysis of outer domain

In the outer domain, the use of curvilinear coordinates is not necessary because the region is far from the interface. Thus, the model is written with the dimensionless cartesian coordinates  $\bar{\mathbf{x}}$ , the dimensionless time  $\bar{t}$  and the parameter of expansion  $\varepsilon$ . The model writes:

$$\begin{aligned} \bar{D}\varepsilon^2 \partial_{\bar{t}} \phi^{out} &= \varepsilon^2 \bar{\nabla}^2 \phi^{out} - \omega'_{dw}(\phi^{out}) - \frac{\varepsilon}{\alpha} \partial_\phi \omega^p(\phi^{out}, \mu^{out}) \\ \partial_{\bar{t}} c &= \bar{\nabla} \cdot [q(\phi^{out}) \bar{\nabla} \mu^{out} - \mathbf{j}_{at}(\phi^{out})] \end{aligned} \quad (\text{A.1})$$

where the notation  $\omega^p = p(\phi)\omega_l(\mu) + [1 - p(\phi)]\omega_s(\mu)$  and  $\mathbf{j}_{at}(\phi^{out}) = -a(\phi^{out})\Delta c^{co} \partial_{\bar{t}} \phi^{out} \mathbf{n}$  with the normal vector  $\mathbf{n} =$

$\bar{\nabla} \phi^{out} / |\bar{\nabla} \phi^{out}|$ . The expansions of  $\phi$ -equation write for each order:

$$O(1): \quad 0 = \omega'_{dw}(\phi_0^{out}) \quad (\text{A.2a})$$

$$O(\varepsilon): \quad 0 = \omega''_{dw}(\phi_0^{out}) \phi_1^{out} + \alpha^{-1} \partial_\phi \omega^p(\phi_0^{out}, \mu_0^{out}) \quad (\text{A.2b})$$

$$\begin{aligned} O(\varepsilon^2): \quad 0 &= \bar{D}\varepsilon^2 \partial_{\bar{t}} \phi_0^{out} - \bar{\nabla}^2 \phi_0^{out} + \omega'''_{dw}(\phi_0^{out}) \phi_2^{out} \\ &+ \frac{1}{2} \omega''_{dw}(\phi_0^{out}) (\phi_1^{out})^2 + \frac{1}{\alpha} \partial_\phi^2 \omega^p(\phi_0^{out}, \mu_0^{out}) \phi_1^{out} \\ &+ \alpha^{-1} \partial_\phi^2 \omega^p(\phi_0^{out}, \mu_0^{out}) \mu_1^{out} \end{aligned} \quad (\text{A.2c})$$

According to Eq. (A.2a),  $\omega_{dw}(\phi_0^{out})$  takes a minimal value in the outer domain, i.e.  $\phi_0^{out}$  is either equal to  $\phi_s = 0$  or  $\phi_l = 1$ . In addition,  $p(\phi)$  must be chosen such that its derivatives vanish in the bulk phases. Then Eq. (A.2b) becomes simply  $\omega''_{dw}(\phi_0^{out}) \phi_1^{out} = 0$ , implying  $\phi_1^{out} = 0$ . Similarly, Eq. (A.2c) simplifies to  $\omega''_{dw}(\phi_0^{out}) \phi_2^{out} = 0$  involving  $\phi_2^{out} = 0$ . Finally, the analysis of  $\phi$ -equation in the outer domain yields

$\phi_0^{out} = \phi_\Phi$  and  $\phi_1^{out} = \phi_2^{out} = 0$  for  $\Phi = s, l$  (A.3) We can complete the matching conditions with the additional relation  $\lim_{\xi \rightarrow \pm\infty} \phi_j^{in} = 0$  for  $j \geq 1$ . Because of Eq. (A.3), the term  $\partial_{\bar{t}} \phi^{out}$  is null in Eq. (A.1), and the  $c$ -equation simplifies to:

$$\partial_{\bar{t}} c = \bar{\nabla} \cdot [q(\phi_\Phi) \bar{\nabla} \mu^{out}] \quad \text{for } \Phi = s, l \quad (\text{A.4})$$

The analysis of the outer domain recovers the standard diffusion equation Eq. (A.4) with a constant phase-field Eq. (A.3) for each bulk phase.

#### Appendix A.3. Analysis of inner domain

Now we focus on the analysis of the inner domain. After expansions of each PDE (Appendix A.3.1), the solutions are calculated order-by-order and used to derive the interface conditions (Appendix A.3.2–Appendix A.3.6).

##### Appendix A.3.1. Expanded equations

The expansions of  $\phi$ -equation and  $c$ -equation write:

$$O(1): \quad \partial_{\xi\xi}^2 \phi_0^{in} - \omega'_{dw}(\phi_0^{in}) = 0 \quad (\text{A.5a})$$

$$O(\varepsilon): \quad \partial_{\xi\xi}^2 \phi_1^{in} - \omega''_{dw}(\phi_0^{in}) \phi_1^{in} = -(\bar{D}\bar{v}_n + \bar{\kappa}) \partial_\xi \phi_0 + \alpha^{-1} \partial_\phi \omega^p(\phi_0^{in}, \mu_0^{in}) \quad (\text{A.5b})$$

$$\begin{aligned} O(\varepsilon^2): \quad \partial_{\xi\xi}^2 \phi_2^{in} - \omega''_{dw}(\phi_0^{in}) \phi_2^{in} &= (1/2) (\phi_1^{in})^2 \omega'''_{dw}(\phi_0^{in}) + \bar{D} \partial_{\bar{t}} \phi_0^{in} - \partial_{\bar{s}\bar{s}}^2 \phi_0^{in} - (\bar{D}\bar{v}_n + \bar{\kappa}) \partial_\xi \phi_1^{in} \\ &+ \xi \bar{\kappa}^2 \partial_\xi \phi_0^{in} + \alpha^{-1} \partial_\phi^2 \omega^p(\phi_0^{in}, \mu_0^{in}) \phi_1^{in} + \alpha^{-1} \partial_\phi^2 \omega^p(\phi_0^{in}, \mu_0^{in}) \mu_1^{in} \end{aligned} \quad (\text{A.5c})$$

$$O(1): \quad \partial_\xi [q(\phi_0^{in}) \partial_\xi \mu_0^{in}] = 0 \quad (\text{A.6a})$$

$$O(\varepsilon): \quad \partial_\xi [q(\phi_0^{in}) \partial_\xi \mu_1^{in}] = -\partial_\xi [\phi_1^{in} \partial_\phi q(\phi_0^{in}) \partial_\xi \mu_0^{in}] - \bar{v}_n \partial_\xi c_0^{in} - \bar{\kappa} q(\phi_0^{in}) \partial_\xi \mu_0^{in} + \partial_\xi [a(\phi_0^{in}) \Delta c^{co} \bar{v}_n \partial_\xi \phi_0^{in}] \quad (\text{A.6b})$$

$$\begin{aligned} O(\varepsilon^2): \quad \partial_\xi [q(\phi_0^{in}) \partial_\xi \mu_2^{in}] &= \partial_{\bar{t}} c_0^{in} + \xi \bar{\kappa}^2 q(\phi_0^{in}) \partial_\xi \mu_0^{in} - \bar{v}_n \partial_\xi c_1^{in} - \bar{\kappa} q(\phi_0^{in}) \partial_\xi \mu_1^{in} \\ &- \partial_{\bar{s}} [q(\phi_0^{in}) \partial_{\bar{s}} \mu_0^{in}] - \bar{\kappa} \phi_1^{in} \partial_\phi q(\phi_0^{in}) \partial_\xi \mu_0^{in} - \partial_\xi [\phi_1^{in} \partial_\phi q(\phi_0^{in}) \partial_\xi \mu_1^{in}] \\ &- \partial_\xi \{ [\phi_2^{in} \partial_\phi q(\phi_0^{in}) + (\phi_1^{in})^2 / 2] \partial_{\phi\phi}^2 q(\phi_0^{in}) \} + \Delta c^{co} \bar{\kappa} a(\phi_0^{in}) \bar{v}_n \partial_\xi \phi_0^{in} \\ &+ \Delta c^{co} \partial_\xi [a(\phi_0^{in}) \bar{v}_n \partial_\xi \phi_1^{in} + a'(\phi_0^{in}) \bar{v}_n \phi_1^{in} \partial_\xi \phi_0^{in}] \end{aligned} \quad (\text{A.6c})$$



The closure equation writes (only  $O(1)$  is necessary):

$$O(1): \quad c_0^{in} = -\partial_\mu \omega^h(\phi_0^{in}, \mu_0^{in}) \quad (\text{A.7})$$

In the rest of this section, the superscript “in” will be removed for all inner variables i.e. for  $0 \leq j \leq 2$  we note  $\phi_j \equiv \phi_j^{in}$ ,  $\mu_j \equiv \mu_j^{in}$  and  $c_j \equiv c_j^{in}$ . The superscript “out” is kept for the variables of outer domain.

#### Appendix A.3.2. Analysis of terms $O(1)$

For  $\phi$ -equation, Eq. (A.5a) can be easily solved by using  $\omega_{dw}$ . At order zero, we obtain the hyperbolic tangent profile of the phase-field:

$$\phi_0(\xi) = \frac{1 + \tanh(2\xi)}{2} \quad (\text{A.8})$$

For  $c$ -equation, two successive integrations of Eq. (A.6a) yield  $\partial_\xi \mu_0 = A(\bar{s})/q(\phi_0)$  and  $\mu_0 = B(\bar{s}) + A(\bar{s}) \int_0^\xi q^{-1}(\phi_0) d\xi$ . Both constants of integration  $A$  and  $B$  can depend on  $\bar{s}$ . We can see that  $A = 0$  is necessary because the integral does not converge when  $\xi \rightarrow +\infty$  (because  $q \rightarrow 1$  when  $\xi \rightarrow +\infty$ ). Hence,  $\mu_0$  depends only on the position along the interface  $\bar{s}$ , and the matching conditions yield:

$$\mu_0^{out}(0^+) = \mu_0^{out}(0^-) \quad (\text{A.9})$$

i.e. the continuity of the chemical potential at order zero.

#### Appendix A.3.3. $\phi$ -equation: analysis of terms $O(\epsilon)$

The Gibbs-Thomson condition at order zero arises from the analysis of terms  $O(\epsilon)$  of  $\phi$ -equation. After multiplication of Eq. (A.5b) by  $\partial_\xi \phi_0$  and integration wrt  $\xi$  from  $-\infty$  to  $+\infty$ , we obtain:

$$\int_{-\infty}^{+\infty} \mathcal{L}(\phi_1) \partial_\xi \phi_0 d\xi = -(\bar{D}\bar{v}_n + \bar{\kappa}) \int_{-\infty}^{+\infty} (\partial_\xi \phi_0)^2 d\xi + \frac{1}{\alpha} \int_{-\infty}^{+\infty} \partial_\xi \phi_0 \partial_\phi \omega^p(\phi_0, \mu_0) d\xi \quad (\text{A.10})$$

where we set  $\mathcal{L}(\phi_1) = \partial_{\xi\xi}^2 \phi_1 - \omega_{dw}'(\phi_0) \phi_1$ . The left-hand side (LHS) of Eq. (A.10) is integrated by parts (using  $O(1)$  phase field for the last equality), we find:

$$\int_{-\infty}^{+\infty} \partial_\xi \phi_0 \mathcal{L}(\phi_1) d\xi = - \int_{-\infty}^{+\infty} \partial_\xi \phi_1 \mathcal{L}(\phi_0) d\xi = 0$$

In the right-hand side (RHS) of Eq. (A.10), the first integral is noted  $\mathcal{J} = \int_{-\infty}^{+\infty} (\partial_\xi \phi_0)^2 d\xi = 2/3$ . The second integral can be calculated because  $\mu_0$  is independent of  $\xi$ . Finally Eq. (A.10) becomes:

$$0 = -(\bar{D}\bar{v}_n + \bar{\kappa}) \mathcal{J} + \frac{1}{\alpha} [\omega_l(\mu_0) - \omega_s(\mu_0)] \quad (\text{A.11})$$

Using the expression  $\omega_l(\mu_0) - \omega_s(\mu_0) = -(c_l^{co} - c_s^{co})(\mu_0 - \mu^{eq})$  and the definitions of  $\bar{D}$ ,  $\bar{v}_n$  and  $\bar{\kappa}$ , we obtain:

$$(\mu_0 - \mu^{eq}) \Delta c^{co} = -\frac{\mathcal{J}W}{\lambda} \kappa - \frac{\mathcal{J}W}{M_\phi \lambda} v_n \quad (\text{A.12})$$

where  $\Delta c^{co} = c_l^{co} - c_s^{co}$ . We identify  $d_0 = \mathcal{J}W/\lambda$ , meaning that  $\alpha = 1/\mathcal{J}$ , and  $\beta_0 = d_0/M_\phi$ .

Another useful result for simplifying the future analyses is the first-order phase-field  $\phi_1$ . The bilinear form  $(\psi, \phi) \rightarrow \int \psi \mathcal{L}(\phi)$  is continuous and coercive where  $\psi$  and  $\phi$  are two functions vanishing at  $+\infty$  and  $-\infty$ . This means that the operator  $\mathcal{L}$  is invertible in this space. Combined with Eq. (A.11), this indicates that  $\phi_1$  is determined by:

$$\phi_1 = \frac{\Delta \omega(\mu_0)}{\alpha} \mathcal{L}^{-1} \left[ p'(\phi_0) - \frac{1}{\mathcal{J}} \partial_\xi \phi_0 \right]$$

With the derivatives of  $p(\phi)$  and  $\phi_0$  defined in Tab 2 and  $\mathcal{J} = 2/3$ , the term inside the brackets vanishes. The unique solution is  $\phi_1 = 0$  meaning that all terms depending on  $\phi_1$  in Eqs. (A.5c), (A.6b) and (A.6c) can be removed.

#### Appendix A.3.4. $c$ -equation: analysis of terms $O(\epsilon)$

The Stefan condition at order zero arises from the analysis of terms  $O(\epsilon)$  of  $c$ -equation. However, the analysis also reveals two spurious terms for the chemical potential: the chemical potentials of first-order  $\mu_1^{out}(0^+)$  and  $\mu_1^{out}(0^-)$  are not identical on both sides of the interface.

We start with a simplification of  $c$ -equation Eq. (A.6b) with the previous result  $\partial_\xi \mu_0 = 0$ :

$$\partial_\xi [q(\phi_0) \partial_\xi \mu_1] = -\bar{v}_n \partial_\xi c_0 + \partial_\xi [\Delta c^{co} a(\phi_0) \bar{v}_n \partial_\xi \phi_0]$$

After one integration, we obtain:

$$q(\phi_0) \partial_\xi \mu_1 = -\bar{v}_n c_0 + A + \Delta c^{co} a(\phi_0) \bar{v}_n \partial_\xi \phi_0 \quad (\text{A.13})$$

Considering the limit  $\xi \rightarrow -\infty$ , the integration constant  $A$  is found equal to  $A = \Lambda_s + \bar{v}_n c_s(\mu_0)$  where  $\Lambda_s = q_s \partial_\eta \mu_0^{out}(0^-)$ . The closure relation Eq. (A.7) writes  $c_0 = h(\phi_0) c_l(\mu_0) + [1 - h(\phi_0)] c_s(\mu_0)$ . Eq. (A.13) becomes

$$\partial_\xi \mu_1 = \frac{1}{q(\phi_0)} [-\bar{v}_n h(\phi_0) \Delta c_0 + \Lambda_s + \Delta c^{co} a(\phi_0) \bar{v}_n \partial_\xi \phi_0] \quad (\text{A.14})$$

where  $\Delta c_0 = c_l(\mu_0) - c_s(\mu_0)$ . Because of the choice of free energies, we also have  $\Delta c_0 = \Delta c^{co}$  (see Eqs. (24a)-(24b)). Integrating once again from 0 to  $\xi$ , we obtain

$$\mu_1 = \Upsilon - \bar{v}_n \Delta c_0 \int_0^\xi \frac{h(\phi_0)}{q(\phi_0)} d\xi + \Lambda_s \int_0^\xi \frac{1}{q(\phi_0)} d\xi + \bar{v}_n \int_0^\xi \frac{a(\phi_0) \Delta c^{co} \partial_\xi \phi_0}{q(\phi_0)} d\xi \quad (\text{A.15})$$

where  $\Upsilon$  is a constant of integration that will be determined in Appendix A.3.5. Now the matching conditions are used when  $\xi \rightarrow \pm\infty$ . When  $\xi \rightarrow +\infty$ , we ensure the convergence of the first two integrals by adding  $+1 - 1$  i.e. the first integral considered is  $\int_0^\xi h(\phi_0)/q(\phi_0) + 1 - 1$  and the second one is  $\Lambda_s \int_0^\xi q^{-1}(\phi_0) + 1 - 1$ . This yields:

$$\mu_1^{out}(0^+) + \partial_\eta \mu_0^{out}(0^+) \xi = \Upsilon + \Delta c_0 \bar{v}_n \mathcal{F}_l - \bar{v}_n \Delta c_0 \xi + q_s \partial_\eta \mu_0^{out}(0^-) [\mathcal{G}_l + \xi] \quad (\text{A.16a})$$

$$\mu_1^{out}(0^-) + \partial_\eta \mu_0^{out}(0^-) \xi = \Upsilon + \Delta c_0 \bar{v}_n \mathcal{F}_s + q_s \partial_\eta \mu_0^{out}(0^-) [\mathcal{G}_s + (\xi/q_s)] \quad (\text{A.16b})$$

where  $\mathcal{F}_l$ ,  $\mathcal{F}_s$ ,  $\mathcal{G}_l$  and  $\mathcal{G}_s$  are four integrals which are defined in Tab. 3. In Eqs. (A.16a)-(A.16b), the  $\xi$ -terms are considered separately and gathered in one additional equation. The three equations write:

$$\mu_1^{out}(0^+) = \Upsilon + \bar{v}_n \Delta c_0 \mathcal{F}_l + q_s \partial_\eta \mu_0^{out}(0^-) \mathcal{G}_l \quad (\text{A.17a})$$

$$\mu_1^{out}(0^-) = \Upsilon + \bar{v}_n \Delta c_0 \mathcal{F}_s + q_s \partial_\eta \mu_0^{out}(0^-) \mathcal{G}_s \quad (\text{A.17b})$$

$$\partial_\eta \mu_0^{out}(0^+) = -\bar{v}_n \Delta c_0 + q_s \partial_\eta \mu_0^{out}(0^-) \quad (\text{A.17c})$$

The last relationship Eq. (A.17c) is the Stefan condition at order zero:

$$\partial_\eta \mu_0^{out}(0^+) - q_s \partial_\eta \mu_0^{out}(0^-) = -\bar{v}_n \Delta c_0 \quad (\text{A.18})$$

Eq. (A.17a) minus Eq. (A.17b) yields the jump of the first-order chemical potential:

$$\mu_1^{out}(0^+) - \mu_1^{out}(0^-) = \bar{v}_n \Delta c_0 \Delta \mathcal{F} + q_s \partial_\eta \mu_0^{out}(0^-) \Delta \mathcal{G} \quad (\text{A.19})$$

where  $\Delta \mathcal{F} = \mathcal{F}_l - \mathcal{F}_s$  and  $\Delta \mathcal{G} = \mathcal{G}_l - \mathcal{G}_s$ . The first-order chemical potentials are not the same on both side of the interface. The discontinuity contains two terms proportional to  $\bar{v}_n \Delta c_0$  and  $q_s \partial_\eta \mu_0^{out}(0^-)$ .

#### Appendix A.3.5. $\phi$ -equation: analysis of terms $O(\varepsilon^2)$

The analysis of terms  $O(\varepsilon^2)$  of  $\phi$ -equation reveals that the discontinuity of the first-order chemical potential adds an error term in the Gibbs-Thomson condition. Since  $\phi_1 = 0$  and  $\phi_0$  does not depend on  $\bar{t}$  and  $\bar{s}$ , Eq. (A.5c) simplifies to:

$$\partial_\xi^2 \phi_2 - \omega''_{dw}(\phi_0) \phi_2 = \alpha^{-1} \partial_{\phi\mu}^2 \omega^p(\phi_0, \mu_0) \mu_1 + \xi \kappa^2 \partial_\xi \phi_0$$

We use the same method applied to  $\phi$ -eq of order  $O(\varepsilon)$ : the LHS is noted  $\mathcal{L}(\phi_2)$  and we multiply the two sides by  $\partial_\xi \phi_0$  before integrating over  $\xi$  varying from  $-\infty$  to  $+\infty$ :

$$\int_{-\infty}^{+\infty} \partial_\xi \phi_0 \mathcal{L}(\phi_2) d\xi = \alpha^{-1} \int_{-\infty}^{+\infty} \partial_\xi \phi_0 \partial_{\phi\mu}^2 \omega^p(\phi_0, \mu_0) \mu_1 d\xi + \int_{-\infty}^{+\infty} \kappa^2 \xi (\partial_\xi \phi_0)^2 d\xi \quad (\text{A.20})$$

With the same arguments as the  $O(\varepsilon)$ -equation, the LHS of Eq. (A.20) is null. The last integral on the RHS vanishes because the integrand is odd. Eq. (A.20) is reduced to:

$$\int_{-\infty}^{+\infty} [\partial_\xi \phi_0 \partial_{\phi\mu}^2 \omega^p(\phi_0, \mu_0) \mu_1] d\xi = 0 \quad (\text{A.21})$$

From this point, the analysis is straightforward. Comparatively, during the analysis of a KKS-type formulation of the model (like in [17, Appendix A]), a similar integral would have been obtained, but with the interpolation of grand potentials  $\omega^p$  which is replaced by the free energy of an interpolation of compositions. A lengthy analysis involving the closure equation A.7 expanded at first-order would have been required to get to the same point. Here, the use of the grand-potential formulation significantly simplifies the analysis. It can also be noted that such a simplification has

already been used for the  $O(\varepsilon)$ -terms of  $\phi$ -equation in Sec. Appendix A.3.3 because the integration of  $\partial_\xi \phi_0 \partial_{\phi\mu} \omega^p(\phi_0, \mu_0)$  is much easier than  $\partial_\xi \phi_0 \partial_{\phi\mu} f(\phi_0, c_0)$  (since  $\mu_0$  is constant and not  $c_0$ ). In Eq. (A.21), we replace  $\mu_1$  by its expression Eq. (A.15):

$$\begin{aligned} \int_{-\infty}^{+\infty} \partial_\xi \phi_0 \partial_{\phi\mu}^2 \omega^p(\phi_0, \mu_0) \mu_1 d\xi &= - \int_{-\infty}^{+\infty} [\partial_\xi \phi_0 p'(\phi_0) \Delta c_0] \times \\ &\left\{ \Upsilon - \bar{v}_n \Delta c_0 \int_0^\xi \left[ \frac{h(\phi_0)}{q(\phi_0)} - \frac{a(\phi_0) \partial_\xi \phi_0}{q(\phi_0)} \right] + \Lambda_s \int_0^\xi \frac{1}{q(\phi_0)} \right\} \\ &= \bar{v}_n (\Delta c_0)^2 \mathcal{K} - \Upsilon \Delta c_0 \\ &\quad - \Lambda_s (\mathcal{G}_l + \tilde{\mathcal{F}}_l - \tilde{\mathcal{F}}_s) \Delta c_0 \end{aligned}$$

where the three integrals  $\mathcal{K}$ ,  $\tilde{\mathcal{F}}_l$  and  $\tilde{\mathcal{F}}_s$  are defined in Tab. 3. For that result we used the two relations  $\int_{-\infty}^{+\infty} \partial_\xi \phi_0 p'(\phi_0) = p(1) - p(0) = 1$  and  $\int_{-\infty}^{+\infty} \partial_\xi \phi_0 p'(\phi_0) \int_0^\xi q^{-1}(\phi_0) = \mathcal{G}_l + \tilde{\mathcal{F}}_l - \tilde{\mathcal{F}}_s$ . From Eq. (A.21) the integral is zero, so  $\Upsilon$  is given by:

$$\Upsilon = \bar{v}_n \Delta c_0 \mathcal{K} - \Lambda_s (\mathcal{G}_l + \tilde{\mathcal{F}}_l - \tilde{\mathcal{F}}_s) \quad (\text{A.22})$$

That relation is used to replace  $\Upsilon$  in Eqs. (A.17a)-(A.17b):

$$\mu_1^{out}(0^+) = \bar{v}_n \Delta c_0 [\mathcal{K} + \mathcal{F}_l] - \Lambda_s \Delta \tilde{\mathcal{F}} \quad (\text{A.23a})$$

$$\mu_1^{out}(0^-) = \bar{v}_n \Delta c_0 [\mathcal{K} + \mathcal{F}_s] - \Lambda_s [\Delta \mathcal{G} + \Delta \tilde{\mathcal{F}}] \quad (\text{A.23b})$$

where we have set  $\Delta \tilde{\mathcal{F}} = \tilde{\mathcal{F}}_l - \tilde{\mathcal{F}}_s$  and  $\Delta \mathcal{G} = \mathcal{G}_l - \mathcal{G}_s$ .

By summing Eq. (A.12) with  $\varepsilon \times$  Eqs. (A.23a)-(A.23b) such as  $\mu^{out}(0^\pm) = \mu_0(0^\pm) + \varepsilon \mu_1^{out}(0^\pm)$ , we get the discontinuity of chemical potential at interface:

$$\mu_l - \mu_s = \varepsilon v_n \frac{\mathcal{J}W}{D_l \lambda} \Delta \mathcal{F} + q_s W \partial_r \mu_0^{out}(0^-) \Delta \mathcal{G} \quad (\text{A.24})$$

where  $\mu_l \equiv \mu^{out}(0^+)$  and  $\mu_s \equiv \mu^{out}(0^-)$ . That jump involves two Gibbs-Thomson conditions, one for each side of the interface:

$$\mu_l - \mu^{eq} = -\frac{d_0}{\Delta c^{co}} \kappa - \frac{\beta_l}{\Delta c^{co}} v_n + \mathbb{E}_1 \Delta \tilde{\mathcal{F}} \quad (\text{A.25a})$$

$$\mu_s - \mu^{eq} = -\frac{d_0}{\Delta c^{co}} \kappa - \frac{\beta_s}{\Delta c^{co}} v_n + \mathbb{E}_1 [\Delta \tilde{\mathcal{F}} - \Delta \mathcal{G}] \quad (\text{A.25b})$$

where the first error term is noted  $\mathbb{E}_1 = q_s W \partial_r \mu_0^{out}(0^-)$  which cancels if  $q_s = 0$  i.e.  $D_s = 0$ . Those two relations are simply written for  $\Phi = s, l$ :

$$\mu_\Phi - \mu^{eq} = -\frac{d_0}{\Delta c^{co}} \kappa - \frac{\beta_\Phi}{\Delta c^{co}} v_n + \mathbb{E}_1 [\Delta \tilde{\mathcal{F}} - \Delta \mathcal{G}_\Phi] \quad (\text{A.26a})$$

where  $\Delta \mathcal{G}_\Phi = \mathcal{G}_l - \mathcal{G}_\Phi$ . The capillary length  $d_0$  and the kinetic coefficient  $\beta_\Phi$  are defined by:

$$d_0 = \frac{\mathcal{J}W}{\lambda} \quad (\text{A.26b})$$

$$\beta_\Phi = \frac{\mathcal{J}W}{\lambda M_\Phi} \left[ 1 - \lambda \frac{M_\Phi}{D_l} \frac{\mathcal{K} + \mathcal{F}_\Phi}{\mathcal{J}} (\Delta c^{co})^2 \right] \quad (\text{A.26c})$$



### Appendix A.3.6. $c$ -equation: analysis of terms $O(\varepsilon^2)$

For  $c$ -equation, two spurious terms in the Stefan condition arise from the analysis of terms  $O(\varepsilon^2)$ . After considering  $\phi_1 = 0$ ,  $\partial_\xi \mu_0 = 0$ , and  $\partial_\tau c_0 = 0$  (because  $c_0$  is constant), Eq. (A.6c) becomes:

$$\partial_\xi [q(\phi_0) \partial_\xi \mu_2] = -\bar{v}_n \partial_\xi c_1 - \bar{\kappa} q(\phi_0) \partial_\xi \mu_1 - q(\phi_0) \partial_{ss}^2 \mu_0 + \bar{\kappa} a(\phi_0) \Delta c^{co} \bar{v}_n \partial_\xi \phi_0$$

In the RHS, the second term  $q(\phi_0) \partial_\xi \mu_1$  is replaced by its expression Eq. (A.14). After integration w.r.t.  $\xi$ , we obtain:

$$q(\phi_0) \partial_\xi \mu_2 = -\bar{v}_n c_1 + \Delta c_0 \bar{\kappa} \bar{v}_n \int_0^\xi h(\phi_0) - \bar{\kappa} \Lambda_s \xi - \partial_{ss}^2 \mu_0 \int_0^\xi q(\phi_0) + B(\bar{s})$$

where  $B(\bar{s})$  is a constant of integration. Then we use the matching conditions and look at the limits when  $\xi$  tends to  $+\infty$  and  $-\infty$ . For  $\xi \rightarrow +\infty$ , we obtain:

$$\begin{aligned} \partial_\eta \mu_1^{out}(0^+) + \partial_{\eta\eta}^2 \mu_1^{out}(0^+) \xi &= -\bar{v}_n c_1(0^+) \\ + \Delta c_0 \bar{\kappa} \bar{v}_n \int_0^\infty [h(\phi_0) - 1] + \Delta c_0 \bar{\kappa} \bar{v}_n \xi + B(\bar{s}) \\ - \bar{\kappa} \Lambda_s \xi - \partial_{ss}^2 \mu_0 \int_0^\infty \{[q(\phi_0) - 1] + \xi\} \end{aligned}$$

and for  $\xi \rightarrow -\infty$ :

$$\begin{aligned} q_s \partial_\eta \mu_1^{out}(0^-) + q_s \partial_{\eta\eta}^2 \mu_1^{out}(0^-) \xi &= -\bar{v}_n c_1(0^-) \\ + \Delta c_0 \bar{\kappa} \bar{v}_n \int_0^{-\infty} h(\phi_0) - \bar{\kappa} \Lambda_s \xi + B(\bar{s}) \\ - \partial_{ss}^2 \mu_0 \int_0^{-\infty} \{[q(\phi_0) - q_s] + q_s \xi\} \end{aligned}$$

We focus on the terms independent of  $\xi$ :

$$\begin{aligned} \partial_\eta \mu_1^{out}(0^+) &= -\bar{v}_n c_1(0^+) - \Delta c_0 \bar{\kappa} \bar{v}_0 \mathcal{H}_l + B(\bar{s}) - \mathcal{J}_l \partial_{ss}^2 \mu_0 \\ q_s \partial_\eta \mu_1^{out}(0^-) &= -\bar{v}_n c_1(0^-) - \Delta c_0 \bar{\kappa} \bar{v}_0 \mathcal{H}_s + B(\bar{s}) - \mathcal{J}_s \partial_{ss}^2 \mu_0 \end{aligned}$$

where the integrals  $\mathcal{H}_l$ ,  $\mathcal{H}_s$ ,  $\mathcal{J}_l$  and  $\mathcal{J}_s$  are defined in Tab. 3. The first equation minus the second one yields:

$$\begin{aligned} \partial_\eta \mu_1^{out}(0^+) - q_s \partial_\eta \mu_1^{out}(0^-) &= -\bar{v}_n \Delta c_1 - \Delta c_0 \bar{\kappa} \bar{v}_n \Delta \mathcal{H} \\ &\quad - \partial_{ss}^2 \mu_0 \Delta \mathcal{J} \end{aligned} \quad (\text{A.27})$$

where  $\Delta \mathcal{H} = \mathcal{H}_l - \mathcal{H}_s$  and  $\Delta \mathcal{J} = \mathcal{J}_l - \mathcal{J}_s$ . To obtain the Stefan condition, we recombine Eq. (A.18) with  $\varepsilon \times$  Eq. (A.27):

$$D_l \partial_r \mu|_l - D_s \partial_r \mu|_s = -v_n \Delta c^{co} - \mathbb{E}_2 \Delta \mathcal{H} - \mathbb{E}_3 \Delta \mathcal{J} \quad (\text{A.28})$$

where  $\mathbb{E}_2 = W \kappa v_0 \Delta c_0$  and  $\mathbb{E}_3 = W D_l \partial_{ss}^2 \mu_0$ .

### Appendix A.4. Removal of error terms $\mathbb{E}_1, \mathbb{E}_2, \mathbb{E}_3$

Three error terms appear in the sharp interface model which is recovered by the analysis:  $\mathbb{E}_1$  in the Gibbs-Thomson condition Eq. (A.26a) and  $\mathbb{E}_2, \mathbb{E}_3$  in the Stefan condition Eq. (A.28). The errors  $\mathbb{E}_2, \mathbb{E}_3$  disappear provided that  $\Delta \mathcal{H} = 0$  and  $\Delta \mathcal{J} = 0$ . The condition  $\Delta \mathcal{H} = 0$  is fulfilled for  $h(\phi)$  defined in Tab. 2. As a matter of fact, that stays true as long as  $h(\phi)$  is an odd function of  $\phi$ . For  $\Delta \mathcal{J}$ , the same property of the interpolation function  $q(\phi)$ :  $\Delta \mathcal{J} = 0$  as long as an odd function is used to interpolate the diffusivities.

The condition  $\Delta \mathcal{F} = 0$  cannot be ensured in the model without antitrapping current (i.e.  $a(\phi) = 0$ ). However, the condition can be respected by choosing appropriately the function  $a(\phi)$  of  $\mathbf{j}_{at}$ . We already know that the integrand  $h(\phi_0)$  verifies  $\Delta \mathcal{H} = 0$ . To fulfill the condition  $\Delta \mathcal{F} = 0$ , the minimal requirement is to equalize the integrand of  $\Delta \mathcal{F}$  with  $h(\phi_0)$ :

$$\frac{h(\phi_0) - a(\phi_0) \partial_\xi \phi_0}{q(\phi_0)} = h(\phi_0)$$

Knowing  $\partial_\xi \phi_0 = 4\phi_0(1 - \phi_0)$ , we have to define the function  $a(\phi_0)$  as:

$$a(\phi_0) = \frac{[1 - q(\phi_0)]}{4\phi_0(1 - \phi_0)} h(\phi_0) = \frac{1 - q_s}{4}$$

As already mentioned, the error term  $\mathbb{E}_1$  is proportional to  $q_s$  and vanishes if  $q_s = 0$  (i.e.  $D_s = 0$ ). If  $q_s \neq 0$  then the error term disappears if  $\Delta \mathcal{F} = 0$  and  $\Delta \mathcal{G} = 0$ . Cancelling the term  $\Delta \mathcal{G}$  is possible by using one harmonic interpolation for the diffusion coefficients instead of the linear interpolation  $q(\phi)$  of Tab. 2. However, in that case,  $\Delta \mathcal{J}$  is no longer zero. To cancel both, one solution is to use a tensorial diffusivity so as to set the interpolation as linear in the direction tangent to the interface and harmonic in the normal direction (see [53, 44]). In our model,  $\mathcal{G}_l = \mathcal{G}_s = 0$  if  $q_s = 1$  (see Tab. 3) i.e. for identical diffusivities of bulk phases. Finally the error term  $\mathbb{E}_1$  disappears for two cases:  $D_s = 0$  and  $D_s = D_l$ .

## References

- [1] T. Krüger, H. Kusumaatmaja, A. Kuzmin, O. Shardt, G. Silva, E. Viggien, The Lattice Boltzmann Method. Principles and Practice, Springer, 2017. doi:10.1007/978-3-319-44649-3.
- [2] C. Pan, L.-S. Luo, C. T. Miller, An evaluation of lattice Boltzmann schemes for porous medium flow simulation, Computers & Fluids 35 (8) (2006) 898–909, proceedings of the First International Conference for Mesoscopic Methods in Engineering and Science. doi:10.1016/j.compfluid.2005.03.008.
- [3] A. Genty, V. Pot, Numerical Simulation of 3D Liquid-Gas Distribution in Porous Media by a Two-Phase TRT Lattice Boltzmann Method, Transport in Porous Media 96 (2013) pp. 271–294. doi:10.1007/s11242-012-0087-9.
- [4] V. Pot, S. Peth, O. Monga, L. Vogel, A. Genty, P. Garnier, L. Vieublé-Gonod, M. Ogurreck, F. Beckmann, P. Baveye, Three-dimensional distribution of water and air in soil pores: Comparison of two-phase two-relaxation-times lattice-Boltzmann and morphological model outputs with synchrotron X-ray computed tomography data, Advances in Water Resources 84 (2015) 87 – 102. doi:10.1016/j.advwatres.2015.08.006.
- [5] Y.-L. He, Q. Liu, Q. Li, W.-Q. Tao, Lattice Boltzmann methods for single-phase and solid-liquid phase-change heat transfer in porous media: A review, International Journal of Heat and Mass Transfer 129 (2019) 160–197. doi:10.1016/j.ijheatmasstransfer.2018.08.135.

- [6] Q. Kang, P. C. Lichtner, D. Zhang, An improved lattice Boltzmann model for multicomponent reactive transport in porous media at the pore scale, *Water Resources Research* 43 (12) (2007) W12S14 1–12. doi:10.1029/2006WR005551.
- [7] Q. Kang, L. Chen, A. J. Valocchi, H. S. Viswanathan, Pore-scale study of dissolution-induced changes in permeability and porosity of porous media, *Journal of Hydrology* 517 (2014) 1049–1055. doi:10.1016/j.jhydrol.2014.06.045.
- [8] Y. Zhang, F. Jiang, T. Tsuji, Influence of pore space heterogeneity on mineral dissolution and permeability evolution investigated using lattice Boltzmann method, *Chemical Engineering Science* 247 (2022) 117048. doi:10.1016/j.ces.2021.117048.
- [9] Z. Xu, P. Meakin, Phase-field modeling of solute precipitation and dissolution, *The Journal of Chemical Physics* 129 (1) (2008) 014705. doi:10.1063/1.2948949.
- [10] W. Mai, S. Soghrati, R. G. Buchheit, A phase field model for simulating the pitting corrosion, *Corrosion Science* 110 (2016) 157 – 166. doi:10.1016/j.corsci.2016.04.001.
- [11] C. Bringedal, L. von Wolff, I. S. Pop, Phase Field Modeling of Precipitation and Dissolution Processes in Porous Media: Upscaling and Numerical Experiments, *Multiscale Modeling & Simulation* 18 (2) (2020) 1076–1112. doi:10.1137/19M1239003.
- [12] H. Gao, L. Ju, R. Duddu, H. Li, An efficient second-order linear scheme for the phase field model of corrosive dissolution, *Journal of Computational and Applied Mathematics* 367 (2020) 112472. doi:10.1016/j.cam.2019.112472.
- [13] A. Karma, W.-J. Rappel, Quantitative phase-field modeling of dendritic growth in two and three dimensions, *Physical Review E* 57 (4) (1998) pp. 4323–4349. doi:10.1103/PhysRevE.57.4323.
- [14] B. Echebarria, R. Folch, A. Karma, M. Plapp, Quantitative phase-field model of alloy solidification, *Phys. Rev. E* 70 (2004) 061604. doi:10.1103/PhysRevE.70.061604.
- [15] J. C. Ramirez, C. Beckermann, A. Karma, H.-J. Diepers, Phase-field modeling of binary alloy solidification with coupled heat and solute diffusion, *Physical Review E* 69 (051607) (2004) 1–16. doi:10.1103/PhysRevE.69.051607.
- [16] S. G. Kim, W. T. Kim, T. Suzuki, Phase-field model for binary alloys, *Phys. Rev. E* 60 (1999) 7186–7197. doi:10.1103/PhysRevE.60.7186.
- [17] N. Provatas, K. Elder, *Phase-Field Methods in Materials Science and Engineering*, Wiley-VCH, 2010.
- [18] M. Plapp, Unified derivation of phase-field models for alloy solidification from a grand-potential functional, *Phys. Rev. E* 84 (2011) 031601. doi:10.1103/PhysRevE.84.031601.
- [19] A. Choudhury, B. Nestler, Grand-potential formulation for multicomponent phase transformations combined with thin-interface asymptotics of the double-obstacle potential, *Phys. Rev. E* 85 (2012) 021602. doi:10.1103/PhysRevE.85.021602.
- [20] D. A. Cogswell, Quantitative phase-field modeling of dendritic electrodeposition, *Phys. Rev. E* 92 (2015) 011301. doi:10.1103/PhysRevE.92.011301.
- [21] L. K. Aagesen, Y. Gao, D. Schwen, K. Ahmed, Grand-potential-based phase-field model for multiple phases, grains, and chemical components, *Phys. Rev. E* 98 (2018) 023309. doi:10.1103/PhysRevE.98.023309.
- [22] P.-C. A. Simon, L. K. Aagesen, A. T. Motta, M. R. Tonks, The effects of introducing elasticity using different interpolation schemes to the grand potential phase field model, *Computational Materials Science* 183 (2020) 109790. doi:10.1016/j.commatsci.2020.109790.
- [23] L. Ratke and P. W. Voorhees, *Growth and Coarsening*, Springer Berlin Heidelberg, 2002. doi:10.1007/978-3-662-04884-9.
- [24] R. Folch, J. Casademunt, A. Hernández-Machado, L. Ramírez-Piscina, Phase-field model for Hele-Shaw flows with arbitrary viscosity contrast. I. Theoretical approach, *Phys. Rev. E* 60 (1999) 1724–1733. doi:10.1103/PhysRevE.60.1724.
- [25] Y. Sun, C. Beckermann, Sharp interface tracking using the phase-field equation, *Journal of Computational Physics* 220 (2) (2007) 626 – 653. doi:10.1016/j.jcp.2006.05.025.
- [26] P.-H. Chiu, Y.-T. Lin, A conservative phase field method for solving incompressible two-phase flows, *Journal of Computational Physics* 230 (1) (2011) 185 – 204. doi:10.1016/j.jcp.2010.09.021.
- [27] W. Verdier, P. Kestener, A. Cartalade, Performance portability of lattice Boltzmann methods for two-phase flows with phase change, *Computer Methods in Applied Mechanics and Engineering* 370 (2020) 113266. doi:10.1016/j.cma.2020.113266.
- [28] A. Choudhury, M. Kellner, B. Nestler, A method for coupling the phase-field model based on a grand-potential formalism to thermodynamic databases, *Current Opinion in Solid State and Materials Science* 19 (5) (2015) 287–300. doi:10.1016/j.cossms.2015.03.003.
- [29] C. Introïni, J. Sercombe, I. Ramière, R. Le Tellier, Phase-field modeling with the TAF-ID of incipient melting and oxygen transport in nuclear fuel during power transients, *Journal of Nuclear Materials* 556 (2021) 153173. doi:10.1016/j.jnucmat.2021.153173.
- [30] B. Sundman, U. R. Kattner, M. Palumbo, S. G. Fries, OpenCalphad - a free thermodynamic software, *Integrating Materials and Manufacturing Innovation* 4 (1) (2015) 1–15. doi:10.1186/s40192-014-0029-1.
- [31] B. Sundman, X.-G. Lu, H. Ohtani, The implementation of an algorithm to calculate thermodynamic equilibria for multi-component systems with non-ideal phases in a free software, *Computational Materials Science* 101 (2015) 127–137. doi:10.1016/j.commatsci.2015.01.029.
- [32] A. Karma, Phase-Field Formulation for Quantitative Modeling of Alloy Solidification, *Phys. Rev. Lett.* 87 (2001) 115701. doi:10.1103/PhysRevLett.87.115701.
- [33] T. Lee, C.-L. Lin, A stable discretization of the lattice Boltzmann equation for simulation of incompressible two-phase flows at high density ratio, *Journal of Computational Physics* 206 (1) (2005) 16–47. doi:10.1016/j.jcp.2004.12.001.
- [34] H. Zheng, C. Shu, Y. Chew, A lattice Boltzmann model for multiphase flows with large density ratio, *Journal of Computational Physics* 218 (2006) pp. 353–371. doi:10.1016/j.jcp.2006.02.015.
- [35] A. Fakhari, D. Bolster, L.-S. Luo, A weighted multiple-relaxation-time lattice Boltzmann method for multiphase flows and its application to partial coalescence cascades, *Journal of Computational Physics* 341 (2017) 22 – 43. doi:10.1016/j.jcp.2017.03.062.
- [36] R. Bayle, Simulation des mécanismes de changement de phase dans des mémoires PCM avec la méthode multi-champ de phase, Phd thesis, Institut Polytechnique de Paris, <https://tel.archives-ouvertes.fr/tel-03043958> (Jul. 2020).
- [37] E. A. Brener, G. Boussinot, Kinetic cross coupling between nonconserved and conserved fields in phase field models, *Phys. Rev. E* 86 (2012) 060601. doi:10.1103/PhysRevE.86.060601.
- [38] A. Fang, Y. Mi, Recovering thermodynamic consistency of the anti-trapping model: A variational phase-field formulation for alloy solidification, *Phys. Rev. E* 87 (2013) 012402. doi:10.1103/PhysRevE.87.012402.
- [39] P. C. Fife, *Dynamics of Internal Layers and Diffusive Interfaces*, Society for Industrial and Applied Mathematics, 1988. doi:10.1137/1.9781611970180.
- [40] G. Caginalp, Stefan and Hele-Shaw type models as asymptotic limits of the phase-field equations, *Phys. Rev. A* 39 (1989) 5887–5896. doi:10.1103/PhysRevA.39.5887.
- [41] R. F. Almgren, Second-Order Phase Field Asymptotics for Unequal Conductivities, *SIAM Journal on Applied Mathematics* 59 (6) (1999) 2086–2107. doi:10.1137/S0036139997330027.
- [42] G. McFadden, A. Wheeler, D. Anderson, Thin interface asymptotics for an energy/entropy approach to phase-field models with unequal conductivities, *Physica D: Nonlinear Phenomena* 144 (1) (2000) 154–168. doi:10.1016/S0167-2789(00)00064-6.
- [43] M. Ohno, K. Matsuura, Quantitative phase-field modeling for dilute alloy solidification involving diffusion in the solid, *Phys. Rev. E* 79 (2009) 031603. doi:10.1103/PhysRevE.79.031603.
- [44] M. Ohno, T. Takaki, Y. Shibuta, Variational formulation and numerical accuracy of a quantitative phase-field model for binary alloy solidification with two-sided diffusion, *Phys. Rev. E* 93 (2016) 012802. doi:10.1103/PhysRevE.93.012802.
- [45] E. W. Hester, L.-A. Couston, B. Favier, K. J. Burns, G. M. Vasil, Improved phase-field models of melting and dissolution in multi-component flows, *Proceedings of the Royal Society A: Mathematical, Physical and Engineering Sciences* 476 (2242) (2020) 20200508. doi:10.1098/rspa.2020.0508.
- [46] D. Jamet, C. Misbah, Thermodynamically consistent picture of the phase-field model of vesicles: Elimination of the surface tension, *Phys. Rev. E* 78 (2008) 041903. doi:10.1103/PhysRevE.78.041903.
- [47] A. Cartalade, A. Younsi, M. Plapp, Lattice Boltzmann simulations of 3D crystal growth: Numerical schemes for a phase-field model with anti-trapping current, *Computers & Mathematics with Applications* 71 (9) (2016) 1784–1798. doi:10.1016/j.camwa.2016.02.029.

- [48] T. Lee, Effects of incompressibility on the elimination of parasitic currents in the lattice Boltzmann equation method for binary fluids, *Computers and Mathematics with Applications* 58 (2009) pp. 987–994. [doi:10.1016/j.camwa.2009.02.017](https://doi.org/10.1016/j.camwa.2009.02.017).
- [49] T. Lee, L. Liu, Lattice Boltzmann simulations of micron-scale drop impact on dry surfaces, *Journal of Computational Physics* 229 (2010) 8045–8063. [doi:10.1016/j.jcp.2010.07.007](https://doi.org/10.1016/j.jcp.2010.07.007).
- [50] A. Fakhari, M. Rahimian, Phase-field modeling by the method of lattice Boltzmann equations, *Physical Review E* 81 (2010) 036707.
- [51] D. W. Hahn, M. N. Özisik, *Heat Conduction*, John Wiley & Sons, Inc., 2012. [doi:10.1002/9781118411285](https://doi.org/10.1002/9781118411285).
- [52] P. Maugis, W. Hopfe, J. Morral, J. Kirkaldy, Multiple interface velocity solutions for ternary biphase infinite diffusion couples, *Acta Materialia* 45 (5) (1997) 1941–1954. [doi:10.1016/S1359-6454\(96\)00321-7](https://doi.org/10.1016/S1359-6454(96)00321-7).
- [53] M. Nicoli, M. Plapp, H. Henry, Tensorial mobilities for accurate solution of transport problems in models with diffuse interfaces, *Phys. Rev. E* 84 (2011) 046707. [doi:10.1103/PhysRevE.84.046707](https://doi.org/10.1103/PhysRevE.84.046707).

Titre : Modélisation et simulations par champ de phase de la démixtion dans le verre de confinement  $\text{Na}_2\text{O-SiO}_2\text{-MoO}_3$

Mots clés : mécanique des fluides numérique, Boltzmann sur réseau, champ de phase, verres de confinement, nucléation-croissance, écoulement diphasique

Résumé : Le confinement des déchets radioactifs issus des centrales est fait à l'aide de verres de confinement nucléaire spécialement élaborés à ce but. Le projet SIVIT du CEA s'intéresse au comportement du verre lors du processus de vitrification, où le verre et les déchets sont mélangés et portés à haute température pour ensuite se solidifier. L'une des propriétés qu'il est souhaitable de contrôler est la cinématique de séparation de phase du verre. Par exemple, le verre  $\text{Na}_2\text{O-SiO}_2\text{-MoO}_3$  peut se séparer en deux phases selon un mécanisme de nucléation-croissance avec des gouttellettes enrichies en molybdène. Le présent travail modélise et simule cette séparation de phase à l'échelle de l'interface qui sépare les deux phases liquides séparées du verre fondu. La modélisation doit satisfaire un certain nombre de contraintes : le suivi de l'interface ; la prise en compte de la diffusion chimique (qui pilote la dynamique de croissance) et de

la dynamique d'écoulement ; et le respect du paysage thermodynamique du verre. Les simulations de ce modèle doivent aussi démontrer un haut degré de performance pour en permettre les comparaisons en 3D et à une échelle satisfaisante avec ces observations expérimentales. Pour répondre à ces contraintes, nous formulons un modèle basé sur la théorie du champ de phase et son couplage à la diffusion chimique et aux équations de Navier-Stokes incompressibles. Nous discrétisons ce modèle avec la méthode de Boltzmann sur réseau et la programmons dans un nouveau code de simulation à haute performance portable, LBM\_saclay, capable d'exploiter les architectures des supercalculateurs modernes multi-GPU. Nous exposons ensuite la capacité du modèle à reproduire quantitativement la dynamique de maturation après séparation de phase et l'influence de l'écoulement et de la sédimentation sur cette dynamique.

Title : Phase-field modelling and simulations of phase separation in the two-phase nuclear glass  $\text{Na}_2\text{O-SiO}_2\text{-MoO}_3$

Keywords : computational fluid dynamics, lattice Boltzmann, phase field, nuclear glass, multiphase flow, nucleation and growth

Abstract : A safe and convenient method for the containment of nuclear waste is its inclusion in nuclear glasses, which are specifically designed to provide the best chemical, thermal and radioactive isolation. The SIVIT (Simulation of Vitrification) project of the CEA studies the behaviour of the glass during the vitrification process, where the glass and the waste are mixed and brought to a high temperature and then solidified. It is desirable to control a whole set of macroscopic properties (chemical, thermodynamic, mechanical...) in the produced material, and one of them in particular is the possible occurrence of phase separation. For example, during the vitrification of waste enriched in molybdenum, phase separation may occur following the nucleation and growth regime, with the molybdenum segregating to the daughter phase. The present work, as part of the SIVIT project, aims to model and simulate this phase separation at the scale of the interface separating the two liquid phases of the melted glass. To this end, the modelling must satisfy a number of constraints : tracking a fully-resolved interface ; accounting for the chemical diffusion (which drives the growth dynamics) and the flow dynamics and the effects of each on the motion of the interfaces ; and the

respect of the equation of state of the glass. We will first examine the case of a model ternary glass, the  $\text{Na}_2\text{O-SiO}_2\text{-MoO}_3$  compound. Its phase diagram was established at the CEA of Saclay, and experimental observations with this glass are being carried out at the CEA Marcoule. Simulations of the model must also have a high numerical efficiency to allow for comparisons in three dimensions at a satisfying scale with the previously mentioned observations. To fulfil these requirements, we formulate a model based on the phase field theory with a grand potential formulation coupled to the diffusion of the chemical components and to the incompressible Navier-Stokes equations. We discretize this model with the lattice Boltzmann method and implement it in a new high-performance simulation code, LBM\_saclay, able to exploit the multi-GPU architectures of modern supercomputers. We then demonstrate the capability of the model to quantitatively reproduce the growth dynamics after nucleation and the influence of flow and sedimentation on these dynamics. This is done with an idealized equation of state. Finally, we detail at the end the method to couple the model to the thermodynamic data of the real nuclear glass.